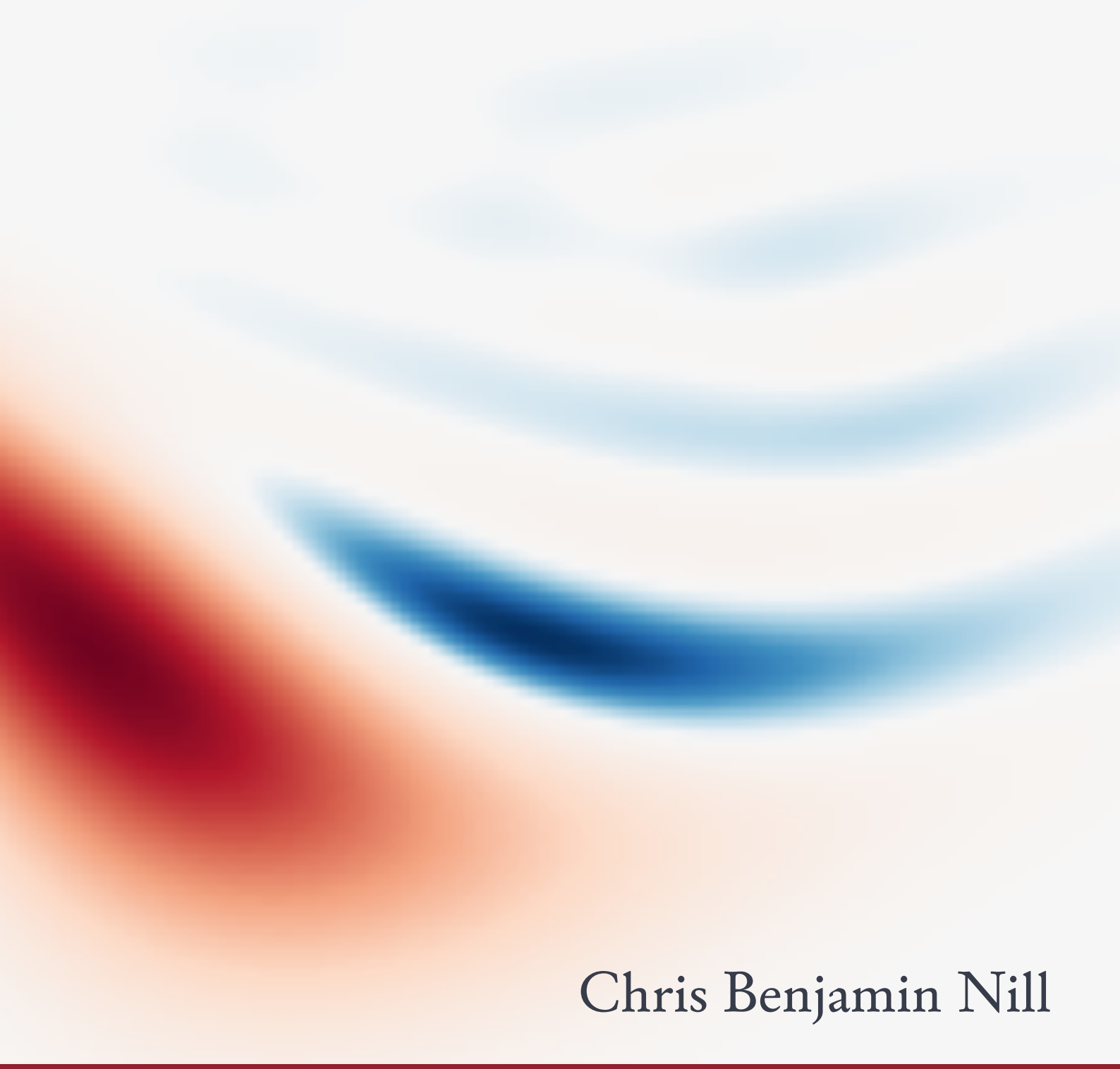

Chris Benjamin Nill

Spin-Motion Coupling and Collective Phenomena in Rydberg Atom Systems

Spin-Motion Coupling and Collective Phenomena in Rydberg Atom Systems: From Thermal Vapors to Engineered Tweezer Arrays

Dissertation

der Mathematisch-Naturwissenschaftlichen Fakultät
der Eberhard Karls Universität Tübingen
zur Erlangung des Grades eines
Doktors der Naturwissenschaften
(Dr. rer. nat.)

vorgelegt von
Chris Benjamin Nill
aus Hechingen

Tübingen
2026

Gedruckt mit Genehmigung der Mathematisch-Naturwissenschaftlichen Fakultät
der Eberhard Karls Universität Tübingen.

Tag der mündlichen Qualifikation:	27. Juli 2026
Dekan:	Prof. Dr. Thilo Stehle
1. Berichterstatter:	Prof. Dr. Igor Lesanovsky
2. Berichterstatter:	Prof. Dr. Sebastian Slama
3. Berichterstatter:	Prof. Dr. Hannes Bernien

Declaration of authenticity

Declarations concerning § 6, section 2, *Promotionsordnung der Mathematisch-Naturwissenschaftlichen Fakultät der Universität Tübingen* (12.03.2015).

I, Chris Benjamin Nill, hereby declare that

1. I have not previously undergone any discontinued or completed doctoral procedures or corresponding examination procedures.

2. The dissertation submitted has not been published, either in whole or in part, and has not already been submitted, either in whole or in part, as a dissertation or other examination paper. The papers included in this cumulative dissertation are publicly available and have been published as listed in Chap. 3.

3. I have written the cumulative dissertation submitted for the doctorate with the title „Spin-Motion Coupling and Collective Phenomena in Rydberg Atom Systems: From Thermal Vapors to Engineered Tweezer Arrays“ independently and have used only the sources and aids indicated. I affirm in lieu of an oath that this information is true and that I have not concealed anything. I am aware that making a false statement in lieu of an oath is punishable by imprisonment of up to three years or a fine.

4. The opportunity for the present doctoral procedure was not commercially procured for me. I affirm that I have not engaged the services of any organization that seeks supervisors for the preparation of dissertations in return for payment or that has taken care of all or part of the examination services incumbent upon me. I confirm that I am aware of the legal consequences of using a commercial doctoral mediator and the legal consequences of untruthfulness in this declaration (exclusion from acceptance as a doctoral candidate, exclusion from admission to the doctoral procedure, termination of the doctoral procedure and withdrawal of the degree obtained due to deception in accordance with § 21).

5. No science-related criminal convictions, disciplinary measures or pending disciplinary proceedings have been initiated against me or are present.

6. I am aware that the usage of texts or content procured by means of AI does not guarantee their quality. I am responsible for any consequences that might arise from using such methods when it comes to breaches of data protection law or copyright or scientific misconduct (e.g. plagiarism).

7. For the preparation of this cumulative dissertation, I employed AI tools for:
    a) Generation of research reports (e.g. Google Deep Research) for obtaining overviews of research fields and identifying potentially relevant references,
    b) rephrasing sentences and paragraphs to improve readability and clarity,
    c) checking for grammar and spelling errors.

Place, Date

Signature

Contents

1. Abstract **1**

2. Zusammenfassung **3**

3. List of publications **5**

3.1. Declaration of contributions 6

4. Introduction **7**

4.1. From thermal vapors to tweezer arrays 10

4.2. From coherent trapping to spin-motion coupling 11

5. Objectives **15**

6. Methods **17**

6.1. Atom-light interaction 17

6.1.1. Minimal coupling 17

6.1.2. Monochromatic field and two-level projection 19

6.1.3. Generalized Rabi Hamiltonian 21

6.1.4. Röntgen coupling 22

6.1.5. Dipole approximation and ponderomotive shift 23

6.1.6. Optical trapping of atoms 24

6.2. Rydberg atoms and the many-body Hamiltonian 26

6.2.1. Single-atom Rydberg properties 26

6.2.2. Interaction between Rydberg atoms 27

6.2.3. The driven Rydberg Hamiltonian 29

7. Results **33**

7.1. Reservoir computing in a Rydberg vapor [P1] 33

7.2. Elementary excitations in facilitated 2D Rydberg lattice [P2] 36

7.3. Rydberg-mediated entanglement of mechanical oscillators [P3] 38

7.4. Magic trapping for highly excited Rydberg states [P4] 41

7.5. Engineering multi-body interactions with stroboscopic Rydberg dressing [P5] 44

7.6. Collective motional squeezing and non-classical states [P6] 46

8. Discussion and future perspectives **51**
8.1. Stroboscopic Rydberg dressing in anharmonic trapping potentials 51
8.2. Dipole approximation breakdown in optical tweezers 51
8.3. Spin-motion coupling and sympathetic cooling in trapped Rydberg ions . . . 52
8.4. Leveraging quantum atomic motion for reservoir computing 52
8.5. Spin-motion coupling in facilitated 2D Rydberg lattices 53
8.6. Röntgen interaction in highly excited Rydberg regimes 53

9. Acknowledgements **55**

A. Publications **69**
A.1. [P1] - Time series learning in a many-body Rydberg system with emergent collective amplification 69
A.2. [P2] - Spectroscopic signatures of emergent elementary excitations in a kinetically constrained long-range interacting two-dimensional spin system 80
A.3. [P3] - Entanglement of mechanical oscillators mediated by a Rydberg tweezer chain 88
A.4. [P4] – Magic running- and standing-wave optical traps for Rydberg atoms . . 97
A.5. [P5] - Resonant stroboscopic Rydberg dressing: Electron-motion coupling and multibody interactions 108
A.6. [P6] - Creating squeezed and non-classical collective motional many-body states through stroboscopic Rydberg dressing 125

1. Abstract

Synthetic quantum systems based on neutral Rydberg atoms are versatile platforms for studying quantum many-body physics. This cumulative dissertation investigates them across scenarios of progressively increasing microscopic control. The first studies refine the control over the atoms and their interactions: from disordered thermal vapors accessible only through collective averages, through structured lattice gases with single-atom resolution, to one-dimensional tweezer arrays of individually positioned atoms. The later studies then extend this control to the optical traps, the laser drive, and ultimately the quantized motion of the atoms themselves. Along this progression, each gain in control unlocks qualitatively new many-body phenomena and applications.

At the lowest level of control, a thermal Rydberg vapor already exhibits exploitable collective behavior. Driven through a regime of optical bistability, it serves as a physical reservoir for time-series prediction. The learning performance peaks near the nonequilibrium phase transition where the collective response is amplified. Gaining single-atom resolution opens access to constrained many-body physics. In two-dimensional Rydberg lattice gases, resonant facilitation conditions based on the strong Rydberg interactions impose kinetic constraints that fragment the Hilbert space. The resulting Hilbert-space sectors support distinct elementary excitations whose spectroscopic signatures exhibit collective many-body enhancement. Narrowing the geometry to one-dimensional tweezer arrays enables precise engineering of coherent transport, and raises the question of what the resulting long-range correlations are good for. A chain of Rydberg atoms is shown to extend quantum correlations to massive objects: it mediates entanglement between two spatially separated mechanical oscillators, through both coherent dynamics and a dissipative scheme exploiting tunable Rydberg decay.

Having considered several scenarios based primarily on controlling atomic positions and interactions, the remaining studies turn to additional degrees of freedom beginning with the fields that trap the atoms. Rydberg-mediated operations require long-lived coherence, which is limited by differential AC Stark shifts from the trapping fields. A study of magic trapping reveals that the optimal detuning differs between running-wave and standing-wave configurations because the extended Rydberg electron wave function resolves the spatial structure of the trapping field. With trapping under control, the remaining frontier is the coupling between electronic excitation and atomic motion, typically a source of decoherence but exploited here as a programmable resource. Stroboscopic Rydberg dressing protocols convert spin-motion coupling into effective multi-body interactions, whose character is tuned by the pulse timing relative to the atomic

motion. Harnessed actively, the same coupling drives the collective motion of an atom chain into squeezed states, reducing interatomic distance fluctuations to a fraction of the ground-state value and producing non-classical states with substantial Wigner negativity.

Together, these studies demonstrate how progressively refining control over the interactions, positions, traps, and motion of Rydberg atoms makes the platform an increasingly powerful setting for studying quantum many-body physics.

2. Zusammenfassung

Synthetische Quantensysteme auf Basis neutraler Rydbergatome stellen äußerst vielseitige Plattformen für das Studium von Quantenvielteilchenphysik dar. Die vorliegende kumulative Dissertation untersucht sie in Szenarien mit fortschreitend zunehmender mikroskopischer Kontrolle. Die ersten Studien verfeinern die Kontrolle über die Atome und ihre Wechselwirkungen: von ungeordneten thermischen Dämpfen, die nur über kollektive Mittelwerte zugänglich sind, über strukturierte Gittergase mit Einzelatomauflösung bis hin zu eindimensionalen Pinzetten- (Tweezer)-Arrays einzeln positionierter Atome. Die späteren Studien erweitern diese Kontrolle anschließend auf die optischen Fallen, die Laseranregung und schließlich die quantisierte Bewegung der Atome selbst. Entlang dieser Abfolge erschließt jeder Zugewinn an Kontrolle qualitativ neuartige Vielteilchenphänomene und Anwendungen.

Bereits auf der grundlegendsten Ebene der Kontrolle weist ein thermischer Rydbergdampf nutzbares kollektives Verhalten auf: Im Regime der optischen Bistabilität fungiert er als physikalisches Reservoir für Zeitreihenvorhersagen. Die Lernleistung erreicht dabei in der Nähe des Nichtgleichgewichtsphasenübergangs ihr Maximum, da dort kollektive Antworten gezielt verstärkt werden. Der Übergang zur Einzelatomauflösung eröffnet den Zugang zur Physik restringierter Vielteilchensysteme. In zweidimensionalen Rydberggittergasen induzieren starke Wechselwirkungen kinetische Zwangsbedingungen, die zu einer Fragmentierung des Hilbertraums führen. Diese bringen charakteristische Elementaranregungen hervor, deren spektroskopische Signaturen eine kollektive Vielteilchenverstärkung aufweisen. Die Reduktion der Geometrie auf eindimensionale Pinzetten- (Tweezer)-Arrays ermöglicht die präzise Steuerung des kohärenten Anregungstransports und wirft die Frage auf, wozu sich die so erzeugten langreichweitigen Korrelationen nutzen lassen. Es wird demonstriert, dass eine Kette von Rydbergatomen Quantenkorrelationen auf massive Objekte ausdehnen kann: Sie vermittelt Verschränkung zwischen zwei räumlich getrennten mechanischen Oszillatoren. Dies gelingt sowohl über kohärente Dynamik als auch durch ein dissipatives Protokoll, welches den einstellbaren radiativen Zerfall der Rydbergzustände gezielt ausnutzt.

Nachdem verschiedene Szenarien betrachtet wurden, die primär auf der Kontrolle atomarer Positionen und Wechselwirkungen basieren, widmen sich die weiteren Untersuchungen zusätzlichen Freiheitsgraden – beginnend mit den Feldern, welche die Atome einfangen. Durch Rydbergatome vermittelte Operationen setzen eine präzise Kontrolle der Fallenumgebung voraus, welche durch differentielle AC-Stark Verschiebungen beeinflusst wird. Eine systematische Untersuchung sogenannter „magischer“ Fallen zeigt, dass die optimale Verstimmung sich zwischen

Lauf- und Stehwellenkonfigurationen unterscheidet. Ursächlich hierfür ist die ausgedehnte Wellenfunktion des Rydbergelektrons, die die Potentiallandschaft abtastet. Ist die Falle optimal kontrolliert, verbleibt als abschließende Herausforderung die Kopplung zwischen elektronischer Anregung und atomarer Bewegung. Was üblicherweise als Quelle von Dekohärenz gilt, wird in dieser Arbeit erfolgreich als programmierbare Ressource nutzbar gemacht: Stroboskopische Rydberg-Dressing-Protokolle wandeln die Spin-Bewegungs-Kopplung in effektive Mehrteilchenwechselwirkungen um, deren Charakter sich über das Verhältnis der Pulsdauer zur atomaren Bewegung einstellen lässt. Aktiv genutzt, treibt dieselbe Kopplung die kollektive Bewegung einer Atomkette in gequetschte (gesqueezte) Zustände: Die Fluktuationen der interatomaren Abstände werden auf einen Bruchteil ihres Grundzustandswertes reduziert, was die Präparation nichtklassischer Zustände mit ausgeprägter Wigner-Negativität erlaubt.

Zusammengenommen zeigen diese Studien, wie die fortschreitende Kontrolle über die Wechselwirkungen, Positionen, Fallen und Bewegung von Rydbergatomen die Plattform zu einem zunehmend leistungsfähigen Schauplatz für das Studium von Quantenvielteilchenphysik macht.

3. List of publications

This cumulative dissertation is based on the following publications. My respective contribution to each publication is detailed in Sec. 3.1.

[P1] Z. Liu*, Q. Ren*, C. Nill*, A. Cabot, W. Xia, Y. Tong, H. Wang, W. Yang, J. Xie, M. Jing, H. Zhang, L. Xiao, S. Jia, I. Lesanovsky, and L. Zhang, "Time series learning in a many-body Rydberg system with emergent collective amplification", Nat. Commun., 10.1038/s41467-026-77083-1 (2026).

[P2] T. Kaltenmark, C. Nill, C. Groß, and I. Lesanovsky, "Spectroscopic signatures of emergent elementary excitations in a kinetically constrained long-range interacting two-dimensional spin system", Phys. Rev. A **113**, 043706 (2026).

[P3] C. Wind*, C. Nill*, J. Gamper, S. Germer, V. Mauth, W. Alt, I. Lesanovsky, and S. Hofferberth, "Entanglement of mechanical oscillators mediated by a Rydberg tweezer chain", Phys. Rev. A **113**, 053705 (2026).

[P4] L. Ahlheit, C. Nill, D. Svirskiy, J. de Haan, S. Schroers, W. Alt, N. Stiesdal, I. Lesanovsky, and S. Hofferberth, "Magic running- and standing-wave optical traps for Rydberg atoms", Phys. Rev. A **111**, Editors' Suggestion, 013115 (2025).

[P5] C. Nill, S. de Léséleuc, C. Groß, and I. Lesanovsky, "Resonant stroboscopic Rydberg dressing: electron-motion coupling and multibody interactions", Phys. Rev. A **111**, L041104 (2025).

[P6] R. Wußler, C. Nill, S. de Léséleuc, C. Groß, and I. Lesanovsky, "Creating squeezed and non-classical collective motional many-body states through stroboscopic Rydberg dressing", 10.48550/arXiv.2606.17849 (2026).

* These authors contributed equally to the work.

3.1. Declaration of contributions

Table 3.1 summarizes my contribution to the publications listed in Chap. 3, as required by § 5, section 2 of the Doctoral Regulations of the Faculty of Science (version 12, March 2015). The following table describes my contributions to each publication.

Table 3.1. Detailed summary of my contributions to the collaborative publications comprising this cumulative dissertation. The table outlines the manuscript acceptance status, the total number of authors, and my position on the author list. The individual contribution for each project is estimated across four core research phases: conceptualization (Ideas), data generation and analytical derivations (Data), formal evaluation and interpretation (Analysis), and manuscript drafting (Writing).

Nr.	Accepted Status	Total Authors	Author Position	Ideas (%)	Data (%)	Analysis (%)	Writing (%)
P1	yes	15	1 (joint)	60	40	60	45
P2	yes	4	2	40	40	50	35
P3	yes	8	1 (joint)	45	45	45	45
P4	yes	9	2	35	50	40	40
P5	yes	4	1	50	90	70	80
P6	no	5	2	60	40	60	45

4. Introduction

Understanding strongly correlated quantum many-body systems is a central goal of modern physics. Their collective behavior underlies phenomena as varied as high-temperature superconductivity [1], the electronic properties of engineered materials [2], the structure and dynamics of complex molecules [3], and the operation of quantum sensors [4]. Such systems are, however, notoriously difficult both to describe and to control. Theoretically, the dimension of the Hilbert space required to represent a quantum many-body system grows exponentially with the number of particles, so that an exact numerical treatment is feasible only for relatively small systems [5, 6]. Experimentally, the relevant degrees of freedom in naturally occurring matter, such as the electrons in a solid, evolve on length and time scales that are far too small and too fast to access directly, and they are dressed by many competing effects that cannot easily be isolated and studied one at a time [7]. Quantum simulation offers a way around both obstacles: instead of solving or probing the original system directly, one assembles a *synthetic quantum system* with well-isolated microscopic building blocks, engineered from the bottom up to realize the same many-body Hamiltonian while remaining experimentally accessible and controllable [8–12].

A particularly versatile platform for building such synthetic systems is provided by neutral atoms: they can be trapped and arranged using optical fields, can be well isolated from their environment, and have internal electronic states that can be addressed coherently with laser light [13, 14]. In their electronic ground state, however, atoms interact only through weak, short-ranged forces [15]. Thus, strong, tunable interactions between neutral atoms have to be added to realize strongly correlated many-body physics.

Such interactions can be supplied by promoting an outermost valence electron to a state of high principal quantum number n, a *Rydberg state* [16–18]. The excited atom then acquires a set of strongly exaggerated properties that scale steeply with n: its spatial extent grows as n^2 and reaches micrometer scales, while its radiative lifetime grows as n^3 and provides a long window for coherent evolution before spontaneous emission occurs [16, 19]. The large separation between the valence electron and the ionic core also renders the atom highly polarizable [20–22], which translates into strong and tunable interatomic Rydberg interactions that are are often of van der Waals [23, 24] or resonant dipole-dipole character [25–27], with their angular dependence determined by the chosen states. Because these interactions extend over several micrometers, they readily exceed the typical spacing between atoms and dominate the remaining energy scales, so that an ensemble of Rydberg atoms naturally realizes a strongly interacting many-body system [28, 29].

To control the correlated many-body system, we utilize a laser drive between the ground and a Rydberg state. With this drive, we can alter the interaction between the atoms: if the drive is weak compared to the interaction strength, a blockade radius emerges around each Rydberg atom, inside which further excitations are strongly suppressed (Rydberg blockade) [30–32]; alternatively, the laser detuning can be chosen to compensate the nearest-neighbor interaction, so that atoms are resonantly excited only when sitting directly next to a Rydberg atom (facilitation) [33–36]. Thus, by tuning the laser frequency relative to the interaction strength, we can realize completely different many-body dynamics.

In the remainder of this chapter, we go through the scenarios considered in this work, ordered by the degree of microscopic control they require, from disordered gases to individually addressed tweezer arrays.

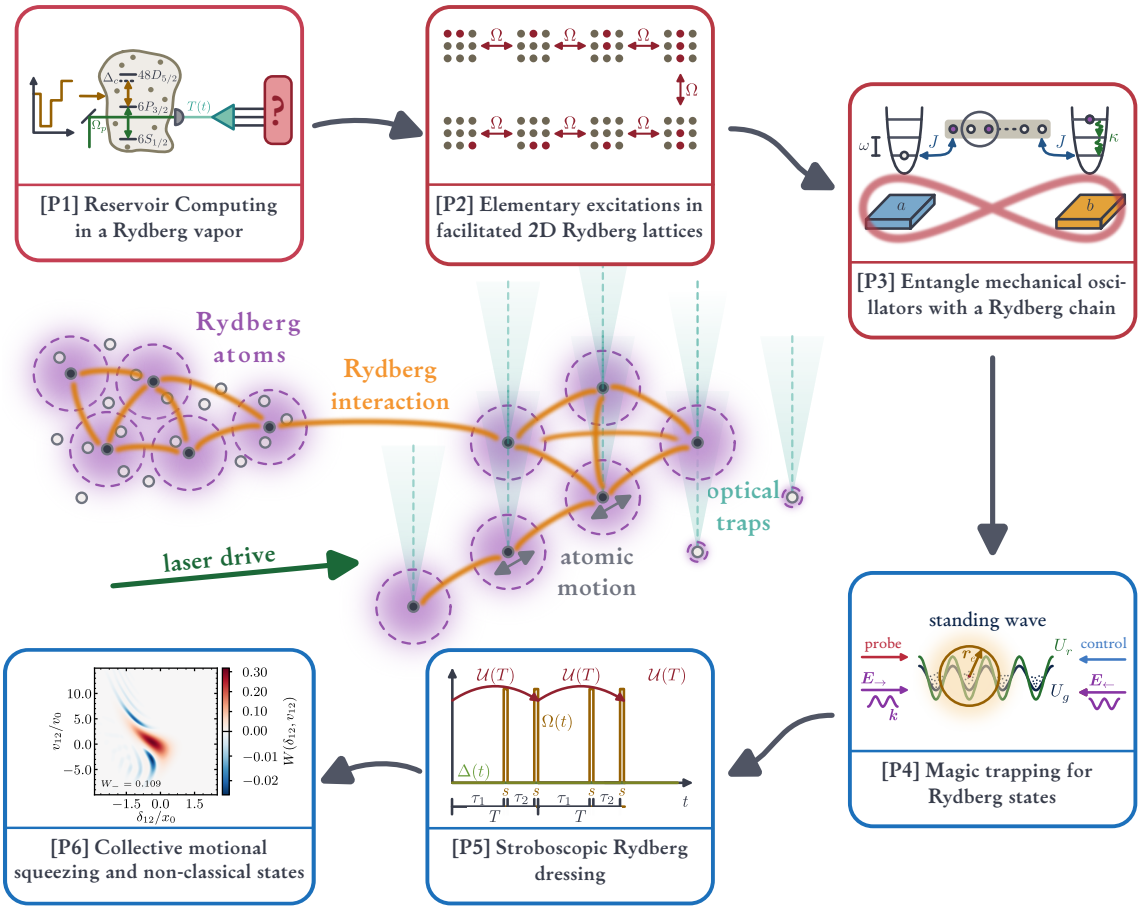

FIG. 4.1. Hierarchy of microscopic control over Rydberg atoms. The figure illustrates the results of this dissertation, which all include Rydberg atoms and their interactions. Progressively increasing microscopic control leads to qualitatively different physical phenomena, following a clockwise progression from the upper left: We start from macroscopic, disordered thermal vapors utilized for reservoir computing **[P1]**. Introducing optical traps allows single-atom resolution in two-dimensional arrays that reveals kinetically constrained elementary excitations **[P2]**. Restricting the geometry to a one-dimensional chain enables the mediation of entanglement between macroscopic mechanical oscillators **[P3]**. Higher microscopic control requires geometry-dependent magic Rydberg trapping to accommodate the large Rydberg electron wavefunction **[P4]**. With the trap optimized, tailored excitation protocols like stroboscopic dressing can control atomic motion and engineer effective multi-body interactions **[P5]**. Ultimately, harnessing the spin-motion coupling enables the active engineering of non-classical motional states with significant Wigner negativity **[P6]**. The colored frames group the studies according to the two parts of this introduction: the red boxes (**[P1]**–**[P3]**) collect the many-body scenarios realized with increasing spatial control, from thermal vapors to tweezer arrays (Sec. 4.1), whereas the blue boxes (**[P4]**–**[P6]**) collect the coherent control over the traps, the laser drive, and the quantized atomic motion that gives rise to spin-motion coupling (Sec. 4.2). The arrows trace the clockwise progression, with each step indicating an increase in control and the qualitatively new phenomena it enables.

4.1. From thermal vapors to tweezer arrays

The simplest setting in which Rydberg many-body effects can be studied is a disordered gas [37–39]. Here a macroscopic, room-temperature ensemble contains atoms that are randomly distributed in space and are continuously driven by laser light into Rydberg states [28, 40]. We control and probe this gas only at the collective level, through macroscopic averages over the whole ensemble. Because typical experimental timescales exceed the finite Rydberg lifetime, the coherent drive competes with spontaneous emission and dephasing, and the gas must be treated as an open system [41].

We describe this open system using a Lindblad master equation for the density matrix [42–44]. The master equation captures the competition between the strong Rydberg interactions and dissipation, and predicts the emergence of collective effects, most notably a bistability with a non-equilibrium phase transition, where the stationary Rydberg density switches between a low- and a high-excitation branch [39, 45, 46].

Such collective nonlinear dynamics make the gas a candidate for processing information. Computing with a physical system requires a substrate whose dynamics are rich and nonlinear, retain a memory of past inputs, and map them into a high-dimensional state space [47–50]. Operating near a phase transition supports this: there the susceptibility is strongly enhanced, so that small differences in the input grow into large and well-separable changes in the state, exactly the response a good feature map needs [51]. Such a substrate is called a reservoir, and processing information with it is known as physical reservoir computing, an approach demonstrated across a wide range of platforms [52–54]. In [P1] we ask whether the driven Rydberg gas near its bistability can itself serve as such a reservoir, and whether the phase transition improves its performance.

So far, we have discussed controlling the gas only at the collective level. Resolving and addressing individual atoms requires fixing them in space, which ordered arrays such as optical lattices or reconfigurable tweezer arrays provide [55–57]. The precise positioning lets us use the facilitation and blockade conditions to shape the dynamics of the many-body system. In particular, facilitation acts as a conditional excitation rule, resonantly exciting an atom only next to an already excited one, and thereby imposes a kinetic constraint on the many-body dynamics [58].

Such kinetic constraints are of broad interest because they limit the configurations the dynamics can reach: in many systems they can fragment the many-body Hilbert space into weakly connected sectors and thereby produce glassy behavior, characterized by slow relaxation, ergodicity breaking, and localized elementary excitations [59, 60]. In facilitated Rydberg systems, however, such constraints have so far been studied almost exclusively in one-dimensional chains [61–63], while the two-dimensional lattice has remained largely unexplored. In [P2] we ask what kinetic

constraints facilitation imposes on a two-dimensional Rydberg lattice, what elementary excitations emerge from the resulting Hilbert space fragmentation, and whether they can be detected spectroscopically.

With the atoms pinned in arrays, strong Rydberg interactions generate controllable many-body correlations. This raises the question of whether these correlations can be harnessed for applications beyond studying many-body physics itself, for example to mediate interactions between external quantum systems. One ambitious goal is to extend quantum behavior to ever larger and more massive objects. Experiments along these lines have prepared macroscopic superpositions and performed matter-wave interferometry with massive particles [64–66], and they have entangled massive macroscopic constituents [67–70]. The central obstacle is decoherence, which grows rapidly with the mass and complexity of the object, so that the scale up to which quantum coherence can be sustained remains an open question [71, 72].

A Rydberg tweezer chain offers a natural way to address this challenge by acting as a quantum bus between distant mechanical oscillators. The interface rests on a matching of energy scales: high-frequency micromechanical oscillators resonate in the gigahertz range [73, 74], which coincides with the transition frequencies between adjacent high-n Rydberg states [16, 75]. By placing one mechanical oscillator at each end of the chain, we can couple them to the respective endpoint atoms. Within the chain, the dipole-dipole interaction between neighboring atoms hops a Rydberg excitation coherently from site to site [76], so that an excitation injected at one boundary travels to the other and mediates an effective interaction between the two oscillators across their macroscopic separation. In [P3] we ask whether such a chain can mediate an interaction strong enough to entangle two distant mechanical oscillators.

4.2. From coherent trapping to spin-motion coupling

We have seen which synthetic quantum systems can be created once the Rydberg atoms and their mutual interactions are controlled: a driven gas operated near its bistability, a two-dimensional facilitated lattice, and a chain that couples distant mechanical oscillators. The required degree of microscopic control grew along the way, from collective averages over a disordered gas to individually positioned atoms in an array. In the following, we push this control onto further degrees of freedom of the platform: the traps that hold the atoms, the laser that drives electronic transitions, and finally the quantized motion of the atoms. We begin with the optical traps, which localize the atoms but can themselves become a source of decoherence.

The difficulty is that an optical trap is generally state-dependent: it shifts the energy of a ground-state atom and a Rydberg atom by different amounts. An atom prepared in a superposition therefore accumulates a state-dependent relative phase. Spatial or temporal variations of this

differential shift lead to dephasing across an atomic ensemble [77, 78]. The established remedy is magic trapping, where the trap parameters are chosen such that both states experience the same shift; this technique is routine in optical atomic clocks [79, 80] and quantum memories [81–83].

For Rydberg states this is more subtle. As the principal quantum number increases, the electron orbit grows until it becomes comparable to the wavelength of the trapping light [22, 77, 78], and the standard dipole approximation can no longer be applied to derive the conditions for a magic trap [84, 85]. The electron then samples the spatial profile of the trap field rather than a locally uniform one, so that the energy shift, and with it the magic condition, depends on the geometry of the optical potential. In [P4] we ask whether magic trapping conditions persist across different trap geometries, and how the geometry shapes the coherence between the ground and a Rydberg state.

In the previous section we considered how a single Rydberg atom can be held coherently in its trap. To realize many-body physics, however, we must hold many interacting Rydberg atoms at once. This is harder, because the strong Rydberg interaction exerts a mechanical force between the atoms, which in turn limits their coherence time. One approach to mitigate this is Rydberg dressing [86], which coherently admixes a small fraction of a Rydberg state into a long-lived ground state. The atoms then inherit a tunable portion of the strong Rydberg interaction while reducing the Rydberg population and the associated mechanical forces and decoherence. This provides a tunable compromise between interaction strength and coherence.

Dressing is usually realized by continuously driving the ground-Rydberg transition with an off-resonant laser. However, this leaves the dressed atoms susceptible to black-body radiation, leading to correlated atomic losses. Stroboscopic Rydberg dressing remedies this by instead exciting the atoms fully into the Rydberg state for short time intervals [87–89], at the price that the motional degree of freedom of the atoms must now be taken into account.

When the atoms move, their separation changes, and with it the strength of the Rydberg interaction. The electronic state and the motion of the atom thereby become coupled, an effect known as electron-motion or spin-motion coupling [90]. Averaging over the motion yields an effective description for the electronic degrees of freedom in which the atoms interact not only in pairs but in groups. This gives access to interactions among three or more atoms that are otherwise difficult to engineer. Such multi-body interactions appear in lattice models studied in statistical mechanics, such as the Baxter-Wu [91–95] and Fredkin [96–100] models, among others [101–103]. In [P5] we investigate how a stroboscopic laser excitation of the atoms together with the atomic motion, shapes the character of these multi-body interactions.

Beyond engineering multi-body interactions, we can exploit spin-motion coupling to control the quantized atomic motion itself. Even in its ground state, the motion retains a finite quantum uncertainty, which can be further reduced through motional squeezing to push the position fluctuations below the ground state limit [73, 104–109]. In a one-dimensional Rydberg chain, this motion is collective and modulates the interatomic spacing. Because the Rydberg interaction

depends nonlinearly on this spacing, this coupling can drive the collective motion into genuinely non-classical states. In [P6] we ask whether spin-motion coupling can prepare collectively squeezed motional states of an atom chain, offering an outlook for quantum-enhanced sensing and more precise control over the interaction strength by reducing fluctuations in the interatomic separation.

The studies collected in this work show how increasing the control over the Rydberg atoms, and over the interactions among them, lets us build ever more sophisticated synthetic quantum systems. In this way, the Rydberg platform becomes a versatile setting for studying increasingly complex quantum many-body systems experimentally. The specific objectives of the six publications are set out in the following chapter.

5. Objectives

The introduction in Chap. 4 established that Rydberg platforms combine strong, tunable interactions with a high degree of architectural flexibility, but also that this flexibility comes at a cost: as experiments gain microscopic control, they increasingly expose the coupling between electronic excitation and atomic motion. The objectives of this dissertation follow this tension through six studies, ordered by the degree of control they demand, with the results detailed in Chap. 7.

The starting point is to establish what collective Rydberg physics can achieve without any microscopic control: can the collective response of a thermal Rydberg vapor near its bistability be harnessed for reservoir computing tasks, and does the non-equilibrium phase transition enhance prediction performance [P1]? Gaining single-atom resolution raises a different class of questions: what constraints do Rydberg facilitation in a two-dimensional lattice impose on the many-body dynamics, what elementary excitations emerge from the resulting Hilbert space fragmentation, and can they be detected spectroscopically [P2]? Restricting the geometry further to one dimension sharpens the question of coherent transport: can a Rydberg chain mediate interactions between external quantum systems strongly enough to entangle two macroscopic mechanical oscillators [P3]?

Pursuing these applications exposes increasingly stringent requirements on the platform itself. Because the extended Rydberg electron wave function breaks the dipole approximation by sampling the trapping light, do magic trapping conditions remain valid across different trap geometries [P4]? Controlling the trap is necessary but not sufficient: the excitation protocol must also be engineered. How does the pulse timescale relative to the motional dynamics determine the character of multi-body interactions generated by stroboscopic Rydberg dressing [P5]? Can spin-motion coupling in stroboscopic Rydberg dressing prepare collectively squeezed, non-classical motional states of an atom chain [P6]?

While these six studies span vastly different experimental settings, from room-temperature vapors to microkelvin tweezer arrays, the underlying physics is governed by the same requirements of local laser driving and long-range Rydberg interactions. The following chapter introduces the common theoretical framework from which the phenomena studied in all six publications emerge.

6. Methods

This chapter establishes the theoretical foundations used across all six publications of this cumulative dissertation, thereby addressing the objectives formulated in Chapter 5. We begin with the coupling of an atom to a monochromatic light field, which yields the Rabi Hamiltonian and the optical trapping potential. We then collect the Rydberg-specific single-atom properties and pair interactions in Sec. 6.2, and assemble them with the trap-induced motion into a single many-body Hamiltonian. The section closes with an overview of the parameter regimes in which the six publications operate, locating each as a controlled reduction of that Hamiltonian.

6.1. Atom-light interaction

This section develops the theory of a neutral atom interacting with an electromagnetic field. The derivation reveals how atoms can be utilized to form qubits and effective spins, how they can be driven and manipulated by coherent light, and how they can be trapped in free space using a laser field. All systems investigated in this cumulative dissertation [P1–P6] rest on this common origin.

We start from the fundamental minimal-coupling Hamiltonian and carefully track the approximations that reduce it to the Rabi Hamiltonian for a driven spin. From the same framework, we then show how a two-level atom can be trapped by an off-resonant laser field.

For low-lying states in alkali atoms, both questions can be addressed within the electric-dipole approximation, in which the laser's spatial profile is replaced by its value at the atomic center of mass. For highly excited Rydberg states, however, the electronic orbit can become comparable to (or even larger than) the optical wavelength of the trapping field, and this approximation breaks down. We therefore derive the generalized Rabi Hamiltonian without invoking the dipole approximation, so that the result remains valid from ground-state trapping through highly excited Rydberg states.

6.1.1. Minimal coupling

We model the atom as a valence electron of mass m_e, charge $-e$, and momentum $\mathbf{p}_e$ at position $\mathbf{r}_e$, together with an ionic core, comprising the nucleus and all remaining closed-shell electrons, whose internal structure is neglected. The core is modeled as a point charge of mass M_c, charge $+e$, and momentum $\mathbf{P}_c$ at position $\mathbf{R}_c$. Working in the Coulomb gauge, $\nabla \cdot \mathscr{A} = 0$, the laser field is described entirely by the transverse vector potential $\mathscr{A}$. In this gauge the scalar potential is fixed

by the instantaneous charge distribution; the only charges present are those of the atom itself, whose mutual interaction is already contained in the Coulomb term V_C, and no external charges are assumed, so the radiation field carries no scalar potential, $\Phi = 0$. Neglecting in addition the coupling of the laser magnetic field to the electron spin, the minimal-coupling Hamiltonian [110, p. 1333] reads

$$H_{\mathrm{mc}} = \frac{\left[\mathbf{p}_c - e\,\mathscr{A}(\mathbf{R}_c, t)\right]^2}{2M_c} + \frac{\left[\mathbf{p}_e + e\,\mathscr{A}(\mathbf{r}_e, t)\right]^2}{2m_e} + V_C(|\mathbf{r}_e - \mathbf{R}_c|), \tag{6.1}$$

where V_C is the Coulomb potential and the signs of the gauge field reflect the canonical substitution $\mathbf{p} \to \mathbf{p} - q\mathscr{A}$ with $q = +e$ for the ionic core and $q = -e$ for the electron. Expanding the squares and using $\nabla \cdot \mathscr{A} = 0$ to commute $\mathscr{A}$ through the momentum operators yields

$$\begin{aligned} H_{\mathrm{mc}} = {} & \frac{\mathbf{p}_c^2}{2M_c} - \frac{e}{M_c}\mathscr{A}(\mathbf{R}_c, t)\cdot\mathbf{p}_c + \frac{e^2\mathscr{A}^2(\mathbf{R}_c, t)}{2M_c} \\ & + \frac{\mathbf{p}_e^2}{2m_e} + V_C(|\mathbf{r}_e - \mathbf{R}_c|) + \frac{e}{m_e}\mathscr{A}(\mathbf{r}_e, t)\cdot\mathbf{p}_e + \frac{e^2\mathscr{A}^2(\mathbf{r}_e, t)}{2m_e}. \end{aligned} \tag{6.2}$$

We now introduce center-of-mass and relative coordinates, $\mathbf{R} = \frac{M_c\mathbf{R}_c + m_e\mathbf{r}_e}{M}$, $\mathbf{r} = \mathbf{r}_e - \mathbf{R}_c$, with total mass $M = M_c + m_e$ and reduced mass $m = m_e M_c/M \approx m_e$. The conjugate momenta are the total and relative momenta, $\mathbf{P} = \mathbf{P}_c + \mathbf{p}_e$, $\mathbf{p} = \frac{M_c\,\mathbf{p}_e - m_e\,\mathbf{P}_c}{M}$, so that the original momenta read $\mathbf{P}_c = \frac{M_c}{M}\mathbf{P} - \mathbf{p}$ and $\mathbf{p}_e = \frac{m_e}{M}\mathbf{P} + \mathbf{p}$, while the particle positions become $\mathbf{R}_c = \mathbf{R} - \frac{m_e}{M}\mathbf{r}$ and $\mathbf{r}_e = \mathbf{R} + \frac{M_c}{M}\mathbf{r}$. Substituting these coordinate and momentum relations into the coupling terms of Eq. (6.2) and grouping them by the momentum operators yields

$$\begin{aligned} -\frac{e}{M_c}\mathscr{A}(\mathbf{R}_c, t)\cdot\mathbf{P}_c + \frac{e}{m_e}\mathscr{A}(\mathbf{r}_e, t)\cdot\mathbf{p}_e = {} & \frac{e}{M}\left[\mathscr{A}(\mathbf{r}_e, t) - \mathscr{A}(\mathbf{R}_c, t)\right]\cdot\mathbf{P} \\ & + e\left[\frac{\mathscr{A}(\mathbf{r}_e, t)}{m_e} + \frac{\mathscr{A}(\mathbf{R}_c, t)}{M_c}\right]\cdot\mathbf{p}. \end{aligned} \tag{6.3}$$

Since $m_e/M_c \approx 5 \times 10^{-5} \ll 1$, the center of mass practically coincides with the core position, $\mathbf{R} \approx \mathbf{R}_c$, and the electron position simplifies to $\mathbf{r}_e \approx \mathbf{R} + \mathbf{r}$. Using the relative center-of-mass approximations, the relative momentum term can be rewritten using the relation $1/m_e = 1/m - 1/M_c$ as:

$$e\left[\frac{\mathscr{A}(\mathbf{R}+\mathbf{r}, t)}{m_e} + \frac{\mathscr{A}(\mathbf{R}, t)}{M_c}\right]\cdot\mathbf{p} = \frac{e}{m}\mathscr{A}(\mathbf{R}+\mathbf{r}, t)\cdot\mathbf{p} - \frac{e}{M_c}\left[\mathscr{A}(\mathbf{R}+\mathbf{r}, t) - \mathscr{A}(\mathbf{R}, t)\right]\cdot\mathbf{p}. \tag{6.4}$$

Since $\mathbf{p} \sim m_e \ll M_c$, the second term on the right-hand side is suppressed by a factor of $\sim 10^{-4}$ relative to the first term and can be neglected. Similarly, the quadratic terms simplify to $\frac{e^2\mathscr{A}^2(\mathbf{R}+\mathbf{r}, t)}{2m}$ plus terms suppressed by the large core mass M_c, which are neglected. Collecting these results,

the Hamiltonian in center-of-mass and relative coordinates becomes:

$$H_{\mathrm{CM}} = \frac{\mathbf{P}^2}{2M} + \underbrace{\frac{e}{M}\left[\mathscr{A}(\mathbf{R}+\mathbf{r},t) - \mathscr{A}(\mathbf{R},t)\right]\cdot\mathbf{P}}_{H_{\mathrm{R}}} + \underbrace{\frac{\mathbf{p}^2}{2m} + V_C(|\mathbf{r}|)}_{H_{\mathrm{el}}} + \frac{e}{m}\mathscr{A}(\mathbf{R}+\mathbf{r},t)\cdot\mathbf{p} + \frac{e^2\mathscr{A}^2(\mathbf{R}+\mathbf{r},t)}{2m}. \tag{6.5}$$

In this center of mass Hamiltonian (6.5), the first term is the kinetic energy of the atom as a whole. The electronic Hamiltonian H_{el} describes the internal electronic structure of the atom and has hydrogen-like eigenstates $|n\rangle$ with energies $\hbar\omega_n$, so that $H_{\mathrm{el}} = \sum_n \hbar\omega_n |n\rangle\langle n|$. The remaining terms describe the coupling of the electronic and center-of-mass degrees of freedom to the electromagnetic field. The Röntgen term H_{R} couples the center-of-mass momentum directly to the spatial variation of the vector potential [111–113]. We carry it through the following derivation and estimate its size in Sec. 6.1.4. An alternative route would be to perform a Power-Zienau-Woolley transformation [114, 115] which recasts the center-of-mass Hamiltonian H_{CM} directly in terms of electric and magnetic fields. The Hamiltonian in the center-of-mass after substitution reads

$$H_{\mathrm{CM}} = \frac{\mathbf{P}^2}{2M} + H_{\mathrm{el}} + H_{\mathrm{R}} + \frac{e}{m}\mathscr{A}(\mathbf{R}+\mathbf{r},t)\cdot\mathbf{p} + \frac{e^2\mathscr{A}^2(\mathbf{R}+\mathbf{r},t)}{2m}, \tag{6.6}$$

with H_{R} as defined in Eq. (6.5). Crucially, $\mathscr{A}$ is still evaluated at the full electron position $\mathbf{R}+\mathbf{r}$: we have not assumed that the field is uniform on the scale of the electronic wavefunction.

6.1.2. Monochromatic field and two-level projection

We assume now that the electromagnetic field is monochromatic, e.g. formed by a single-mode laser of frequency ω_L, so that the vector potential takes the form

$$\mathscr{A}(\mathbf{R}+\mathbf{r},t) = \mathscr{A}(\mathbf{R}+\mathbf{r})\, e^{-i\omega_L t} + \mathscr{A}^*(\mathbf{R}+\mathbf{r})\, e^{i\omega_L t}, \tag{6.7}$$

where $\mathscr{A}(\mathbf{R}+\mathbf{r})$ is the complex spatial amplitude of the field. Inserting (6.7) into the center-of-mass Hamiltonian (6.6), abbreviating $\mathbf{A} \equiv \mathscr{A}(\mathbf{R}+\mathbf{r})$, and writing $\delta\mathbf{A} \equiv \mathscr{A}(\mathbf{R}+\mathbf{r}) - \mathscr{A}(\mathbf{R})$ for the field variation across the atom, yields

$$\begin{aligned} H_{\mathrm{mono}} = {} & \frac{\mathbf{P}^2}{2M} + \sum_n \hbar\omega_n |n\rangle\langle n| + \frac{e}{m}\left[\mathbf{A}\, e^{-i\omega_L t} + \mathbf{A}^* e^{i\omega_L t}\right]\cdot\mathbf{p} \\ & + \frac{e}{M}\left[\delta\mathbf{A}\, e^{-i\omega_L t} + \delta\mathbf{A}^* e^{i\omega_L t}\right]\cdot\mathbf{P} \\ & + \frac{e^2}{2m}\left[\mathbf{A}^2\, e^{-2i\omega_L t} + (\mathbf{A}^*)^2 e^{2i\omega_L t} + 2\,|\mathbf{A}|^2\right]. \end{aligned} \tag{6.8}$$

where the second line arises from the Röntgen coupling H_{R}. We treat the coupling terms in Hamiltonian (6.8) using time-dependent perturbation theory [116, 117] and assume that the laser is near-resonant with a particular pair of electronic levels: a lower-lying ground state $|g\rangle$ with energy $\hbar\omega_g$ and an excited state $|e\rangle$ with energy $\hbar\omega_e$, separated by the transition frequency $\omega_{eg} \equiv \omega_e - \omega_g > 0$. The absolute value of the detuning $\Delta = \omega_L - \omega_{eg}$ is assumed much smaller than the absolute value of the detuning to any other pair of levels. This *resonance approximation* allows us to restrict the electronic Hilbert space of the atom to the two-level subspace spanned by $|e\rangle$ and $|g\rangle$ and discard all matrix elements that connect to other levels.

Projecting onto this two-level subspace replaces each coupling operator by its 2×2 matrix in the $\{|e\rangle, |g\rangle\}$ basis. Keeping all four matrix elements of every operator, we abbreviate the paramagnetic $\Pi_{kk'}$, Röntgen $\mathscr{R}_{kk'}$, static diamagnetic $\Lambda_{kk'}$, and counter-rotating diamagnetic $\Xi_{kk'}$ couplings as

$$\begin{aligned} \Pi_{kk'} &= \frac{e}{m}\langle k|\mathbf{A}\cdot\mathbf{p}|k'\rangle, \quad \mathscr{R}_{kk'} = \frac{e}{M}\langle k|\delta\mathbf{A}|k'\rangle, \\ \Lambda_{kk'} &= \frac{e^2}{m}\langle k||\mathbf{A}|^2|k'\rangle, \quad \Xi_{kk'} = \frac{e^2}{2m}\langle k|\mathbf{A}^2|k'\rangle, \end{aligned} \tag{6.9}$$

with $k, k' \in \{e, g\}$. The diamagnetic matrix is Hermitian, $\Lambda_{kk'} = \Lambda^*_{k'k}$. The Röntgen entries multiply the center-of-mass momentum operator $\mathbf{P}$, and off the diagonal they simplify: since the subtracted amplitude $\mathscr{A}(\mathbf{R})$ does not depend on the electronic coordinate $\mathbf{r}$, it can be pulled out of the matrix element, where it vanishes by orthogonality, $\langle e|\mathscr{A}(\mathbf{R})|g\rangle = \mathscr{A}(\mathbf{R})\langle e|g\rangle = 0$, leaving $\mathscr{R}_{eg} = \frac{e}{M}\langle e|\mathbf{A}|g\rangle$. The projected Hamiltonian reads

$$\begin{aligned} H_{2\mathrm{L}} = \frac{\mathbf{P}^2}{2M} &+ \hbar\omega_e\,|e\rangle\langle e| + \hbar\omega_g\,|g\rangle\langle g| \\ &+ \left[\begin{pmatrix} \Pi_{ee} & \Pi_{eg} \\ \Pi_{ge} & \Pi_{gg} \end{pmatrix} e^{-i\omega_L t} + \begin{pmatrix} \mathscr{R}_{ee} & \mathscr{R}_{eg} \\ \mathscr{R}_{ge} & \mathscr{R}_{gg} \end{pmatrix} \cdot \mathbf{P} e^{-i\omega_L t} + \mathrm{h.c.}\right] \\ &+ \begin{pmatrix} \Lambda_{ee} & \Lambda_{eg} \\ \Lambda_{ge} & \Lambda_{gg} \end{pmatrix} + \left[\begin{pmatrix} \Xi_{ee} & \Xi_{eg} \\ \Xi_{ge} & \Xi_{gg} \end{pmatrix} e^{-2i\omega_L t} + \mathrm{h.c.}\right]. \end{aligned} \tag{6.10}$$

The first bracket collects the linear (paramagnetic plus Röntgen) couplings, oscillating at the laser frequency ω_L. The static matrix Λ is the time-averaged diamagnetic term: its diagonal entries are the state-dependent ponderomotive shifts, while its off-diagonal entries are a static, far off-resonant coupling between $|e\rangle$ and $|g\rangle$. The last bracket is the remaining diamagnetic contribution, oscillating at frequency $2\omega_L$.

6.1.3. Generalized Rabi Hamiltonian

We transform into the frame rotating at the laser frequency by applying the unitary $U(t) = e^{i\omega_L t|e\rangle\langle e|}$. The transformed Hamiltonian is

$$H_{\text{rot}} = U H_{2\text{L}} U^\dagger + i\hbar \dot{U} U^\dagger, \tag{6.11}$$

with $i\hbar \dot{U} U^\dagger = -\hbar\omega_L |e\rangle\langle e|$. We set the zero of energy at $\omega_g = 0$, so that $\omega_{eg} = \omega_e$. Under this transformation the diagonal projectors are unchanged, while $U |e\rangle\langle g| U^\dagger = e^{i\omega_L t} |e\rangle\langle g|$ and $U |g\rangle\langle e| U^\dagger = e^{-i\omega_L t} |g\rangle\langle e|$.

One entry loses all time dependence: the resonant linear coupling $(\Pi_{eg} + \mathscr{R}_{eg}\mathbf{P}) |e\rangle\langle g| e^{-i\omega_L t}$, whose phase is cancelled by the $e^{+i\omega_L t}$ of the rotated projector. Together with the diagonal energies shifted by $i\hbar\dot{U}U^\dagger$ and the static ponderomotive entries $\Lambda_{ee}, \Lambda_{gg}$, the rotated Hamiltonian splits into a time-independent part and a purely oscillating remainder,

$$\begin{aligned} H_{\text{rot}} = {} & \frac{\mathbf{P}^2}{2M} - \hbar\Delta |e\rangle\langle e| + \Lambda_{ee} |e\rangle\langle e| + \Lambda_{gg} |g\rangle\langle g| \\ & + \Big[(\Pi_{eg} + \mathscr{R}_{eg}\mathbf{P}) |e\rangle\langle g| + \text{h.c.}\Big] \\ & + \Big[Q_1 e^{-i\omega_L t} + Q_2 e^{-2i\omega_L t} + Q_3 e^{-3i\omega_L t} + \text{h.c.}\Big] \end{aligned} \tag{6.12}$$

with the constant matrices,

$$Q_1 = \begin{pmatrix} \Pi_{ee} + \mathscr{R}_{ee}\mathbf{P} & \Xi_{eg} \\ \Lambda_{ge} & \Pi_{gg} + \mathscr{R}_{gg}\mathbf{P} \end{pmatrix}, \; Q_2 = \begin{pmatrix} \Xi_{ee} & 0 \\ \Pi_{ge} + \mathscr{R}_{ge}\mathbf{P} & \Xi_{gg} \end{pmatrix}, \; Q_3 = \begin{pmatrix} 0 & 0 \\ \Xi_{ge} & 0 \end{pmatrix}. \tag{6.13}$$

Now, we apply the *rotating-wave approximation*, which consists in dropping the fast-oscillating terms. This is justified, since we are interested in the slow dynamics on timescales much longer than $1/\omega_L$, and the oscillating terms average to zero over these timescales. The resulting time-independent Hamiltonian is the *generalized Rabi Hamiltonian*, which describes effective dynamics of a two-level system under the near-resonant drive, including the Röntgen coupling and the ponderomotive shifts

$$\boxed{\begin{aligned} H_{\text{Rabi}} = {} & \frac{\mathbf{P}^2}{2M} - \hbar\Delta |e\rangle\langle e| + V^{(e)}_{\text{pond}}(\mathbf{R}) |e\rangle\langle e| + V^{(g)}_{\text{pond}}(\mathbf{R}) |g\rangle\langle g| \\ & + \frac{\hbar\Omega(\mathbf{R})}{2} |e\rangle\langle g| + \frac{\hbar\Omega^*(\mathbf{R})}{2} |g\rangle\langle e| + \underbrace{\Big[\mathscr{R}_{eg} \cdot \mathbf{P} |e\rangle\langle g| + \text{H.c.}\Big]}_{H'_{\text{R}}}. \end{aligned}} \tag{6.14}$$

Its off-diagonal entries describe the coherent coupling between $|e\rangle$ and $|g\rangle$ at the *generalized Rabi frequency*

$$\frac{\hbar\Omega(\mathbf{R})}{2} = \Pi_{eg} = \frac{e}{m} \langle e|\mathscr{A}(\mathbf{R} + \mathbf{r})\cdot\mathbf{p}|g\rangle \,. \tag{6.15}$$

The state-dependent *ponderomotive potentials*

$$V^{(k)}_{\text{pond}}(\mathbf{R}) = \Lambda_{kk} = \frac{e^2}{m}\,\langle k|\,|\mathcal{A}(\mathbf{R}+\mathbf{r})|^2\,|k\rangle\,, \tag{6.16}$$

shift each level by the local field intensity sampled over the electronic wavefunction. The contribution $-\hbar\Delta\,|e\rangle\langle e|$ is the residual energy of $|e\rangle$ in the rotating frame.

The last term is the residual Röntgen coupling H'_{R}, which, like the Rabi coupling, drives transitions between the internal states $|e\rangle$ and $|g\rangle$. In the next subsection we estimate its magnitude for a plane-wave electromagnetic field, for which it is suppressed by a factor of order v/c relative to the Rabi coupling. This is why we do not consider this term for the rest of this dissertation.

Crucially, $\mathbf{R}$ has remained a quantum-mechanical operator throughout this derivation. The spatial dependence of $\Omega(\mathbf{R})$ couples the internal transition to the center-of-mass motion, encoding the momentum exchange between laser field and atom, for example the photon-recoil kick that follows absorption [118, 119]. This coupling between the electronic and motional degrees of freedom contributes to the spin-motion dynamics investigated in [P5, P6].

The generalized Rabi Hamiltonian (6.14) is the central result of this section. Starting from the minimal-coupling Hamiltonian (6.1), we have arrived at a two-level (spin-$\frac{1}{2}$) system coherently driven by a laser field that provides a common building block of the systems studied in this dissertation.

6.1.4. Röntgen coupling

We now estimate the magnitude of the residual Röntgen coupling H'_{R} in the generalized Rabi Hamiltonian (6.14) relative to the Rabi coupling. For this estimate we assume a running wave with the spatial dependence $\mathcal{A}(\mathbf{R}+\mathbf{r}) = \mathcal{A}_0\, e^{i\mathbf{k}_L\cdot(\mathbf{R}+\mathbf{r})}$, where $\mathcal{A}_0$ is a constant amplitude and $\mathbf{k}_L$ the laser wavevector with magnitude $k_L = \omega_L/c$; a standing wave is a superposition of two such waves and leads to the same estimate. Inserting this form into the off-diagonal Röntgen entry $\mathcal{R}_{eg} = \frac{e}{M}\,\langle e|\mathbf{A}|g\rangle$ obtained in the two-level projection yields

$$\mathcal{R}_{eg} = \frac{e}{M}\,\mathcal{A}_0\, e^{i\mathbf{k}_L\cdot\mathbf{R}}\,\langle e|e^{i\mathbf{k}_L\cdot\mathbf{r}}|g\rangle \approx \frac{ie}{M}\,\mathcal{A}_0\, e^{i\mathbf{k}_L\cdot\mathbf{R}}\,\langle e|\mathbf{k}_L\cdot\mathbf{r}|g\rangle\,, \tag{6.17}$$

where we expanded $e^{i\mathbf{k}_L\cdot\mathbf{r}} \approx 1 + i\,\mathbf{k}_L\cdot\mathbf{r}$ to leading order; the constant term vanishes by orthogonality, as shown above. Truncating the expansion after the linear term is justified only as long as the spatial extent of the electronic wavefunction remains small compared to the laser wavelength, $\langle\mathbf{k}_L\cdot\mathbf{r}\rangle \ll 1$, which is the same condition that underlies the dipole approximation discussed in the next subsection. It is well satisfied for low-lying electronic states, but not guaranteed for highly excited Rydberg states, whose orbit size can become comparable to the wavelength. Within this regime the magnitude is bounded by $|\mathcal{R}_{eg}| \lesssim \frac{e}{M}\,k_L\,|\mathcal{A}_0|\,\cdot\,|\,\langle e|\mathbf{r}|g\rangle\,|$. The Rabi

coupling (6.15) evaluates, to the same leading order, to

$$|\Pi_{eg}| = \frac{e}{m} \, |\langle e|\mathbf{A}\cdot\mathbf{p}|g\rangle| \approx \frac{e}{m} \, |\mathcal{A}_0| \cdot |\langle e|\mathbf{p}|g\rangle| = e\,\omega_{eg} \, |\mathcal{A}_0| \cdot |\langle e|\mathbf{r}|g\rangle|, \tag{6.18}$$

where we used the sum rule $\langle e|\mathbf{p}|g\rangle = im\omega_{eg}\langle e|\mathbf{r}|g\rangle$, which follows from the operator identity $\mathbf{p} = \frac{im}{\hbar}[H_{\mathrm{el}}, \mathbf{r}]$. Replacing the center-of-mass momentum operator $\mathbf{P}$ in H'_{R} by the typical momentum Mv of a cold atom moving at velocity v, the ratio of the two couplings becomes

$$\frac{|\mathcal{R}_{eg}\cdot\mathbf{P}|}{|\Pi_{eg}|} \approx \frac{k_L v}{\omega_{eg}} \approx \frac{v}{c}, \tag{6.19}$$

where we used $\omega_{eg} \approx \omega_L = ck_L$ at near resonance [111–113]. For the cold atoms considered throughout this dissertation this ratio is many orders of magnitude below unity, and we therefore neglect H'_{R} in the following considerations. We emphasize that this estimate rests on two assumptions: the plane-wave form of the field and the truncation of $e^{i\mathbf{k}_L\cdot\mathbf{r}}$ after the linear term, which requires $\langle \mathbf{k}_L\cdot\mathbf{r}\rangle \ll 1$. Neither holds in general — the former excludes structured light fields such as tightly focused optical tweezers, the latter highly excited Rydberg states — so whether the suppression of the Röntgen coupling persists in these situations remains to be shown explicitly; we return to this question in Sec. 8.6.

6.1.5. Dipole approximation and ponderomotive shift

For completeness, we discuss how the familiar electric-dipole coupling and the free-electron ponderomotive shift emerge from the generalized Rabi Hamiltonian (6.14) in the electric-dipole limit, and clarify the physical meaning of the ponderomotive term.

The ponderomotive potential $V^{(n)}_{\mathrm{pond}}(\mathbf{R})$ represents the energy shift of an atomic state due to the rapid quiver motion of the electron in the oscillating electromagnetic field. In the electric-dipole approximation, which is valid when the spatial extent of the electronic wavefunction is much smaller than the wavelength of the trapping light, we approximate the vector potential as uniform over the electronic orbit, $\mathcal{A}(\mathbf{R}+\mathbf{r}) \to \mathcal{A}(\mathbf{R})$. The field amplitude then no longer depends on the electronic coordinate and factors out of the expectation values in Eq. (6.16), which become identical for both states:

$$V^{(e)}_{\mathrm{pond}}(\mathbf{R}) = V^{(g)}_{\mathrm{pond}}(\mathbf{R}) = V^{\mathrm{free}}_{\mathrm{pond}}(\mathbf{R}) = \frac{e^2|\mathcal{A}(\mathbf{R})|^2}{m}. \tag{6.20}$$

Here, $V^{\mathrm{free}}_{\mathrm{pond}}(\mathbf{R})$ in Eq. (6.20) is the free-electron ponderomotive energy. Because it shifts both electronic states $|e\rangle$ and $|g\rangle$ identically, it acts as a global energy offset and does not affect the transition frequency or drive spatial dephasing between them.

Similarly, the off-diagonal coupling reduces to its dipole form. With $\mathscr{A}(\mathbf{R}+\mathbf{r}) \to \mathscr{A}(\mathbf{R})$ the amplitude is pulled out of the matrix element in Eq. (6.15), leaving $\langle e|\mathbf{p}|g\rangle$, which we convert to a position matrix element using again the sum rule $\langle e|\mathbf{p}|g\rangle = im\omega_{eg}\langle e|\mathbf{r}|g\rangle$. The Rabi frequency then collapses to

$$\frac{\hbar\Omega_{\mathrm{dip}}(\mathbf{R})}{2} = \frac{e}{m}\mathscr{A}(\mathbf{R})\cdot\langle e|\mathbf{p}|g\rangle = ie\omega_{eg}\mathscr{A}(\mathbf{R})\cdot\langle e|\mathbf{r}|g\rangle \approx -\mathscr{E}(\mathbf{R})\cdot\mathbf{d}_{eg}. \tag{6.21}$$

The familiar electric-dipole coupling is obtained with $\mathscr{E}(\mathbf{R}) = i\omega_L\mathscr{A}(\mathbf{R})$ the spatial amplitude of the electric field and $\mathbf{d}_{eg} = -e\langle e|\mathbf{r}|g\rangle$ the transition dipole moment (using $\omega_{eg} \approx \omega_L$ at near resonance).

For highly excited Rydberg states, however, the dipole approximation breaks down because the size of the electron orbit ($\langle r\rangle \propto n^2$) becomes comparable to the wavelength of the light field. In this regime, the electron samples the spatial intensity gradients of the laser over its wavefunction, meaning the state-dependent shifts $V^{(n)}_{\mathrm{pond}}(\mathbf{R})$ must be computed using the full spatial average in Eq. (6.16). This makes the ponderomotive potential state-dependent ($V^{(e)}_{\mathrm{pond}} \neq V^{(g)}_{\mathrm{pond}}$), depending strongly on the geometry of the light field (e.g., running-wave vs. standing-wave), which is the core physics investigated in [P4].

In the next subsection we show that tuning the laser far off resonance turns the atom-light coupling into an optical trap for a neutral atom. The formulas describing this trapping can be derived either with or without the dipole approximation.

6.1.6. Optical trapping of atoms

Our aim in this subsection is to recover the well-known formula for the optical trapping of a two-level atom and to state explicitly the assumptions under which it holds. We start from the generalized Rabi Hamiltonian (6.14), which already embodies the monochromatic-field, two-level (resonance), and rotating-wave approximations, and we discard the residual Röntgen coupling H'_{R}. We consider a laser tuned off resonance whose spatial intensity profile possesses a local maximum at some position $\mathbf{R}_0$, so that the physics is dominated by the position-dependent energy shifts of the *dressed states*, the eigenstates of the atom coupled to the laser field [120, 121]. Reducing this Hamiltonian to a trapping potential for the center of mass rests on two further assumptions.

First, the laser is tuned far from resonance, $|\Delta| \gg |\Omega(\mathbf{R})|$, so that the atom is only weakly excited and the dressed states stay close to the bare states $|e\rangle$ and $|g\rangle$. This justifies expanding the dressed-state energies to leading order in $|\Omega|/|\Delta|$. The leading term of this expansion is the position-dependent energy shift that traps the atom.

Second, the internal level splitting $\hbar\sqrt{\Delta^2 + |\Omega(\mathbf{R})|^2}$ is the largest energy scale of the problem—in particular large compared with the energies of the center-of-mass motion, the photon-recoil energy $\hbar^2k_L^2/2M$ and the vibrational quantum of the resulting trap. The internal state then

follows the slowly moving atom adiabatically, the non-adiabatic couplings $\propto \nabla\Omega(\mathbf{R})$ between dressed states are negligible, and the internal Hamiltonian may be diagonalized parametrically at fixed $\mathbf{R}$. This is the Born–Oppenheimer approximation of molecular physics [122], with the internal dynamics in the role of the fast electronic motion and the center of mass in that of the slow nuclei.

For clarity we first neglect the ponderomotive contributions $V^{(k)}_{\mathrm{pond}}(\mathbf{R})$ and restore them at the end of this subsection. Under these assumptions we diagonalize the internal part of the Hamiltonian at fixed position,

$$H_{\mathrm{int}}(\mathbf{R}) = \begin{pmatrix} -\hbar\Delta & \hbar\Omega(\mathbf{R})/2 \\ \hbar\Omega^{*}(\mathbf{R})/2 & 0 \end{pmatrix}. \tag{6.22}$$

Keeping $\mathbf{R}$ as a quantum-mechanical operator would obstruct this diagonalization: the position-dependent unitary that diagonalizes $H_{\mathrm{int}}(\mathbf{R})$ does not commute with the kinetic energy $\mathbf{P}^2/2M$ and generates the derivative couplings $\propto \nabla\Omega(\mathbf{R})$ neglected above. Treating $\mathbf{R}$ parametrically when diagonalizing the internal Hamiltonian therefore neglects the non-adiabatic derivative couplings that induce transitions between the dressed-state potential surfaces, in direct analogy to the Born–Oppenheimer approximation in molecules. The eigenvalues of the internal Hamiltonian (6.22) are

$$E_{\pm}(\mathbf{R}) = \frac{\hbar}{2}\left(-\Delta \pm \sqrt{\Delta^2 + |\Omega(\mathbf{R})|^2}\right). \tag{6.23}$$

Expanding the square root of the eigenvalues in Eq. (6.23) to leading order in $|\Omega|/|\Delta| \ll 1$, with $\sqrt{\Delta^2 + |\Omega|^2} \approx |\Delta|\left(1 + |\Omega|^2/(2\Delta^2)\right)$, we focus on the red-detuned case $\Delta < 0$, i.e. $\omega_L < \omega_{eg}$, which is the regime relevant for attractive optical trapping. In this limit the eigenvalues become

$$E_{+}(\mathbf{R}) \approx -\hbar\Delta + \frac{\hbar|\Omega(\mathbf{R})|^2}{4|\Delta|}, \qquad E_{-}(\mathbf{R}) \approx -\frac{\hbar|\Omega(\mathbf{R})|^2}{4|\Delta|}. \tag{6.24}$$

Since $|\Omega(\mathbf{R})|^2$ in Eq. (6.24) is proportional to the local field intensity, both eigenvalues acquire a position-dependent energy shift of the form

$$V^{(\pm)}_{\mathrm{AC}}(\mathbf{R}) = \pm\frac{\hbar|\Omega(\mathbf{R})|^2}{4|\Delta|}, \tag{6.25}$$

referred to as the AC Stark shift in the literature [22, 116]. In the far-detuning limit $|\Omega| \ll |\Delta|$ and for $\Delta < 0$, the dressed state $|-\rangle$ correlates with the lower-lying state $|g\rangle$, and $|+\rangle$ correlates with the energetically higher state $|e\rangle$. The energy shift of $|-\rangle$ is then negative: its energy decreases with intensity, so the atom is attracted towards the intensity maximum at $\mathbf{R}_0$ and is thereby trapped. The dressed state $|+\rangle$ experiences the opposite sign and is *anti-trapped*, i.e. repelled from the intensity maximum. For blue detuning, $\Delta > 0$, the roles of $|+\rangle$ and $|-\rangle$ are reversed, and trapping of the lower-lying state instead requires an intensity minimum.

When the ponderomotive potentials (6.16) are restored, each dressed-state potential receives an additional contribution $V^{(k)}_{\text{pond}}(\mathbf{R})$. The total trapping potential for the lower-lying branch $|-\rangle \sim |g\rangle$ then reads

$$V_{\text{trap}}(\mathbf{R}) = -\frac{\hbar|\Omega(\mathbf{R})|^2}{4|\Delta|} + V^{(g)}_{\text{pond}}(\mathbf{R}). \tag{6.26}$$

In the dipole limit, the trapping potential $V_{\text{trap}}(\mathbf{R})$ in Eq. (6.26) simplifies since $V^{(e)}_{\text{pond}} = V^{(g)}_{\text{pond}} = V^{\text{free}}_{\text{pond}}$ is state-independent and, for typical optical trapping parameters, small compared to the AC Stark shift; the trapping potential is then governed entirely by (6.25). For highly excited Rydberg states, in contrast, $V^{(k)}_{\text{pond}}$ resolves the orbital structure of the electron wavefunction and can become comparable to or even exceed the energy shift. This regime, in which the dipole approximation breaks down and the generalized expressions (6.15) and (6.16) are required, is the subject of [P4] and motivates the detailed introduction of the properties of Rydberg atoms in the next section.

6.2. Rydberg atoms and the many-body Hamiltonian

This section assembles the many-body Hamiltonian that governs every system studied in this cumulative dissertation, and identifies the specific regime in which each of [P1–P6] operates. The physics rests on two properties of Rydberg atoms. Their large orbitals provide strong, controllable pair interactions on micrometer scales. Their finite radiative and black-body lifetimes set the time budget for any coherent protocol. We develop the single-atom and pair-interaction ingredients in the first two subsections, combine them with the generalized Rabi Hamiltonian of Sec. 6.1 in the third, and close by locating each publication within this parameter space.

6.2.1. Single-atom Rydberg properties

A Rydberg atom is an atom with a valence electron excited to a high principal quantum number n. The resulting hydrogen-like spectrum is modified by the ionic core, which gives rise to an atomic-species-specific quantum defect that accounts for the penetration of the Rydberg electron into the core and shifts the level positions from their hydrogenic values [16, 18, 19]. In this dissertation, we investigate Rydberg atoms across different physical behaviors. This is possible because the properties of Rydberg atoms scale strongly with n. The most important of these properties are detailed below.

Orbital size $\langle r\rangle \propto n^2$. The extension of an atom can be quantified by the mean orbital radius of the electron $\langle r\rangle$. For ground states of alkali atoms $\langle r\rangle$ is on the order of the Bohr radius a_0 [110], but it grows as n^2 for Rydberg states [16, 19]. For $n \gtrsim 70$, $\langle r\rangle$ becomes comparable to the period of an optical lattice with wavelength 1064 nm [P4]. The electric-dipole approximation, which

replaces $\mathbf{A}(\mathbf{R}+\mathbf{r})$ by $\mathbf{A}(\mathbf{R})$ in Sec. 6.1, then fails. The Rydberg electron resolves the spatial structure of the trapping light, and the ponderomotive shift (6.16) becomes a state-selective potential that depends on the trap geometry.

Dipole matrix elements. Dipole matrix elements between atomic states determine the strength of the atom-light coupling when the laser is near-resonant to a transition. For hydrogen-like atoms the transition dipole matrix element scales as n^2 for transitions between close-lying Rydberg states ($n \approx n'$) [16, 19]. Thus, Rydberg atoms host a wide range of possible transition frequencies of optical transitions from ground to Rydberg state or down to microwave and GHz transitions between nearby high-n Rydberg states. These transitions enable the resonant coupling to microelectromechanical oscillators discussed in [P3].

Radiative lifetime $\tau_{\text{rad}} \propto n^3$. The spontaneous-emission lifetime defines how long an atom is expected to stay in a specified state before decaying to a lower-lying state. The spontaneous decay rate is set by the sum over all squared dipole matrix elements for transitions to lower-lying states, which scales with the transition frequency cubed and the squared dipole matrix element, $\Gamma_{n\to n'} \propto \omega_{nn'}^3 \left|\langle n|\mathbf{d}|n'\rangle\right|^2$ [110]. For alkali states with low angular momentum, at $n \sim 70$, $\tau_{\text{rad}} \sim 100\,\mu\text{s}$ [16]. This defines an upper bound on coherence time that every coherent protocol of [P2, P3, P5, P6] must respect.

Black-body induced transitions $\Gamma_{\text{BBR}} \propto n^{-2}$. Black-body radiation drives incoherent transitions between neighboring Rydberg levels through both absorption and stimulated emission. At room temperature the energy gap between neighboring Rydberg manifolds, $\Delta E_{n,n\pm1} \ll k_B T$ for $n \gtrsim 30$, is bridged by thermal photons. These drive incoherent transitions $|r\rangle \to |r'\rangle$ at a rate $\Gamma_{\text{BBR}} \propto n^{-2}$ [123, 124]. Above $n \approx 60$ at 300 K the BBR rate dominates the total decay $1/\tau_{\text{eff}} = 1/\tau_{\text{rad}} + 1/\tau_{\text{BBR}}$ and becomes the leading decoherence channel for the high-n regime needed in [P3]. Cryogenic shielding suppresses BBR at the platform level but is challenging for tweezer experiments. Stroboscopic Rydberg dressing addresses the same problem at the protocol level by populating $|r\rangle$ only briefly, so that the time-integrated BBR loss stays small. This mechanism is explored in [P5, P6].

6.2.2. Interaction between Rydberg atoms

Due to the large distance of the valence electron from the ionic core, Rydberg atoms can form large electric dipoles. When a pair of Rydberg atoms is placed at a separation of a few micrometers, they interact electrostatically, and at these distances the dipole-dipole term dominates [16, 28]. For two atoms with relative position $\mathbf{R}$, the dipole-dipole interaction reads

$$V_{\text{dd}}(\mathbf{R}) = \frac{1}{4\pi\epsilon_0 R^3}\left[\mathbf{d}_1\cdot\mathbf{d}_2 - 3\,(\mathbf{d}_1\cdot\hat{\mathbf{R}})(\mathbf{d}_2\cdot\hat{\mathbf{R}})\right], \tag{6.27}$$

with the dipole operators $\mathbf{d}_i$ of the two atoms, $R = |\mathbf{R}|$, and $\hat{\mathbf{R}} = \mathbf{R}/R$. The Hamiltonian of the two atoms is then

$$H_{\text{pair}} = H_1 + H_2 + V_{\text{dd}}(\mathbf{R}), \tag{6.28}$$

where H_i is the single-atom Hamiltonian of atom i with known eigenstates $|n\rangle_i$ and eigenenergies $E_n^{(i)}$. The eigenstates of $H_1 + H_2$ are the pair states $|nn'\rangle = |n\rangle_1 \otimes |n'\rangle_2$ with energies $E_{nn'} = E_n + E_{n'}$.

If the atoms are too close together, the dipole-dipole interaction becomes comparable to the single-atom level spacing and the eigenstates of H_{pair} are strongly hybridized superpositions of many pair states. This is the regime of Rydberg macrodimers [125, 126]. However, in the regime of interest for this dissertation, the atoms are sufficiently far apart that the eigenstates of H_{pair} are well approximated by the pair states $|nn'\rangle$. The dipole-dipole interaction then produces energy shifts of these pair states, which we calculate using perturbation theory. We treat V_{dd} as a perturbation to $H_1 + H_2$. The first-order shift of a pair state vanishes by parity,

$$E_{nn'}^{(1)} = \langle nn'| V_{\text{dd}} |nn'\rangle = 0, \tag{6.29}$$

so the leading correction is of second order,

$$E_{nn'}^{(2)} = \sum_{mm'} \frac{\langle mm'|V_{\text{dd}}|nn'\rangle^2}{E_{nn'} - E_{mm'}}, \tag{6.30}$$

where the sum runs over the relevant dipole-coupled pair states $|mm'\rangle$. For two atoms in the same Rydberg state $|r\rangle$, and away from Förster resonances, the relevant dipole-coupled pair states $|n_1' n_2'\rangle$ are separated from $|rr\rangle$ by finite Förster defects $\delta_{n_1' n_2'} = E_{n_1' n_2'} - E_{rr}$ [16, 28, 29]. Provided that the dipole-dipole coupling is small compared with these energy defects, $|\langle n_1' n_2'| V_{\text{dd}} |rr\rangle| \ll |\delta_{n_1' n_2'}|$, the interaction can be treated perturbatively. Since $V_{\text{dd}} \propto 1/R^3$, Eq. (6.30) then yields the van der Waals shift

$$E_{rr}^{(\text{vdW})} = -\sum_{n_1' n_2'} \frac{|\langle n_1' n_2'| V_{\text{dd}} |rr\rangle|^2}{\delta_{n_1' n_2'}} \equiv -\frac{C_6}{R^6}. \tag{6.31}$$

For two atoms in different Rydberg states $|r\rangle$ and $|r'\rangle$ of opposite parity, the pair states $|rr'\rangle$ and $|r'r\rangle$ are degenerate, $\delta = 0$. The second-order expression (6.30) then diverges, and the degenerate pair must instead be treated by degenerate perturbation theory, which diagonalizes V_{dd} in the subspace $\{|rr'\rangle, |r'r\rangle\}$,

$$V_{\text{dd}}\big|_{\{rr', r'r\}} = \begin{pmatrix} 0 & C_3/R^3 \\ C_3/R^3 & 0 \end{pmatrix}, \tag{6.32}$$

where the coupling $C_3/R^3 = \left|\langle r'r|V_{\mathrm{dd}}|rr'\rangle\right|$ inherits the $1/R^3$ scaling of V_{dd} directly. Unlike the van der Waals shift, which arises at second order, the resonant exchange already appears at first order, giving the dipole-dipole interaction energy

$$E_{rr'}^{(\mathrm{dd})} = \pm\left|\langle r'r|V_{\mathrm{dd}}|rr'\rangle\right| \equiv \pm\frac{C_3}{R^3}, \tag{6.33}$$

for the symmetric and antisymmetric combinations $(|rr'\rangle \pm |r'r\rangle)/\sqrt{2}$ among pairs in opposite-parity Rydberg states.

Perturbation theory thus yields two distinct interaction regimes for a pair of hydrogen-like Rydberg atoms: the van der Waals shift and the resonant dipole-dipole exchange. They differ in their distance dependence (C_6/R^6 versus C_3/R^3), and in the pairs they govern: the van der Waals shift dominates for pairs of same Rydberg states, while the longer-ranged resonant exchange dominates for pairs in opposite-parity Rydberg states [110]. These interaction processes can be summarized in an effective Hamiltonian on the pair-state basis $\{|rr\rangle, |r'r'\rangle, |rr'\rangle, |r'r\rangle\}$, which decomposes into a diagonal block for the same-parity states and a coupled block for the opposite-parity states:

$$H_{\mathrm{pair}} = \begin{pmatrix} V_{rr}^{(\mathrm{vdW})}(\mathbf{R}) & 0 & 0 & 0 \\ 0 & V_{r'r'}^{(\mathrm{vdW})}(\mathbf{R}) & 0 & 0 \\ 0 & 0 & V_{rr'}^{(\mathrm{vdW})}(\mathbf{R}) & V_{rr'}^{(\mathrm{dd})}(\mathbf{R}) \\ 0 & 0 & V_{rr'}^{(\mathrm{dd})}(\mathbf{R}) & V_{rr'}^{(\mathrm{vdW})}(\mathbf{R}) \end{pmatrix}. \tag{6.34}$$

The diagonal terms $V_{rr}, V_{rr'}, V_{r'r'} \propto C_6/R^6$ are the van der Waals shifts of the interaction Hamiltonian (6.34); the off-diagonal term $V_{rr'} \propto C_3/R^3$ is the resonant dipole-dipole interaction strength; it leads to a flip-flop interaction for Rydberg excitations between atoms and underlies the transport dynamics of [P3]. Every coupling in Hamiltonian (6.34) depends on the interatomic distance $\mathbf{R}$, and this dependence couples the electronic degrees of freedom to the centre-of-mass motion of the atoms which we further investigate in [P5, P6].

6.2.3. The driven Rydberg Hamiltonian

The generalized Rabi Hamiltonian derived in Sec. 6.1 and the pair interactions developed above are functions of the same variables, the atomic positions $\mathbf{R}_i$. We now combine these ingredients to formulate the many-body Hamiltonian that governs the physics of many Rydberg atoms in the presence of laser driving and interactions.

We also include the motional degrees of freedom of the atoms, which are crucial for the physics of [P5, P6]. We assume that the atoms are trapped in independent three-dimensional optical potentials, where their motion is described by quantum harmonic oscillations along the three orthogonal axes $\alpha \in \{x, y, z\}$ with trap frequencies ω_α. The position of atom i is then

$\mathbf{R}_i = \mathbf{R}_i^{(0)} + \delta\mathbf{R}_i$, where the displacement vector is quantized as:

$$\delta\mathbf{R}_i = \sum_{\alpha\in\{x,y,z\}} x_{0,\alpha}(a_{i,\alpha} + a_{i,\alpha}^\dagger)\hat{\mathbf{e}}_\alpha, \tag{6.35}$$

with the displacement vector defined in Eq. (6.35), $x_{0,\alpha} = \sqrt{\hbar/(2M\omega_\alpha)}$ the harmonic oscillator length scales, and $a_{i,\alpha}$, $a_{i,\alpha}^\dagger$ the phonon operators in direction α.

We consider an N-atom system where each atom has a ground state $|g\rangle$ and two opposite-parity Rydberg states $|r\rangle$ and $|r'\rangle$. The atom is driven by a laser with Rabi frequency $\Omega(t)$ from $|g\rangle \leftrightarrow |r\rangle$; in a frame rotating with the laser, the coherent Hamiltonian reads

$$\begin{aligned} H/\hbar = &\sum_i \left[\frac{\Omega(t)}{2}\,|g\rangle\langle r|_i + \text{h.c.}\right] + \sum_i \Delta_r(t)\,|r\rangle\langle r|_i + \sum_i \Delta_{r'}(t)\,|r'\rangle\langle r'|_i \\ &+ \sum_{i<j} V_{ij}^{(rr)}(\mathbf{R}_{ij})\,|r\rangle\langle r|_i \otimes |r\rangle\langle r|_j + \sum_{i<j} V_{ij}^{(r'r')}(\mathbf{R}_{ij})\,|r'\rangle\langle r'|_i \otimes |r'\rangle\langle r'|_j \\ &+ \sum_{i<j} \left(V_{ij}^{(rr')}(\mathbf{R}_{ij})\,|r\rangle\langle r'|_i \otimes |r'\rangle\langle r|_j + \text{h.c.}\right) + \sum_i \sum_{\alpha\in\{x,y,z\}} \omega_\alpha a_{i,\alpha}^\dagger a_{i,\alpha}. \end{aligned} \tag{6.36}$$

Here, the single-atom detunings Δ_r and $\Delta_{r'}$ collect the energies of the internal states relative to the laser frequency. The pair couplings $V^{(rr)}, V^{(r'r')} \propto C_6/R^6$ are the van der Waals shifts of Hamiltonian (6.34); the dipole-dipole exchange $V^{(rr')} \propto C_3/R^3$ is the longest-ranged term and is active only when both Rydberg levels are populated. In publications [P5, P6], this motion is specialized to the longitudinal direction along the chain axis, for example by setting $\delta\mathbf{R}_i = \delta R_i \hat{\mathbf{e}}_z$, so that the phonon term in Hamiltonian (6.36) simplifies to the single-mode form $\omega \sum_i a_i^\dagger a_i$. Spontaneous emission from $|r\rangle$, $|r'\rangle$ at rate $\gamma_r, \gamma_{r'}$ and black-body-induced transitions out of $|r\rangle$ and $|r'\rangle$ at rates Γ_{BBR} enter as Lindblad dissipators [42–44] on top of Hamiltonian (6.36).

Parameter regimes of the publications. Each publication [P1–P6] derives its working Hamiltonian as a controlled reduction of Hamiltonian (6.36). The following overview organizes the reductions along the four physical ingredients of this Hamiltonian – the laser drive, the Rydberg interactions, the dissipation, and the atomic motion – and records under each which publications share a given regime.

- **Laser drive.** Most publications drive a single ground-to-Rydberg transition $|g\rangle \leftrightarrow |r\rangle$ with Rabi frequency $\Omega(t)$ [P2, P4–P6]. In the vapor of [P1] this is extended to a three-level ladder $|g\rangle \leftrightarrow |e\rangle \leftrightarrow |r\rangle$ with an intermediate state $|e\rangle$. In [P3] the laser drive does not appear in the working Hamiltonian but is required to initialize the system in the desired Rydberg configuration $\{r, r'\}$ of opposite parity, after which the dynamics arise through the interactions alone.

- **Rydberg interactions.** The van der Waals density-density shift $V^{(rr)} \propto C_6/R^6$ governs all publications that keep atoms in the same Rydberg state [P1, P2, P5, P6]. It enters in an all-to-all mean-field form in the vapor [P1], as a long-range interaction with a dominant nearest-neighbor term and weaker tails in [P2], and as a nearest-neighbor interaction in [P5, P6]. The resonant dipole-dipole exchange $V^{(rr')} \propto C_3/R^3$ between the opposite-parity states $\{r, r'\}$ instead drives the transport dynamics of [P3]. The single-atom study [P4] retains no pair interaction due to a very low Rydberg density.

- **Dissipation.** The coherent protocols of [P2, P4–P6] are treated as closed systems on the relevant timescale, with the radiative and black-body lifetimes setting the time budget but not entering as explicit dissipators. The vapor of [P1] is genuinely driven-dissipative, with spontaneous emission from the intermediate state $|e\rangle$ and additional dephasing. In [P3] engineered decay is used as a resource alongside the spontaneous emission from $|r\rangle$ and $|r'\rangle$.

- **Atomic motion.** In [P2, P3], the internal-state dynamics is much faster than the atomic motion, such that the atomic positions remain effectively fixed during the dynamics. Atomic motion is therefore neglected. In [P5, P6], the internal-state dynamics takes place on timescales comparable to the motional oscillation period. The atomic motion can therefore influence the dynamics and is retained explicitly as quantized vibrational modes. In [P1], the experiment probes a macroscopic thermal vapor without resolving individual atomic positions. The measured response is therefore an ensemble quantity, and the atomic positions are treated statistically by averaging over their spatial distribution. In [P4], the atoms are trapped but occupy different positions within the finite atomic cloud, while the light shifts vary across the trap. The experimentally observed coherence therefore is described by an ensemble average over these position-dependent light shifts.

7. Results

This chapter presents the results of the six publications that constitute this cumulative dissertation. Each section is devoted to one publication: it states the objective from Chap. 5 that the publication addresses, introduces the physical setting, and summarizes the central results. The sections are ordered by the degree of microscopic control, following the hierarchy of Fig. 4.1. The starting point is a thermal Rydberg vapor with no microscopic control, which already exhibits collectively amplified response near its bistability, enough to turn the system into a substrate for computation (Sec. 7.1). Resolving individual atoms in two-dimensional arrays opens a richer regime: strong Rydberg interactions impose kinetic constraints that fragment the Hilbert space and give rise to elementary excitations with qualitatively different mobilities, probed here through a spectroscopic scheme (Sec. 7.2). Changing the geometry to a one-dimensional chain sharpens control over coherent excitation transport such that the chain can mediate interactions between external quantum systems, concretely two macroscopic mechanical oscillators (Sec. 7.3).

Operating at this level of precision exposes requirements hidden by coarser experiments. When the Rydberg electron's orbital exceeds the spatial length scale of the trapping light structure, the magic condition becomes geometry-dependent, motivating a careful investigation of different trapping geometries (Sec. 7.4). With the trap controlled, the next lever is the excitation protocol itself: stroboscopic Rydberg dressing generates spin-motion coupling and effective multi-body interactions whose properties depend on whether the pulses are fast or adiabatic (Sec. 7.5). That same spin-motion coupling, usually treated as a source of decoherence, can then be deliberately harnessed to manipulate the collective motional state of the Rydberg atom chain (Sec. 7.6).

Throughout, the many-body Hamiltonian developed in Chap. 6 provides the common theoretical framework.

7.1. Reservoir computing in a Rydberg vapor [P1]

This section addresses the first objective of this dissertation: can the collective response of a thermal Rydberg vapor near its bistability be harnessed for reservoir computing, and does the non-equilibrium phase transition enhance the prediction performance [P1]? Such a vapor, realized here as a hot caesium gas enclosed in a glass cell and illustrated in Fig. 7.1, is the simplest setting among the six studies: it offers no microscopic control over individual atoms, so any computational capability must emerge from the collective response alone. The atoms form an untrapped gas in which Rydberg excitations interact via the van der Waals interaction. A probe

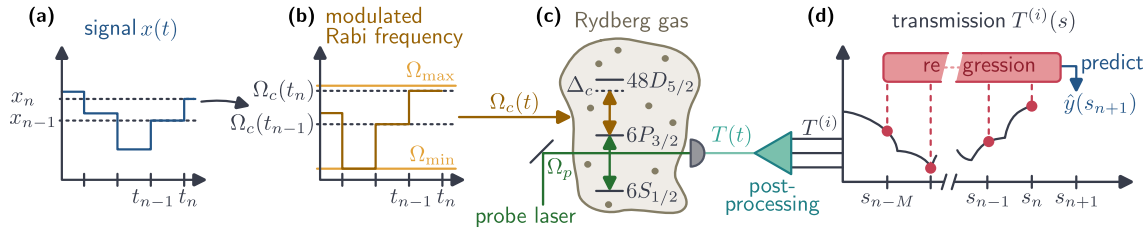

FIG. 7.1. Enhanced prediction performance of a reservoir computer based on a Rydberg vapor near the bistable region. (a) The time-dependent input signal $x(t)$ is sampled at discrete time steps t_n, yielding a piecewise constant waveform with values $x_n = x(t_n)$. **(b)** The sampled values are mapped onto the Rabi frequency $\Omega_c(t_n)$ of the coupling laser, which drives the transition from the intermediate state $6P_{3/2}$ to the Rydberg state $48D_{5/2}$ at detuning Δ_c, spanning the interval $[\Omega_{\min}, \Omega_{\max}]$ that covers the bistable window. **(c)** A probe laser with constant Rabi frequency Ω_p drives the ground state transition $6S_{1/2} \rightarrow 6P_{3/2}$; simultaneously, the modulated coupling laser addresses $6P_{3/2} \rightarrow 48D_{5/2}$, forming an electromagnetically induced transparency (EIT) ladder scheme. The optical response of the Cs vapor is monitored via the probe transmission $T(t)$. **(d)** The measured transmission $T(t)$ is smoothed with a Savitzky–Golay filter and downsampled by a factor of 20, yielding samples $T^{(i)} = T(t_{i+20n})$ for $i \in \{1, \ldots, 20\}$. The block of M consecutive samples preceding step n is fed to a linear readout trained to predict $x(t_{n+1})$ (denoted $\hat{y}_{n+1}$).

laser monitors the optical transmission while a coupling laser with Rabi frequency Ω_c dresses the atoms to a Rydberg state. The two beams form an EIT ladder scheme in which the probe transmission is sensitive to the coupling-laser amplitude through a collective Rydberg-mediated nonlinearity. It is this nonlinearity that the objective asks to put to work: if the gas acts as a physical reservoir, the collective gain that Rydberg interactions impart to the optical response should be what enables the system to predict future values of a chaotic time series.

The dynamics of the Rydberg vapor are captured by a three-level model in which atoms are driven from the ground state $|g\rangle$ through an intermediate state $|e\rangle$ to a Rydberg state $|r\rangle$. The Rydberg state has spontaneous decay rate γ. The van der Waals interaction of strength V between Rydberg atoms shifts the single-atom detuning; in the mean-field limit, after averaging over the thermal ensemble of the atoms, this becomes a density-dependent offset $\bar{n}V$, where $\bar{n}$ is the average Rydberg population fraction. The driven-dissipative dynamics are governed by a Lindblad master equation, detailed in the Methods section of [P1]. In the thermal-vapor regime, Rydberg excitations are dominated by dephasing with rate γ_d. By adiabatically eliminating the intermediate state $|e\rangle$ and subsequently the optical coherence between state $|g\rangle$ and $|r\rangle$, in the fast-dephasing limit ($\gamma_d \gg \gamma, \Omega_c$), the dynamics of $\bar{n}$ reduce to a single rate equation:

$$\dot{\bar{n}} = -\frac{\Omega_c^2 \, \Gamma \, (\bar{n} - 1/2)}{\Gamma^2 + (\Delta - \bar{n}V)^2} - \gamma \bar{n}, \tag{7.1}$$

with combined decay rate $\Gamma = (\gamma + \gamma_d)/2$. Analysis of Eq. (7.1) reveals that for specific parameters, two stable solutions for the Rydberg density $\bar{n}$ coexist. This is the *bistable region*, which appears experimentally as a hysteresis loop of the transmission against the coupling detuning scanned

forwards and backwards at fixed Rabi frequency, as shown in Fig. 2(i) of [P1]. The bistability is a collective effect arising from the interplay of Rydberg interactions and driven-dissipative dynamics.

Reservoir computing turns this collective response into a learning resource. A scalar input time series is encoded as amplitude modulation of Ω_c; the transmitted probe intensity is sampled at a fixed rate; and from those samples, a linear readout is trained to predict the next value of the input. Concretely, a sliding window of $M = 200$ consecutive transmission samples is passed to the readout layer, whose output weights are determined using a training set by least-squares regression and kept fixed for the prediction thereafter.

To quantify the prediction quality, we use the Normalized Root Mean Square Error (NRMSE), defined as:

$$\mathrm{NRMSE} = \mathrm{avg}_i \left(\sqrt{\frac{\sum_k (y_k^{(i)} - \hat{y}_k^{(i)})^2}{\sum_k (y_k^{(i)} - \bar{y}^{(i)})^2}} \right), \tag{7.2}$$

where $y_k^{(i)}$ is the target, $\hat{y}_k^{(i)}$ is the prediction, and $\bar{y}^{(i)}$ is the target mean. This measure defines the trivial baseline of NRMSE = 1 which corresponds to simply predicting the temporal average of the target sequence. Thus, a successful prediction must yield NRMSE < 1, and the smaller the NRMSE, the better the prediction quality.

The central result of [P1] is that the prediction quality is set, almost entirely, by where the operating point (in terms of Rabi frequency and detuning) sits relative to the bistable region. For specific time prediction benchmarks like the chaotic Lorenz attractor [127] (x-component prediction task) and the Mackey-Glass delay-differential equation [128] at delays $\tau = 16$ and 17, the NRMSE falls to roughly 0.3 when Δ is tuned inside the bistable region. The detailed equations for these benchmarks are given in the Supplemental Material of [P1]. On the NARMA-n (Nonlinear Auto-Regressive Moving Average) family of tasks [48], moving the operating point out of the bistable region raises the error by a factor of two to three, bringing performance close to the trivial average-predictor baseline. Furthermore, by evaluating complexities up to $n = 500$ and computing the Information Processing Capacity (IPC) [129], we find that the temporal memory available to the system is bounded by the size of the sliding readout window ($M = 200$) rather than by the physical relaxation time of the vapor. Importantly, the enhanced learning capability in the bistable region does not stem from an improved signal-to-noise ratio, which remains approximately flat across detunings. Instead, the high effective gain near the phase transition amplifies small input variations into a wide dynamic range of transmission values, providing a rich feature space that the linear readout can exploit. Outside the bistable region, the transmission response is compressed and weakly dependent on the input, leaving the linear readout insufficient to distinguish nearby input values.

Our results show that the collective response of an untrapped thermal Rydberg vapor near its bistability can be harnessed for reservoir computing, and that proximity to the non-equilibrium phase transition enhances prediction performance. However, the best-achieved NRMSE of

approximately 0.3 remains well above values reported for optimized software reservoirs [48]. Future work should investigate whether established strategies, such as input scaling or time multiplexing [47], can narrow this gap in the Rydberg vapor.

In conclusion, this section answers the first objective of this dissertation: the collectively generated gain near the non-equilibrium phase transition substantially improves the prediction of complex time-series data. However, this collective mechanism operates on a single macroscopically averaged variable and does not exploit single-atom control. Accessing single-atom resolution opens a qualitatively different class of questions, addressed in Sec. 7.2.

7.2. Elementary excitations in facilitated 2D Rydberg lattice [P2]

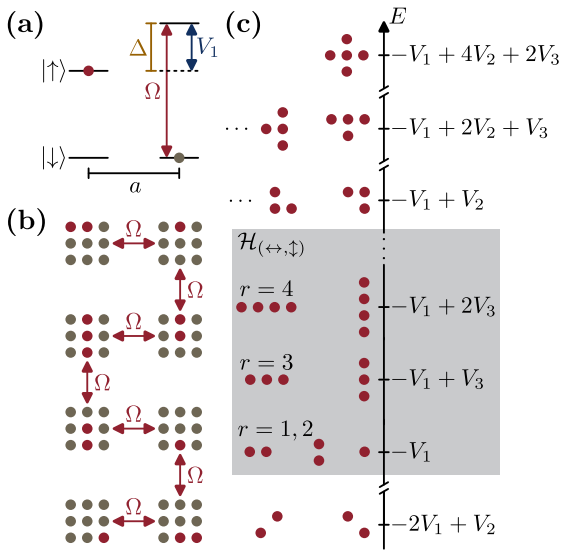

FIG. 7.2. Facilitation condition in a 2D Rydberg lattice leads to kinetic constraints and elementary excitations. (a) Level scheme of two atoms separated by one lattice constant a. The atoms are modeled by a ground state $|\downarrow\rangle$ (beige) and a Rydberg state $|\uparrow\rangle$ (red). Both states are coupled by a laser with Rabi frequency Ω and detuning Δ. The latter is chosen to compensate the nearest-neighbor Rydberg interaction, i.e. , $V_1 + \Delta = 0$, which is the so-called facilitation condition. **(b)** Some near-resonant processes in a 3×3-lattice, assuming that Ω is much larger than the next-next-nearest-neighbor interaction V_3. **(c)** Structure and energy of some elementary excitations. Here, V_2 and V_3 are the interaction energies between next-nearest and next-next-nearest neighbors, respectively. The grey box marks the Hamiltonian subspace, where elementary excitations are formed by chains of Rydberg atoms. These carry energy $r\Delta$ from their r Rydberg excitations and energy $(r-1)V_1$ from the $r-1$ nearest-neighbor pairs. Under facilitation condition, this implies a constant energy shift $-V_1$ for these elementary excitations.

This section addresses the second objective of this dissertation: what constraints does Rydberg facilitation impose on the many-body dynamics in a two-dimensional lattice, which elementary excitations emerge from the resulting fragmentation of the Hilbert space, and can they be detected spectroscopically [P2]? To pose these questions concretely, we consider a two-dimensional

tweezer array with a square lattice of spacing a, as shown in Fig. 7.2, in which atoms are modelled as two-level systems with a ground state $|\downarrow\rangle$ and a Rydberg state $|\uparrow\rangle$, driven by a laser with Rabi frequency Ω and detuning Δ. When an atom is excited to $|\uparrow\rangle$, its nearest neighbors acquire a van der Waals energy shift $V_1 = C_6/a^6$ that would ordinarily suppress their excitation, a phenomenon known as the Rydberg blockade. Choosing $\Delta = -V_1$ inverts this suppression into a facilitation (anti-blockade) condition: an atom can be resonantly excited only when it has exactly one already-excited nearest neighbor. This conditional excitation rule kinetically constrains the many-body dynamics. Since Rydberg interactions are long-ranged, they also extend to next-nearest and next-next-nearest neighbors, with interaction strengths V_2 and V_3, respectively. These interactions are weaker than V_1 but cannot generally be neglected in two dimensions. In a square lattice, the diagonal next-nearest-neighbor distance is only $\sqrt{2}\,a$, such that $V_2 = C_6/(\sqrt{2}\,a)^6 = V_1/2^3 = V_1/8$. Similarly, next-next-nearest neighbors at distance $2a$ interact with strength $V_3 = V_1/2^6 = V_1/64$.

Within the kinetically constrained Hilbert space, we identify two classes of elementary excitations with qualitatively different mobility. Mobile excitations consist of consecutive one-dimensional chains of Rydberg atoms along rows or columns of the lattice. Facilitation allows atoms to be added to or removed from the ends of these chains, enabling them to grow, shrink, and thereby explore the lattice. In contrast, immobile excitations contain Rydberg atoms on next-nearest-neighboring, i.e., diagonal, lattice sites, which introduces an additional interaction energy V_2. When $\Omega/2 \ll V_2$, removal of these diagonal Rydberg atoms is off-resonant, spatially pinning the excitation. Additional atoms can nevertheless be added or removed resonantly, such that the resulting pinned chains can still grow and shrink but cannot propagate across the lattice. A clear separation between the two types of dynamics is obtained in the regime $V_3 \ll \Omega/2 \ll V_2$: the large V_2 makes processes involving next-nearest-neighbor Rydberg pairs off-resonant, while the much smaller V_3 leaves the different mobile chain configurations near-resonantly coupled [P2].

Projecting onto the mobile sector reduces the exponentially large Hilbert space to a tractable subspace spanned by all valid mobile one-dimensional chain configurations, parametrized by chain position, orientation, and length. The dimension of this reduced space scales polynomially with the number of lattice sites, making systems as large as 11×11 sites numerically accessible. We numerically validate the effective model against the full many-body time evolution and find quantitative agreement in the limit where the next-nearest-neighbor interactions V_2 are strong enough to shift the immobile sector out of resonance and decouple it from the mobile one.

To connect the effective theory to an experimentally accessible observable, we propose a spectroscopy scheme based on a modulated drive. The Rabi frequency is varied sinusoidally at a probe frequency ν while the time-averaged Rydberg density is recorded as a function of ν. When ν matches the energy of an elementary excitation, a Fermi's Golden Rule resonance appears as a peak in the density response and the resonance position encodes the excitation energy directly. Among all the spectral lines we identify, one carries a transition rate that grows linearly

with the number of lattice sites N: the line corresponding to the coherent superposition of all symmetry-equivalent chain configurations spread uniformly across the lattice. This collectively enhanced line, a bright superradiant-like state with N-fold amplification over the single-site transition rate, is the most robust experimental signature the scheme provides, because it requires only a global laser modulation.

The 2D facilitated array of [P2] demonstrates how Rydberg facilitation under single-atom resolution imposes kinetic constraints that fragment the Hilbert space, giving rise to distinct mobile and immobile excitation classes. We show that these excitations can be probed spectroscopically, and that the collective enhancement of the mobile chains yields a robust experimental signature with a bright superradiant-like state. This answers the second objective of this dissertation: we have identified the constraints and excitations of the 2D facilitated lattice gas and demonstrated their spectroscopic observability. Moving from isolated many-body dynamics in a tweezer array, we now turn to a hybrid system where a Rydberg chain realized in a 1D tweezer array acts as a bus to couple two macroscopic mechanical oscillators, detailed in Sec. 7.3.

7.3. Rydberg-mediated entanglement of mechanical oscillators [P3]

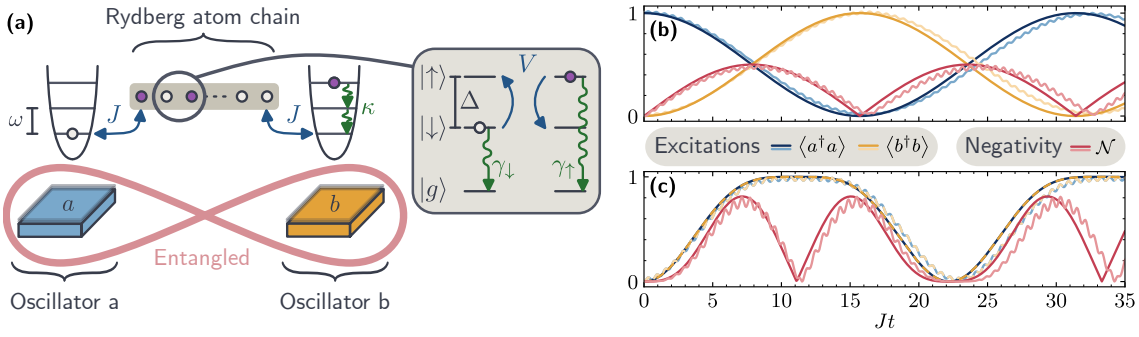

FIG. 7.3. A Rydberg chain acting as a quantum bus to entangle distant massive mechanical resonators. (a) Schematic of the oscillator-atom system illustrating the levels, coupling strengths and decay rates. Excitations in the Rydberg spin chain and the oscillators are depicted as violet filled circles, while white filled circles indicate the absence of excitations. **(b,c)** Coherent evolution of the number of excitations in the oscillators $\langle a^\dagger a\rangle$, $\langle b^\dagger b\rangle$ and oscillator entanglement quantified by the negativity $\mathcal{N}$. The results correspond to the system presented in (a) with $N = 2$ atoms and $V = 10J$. In panel (b) the system is initialized in $|\psi_1\rangle$ and in panel (c) in $|\psi_2\rangle$, as described in the text. Dark lines are obtained from the effective Hamiltonian, while lighter, semi-transparent lines show the exact dynamics under the full Hamiltonian. In panel **(c)**, $\langle b^\dagger b\rangle$ is shown as a dashed curve to improve visibility.

This section addresses the third objective of this dissertation: can a Rydberg chain mediate interactions between external quantum systems strongly enough to entangle two macroscopic mechanical oscillators [P3]? The first requirement for such a hybrid interface is that the external systems match the energy scales of the chain. As already motivated in the introduction in Sec. 4.1,

Rydberg states near principal quantum number $n \approx 90$ carry electric dipole transitions in the gigahertz regime, matching the resonance frequencies of high-overtone bulk acoustic resonators (HBARs) [73, 74], which are microelectromechanical resonators that have recently demonstrated coherence times on the order of one millisecond. This makes Rydberg atoms and HBARs a natural hybrid system: the endpoint atoms of a tweezer-trapped Rydberg chain can couple resonantly to the evanescent electric field of an adjacent oscillator, making spin and mechanical excitations dynamically interchangeable. In [P3] we exploit this interface to show that the chain can act as a quantum bus, schematically shown in Fig. 7.3, converting its intrinsic coherent spin dynamics into entanglement between two distant macroscopic mechanical oscillators.

Each Rydberg atom in the chain is modeled as a spin-$\frac{1}{2}$ system with states $|\uparrow\rangle$ and $|\downarrow\rangle$ separated by energy Δ. Nearest-neighbor atoms interact at rate V through the resonant dipole-dipole flip-flop exchange detailed in Sec. 6.2.2, transporting spin excitations along the chain. The two endpoint atoms couple resonantly to their adjacent oscillators at oscillator frequency $\omega = \Delta$ and coupling strength J, with $J \ll V$ so that the chain acts as an off-resonant mediator. Both Rydberg states can decay to an electronic ground state $|g\rangle$: the upper state $|\uparrow\rangle$ at rate $\gamma_\uparrow$ and the lower state $|\downarrow\rangle$ at rate $\gamma_\downarrow$, both of which are tunable by laser dressing of the Rydberg level.

In the limit $J \ll V$, the oscillator coupling perturbs the chain weakly and the chain remains close to its own eigenstates. To illustrate this, we perform a Schrieffer-Wolff transformation [130], a systematic perturbative elimination of off-resonant transitions, for a chain of two atoms that projects the full Hamiltonian onto the effective Hamiltonian

$$\begin{aligned} H_{\text{eff}} = &- \frac{J^2}{V}\left(a^\dagger b + a b^\dagger\right)\left(|\downarrow\downarrow\rangle\langle\downarrow\downarrow| + |\uparrow\uparrow\rangle\langle\uparrow\uparrow| - |S\rangle\langle S| - |T\rangle\langle T|\right) \\ &- \frac{J^2}{V}\left[\left(a^{\dagger 2} + b^{\dagger 2}\right)|\downarrow\downarrow\rangle\langle\uparrow\uparrow| + \left(a^2 + b^2\right)|\uparrow\uparrow\rangle\langle\downarrow\downarrow|\right] \\ &+ \left(V + \frac{J^2 \mathscr{M}}{V}\right)\left(|T\rangle\langle T| - |S\rangle\langle S|\right) + \mathscr{M}\omega. \end{aligned} \tag{7.3}$$

Here $|S\rangle\langle S|$ and $|T\rangle\langle T|$ are the projectors onto the singlet and triplet subspaces of the two spins, $\mathscr{M} = \sum_i |\uparrow\rangle\langle\uparrow|_i + a^\dagger a + b^\dagger b$ is the total excitation number operator, and two effective oscillator couplings emerge: a direct oscillator-oscillator exchange at rate J^2/V and pair-exchange terms that coherently transfer two excitations between the chain and the oscillator pair. Importantly, the dynamics under the effective Hamiltonian conserve the total excitation number $\mu = \langle\mathscr{M}\rangle$.

Because μ is conserved, the initial state sets a ceiling on the achievable entanglement. We show that μ defines an upper bound on the oscillator entanglement of the reduced two-oscillator state, quantified by the negativity $\mathcal{N}$ [131]. This negativity is a measure of quantum entanglement that is zero for separable states and can be positive for entangled ones. The bound satisfies:

$$\mathcal{N} \leq \frac{1}{2}[\mu]. \tag{7.4}$$

We demonstrate this bound by computing the coherent dynamics for two choices of initial state, shown in Fig. 7.3(b,c). Both initial states, $|\psi_1\rangle = |1\rangle_a \otimes |S\rangle \otimes |0\rangle_b$ and $|\psi_2\rangle = |0\rangle_a \otimes |\uparrow\uparrow\rangle \otimes |0\rangle_b$, have the same total excitation number $\mu = 2$ and therefore share the general bound $\mathcal{N} \leq 1$. For $|\psi_1\rangle$, however, only single-excitation exchange between the oscillators is possible, such that their total excitation number remains fixed at one. This imposes the tighter bound $\mathcal{N} \leq 1/2$. For $|\psi_2\rangle$, the pair-exchange terms in H_{eff} can transfer both spin excitations into the oscillators, allowing their excitation number to reach two and the negativity to approach the general bound $\mathcal{N} \leq 1$. In principle, the coherent dynamics can be halted at the moment of maximum negativity. This can be achieved, for example, by ionizing the atoms out of their tweezers, thereby freezing the oscillators in the desired entangled state. In practice, such precise timing is demanding.

Timing coherent evolution to stop at maximum negativity requires precise external control and timing. We additionally propose a dissipative scheme that generates entanglement and stops automatically by exploiting the structure of atomic decay. To do so, we initialize all N atoms in $|\uparrow\rangle$ and both oscillators in the ground state. The chain evolves according to a quantum jump trajectory. When an atom decays through $\gamma_\downarrow$, the jump operator $|g\rangle\langle\downarrow|$ removes it from a state that μ never counted: only $|\uparrow\rangle$ occupancy enters μ, so a $|\downarrow\rangle \rightarrow |g\rangle$ transition leaves the conserved quantity unchanged. The oscillator excitations already resident in the oscillators are therefore unaffected, and the full entanglement budget remains available. Decay through $\gamma_\uparrow$ instead removes one unit from μ per event and reduces the achievable negativity. Once all atoms have reached $|g\rangle$, the atom-oscillator coupling switches off and the oscillator state is frozen; a trajectory in which every atom decays through $\gamma_\downarrow$ transfers the full excitation budget $\mu = N$ into the oscillator pair and can approach the bound $\mathcal{N} \leq N/2$.

Having understood the entanglement mechanism of the dissipative dynamics, we turn to the investigation of optimal parameters. We find that the average final-state negativity over many quantum trajectories peaks as a function of $\gamma_\downarrow$, and two competing mechanisms set the position of this peak. If $\gamma_\downarrow$ is too small, the total evolution time is long and the probability of a harmful $\gamma_\uparrow$ decay increases. If $\gamma_\downarrow$ is too large, the first decay event splits the chain prematurely into two uncoupled sub-chains, each coupled to only one oscillator, before correlations have propagated to both endpoints; the two oscillators then cannot become entangled with each other. The optimal $\gamma_\downarrow$ is therefore smaller than the coherent coupling J and shifts to lower values as N increases, because longer chains require more time to build up correlations between their endpoints. Taking into account the realistic oscillator decay at rate κ, stemming from a finite coherence time of the HBARs, post-selecting on trajectories in which all atoms reach $|g\rangle$ within a window short compared to $1/\kappa$ recovers near-ideal average negativity.

The analysis of [P3] establishes the Rydberg tweezer chain as a quantum interface capable of exporting nonclassical correlations to macroscopic mechanical objects, using engineered atomic dissipation as a practical alternative to precise coherent timing. This directly addresses the third objective of this dissertation: demonstrating that a Rydberg chain can mediate coupling to external macroscopic resonators strongly enough to generate entanglement.

The first three results sections covered applications of Rydberg arrays under progressively richer control. In Sec. 7.4, the chapter shifts focus from applications to the platform itself, beginning with the requirements for trapping a Rydberg atom when its large orbital causes the point-particle treatment in the optical potential to break down.

7.4. Magic trapping for highly excited Rydberg states [P4]

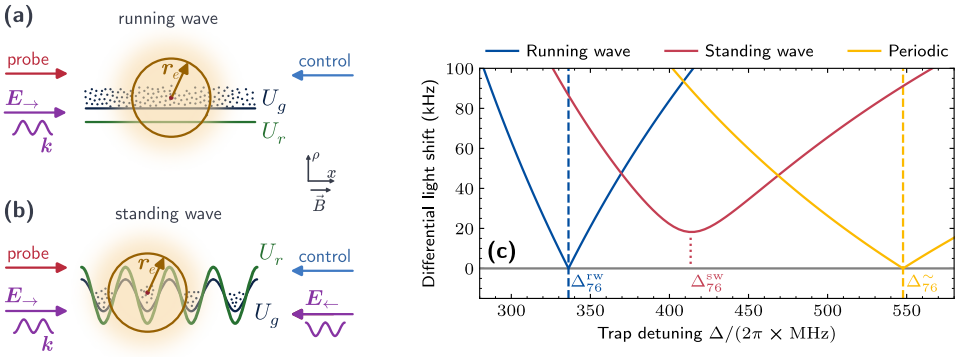

FIG. 7.4. Magic trapping conditions depend strongly on the trapping geometry due to finite Rydberg electron wavefunction size. (a,b) Comparison between a running-wave trap and a standing-wave optical lattice. When the principal quantum number is high, the Rydberg electron orbit becomes comparable in size to the lattice period, causing the electron to average over the periodic potential landscape and making the magic condition strongly geometry-dependent. **(c)** Standard deviation of the differential light shift between ground and Rydberg state, integrated over the atomic cloud volume, as a function of trap detuning Δ for the running-wave, full standing-wave, and purely periodic potential components. The optimal standing-wave magic detuning Δ_n^{sw} minimises this standard deviation and lies between the analytic running-wave optimum Δ_n^{rw} and the purely periodic optimum $\Delta_n^{\sim}$.

Operating any of these Rydberg systems with high principal quantum numbers exposes a fundamental platform constraint: the point-particle treatment of the atom in the trapping potential breaks down when the electron orbital grows comparable to the trap wavelength, see Chap. 6. This breakdown raises the fourth objective of this dissertation: does the magic detuning that is supposed to equalize the light shifts of the ground and Rydberg states remain valid across different trap geometries [P4]? To address this question, we study laser-cooled ^{87}Rb atoms at $T \sim 2\,\mu$K, trapped in two distinct geometries, schematically compared in Fig. 7.4: a single-beam running-wave optical dipole trap and a retro-reflected one-dimensional standing-wave lattice, both operating at a trap wavelength $\lambda_T \approx 1012\,$nm. At this wavelength the laser is far

red-detuned for the ground state $|g\rangle = |5S_{1/2}\rangle$, providing a standard attractive dipole potential, while near-resonantly coupling the Rydberg state $|r\rangle = |nS_{1/2}\rangle$ to the lower-lying $|a\rangle = |6P_{3/2}\rangle$ manifold and thereby generating an attractive potential for the Rydberg state as well.

In this setup, we investigate the coherence time t_c between $|g\rangle$ and $|r\rangle$ which we probe via electromagnetically induced transparency (EIT) in a storage and retrieval experiment: few-photon probe pulses at 780 nm are stored as collective Rydberg excitations by a 480 nm control beam and retrieved after a variable storage time t_s. The central decoherence mechanism for Rydberg excitations in the trap is the inhomogeneous differential light shift between $|g\rangle$ and $|r\rangle$, which causes dephasing across the atomic ensemble. By tuning the trap detuning Δ to the *magic detuning*, the differential shift can be minimized, or ideally cancelled.

To quantify this, we derive the magic trapping conditions for both geometries using a theoretical model and compare the results to experiment. The central modeling challenge is set by the scale of the Rydberg electron orbit. A Rydberg atom at principal quantum number n carries an electron whose mean orbital radius scales as $n^2 a_0$, where a_0 is the Bohr radius. For $n \sim 70$, the orbital diameter reaches several hundred nanometers, comparable to the lattice period $\lambda_T/2 \approx 506$ nm. At that scale the electron samples the alternating nodes and antinodes of the trapping field across its own orbit. According to the derivation in Chap. 6, and also carried out in the supplemental material of [P4], the Rabi Hamiltonian must be evaluated without the dipole approximation. Therefore, the integral over the Rydberg electron wavefunction of the spatially varying trap field must be performed to compute the light shift. For the considered fields and owing to the spherical symmetry of an nS state we can express this as the one-dimensional integral

$$\theta_n = \langle nS|\cos(2kx_e)|nS\rangle = \int_0^\infty \mathrm{d}r_\mathrm{e}\, P_{n,0}(r_\mathrm{e})\, j_0(2kr_\mathrm{e}), \tag{7.5}$$

where $P_{n,0}(r_\mathrm{e})$ is the radial probability density of the nS state and j_0 is the zeroth-order spherical Bessel function. We call θ_n the landscape factor [77]. For the ground state, $kr_\mathrm{e} \ll 1$ and $\theta_g \approx 1$; for a high-n Rydberg state, the orbit spans many optical fringes and θ_n decreases toward zero as the electron averages over the periodic potential like a free charge.

Following the derivation for the running-wave and purely periodic standing-wave components of the trap field separately yields two distinct analytic magic conditions:

$$\Delta_n^{\mathrm{rw}} = \frac{D_{ar}^2}{4\hbar(\alpha_g - \alpha_f)}, \tag{7.6}$$

$$\Delta_n^{\sim} = \frac{D_{ar}^2}{4\hbar(\alpha_g - \alpha_f\,\theta_n)}, \tag{7.7}$$

where D_{ar} is the reduced dipole matrix element of the near-resonant transition the trap laser drives, α_g is the ground state polarizability, $\alpha_f = -e^2/m_\mathrm{e}\omega^2$ is the free-electron polarizability, and θ_n is the landscape factor defined in Eq. (7.5).

Because the landscape factor satisfies $\theta_n < 1$ for any finite n, the standing-wave magic detuning $\tilde{\Delta_n}$ in Eq. (7.7) differs from the running-wave value. A realistic standing wave also carries a non-periodic radial component with a different spatial dependence. Thus, no single detuning can cancel the differential shift at every position simultaneously. We define the optimal standing-wave detuning Δ_n^{sw} as the one minimizing the standard deviation of the differential light shift integrated over the atomic cloud volume, see Fig. 7.4(c).

In the storage and retrieval experiment, the retrieved signal decays exponentially with a coherence time t_c governed by the inhomogeneous differential light shift across the atomic ensemble. Scanning the trap detuning Δ locates the point of minimal dephasing for each trap geometry and thereby identifies the magic condition experimentally. For the $76S$ state, the running-wave t_c peaks sharply at $\Delta_{76}^{\mathrm{rw}}$, confirming the analytic condition. The standing-wave t_c peaks at $\Delta_{76}^{\mathrm{sw}}$, shifted between the running-wave and purely periodic optima in agreement with the standard-deviation minimisation criterion, see Fig. 7.4(c). Applying the geometry-correct detuning recovers a coherence time substantially longer than at either single-component optimum, demonstrating that the geometry-aware criterion is necessary, not merely a refinement.

We repeat the measurement across principal quantum numbers from $n \approx 25$ to $n > 100$, extracting an effective trap polarizability $\alpha_n^{\mathrm{trap}} = D_{ar}^2 / 4\hbar\Delta_n^{\mathrm{trap}}$ from each optimal detuning. For $n \lesssim 30$, the Rydberg orbital fits well within the lattice period, $\theta_n \approx 1$, and the running-wave and standing-wave optima coincide. Above $n \approx 70$, where the electron orbital diameter exceeds the 506 nm lattice period, θ_n falls measurably below one and the two polarizabilities diverge. The gap encodes the n-scaling of θ_n directly: as n continues to grow, $\theta_n \to 0$ and the polarizability difference saturates at $|\alpha_f|$, the ponderomotive response of a completely free electron. The trap geometry is therefore not a detail for high-n Rydberg states; it sets the effective polarizability and, through it, the magic detuning.

Magic trapping at the geometry-specific optimum fixes the atom's spatial degree of freedom, minimizing the differential phase shift between atoms at different positions in the cloud and extending the coherence time toward the Rydberg state lifetime. This answers the fourth objective of this dissertation: magic trapping conditions depend on the geometry of the trap because the extended Rydberg electron wavefunction averages over the spatial structure of the field, so running-wave and standing-wave configurations require distinct magic detunings. The optimized trap is, however, static: the atom sits where the lattice places it and the Hamiltonian remains fixed. In Sec. 7.5, the focus shifts from the trapping platform to the excitation protocol itself, where stroboscopic Rydberg dressing generates spin-motion coupling and effective multi-body interactions.

7.5. Engineering multi-body interactions with stroboscopic Rydberg dressing [P5]

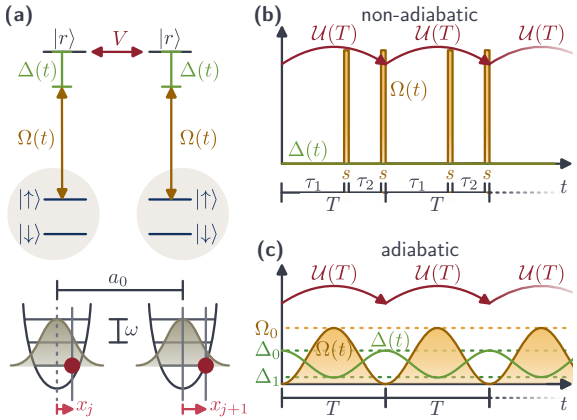

FIG. 7.5. Stroboscopic Rydberg dressing with two dressing protocols. (a) Two atoms trapped in tweezers which are modeled as one-dimensional harmonic oscillators with trapping frequency ω. Their equilibrium separation is a_0, and the displacement from their individual equilibrium positions is given by x_j and x_{j+1}, respectively. Each atom is modeled by two long-lived ground states ($|\uparrow\rangle$, $|\downarrow\rangle$) and a Rydberg state $|r\rangle$. Neighboring atoms in the state $|r\rangle$ interact with strength V. A globally applied laser couples $|\uparrow\rangle$ and $|r\rangle$ with time-dependent Rabi frequency $\Omega(t)$ and detuning $\Delta(t)$. **(b)** The dressing protocols consist of periodic sequences of pulses of length T. In the non-adiabatic dressing protocol, two strong π pulses of duration s are applied, which break the Rydberg blockade. In between the two pulses, interacting Rydberg states are excited, which generates effective interactions among atoms in the state $|\uparrow\rangle$. **(c)** In the adiabatic dressing protocol, the Rabi frequency $\Omega(t)$ and the detuning $\Delta(t)$ are varied smoothly, see text. Rydberg states are excited during the pulses, but de-excited at the end. Dynamical phases accumulated during this process translate into effective interactions among atoms in the state $|\uparrow\rangle$.

This section addresses the fifth objective of this dissertation: how does the pulse timescale relative to the motional dynamics determine the character of the multi-body interactions generated by stroboscopic Rydberg dressing [P5]? To answer this question, we study stroboscopic Rydberg dressing in a one-dimensional tweezer array, where periodic resonant pulses map Rydberg interactions onto the ground state spin manifold. We show, for both an adiabatic and a non-adiabatic protocol, that the pulse timescale relative to the trap period determines whether atomic motion decouples cleanly, and that both protocols generate genuine multi-body interactions.

We consider a one-dimensional chain of optical tweezer-trapped atoms with lattice constant a_0. Each atom carries two long-lived ground states $|\uparrow\rangle$ and $|\downarrow\rangle$, alongside a Rydberg state $|r\rangle$. For the model considered here, we assume state-insensitive trapping potentials, which may be realized using magic trapping as discussed in Sec. 7.4. The atoms oscillate in their individual tweezers at trap frequency ω; the displacement of atom j from its equilibrium position is x_j. When neighboring atoms are both in $|r\rangle$, they interact through the van der Waals potential $V(x_{j+1} - x_j)$; because that potential varies with separation, its gradient $G = \partial V / \partial (x_{j+1} - x_j)\big|_{a_0}$

couples the electronic excitation to the atomic motion. This electron-motion coupling is the key mechanism of the non-adiabatic protocol: it is simultaneously the origin of multi-body interactions and, without care, a channel for spin decoherence.

Non-adiabatic protocol. The non-adiabatic protocol, see Fig. 7.5(b), applies two resonant π-pulses per dressing cycle of duration T. Each pulse is strong enough ($\Omega \gg V$) to flip all $|\uparrow\rangle$ atoms simultaneously into $|r\rangle$, overcoming the Rydberg blockade; the atoms then evolve under the Rydberg interaction for an interval τ_2; a second π-pulse returns them to $|\uparrow\rangle$. In the limit of instantaneous pulses, the time-evolution operator over one cycle can be calculated analytically as

$$\mathcal{U}(T) = \prod_j e^{-iTH_{j,\text{eff}}} \mathcal{D}(\mathcal{J}_j) e^{-iT\omega a_j^\dagger a_j} \tag{7.8}$$

and factorizes into three contributions: a free oscillation of each atom in its trap with phonon occupation operators $a_j^\dagger a_j$, a displacement operator $\mathcal{D}(\mathcal{J}_j) = e^{\mathcal{J}_j a_j^\dagger - \mathcal{J}_j^* a_j}$ coupling the motional state to the spin manifold, and an effective spin-only time-evolution operator. The displacement argument $\mathcal{J}_j \propto (e^{-i\omega\tau_2} - 1)$, is a spin-dependent operator that senses the configuration of neighboring atoms [P5]. When atom j is surrounded by two excited neighbors, or by none, the net force on it from both sides cancels and $\mathcal{J}_j = 0$; when it has exactly one excited neighbor, the displacement is non-zero. Distinguishing these two configurations requires an operator acting simultaneously on three adjacent sites; this generates a genuine three-body interaction in the effective spin Hamiltonian.

The oscillatory factor $(e^{-i\omega\tau_2} - 1)$ vanishes whenever $\omega\tau_2 = 2\pi$: the atom completes exactly one oscillation between the two pulses and returns to its starting phase. At this timing, the displacement operator $\mathcal{D}(\mathcal{J}_j)$ becomes the identity and spin and motional degrees of freedom fully decouple. The stroboscopic dressing protocol then dynamically generates a clean effective interaction among the atoms in the low-lying ground states, fully described by the time evolution under H_{eff}. We verify this numerically by computing the interatomic distance $\langle \delta x \rangle$ at each stroboscopic time step: for $\omega\tau_2 = 0.01\pi$, electron-motion coupling causes $\langle \delta x \rangle$ to oscillate strongly after each cycle; for $\omega\tau_2 = 2\pi$, the motional state returns to its initial value after each cycle while the spin dynamics are unaffected.

Adiabatic protocol. The adiabatic protocol generates multi-body interactions through a complementary mechanism. In this protocol, the Rabi frequency and detuning are varied smoothly over the cycle. The Rabi frequency is swept as $\Omega(t) = \Omega_0 \sin^2(\pi t/T)$ with peak value Ω_0, while the detuning is swept as $\Delta(t) = \Delta_0 - (\Delta_0 - \Delta_1)\sin^2(\pi t/T)$ from initial detuning Δ_0 to final detuning Δ_1. Consequently, the state begins and ends in the spin manifold while passing through Rydberg-admixed configurations during the pulse, as shown in Fig. 7.5(c). Each spin configuration C accumulates a distinct dynamical phase φ_C because the energy of the instantaneous eigenstate depends on how many atoms simultaneously approach the Rydberg state. As a concrete three-atom example, we take an equilateral triangle geometry: the phase differences

define an effective spin Hamiltonian between stroboscopic times nT, which can be expressed as a sum of multi-body terms, with $\mathcal{P}_i = |\uparrow\rangle\langle\uparrow|_i$ the projector onto the spin-up state of atom i, this is

$$H_{\text{eff}} = \mathcal{V}_3 \mathcal{P}_1\mathcal{P}_2\mathcal{P}_3 + \mathcal{V}_2 \sum_{i\neq j} \mathcal{P}_i\mathcal{P}_j + \mathcal{V}_1 \sum_i \mathcal{P}_i + \mathcal{V}_0, \tag{7.9}$$

where the three-body term $\mathcal{V}_3 \mathcal{P}_1\mathcal{P}_2\mathcal{P}_3$ in Hamiltonian (7.9) is nonzero and cannot be decomposed into any sum of two-body operators. The interaction strengths $\mathcal{V}_k$ are extracted from the dynamical phases by a finite-difference relation: $\mathcal{V}_3 T = \varphi_{\uparrow\uparrow\uparrow} - 3\varphi_{\uparrow\uparrow} + 3\varphi_{\uparrow} - \varphi_0$, where the subscript counts the number of atoms in $|\uparrow\rangle$.

We identify that the relative weight of the three-body term depends on the interatomic distance a_0 through the bare van der Waals interaction $V = C_6/a_0^6$. At large separations V is small and the two-body interaction $\mathcal{V}_2$ dominates, while the three-body term $\mathcal{V}_3$ remains negligible. At shorter distances V is large and the protocol probes deeply interacting configurations, amplifying the three-body phase accumulation in $\varphi_{\uparrow\uparrow\uparrow}$. For the $61S_{1/2}$ state of potassium with $C_6 = 119\,\text{GHz}\mu\text{m}^6$ and $\Omega_0 = 2\pi \times 1\,\text{MHz}$, the ratio $\mathcal{V}_3/\mathcal{V}_2$ grows substantially as a_0 decreases from 7 μm toward 4 μm, a range accessible in current tweezer experiments.

The two protocols thus realize multi-body interactions by complementary routes. The non–adiabatic protocol exploits state-dependent forces via the gradient G and recovers a clean effective spin Hamiltonian by satisfying $\omega\tau_2 = 2\pi$. The adiabatic protocol uses adiabatic phase accumulation and tunes the three-body weight through the interatomic distance. Both show that multi-body interactions are not exotic additions to the Rydberg platform but emerge naturally from how the periodic drive samples interacting configurations. This addresses the fifth objective of this dissertation: we have shown how the pulse sequence determines the interaction mechanism, with fast pulses generating multi-body interactions via state-dependent motional displacements that vanish at specific cycle periods, and slow adiabatic pulses generating them through dynamical phase accumulation. Looking ahead, the same electron-motion coupling that must be suppressed here to isolate clean electronic-state dynamics can be deliberately exploited as a resource to engineer the motional state of the chain. Section 7.6 pursues this direction.

7.6. Collective motional squeezing and non-classical states [P6]

This section picks up directly from the stroboscopic protocol of Sec. 7.5 and addresses the sixth objective of this dissertation: can the spin-motion coupling, which there had to be suppressed at specific timing conditions to isolate clean spin interactions, instead be deliberately retained and exploited to prepare collectively squeezed, non-classical motional states of the atom chain [P6]? The motivation is direct: Rydberg interaction gates are sensitive to interatomic distances through the C_6/r^6 potential, so quantum position fluctuations translate immediately into gate infidelities.

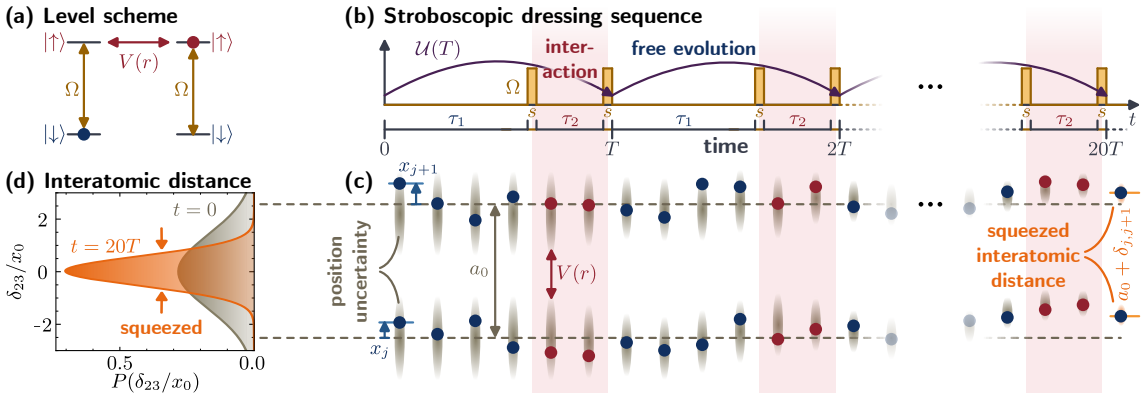

FIG. 7.6. Stroboscopic Rydberg dressing collectively reduces relative distance uncertainty below the ground state limit. (a) Level scheme of the atom's electronic states: ground state $|\downarrow\rangle$ (blue) and Rydberg state $|\uparrow\rangle$ (red), coupled by a laser with Rabi frequency Ω. Neighboring atoms simultaneously in $|\uparrow\rangle$ interact via the van der Waals potential $V(r) = C_6/r^6$. **(b)** The stroboscopic dressing protocol proceeds in periodic cycles of duration T, repeated up to $20T$ as shown. Each cycle consists of: free evolution of duration τ_1, a resonant π-pulse of duration s and Rabi frequency Ω that transfers all atoms to $|\uparrow\rangle$, an interaction interval of duration τ_2 during which atoms in $|\uparrow\rangle$ interact via $V(r)$ and develop motional correlations, and a second π-pulse returning all atoms to $|\downarrow\rangle$. **(c)** Schematic time evolution of two neighboring atoms confined in optical traps with equilibrium spacing a_0 and displacements x_j from their respective equilibrium positions. Grey shading indicates the single-atom position variance of each atom. After multiple dressing cycles, the atoms' motions become correlated, reducing the fluctuations of the interatomic distance $\delta_{j,j+1} = x_{j+1} - x_j$ below the ground state level (squeezed interatomic distance, right). **(d)** Probability distribution of the interatomic distance δ_{23} at $t = 0$ (motional ground state, broad) and after $m = 20$ dressing cycles (narrow), demonstrating the reduction of distance fluctuations. Results are calculated for $N = 5$ atoms using the parameters described in the text.

Even in the motional ground state, each atom's position is uncertain by the harmonic oscillator length $x_0 = \sqrt{\hbar/2M\omega}$. Crucially, reducing the variance of the *interatomic distance* $\delta_{j,j+1} = x_{j+1} - x_j$ benefits not only from squeezing individual positions but also from correlating the motions of neighboring atoms — a genuinely many-body task that single-atom protocols cannot accomplish.

The model is a one-dimensional chain of N atoms, each trapped harmonically at frequency ω with equilibrium spacing a_0, schematically outlined in Fig. 7.6. Each atom carries a ground state $|\downarrow\rangle$ and a Rydberg state $|\uparrow\rangle$; when neighboring atoms are simultaneously in $|\uparrow\rangle$, they interact through the van der Waals potential $V(r) = C_6/r^6$. Because V depends on the atomic separation, the Rydberg interaction couples electronic excitation to atomic motion along the chain axis. The stroboscopic protocol proceeds in repeated cycles of duration T: free evolution for time τ_1, a resonant π-pulse that excites all atoms to $|\uparrow\rangle$, an interaction interval τ_2 during which atoms in the Rydberg state experience mutual repulsion and build motional correlations, and a second π-pulse returning them all to $|\downarrow\rangle$.

To obtain closed-form expressions, we expand $V(r)$ to second order around a_0 which is one order higher than in Sec. 7.5. Since the expansion is only up to second order, the time evolution of the motional degree of freedom remains Gaussian and can be solved analytically. Here, we work in the basis of the collective normal modes b_k of the chain which enables us to perform a Bloch-Messiah decomposition of the m-cycle time-evolution operator that decomposes the Gaussian dynamics of the time evolution operator into a product of independent single-mode unitaries (squeezing $\mathcal{S}_k$, displacement $\mathcal{D}_k$, and rotation $\mathcal{R}_k$):

$$\mathcal{U}(mT) = \prod_{k=1}^{N} \mathcal{S}_k(Z_k)\, \mathcal{D}_k(J_k)\, \mathcal{R}_k(\beta_k), \tag{7.10}$$

where the squeezing, displacement, and rotation parameters are known in closed form [P6]. This analytical expression makes optimizing the motional states over protocol parameters tractable for arbitrary chain length N; a direct simulation of the combined spin-motion Hilbert space beyond $N \gtrsim 3$ becomes computationally demanding. The squeezing of each relative mode ($k \geq 2$, which governs interatomic distances) originates from the potential curvature $V_2 = \frac{\partial^2 V}{\partial r^2}\big|_{a_0}$: during the interaction interval, V_2 shifts each relative mode to an effective frequency

$$\tilde{\omega}_k = \sqrt{\omega^2 + 2\lambda_k x_0^2 V_2 \omega}, \tag{7.11}$$

where $\lambda_k = 4\sin^2((k-1)\pi/2N)$ encodes the mode index and chain length. The alternation between this frequency and the free-trap frequency ω constitutes a parametric modulation that squeezes the mode, analogous to single-atom squeezing by trap-frequency modulation [109] but now acting on the collective normal modes of the entire chain.

The central quantity of interest is the variance of the nearest-neighbor distance $\delta_{j,j+1} = x_{j+1} - x_j$. Using the covariance matrix $\mathscr{C}_{jk} = \langle x_j x_k \rangle - \langle x_j \rangle \langle x_k \rangle$, this variance decomposes as

$$\mathrm{Var}(\delta_{j,j+1}) = \mathrm{Var}(x_{j+1}) + \mathrm{Var}(x_j) - 2\,\mathscr{C}_{j,j+1}. \tag{7.12}$$

Two complementary mechanisms reduce the distance fluctuation below the ground state level in Eq. (7.12): squeezing the individual position variances $\mathrm{Var}(x_j)$, and generating positive correlations $\mathscr{C}_{j,j+1} > 0$ that synchronize the motion of neighbors. Single-atom squeezing acts only on the first term. The stroboscopic Rydberg protocol exploits both simultaneously: the normal-mode squeezing suppresses the diagonal elements of $\mathscr{C}_{jk}$, while the collective character of the modes builds positive off-diagonal entries between neighboring atoms.

We optimize the protocol for a chain of $N = 5$ atoms of ^{87}Rb at spacing $a_0 = 2.7\,\mu\mathrm{m}$ and trap frequency $\omega = 2\pi \times 100\,\mathrm{kHz}$. This corresponds to a harmonic oscillator length $x_0 \approx 24.1\,\mathrm{nm}$ and a ratio $x_0/a_0 \approx 0.009$, values achievable in current tweezer arrays. Evaluating the dynamics analytically for five atoms reveals: Starting from the motional ground state, which has no interatomic correlations, repeated dressing cycles fill the off-diagonal entries of $\mathscr{C}_{jk}$ while simultaneously reducing the diagonal ones. After $m = 20$ cycles, the variance of all nearest-neighbor distances reaches approximately 19 % of its ground state value, and the interaction time τ_2 fits well within the atomic coherence time of several tens up to hundreds of microseconds.

The quadratic expansion of the van der Waals potential restricts the motional dynamics to Gaussian states. When the harmonic oscillator length x_0 is no longer small compared to a_0, higher-order terms of the C_6/r^6 potential become significant and the Gaussianity breaks down. We compare the Wigner function of the relative coordinate predicted by the quadratic model against the exact dynamics under the full van der Waals potential for a two-atom system after two dressing cycles. At the spacing $x_0/a_0 \approx 0.009$, the two Wigner functions are indistinguishable: the analytic framework faithfully captures the full dynamics, as shown in Fig. 3 of [P6]. At a tighter spacing of $a_0 = 1\,\mu\mathrm{m}$ and trap frequency $\omega = 2\pi \times 18\,\mathrm{kHz}$, the harmonic oscillator length is $x_0 \approx 56.8\,\mathrm{nm}$ and the ratio is $x_0/a_0 \approx 0.057$. For these parameters, the quadratic model still predicts a Gaussian squeezed state, but the exact dynamics produces a Wigner function with pronounced negative regions, reaching a Wigner negativity of 0.109. Wigner negativity is an unambiguous signature of quantum non-classical states. The higher-order terms of the van der Waals potential, neglected in the quadratic model, are the direct source of this non-classicality. This breakdown of the quadratic approximation at small distances is physically analogous to the breakdown of the dipole approximation in Sec. 7.4; here, the relative atomic motion explores the non-quadratic spatial dependence of the C_6/r^6 interaction potential. These Wigner-negative states are a potential resource for quantum-enhanced sensing [132, 133].

The chapter's progression ends here, at the finest level of motional control the Rydberg platform has been shown to support. We opened in Sec. 7.1 with the simplest possible Rydberg setup, a thermal vapor addressed as a whole, and showed that its mean-field bistability is already a

usable computational resource. Each subsequent section added one lever of control: microscopic addressing of a 2D lattice in Sec. 7.2, a chain-mediated quantum bus in Sec. 7.3, geometry-aware magic trapping in Sec. 7.4, and stroboscopic engineering of multi-body interactions in Sec. 7.5. This section adds the final lever by deliberately exploiting spin-motion coupling, and reaches the endpoint of that progression: collective quantum correlations across the chain that reduce distance fluctuations to a fraction of the ground state limit and produce states with no classical analogue.

A broader discussion of these results and future perspectives for Rydberg platforms is presented in the following Chap. 8.

8. Discussion and future perspectives

This work demonstrates a new perspective in the treatment of interacting Rydberg arrays, reframing atomic motion from a dominant decoherence channel into a highly controllable resource for quantum state engineering [P4–P6]. Furthermore, the many-body Hamiltonian framework summarized in the Methods section provides a common language that connects these systems to kinetically constrained models, reservoir computing, and hybrid quantum systems [P1–P3]. To increase the potential of controlling electron-motion coupling of Rydberg platforms, several fundamental and experimental challenges should be addressed. In this chapter, I discuss future research directions and outlooks arising from connecting these results.

8.1. Stroboscopic Rydberg dressing in anharmonic trapping potentials

Throughout this dissertation, the development of minimal and effective models enabled the quantification of quantum many-body problems. However, intrinsically, these models hide important effects. In the works comprising this dissertation, trapping potentials were generally approximated as perfect harmonic oscillators [P5, P6]. In practice, optical tweezers possess inherent anharmonicity [134, 135]. This anharmonicity becomes particularly relevant when considering squeezed motional states, since the generated states can occupy higher-lying Fock states that sample the anharmonic regions of the trap [109]. Future studies could extend the stroboscopic Rydberg dressing [P5, P6] with anharmonic trapping potentials which might enable interesting spin-motion couplings and transitions. This is not limited to tweezer traps; anharmonicity in other trap geometries may also be worth exploring.

8.2. Dipole approximation breakdown in optical tweezers

The large spatial extent of highly excited Rydberg states introduces a fundamental breakdown of the electric-dipole approximation in optical trapping potentials. For principal quantum numbers $n \gtrsim 70$, the electron's orbit diameter reaches several hundred nanometers, which is comparable to the spatial variation of the trapping light field. In this regime, the electron averages the optical field over its wavefunction, such that the geometry of the trapping potentials becomes relevant. While this breakdown was studied and experimentally verified for standing-wave optical lattices in [P4], similar corrections (characterized by spatial landscape factors) must be investigated for

optical tweezer traps. To do so, the derivation in Chap. 6 might be a good starting point. Future theoretical work should model how the sudden change of the state-dependent trapping potential upon Rydberg excitation constitutes a quench of the motional Hamiltonian and may induce motional excitations or offers new channels for coherent spin-motion control.

8.3. Spin-motion coupling and sympathetic cooling in trapped Rydberg ions

Despite the proposition of a spin-motion-echo protocol to mitigate motional decoherence using stroboscopic Rydberg dressing [P5], the lack of channels to dissipate motional excitations in neutral atom optical tweezers limits long coherent operations. Inevitable motional heating [136] remains a significant bottleneck. A pragmatic and powerful solution lies in transitioning the developed motional engineering framework from neutral atoms to trapped Rydberg ions. By leveraging the capability for sympathetic cooling inherent to ion chains, it becomes possible to continuously dissipate the motional heat generated by Rydberg interactions [137]. Theoretical investigations into whether sympathetic cooling of spectator ions can dissipate the motional excitations could pave the way for long-lived coherent spin-motion dynamics.

8.4. Leveraging quantum atomic motion for reservoir computing

The cumulative dissertation also explored the intersection of quantum dynamics and machine learning through the lens of reservoir computing [P1]. Quantum reservoir computing can benefit from a large accessible state space. I propose a physical reservoir system based on a 1D or 2D array of trapped Rydberg atoms where the coupling between electronic spin states and their motional degree of freedom is used to expand the reservoir's state space. Since the bosonic motional degrees of freedom with large local Hilbert spaces inherent in these arrays offer a massive, naturally high-dimensional resource, incorporating this atomic motion into the reservoir state could drastically alter its Information Processing Capacity. The large local bosonic Hilbert spaces make straightforward simulations based on matrix product states challenging. Tree Tensor Networks (TTNs) [138] combined with Basis-Update-Galerkin (BUG) integrators [139, 140] offer one promising route. These algorithms are mathematically established but not yet adopted in the quantum many-body community. They could enable the simulation of such spin-boson models to determine if motional degrees of freedom provide a tangible resource for quantum reservoir computing.

8.5. Spin-motion coupling in facilitated 2D Rydberg lattices

In the realm of quantum many-body dynamics, we investigated kinetically constrained systems in a facilitated 2D Rydberg lattice [P2]. Here, the kinetic constraints emerging from the facilitation condition relied on static interatomic distances. However, the steep van der Waals potentials inherently induce atomic motion [P6], making the facilitation condition dynamical and position-dependent. I propose to study 2D facilitation in the presence of spin-motion coupling, which could be combined with stroboscopic Rydberg dressing [P5, P6] and simulated via the novel TTNs and the BUG integrator. A key question is whether interaction-induced motion relaxes the kinetic constraints responsible for Hilbert-space fragmentation, potentially rendering immobile excitations mobile. Resolving this is essential for defining the upper limit on the lifetime of the elementary excitations.

8.6. Röntgen interaction in highly excited Rydberg regimes

In the derivation of the light-matter coupling Hamiltonian in Chap. 6, we retained the Röntgen interaction term and subsequently neglected it based on the estimate discussed in Sec. 6.1.4. This term couples the atomic center-of-mass momentum directly to the spatial variation of the vector potential over the electronic orbit. For plane-wave fields and within the electric-dipole regime, its strength is suppressed by a factor of order v/c relative to the conventional Rabi coupling. However, for highly excited Rydberg states ($n \gtrsim 70$), the electronic extent becomes comparable to the spatial variation of the trapping field, such that the assumptions underlying this estimate may no longer hold. Under these conditions, the magnitude of the Röntgen term

$$H_{\mathrm{R}} = \frac{e}{M}\left[\mathbf{A}(\mathbf{R}+\mathbf{r},t) - \mathbf{A}(\mathbf{R},t)\right]\cdot\mathbf{P} \tag{8.1}$$

has to be evaluated explicitly. Investigating the Röntgen interaction in tweezer-trapped Rydberg systems therefore represents an interesting outlook, potentially revealing additional spin-motion coupling channels that may become relevant in future high-precision quantum experiments.

9. Acknowledgements

First and foremost, I would like to express my deepest gratitude to **Igor Lesanovsky**, my supervisor. Thank you Igor, for giving me the opportunity to pursue my research in your group and for your invaluable, long-lasting mentorship. Your guidance, patience, and profound physical insights have not only shaped this cumulative dissertation but also my development as a scientist.

I would also like to thank my second supervisor, **Sebastian Hofferberth**, for his insightful comments and for providing an invaluable experimental perspective on my theoretical work.

I am sincerely grateful to all my **collaborators and PhD colleagues**. The countless discussions, joint efforts on manuscripts, and the collaborative atmosphere in the office made this journey both productive and enjoyable. It has been a privilege to work with such a talented group of people.

I also want to thank my **fraternity** ATV Arminia zu Tübingen. The many friends I have found there have enriched my life in so many ways: academically, through sports, and in many other aspects of life. The balance and camaraderie provided by our community were essential to my well-being during the more intense phases of my PhD.

Special thanks go to my **family** for their unconditional support throughout the years. Thank you for always being there for me and for your constant efforts "um mir den Rücken frei zu halten". Your support provided the foundation that allowed me to focus entirely on my work.

Finally, I want to thank my girlfriend, **Angelina**, for her incredible patience and understanding. I know it hasn't always been easy when I had to spend long nights in the office, and I am deeply grateful for your love and for being by my side.

Bibliography

[1] B. Keimer, S. A. Kivelson, M. R. Norman, S. Uchida, and J. Zaanen, "From quantum matter to high-temperature superconductivity in copper oxides", Nature **518**, 179–186 (2015).

[2] D. N. Basov, R. D. Averitt, and D. Hsieh, "Towards properties on demand in quantum materials", Nature Materials **16**, 1077–1088 (2017).

[3] Y. Cao, J. Romero, J. P. Olson, M. Degroote, P. D. Johnson, M. Kieferová, I. D. Kivlichan, T. Menke, B. Peropadre, N. P. D. Sawaya, et al., "Quantum chemistry in the age of quantum computing", Chemical Reviews **119**, 10856–10915 (2019).

[4] C. L. Degen, F. Reinhard, and P. Cappellaro, "Quantum sensing", Reviews of Modern Physics **89**, 035002 (2017).

[5] U. Schollwöck, "The density-matrix renormalization group", Reviews of Modern Physics **77**, 259–315 (2005).

[6] J. Preskill, "Quantum Computing in the NISQ era and beyond", Quantum **2**, 79 (2018).

[7] N. W. Ashcroft and N. D. Mermin, *Solid state physics* (Saunders college publ, Fort Worth Philadelphia San Diego [etc.], 1976).

[8] R. P. Feynman, "Simulating physics with computers", International Journal of Theoretical Physics **21**, 467–488 (1982).

[9] I. Bloch, J. Dalibard, and S. Nascimbène, "Quantum simulations with ultracold quantum gases", Nature Physics **8**, 267–276 (2012).

[10] J. I. Cirac and P. Zoller, "Goals and opportunities in quantum simulation", Nature Physics **8**, 264–266 (2012).

[11] I. M. Georgescu, S. Ashhab, and F. Nori, "Quantum simulation", Reviews of Modern Physics **86**, 153–185 (2014).

[12] E. Altman, K. R. Brown, G. Carleo, L. D. Carr, E. Demler, C. Chin, B. DeMarco, S. E. Economou, M. A. Eriksson, K.-M. C. Fu, M. Greiner, K. R. Hazzard, R. G. Hulet, A. J. Kollár, B. L. Lev, M. D. Lukin, R. Ma, X. Mi, S. Misra, C. Monroe, K. Murch, Z. Nazario, K.-K. Ni, A. C. Potter, P. Roushan, M. Saffman, M. Schleier-Smith, I. Siddiqi, R. Simmonds, M. Singh, I. Spielman, K. Temme, D. S. Weiss, J. Vučković, V. Vuletić, J. Ye, and M. Zwierlein, "Quantum Simulators: Architectures and Opportunities", PRX Quantum **2**, 017003 (2021).

[13] I. Bloch, J. Dalibard, and W. Zwerger, "Many-body physics with ultracold gases", Reviews of Modern Physics **80**, 885–964 (2008).

[14] C. Gross and I. Bloch, "Quantum simulations with ultracold atoms in optical lattices", Science **357**, 995–1001 (2017).

[15] C. Chin, R. Grimm, P. Julienne, and E. Tiesinga, "Feshbach resonances in ultracold gases", Reviews of Modern Physics **82**, 1225–1286 (2010).

[16] T. F. Gallagher, *Rydberg Atoms*, Cambridge Monographs on Atomic, Molecular and Chemical Physics (Cambridge University Press, 1994).

[17] J.-H. Choi, B. Knuffman, T. C. Liebisch, A. Reinhard, and G. Raithel, *Cold Rydberg Atoms*, Vol. 54 (Elsevier, Jan. 2007), 131–202.

[18] N. Šibalić and C. S. Adams, *Rydberg Physics*, 2399-2891 (IOP Publishing, 2018).

[19] N. Šibalić, J. Pritchard, C. Adams, and K. Weatherill, "ARC: An open-source library for calculating properties of alkali Rydberg atoms", Computer Physics Communications **220**, 319–331 (2017).

[20] E. Y. Il'inova, A. A. Kamenski, and V. D. Ovsiannikov, "Hyperpolarizabilities of Rydberg states in helium and alkali-metal atoms", Journal of Physics B: Atomic, Molecular and Optical Physics **42**, 145004 (2009).

[21] J. Mitroy, M. S. Safronova, and C. W. Clark, "Theory and applications of atomic and ionic polarizabilities", Journal of Physics B: Atomic, Molecular and Optical Physics **43**, 202001 (2010).

[22] T. Topcu and A. Derevianko, "Dynamic polarizability of Rydberg atoms: Applicability of the near-free-electron approximation, gauge invariance, and the Dirac sea", Physical Review A **88**, 042510 (2013).

[23] L. Béguin, A. Vernier, R. Chicireanu, T. Lahaye, and A. Browaeys, "Direct measurement of the van der Waals interaction between two Rydberg atoms", Physical Review Letters **110**, 263201 (2013).

[24] K. Wadenpfuhl and C. S. Adams, "Unraveling the structures in the van der Waals interactions of alkali-metal Rydberg atoms", Physical Review A **111**, 062803 (2025).

[25] T. F. Gallagher and P. Pillet, "Dipole–dipole interactions of Rydberg atoms", in *Advances in atomic, molecular, and optical physics*, Vol. 56, Advances in Atomic, Molecular, and Optical Physics (Academic Press, 2008), pp. 161–218.

[26] S. Ravets, H. Labuhn, D. Barredo, T. Lahaye, and A. Browaeys, "Measurement of the angular dependence of the dipole-dipole interaction between two individual Rydberg atoms at a Förster resonance", Physical Review A **92**, 020701 (2015).

[27] A. Browaeys, D. Barredo, and T. Lahaye, "Experimental investigations of dipole–dipole interactions between a few Rydberg atoms", Journal of Physics B: Atomic, Molecular and Optical Physics **49**, 152001 (2016).

[28] M. Saffman, T. G. Walker, and K. Mølmer, "Quantum information with Rydberg atoms", Reviews of Modern Physics **82**, 2313–2363 (2010).

[29] A. Browaeys and T. Lahaye, "Many-body physics with individually controlled Rydberg atoms", Nature Physics **16**, 132–142 (2020).

[30] D. Jaksch, J. I. Cirac, P. Zoller, S. L. Rolston, R. Côté, and M. D. Lukin, "Fast Quantum Gates for Neutral Atoms", Physical Review Letters **85**, 2208–2211 (2000).

[31] A. Gaëtan, Y. Miroshnychenko, T. Wilk, A. Chotia, M. Viteau, D. Comparat, P. Pillet, A. Browaeys, and P. Grangier, "Observation of collective excitation of two individual atoms in the Rydberg blockade regime", Nature Physics **5**, 115–118 (2009).

[32] M. Weidemüller, "There can be only one", Nature Physics **5**, 91–92 (2009).

[33] C. Ates, T. Pohl, T. Pattard, and J. M. Rost, "Antiblockade in Rydberg Excitation of an Ultracold Lattice Gas", Physical Review Letters **98**, 023002 (2007).

[34] M. Marcuzzi, J. Minář, D. Barredo, S. de Léséleuc, H. Labuhn, T. Lahaye, A. Browaeys, E. Levi, and I. Lesanovsky, "Facilitation Dynamics and Localization Phenomena in Rydberg Lattice Gases with Position Disorder", Physical Review Letters **118**, 063606 (2017).

[35] F. Liu, Z.-C. Yang, P. Bienias, T. Iadecola, and A. V. Gorshkov, "Localization and Criticality in Antiblockaded Two-Dimensional Rydberg Atom Arrays", Physical Review Letters **128**, 013603 (2022).

[36] X. Wang, Y. Wang, and Q.-Y. Liang,
"Robust Rydberg facilitation via rapid adiabatic passage",
Physical Review Research **8**, 013154 (2026).

[37] R. Heidemann, U. Krohn, V. Bendkowsky, B. Butscher, R. Löw, L. Santos, and T. Pfau,
"Evidence for Coherent Collective Rydberg Excitation in the Strong Blockade Regime",
Physical Review Letters **99**, 163601 (2007).

[38] R. Löw, H. Weimer, U. Krohn, R. Heidemann, V. Bendkowsky, B. Butscher,
H. P. Büchler, and T. Pfau, "Universal Scaling in a Strongly Interacting Rydberg Gas",
Physical Review A **80**, 033422 (2009).

[39] C. Carr, R. Ritter, C. G. Wade, C. S. Adams, and K. J. Weatherill,
"Nonequilibrium Phase Transition in a Dilute Rydberg Ensemble",
Physical Review Letters **111**, 113901 (2013).

[40] C. S. Adams, J. D. Pritchard, and J. P. Shaffer, "Rydberg atom quantum technologies",
Journal of Physics B: Atomic, Molecular and Optical Physics **53**, 012002 (2019).

[41] M. Marcuzzi, E. Levi, S. Diehl, J. P. Garrahan, and I. Lesanovsky,
"Universal Nonequilibrium Properties of Dissipative Rydberg Gases",
Physical Review Letters **113**, 210401 (2014).

[42] V. Gorini, A. Kossakowski, and E. C. G. Sudarshan,
"Completely positive dynamical semigroups of N-level systems",
Journal of Mathematical Physics **17**, 821–825 (1976).

[43] G. Lindblad, "On the generators of quantum dynamical semigroups",
Communications in Mathematical Physics **48**, 119–130 (1976).

[44] H.-P. Breuer and F. Petruccione, *The Theory of Open Quantum Systems*
(Oxford University Press, USA, Mar. 5, 2007), 636 pp.

[45] N. R. de Melo, C. G. Wade, N. Šibalić, J. M. Kondo, C. S. Adams, and K. J. Weatherill,
"Intrinsic optical bistability in a strongly driven Rydberg ensemble",
Physical Review A **93**, 063863 (2016).

[46] K. Wadenpfuhl and C. S. Adams,
"Emergence of Synchronization in a Driven-Dissipative Hot Rydberg Vapor",
Physical Review Letters **131**, 143002 (2023).

[47] L. Appeltant, M. Soriano, G. Van der Sande, J. Danckaert, S. Massar, J. Dambre,
B. Schrauwen, C. Mirasso, and I. Fischer,
"Information processing using a single dynamical node as complex system",
Nature Communications **2**, 468 (2011).

[48] K. Fujii and K. Nakajima,
"Harnessing Disordered-Ensemble Quantum Dynamics for Machine Learning",
Physical Review Applied **8**, 024030 (2017).

[49] P. Mujal, R. Martínez-Peña, J. Nokkala, J. García-Beni, G. L. Giorgi, M. C. Soriano, and R. Zambrini,
"Opportunities in Quantum Reservoir Computing and Extreme Learning Machines",
Advanced Quantum Technologies **4**, 2100027 (2021).

[50] M. Yan, C. Huang, P. Bienstman, P. Tino, W. Lin, and J. Sun,
"Emerging opportunities and challenges for the future of reservoir computing",
Nature Communications **15**, 2056 (2024).

[51] K. Kobayashi and Y. Motome,
"Edge of Many-Body Quantum Chaos in Quantum Reservoir Computing",
Physical Review Letters **136**, 040602 (2026).

[52] S. Ghosh, A. Opala, M. Matuszewski, T. Paterek, and T. C. H. Liew,
"Quantum reservoir processing", npj Quantum Information **5**, 35 (2019).

[53] R. Martínez-Peña, J. Nokkala, G. L. Giorgi, R. Zambrini, and M. C. Soriano,
"Information Processing Capacity of Spin-Based Quantum Reservoir Computing Systems", Cognitive Computation **15**, 1440–1451 (2020).

[54] A. H. Abbas, H. Abdel-Ghani, and I. S. Maksymov, *Classical and Quantum Physical Reservoir Computing for Onboard Artificial Intelligence Systems: A Perspective*, (June 14, 2024) pre-published.

[55] G. Bornet, G. Emperauger, C. Chen, F. Machado, S. Chern, L. Leclerc, B. Gély, Y. T. Chew, D. Barredo, T. Lahaye, N. Y. Yao, and A. Browaeys, "Enhancing a Many-Body Dipolar Rydberg Tweezer Array with Arbitrary Local Controls",
Physical Review Letters **132**, 263601 (2024).

[56] D. Adler, D. Wei, M. Will, K. Srakaew, S. Agrawal, P. Weckesser, R. Moessner, F. Pollmann, I. Bloch, and J. Zeiher,
"Observation of Hilbert space fragmentation and fractonic excitations in 2D",
Nature **636**, 80–85 (2024).

[57] P. Osterholz, F. Bensch, S. Tang, S. B. Sheela, I. Lesanovsky, and C. Groß,
Collective cluster nucleation dynamics in 2D Ising quantum magnets, (Dec. 9, 2025) pre-published.

[58] M. Magoni, P. Mazza, and I. Lesanovsky,
"Phonon dressing of a facilitated one-dimensional Rydberg lattice gas",
SciPost Physics Core **5**, 041 (2022).

[59] P. Sala, T. Rakovszky, R. Verresen, M. Knap, and F. Pollmann, "Ergodicity Breaking Arising from Hilbert Space Fragmentation in Dipole-Conserving Hamiltonians", Physical Review X **10**, 011047 (2020).

[60] T. Zhang and Z. Cai, "Quantum Slush State in Rydberg Atom Arrays", Physical Review Letters **132**, 206503 (2024).

[61] M. Magoni, C. Nill, and I. Lesanovsky, "Coherent Spin-Phonon Scattering in Facilitated Rydberg Lattices", Physical Review Letters **132**, 133401 (2024).

[62] D. Brady, J. Bender, P. Mischke, S. Ohler, T. Niederprüm, H. Ott, and M. Fleischhauer, "Griffiths phase in a facilitated Rydberg gas at low temperatures", Physical Review Research **6**, 013052 (2024).

[63] C. Nill, A. Cabot, A. Trautmann, C. Groß, and I. Lesanovsky, "Avalanche Terahertz Photon Detection in a Rydberg Tweezer Array", Physical Review Letters **133**, 073603 (2024).

[64] M. Arndt, O. Nairz, J. Vos-Andreae, C. Keller, G. van der Zouw, and A. Zeilinger, "Wave–particle duality of C60 molecules", Nature **401**, 680–682 (1999).

[65] Y. Y. Fein, P. Geyer, P. Zwick, F. Kiałka, S. Pedalino, M. Mayor, S. Gerlich, and M. Arndt, "Quantum superposition of molecules beyond 25 kDa", Nature Physics **15**, 1242–1245 (2019).

[66] A. Shayeghi, P. Rieser, G. Richter, U. Sezer, J. H. Rodewald, P. Geyer, T. J. Martinez, and M. Arndt, "Matter-wave interference of a native polypeptide", Nature Communications **11**, 1447 (2020).

[67] B. Julsgaard, A. Kozhekin, and E. S. Polzik, "Experimental long-lived entanglement of two macroscopic objects", Nature **413**, 400–403 (2001).

[68] K. C. Lee, M. R. Sprague, B. J. Sussman, J. Nunn, N. K. Langford, X.-M. Jin, T. Champion, P. Michelberger, K. F. Reim, D. England, D. Jaksch, and I. A. Walmsley, "Entangling Macroscopic Diamonds at Room Temperature", Science **334**, 1253–1256 (2011).

[69] C. F. Ockeloen-Korppi, E. Damskägg, J.-M. Pirkkalainen, M. Asjad, A. A. Clerk, F. Massel, M. J. Woolley, and M. A. Sillanpää, "Stabilized entanglement of massive mechanical oscillators", Nature **556**, 478–482 (2018).

[70] S. Kotler, G. A. Peterson, E. Shojaee, F. Lecocq, K. Cicak, A. Kwiatkowski, S. Geller, S. Glancy, E. Knill, R. W. Simmonds, J. Aumentado, and J. D. Teufel, "Direct observation of deterministic macroscopic entanglement", Science **372**, 622–625 (2021).

[71] W. H. Zurek, "Decoherence, einselection, and the quantum origins of the classical", Reviews of Modern Physics **75**, 715–775 (2003).

[72] C. Anastopoulos and B.-L. Hu, "Gravitational decoherence: A thematic overview", AVS Quantum Science **4**, 015602 (2022).

[73] Y. Chu, P. Kharel, T. Yoon, L. Frunzio, P. T. Rakich, and R. J. Schoelkopf, "Creation and control of multi-phonon Fock states in a bulk acoustic-wave resonator", Nature **563**, 666–670 (2018).

[74] V. J. Gokhale, B. P. Downey, D. S. Katzer, N. Nepal, A. C. Lang, R. M. Stroud, and D. J. Meyer, "Epitaxial bulk acoustic wave resonators as highly coherent multi-phonon sources for quantum acoustodynamics", Nature Communications **11**, 2314 (2020).

[75] F. Bariani, J. Otterbach, H. Tan, and P. Meystre, "Single-atom quantum control of macroscopic mechanical oscillators", Physical Review A **89**, 011801 (2014).

[76] D. Barredo, H. Labuhn, S. Ravets, T. Lahaye, A. Browaeys, and C. S. Adams, "Coherent Excitation Transfer in a Spin Chain of Three Rydberg Atoms", Physical Review Letters **114**, 113002 (2015).

[77] J. Lampen, H. Nguyen, L. Li, P. R. Berman, and A. Kuzmich, "Long-lived coherence between ground and Rydberg levels in a magic-wavelength lattice", Physical Review A **98**, 033411 (2018).

[78] P. Yang, G. Li, Z. Wang, P. Zhang, and T. Zhang, "Gate fidelity, dephasing, and 'magic' trapping of optically trapped neutral atom", New Journal of Physics **24**, 083028 (2022).

[79] P. Lemonde and P. Wolf, "Optical lattice clock with atoms confined in a shallow trap", Physical Review A **72**, 033409 (2005).

[80] V. Gerginov and K. Beloy, "Two-photon Optical Frequency Reference with Active ac Stark Shift Cancellation", Physical Review Applied **10**, 014031 (2018).

[81] M. Fleischhauer, A. Imamoglu, and J. P. Marangos, "Electromagnetically induced transparency: Optics in coherent media", Reviews of Modern Physics **77**, 633–673 (2005).

[82] S. Kuhr, W. Alt, D. Schrader, I. Dotsenko, Y. Miroshnychenko, A. Rauschenbeutel, and D. Meschede, "Analysis of dephasing mechanisms in a standing-wave dipole trap", Physical Review A **72**, 023406 (2005).

[83] X. Lei, L. Ma, J. Yan, X. Zhou, Z. Yan, and X. Jia, "Electromagnetically induced transparency quantum memory for non-classical states of light", Advances in Physics: X **7**, 2060133 (2022).

[84] T. Topcu and A. Derevianko, "Tune-out wavelengths and landscape-modulated polarizabilities of alkali-metal Rydberg atoms in infrared optical lattices", Physical Review A **88**, 053406 (2013).

[85] T. Topcu and A. Derevianko, "Intensity landscape and the possibility of magic trapping of alkali-metal Rydberg atoms in infrared optical lattices", Physical Review A **88**, 043407 (2013).

[86] J. Zeiher, R. van Bijnen, P. Schauß, S. Hild, J.-y. Choi, T. Pohl, I. Bloch, and C. Gross, "Many-body interferometry of a Rydberg-dressed spin lattice", Nature Physics **12**, 1095–1099 (2016).

[87] J. A. Hines, S. V. Rajagopal, G. L. Moreau, M. D. Wahrman, N. A. Lewis, O. Marković, and M. Schleier-Smith, "Spin Squeezing by Rydberg Dressing in an Array of Atomic Ensembles", Physical Review Letters **131**, 063401 (2023).

[88] A. Cao, T. L. Yelin, W. J. Eckner, N. D. Oppong, and A. M. Kaufman, *Autoionization-enhanced Rydberg dressing by fast contaminant removal*, (Oct. 13, 2024) pre-published.

[89] P. Weckesser, K. Srakaew, T. Blatz, D. Wei, D. Adler, S. Agrawal, A. Bohrdt, I. Bloch, and J. Zeiher, "Realization of a Rydberg-dressed extended Bose-Hubbard model", Science **390**, 849–853 (2025).

[90] V. Bharti, S. Sugawa, M. Kunimi, V. S. Chauhan, T. P. Mahesh, M. Mizoguchi, T. Matsubara, T. Tomita, S. de Léséleuc, and K. Ohmori, "Strong Spin-Motion Coupling in the Ultrafast Dynamics of Rydberg Atoms", Physical Review Letters **133**, 093405 (2024).

[91] R. J. Baxter and F. Y. Wu, "Exact Solution of an Ising Model with Three-Spin Interactions on a Triangular Lattice", Physical Review Letters **31**, 1294–1297 (1973).

[92] S. Martinos, A. Malakis, and I. Hadjiagapiou, "Finite-size scaling at first- and second-order phase transitions of Baxter–Wu model", Physica A: Statistical Mechanics and its Applications **355**, 393–407 (2005).

[93] S. Capponi, S. S. Jahromi, F. Alet, and K. P. Schmidt, "Baxter-Wu model in a transverse magnetic field", Physical Review E **89**, 062136 (2014).

[94] A. Vasilopoulos, N. G. Fytas, E. Vatansever, A. Malakis, and M. Weigel, "Universality in the two-dimensional dilute Baxter-Wu model", Physical Review E **105**, 054143 (2022).

[95] C. Tang, K. Sfairopoulos, W. Zhang, and C. Ding, *Dynamics of Baxter-Wu model*, (Mar. 30, 2025) pre-published.

[96] O. Salberger and V. Korepin, "Entangled spin chain", Reviews in Mathematical Physics **29**, 1750031 (2017).

[97] K. Adhikari and K. S. D. Beach, "Slow dynamics of the Fredkin spin chain", Physical Review B **104**, 115149 (2021).

[98] L. Causer, M. C. Bañuls, and J. P. Garrahan, "Nonthermal eigenstates and slow relaxation in quantum Fredkin spin chains", Physical Review B **110**, 134322 (2024).

[99] W.-M. Fan, K. Hao, Y.-Y. Chen, K. Zhang, X.-H. Wang, and V. Korepin, "Absence of local conserved charges of the Fredkin spin chain and its truncated versions", Physical Review B **112**, 205124 (2025).

[100] C. M. Langlett and S. Xu, "Hilbert space fragmentation and exact scars of generalized Fredkin spin chains", Physical Review B **103**, L220304 (2021).

[101] A. Yu. Kitaev, "Fault-tolerant quantum computation by anyons", Annals of Physics **303**, 2–30 (2003).

[102] K. Sfairopoulos and J. P. Garrahan, "Quantum Newman-Moore model in a longitudinal field", Physical Review B **112**, 094103 (2025).

[103] L. Zhang, S.-P. Kou, and Y. Deng, "Quench dynamics of the topological quantum phase transition in the Wen-plaquette model", Physical Review A **83**, 062113 (2011).

[104] D. Leibfried, D. M. Meekhof, B. E. King, C. Monroe, W. M. Itano, and D. J. Wineland, "Experimental Determination of the Motional Quantum State of a Trapped Atom", Physical Review Letters **77**, 4281–4285 (1996).

[105] D. Kienzler, C. Flühmann, V. Negnevitsky, H.-Y. Lo, M. Marinelli, D. Nadlinger, and J. P. Home, "Observation of Quantum Interference between Separated Mechanical Oscillator Wave Packets", Physical Review Letters **116**, 140402 (2016).

[106] M. O. Brown, S. R. Muleady, W. J. Dworschack, R. J. Lewis-Swan, A. M. Rey, O. Romero-Isart, and C. A. Regal, "Time-of-flight quantum tomography of an atom in an optical tweezer", Nature Physics **19**, 569–573 (2023).

[107] S. C. Burd, H. M. Knaack, R. Srinivas, C. Arenz, A. L. Collopy, L. J. Stephenson, A. C. Wilson, D. J. Wineland, D. Leibfried, J. J. Bollinger, D. T. C. Allcock, and D. H. Slichter, "Experimental Speedup of Quantum Dynamics through Squeezing", PRX Quantum **5**, 020314 (2024).

[108] C. A. Rosiek, M. Rossi, A. Schliesser, and A. S. Sørensen, "Quadrature Squeezing Enhances Wigner Negativity in a Mechanical Duffing Oscillator", PRX Quantum **5**, 030312 (2024).

[109] V. Lienhard, R. Martin, Y. T. Chew, T. Tomita, K. Ohmori, and S. de Léséleuc, "Generation of Motional Squeezed States for Neutral Atoms in Optical Tweezers", Physical Review Letters **135**, 253404 (2025).

[110] C. Cohen-Tannoudji, *Quantenmechanik: Band 2*, Vol. 2 (De Gruyter, July 2019).

[111] C. Baxter, M. Babiker, and R. Loudon, "Canonical approach to photon pressure", Physical Review A **47**, 1278–1287 (1993).

[112] M. Sonnleitner and S. M. Barnett, "Mass-energy and anomalous friction in quantum optics", Physical Review A **98**, 042106 (2018).

[113] R. Lopp and E. Martín-Martínez, "Quantum delocalization, gauge, and quantum optics: Light-matter interaction in relativistic quantum information", Physical Review A **103**, 013703 (2021).

[114] D. L. Andrews, G. A. Jones, A. Salam, and R. G. Woolley, "Perspective: Quantum Hamiltonians for optical interactions", The Journal of Chemical Physics **148**, 040901 (2018).

[115] R. G. Woolley, "Gauge invariant wave mechanics and the Power-Zienau-Woolley transformation", Journal of Physics A: Mathematical and General **13**, 2795–2805 (1980).

[116] N. B. Delone, *Atoms in strong light fields*, Springer Series in Chemical Physics 28 (Springer-Verlag, Berlin, 1985), 339 pp.

[117] N. B. Delone and V. P. Krainov, "AC Stark shift of atomic energy levels", Physics-Uspekhi **42**, 669–687 (1999).

[118] S. Stenholm, "The semiclassical theory of laser cooling", Reviews of Modern Physics **58**, 699–739 (1986).

[119] D. Leibfried, R. Blatt, C. Monroe, and D. Wineland, "Quantum dynamics of single trapped ions", Reviews of Modern Physics **75**, 281–324 (2003).

[120] C. Cohen-Tannoudji, J. Dupont-Roc, and G. Grynberg, *Atom-photon interactions* (Wiley, New York, 1992), 656 pp.

[121] J. Dalibard and C. Cohen-Tannoudji, "Dressed-atom approach to atomic motion in laser light: the dipole force revisited", Journal of the Optical Society of America B **2**, 1707 (1985).

[122] M. Born and R. Oppenheimer, "Zur Quantentheorie der Molekeln", Annalen der Physik **389**, 457–484 (1927).

[123] I. I. Beterov, I. I. Ryabtsev, D. B. Tretyakov, and V. M. Entin, "Quasiclassical calculations of blackbody-radiation-induced depopulation rates and effective lifetimes of Rydberg nS, nP, and nD alkali-metal atoms with $n \leq 80$", Physical Review A **79**, 052504 (2009).

[124] T. F. Gallagher and W. E. Cooke, "Interactions of blackbody radiation with atoms", Physical Review Letters **42**, 835–839 (1979).

[125] C. Boisseau, I. Simbotin, and R. Côté, "Macrodimers: Ultralong Range Rydberg Molecules", Physical Review Letters **88**, 133004 (2002).

[126] J. P. Shaffer, S. T. Rittenhouse, and H. R. Sadeghpour, "Ultracold Rydberg molecules", Nature Communications **9**, 1965 (2018).

[127] É. Ghys, "The Lorenz Attractor, a Paradigm for Chaos", in *Chaos: Poincaré Seminar 2010*, edited by B. Duplantier, S. Nonnenmacher, and V. Rivasseau (Springer, Basel, 2013), pp. 1–54.

[128] M. C. Soriano, S. Ortin, L. Keuninckx, L. Appeltant, J. Danckaert, L. Pesquera, and G. van der Sande, "Delay-Based Reservoir Computing: Noise Effects in a Combined Analog and Digital Implementation", IEEE Transactions on Neural Networks and Learning Systems **26**, 388–393 (2015).

[129] J. Dambre, D. Verstraeten, B. Schrauwen, and S. Massar, "Information Processing Capacity of Dynamical Systems", Scientific Reports **2**, 514 (2012).

[130] S. Bravyi, D. P. DiVincenzo, and D. Loss, "Schrieffer–Wolff transformation for quantum many-body systems", Annals of Physics **326**, 2793–2826 (2011).

[131] G. Vidal and R. F. Werner, "Computable measure of entanglement", Physical Review A **65**, 032314 (2002).

[132] F. Wolf, C. Shi, J. C. Heip, M. Gessner, L. Pezzè, A. Smerzi, M. Schulte, K. Hammerer, and P. O. Schmidt, "Motional Fock states for quantum-enhanced amplitude and phase measurements with trapped ions", Nature Communications **10**, 2929 (2019).

[133] S. C. Burd, R. Srinivas, J. J. Bollinger, A. C. Wilson, D. J. Wineland, D. Leibfried, D. H. Slichter, and D. T. C. Allcock, "Quantum amplification of mechanical oscillator motion", Science **364**, 1163–1165 (2019).

[134] T. A. Nieminen, G. Knöner, N. R. Heckenberg, and H. Rubinsztein-Dunlop, "Physics of optical tweezers", in *Laser manipulation of cells and tissues*, Vol. 82, Methods in Cell Biology (Academic Press, 2007), pp. 207–236.

[135] P. Lunt, P. Hill, J. Reiter, P. M. Preiss, M. Gałka, and S. Jochim, "Engineering single-atom angular momentum eigenstates in an optical tweezer", Physical Review A **110**, 063315 (2024).

[136] F. Robicheaux, T. M. Graham, and M. Saffman, "Photon-recoil and laser-focusing limits to Rydberg gate fidelity", Physical Review A **103**, 022424 (2021).

[137] G. Higgins, F. Pokorny, C. Zhang, Q. Bodart, and M. Hennrich, "Coherent Control of a Single Trapped Rydberg Ion", Physical Review Letters **119**, 220501 (2017).

[138] P. Silvi, F. Tschirsich, M. Gerster, J. Jünemann, D. Jaschke, M. Rizzi, and S. Montangero, "The Tensor Networks Anthology: Simulation techniques for many-body quantum lattice systems", SciPost Physics Lecture Notes, 8 (2019).

[139] C. Lubich and I. V. Oseledets, "A projector-splitting integrator for dynamical low-rank approximation", BIT Numerical Mathematics **54**, 171–188 (2013).

[140] B. Kloss, D. Reichman, and Y. Bar Lev, "Studying dynamics in two-dimensional quantum lattices using tree tensor network states", SciPost Physics **9**, 070 (2020).

A. Publications

A.1. [P1] - Time series learning in a many-body Rydberg system with emergent collective amplification

nature communications

Article | Article in Press

https://doi.org/10.1038/s41467-026-77083-1

Time series learning in a many-body Rydberg system with emergent collective amplification

Received: 11 December 2025

Accepted: 7 August 2026

Published online: 24 August 2026

Check for updates

Zongkai Liu[1,2,8] ✉, Qiming Ren[1,2,8], Chris Nill[3,4,8] ✉, Albert Cabot[3,5], Wei Xia[6], Yanjie Tong[1,2], Huizhen Wang[1,2], Wenguang Yang[1,2], Junyao Xie[1,2], Mingyong Jing[1,2], Hao Zhang[1,2], Liantuan Xiao[1,2], Suotang Jia[1,2], Igor Lesanovsky[3,7] & Linjie Zhang[1,2] ✉

Interacting Rydberg atoms constitute a versatile platform for the realization of non-equilibrium states of matter. Close to phase transitions, they respond collectively to external perturbations, which can be harnessed for technological applications in the domain of quantum metrology and sensing. Owing to the controllable complexity and straightforward interpretability of Rydberg atoms, we can observe and tune the emergent collective amplification. Here, we investigate the application of an interacting Rydberg vapour for the purpose of time series prediction. The vapour is driven by a laser field whose Rabi frequency is modulated in order to input the time series. We find that close to a non-equilibrium phase transition, where collective effects are amplified, the capability of the system to learn the input becomes enhanced. This is reflected in an increase of the accuracy with which future values of the time series can be predicted. Using the Lorenz time series and temperature data as examples, our work demonstrates how emergent phenomena enhance the capability of noisy many-body systems for data processing and forecasting.

Computation, information processing, and dynamics in many-body systems are inherently intertwined. One paradigmatic example is the Hopfield network[1], whose architecture, energy function, and memory retrieval are directly derived from the Ising model. Other examples include swarm intelligence algorithms, such as particle swarm optimization[2–4] and ant colony optimization[5,6]. These systems exploit collective interactions across scales to exhibit emergent computational capabilities, where nonlinear coupling between microscopic degrees of freedom generates information-processing capabilities. This interplay underscores both the potential of physical systems as computational platforms and the need to decode how collective behaviour enables specific computational tasks.

A particularly relevant and challenging task is time-series prediction of complex systems, for example, chaotic dynamics such as the Lorenz attractor[7,8] or weather forecasting[9]. A computational framework that has proven effective for such problems is reservoir computing[10–13]. In reservoir computing, only a linear readout layer is trained, while the high-dimensional, nonlinear reservoir dynamics remain fixed. This significantly simplifies training, as it avoids tuning a large number of internal degrees of freedom and instead leverages the

[1]State Key Laboratory of Quantum Optics Technologies and Devices, Institute of Laser Spectroscopy, Shanxi University, Taiyuan, China. [2]Collaborative Innovation Center of Extreme Optics, Shanxi University, Taiyuan, Shanxi, China. [3]Institut für Theoretische Physik and Center for Integrated Quantum Science and Technology (IQST), Eberhard Karls Universität Tübingen, Tübingen, Germany. [4]Institute for Applied Physics, University of Bonn, Bonn, Germany. [5]Institute for Cross-Disciplinary Physics and Complex Systems (IFISC) UIB-CSIC, Campus Universitat Illes Balears, Palma de Mallorca, Spain. [6]Department of Physics and The Hong Kong Institute of Quantum Information Science and Technology, The Chinese University of Hong Kong, Hong Kong, China. [7]School of Physics and Astronomy and Centre for the Mathematics and Theoretical Physics of Quantum Non-Equilibrium Systems, The University of Nottingham, Nottingham, UK. [8]These authors contributed equally: Zongkai Liu, Qiming Ren, Chris Nill. ✉e-mail: lzk1997@sxu.edu.cn; chris.nill@uni-tuebingen.de; zlj@sxu.edu.cn

computational power of the intrinsic dynamics of the system, provided they are sufficiently rich[14–16]. Reservoir computing has been implemented in a variety of settings, such as in echo state networks[17–19] and liquid state machines[20] as well as in physical systems such as delay-based electronic circuit reservoirs[21], and quantum reservoir computing platforms[22–24]. Despite this diversity, understanding the fundamental mechanisms that endow complex physical reservoirs with learning and prediction capabilities remains subject to current research[25].

Thermal Rydberg vapours are a promising platform in this context. These many-body systems feature strong interatomic interactions and coexisting drive-dissipation processes, whose competition gives rise to a rich phase diagram[26–30] and a wealth of emergent non-equilibrium phenomena, including collective jumps[31,32], ergodicity breaking[33,34], self-induced transparency[35], and dissipative time crystals[36]. These features make Rydberg ensembles attractive candidates as platforms for reservoir computing and, at the same time, ideal systems for probing the microscopic origin of learning capabilities in complex many-body dynamics at the atomic level.

In this work, we exploit the response of a Rydberg vapour as a physical reservoir for time-series prediction. The experimental control over the collective behaviour of the system enables us to systematically analyse how its internal dynamics give rise to learning capabilities. We find that the learning performance is improved in the vicinity of a phase transition, where the collective response is strongly amplified in the Rydberg vapour. This behaviour is in good agreement with a corresponding theoretical minimal model, providing insight into how critical many-body dynamics augment the computational power of physical reservoirs.

Results

Before discussing the detailed experimental results, we briefly outline the overall aim and approach of our study. The experiment is designed to test whether the vapour of interacting Rydberg atoms can process and predict time-dependent input signals by exploiting its intrinsic nonlinear and collective dynamics; see Fig. 1. To achieve this, we encode time-series data $x(t)$ in an amplitude modulation of the coupling laser's Rabi frequency Ω_c. The coupling laser drives the atomic ensemble under fixed detuning Δ_c and serves as the input signal. The transmission of a probe laser serves as the measurable output that reflects how the Rydberg vapour responds to and processes the input information. We record this transmission signal as a time series and use it as input to a simple linear regression model that is trained to predict future values of the original time series $x(t)$. By comparing the system's behaviour for different detunings Δ_c, particularly within and outside regions of bistability, we can assess how collective nonlinear effects of the Rydberg vapour influence its predictive capability.

Experimental setup

In our experiment, caesium (Cs) atoms are placed inside a $(5 \times 5 \times 5)$ cm^3 heated cube glass cell, with the temperature maintained at 47.0 °C, corresponding to an atomic density of 3.6×10^{11}cm^{-3}[37]. As shown in Fig. 1, a probe laser with wavelength 852nm and Rabi frequency $\Omega_p/2\pi \sim 84.92$MHz drives the $|6S_{1/2}, F=4\rangle \leftrightarrow |6P_{3/2}, F=5\rangle$ transition (D2 line). The coupling laser with wavelength 510nm and Rabi frequency Ω_c is used to excite atoms to the $|48D_{5/2}\rangle$ Rydberg state. The coupling and probe lasers are aligned counter propagating in the atomic vapour cell to partially suppress Doppler broadening, forming an electromagnetically induced transparency (EIT) configuration. In this configuration, the transmission of the probe laser through the Rydberg vapour is controlled by the coupling laser[38]. The Rabi frequency Ω_c of the coupling laser is amplitude-modulated using an acousto-optic modulator (AOM) and an arbitrary waveform generator (AWG), which operates between minimal $\Omega_{\min}/2\pi \sim 2.56$MHz and peak Rabi frequency $\Omega_{\max}/2\pi \sim 3.14$MHz. The Cs D2 line is utilized to lock the probe laser frequency, while the coupling laser frequency is stabilized to a super-stable cavity with finesse 2×10^5. The frequency difference between coupling (probe) light and the corresponding transition $|6P_{3/2}\rangle \leftrightarrow |48D_{5/2}\rangle$ ($|6S_{1/2}\rangle \leftrightarrow |6P_{3/2}\rangle$) is defined as the detuning Δ_c (Δ_p). To measure the EIT spectrum, the frequency of the coupling light is scanned with Δ_c swept back and forth from 0 MHz to 20 MHz, while the probe light is kept resonant with the D2 line ($\Delta_p = 0$), and the probe transmission is recorded by a photodetector.

Time series prediction

We benchmark the predictive capability of the Rydberg ensemble using two qualitatively different time series: the x-component of the Lorenz attractor, x_{Lor} (see Methods), and the daily maximum temperature in Beijing, from 2011-01-01 to 2020-03-23, x_{temp}[39]. These examples probe the system's performance and generalization capability across different types of data, specifically chaotic and stochastic signals.

The input signal $x(t)$ is first discretized at equidistant times t_n to obtain $x_n = x(t_n)$. Each value x_n is then mapped linearly to the interval $[\Omega_{\min}, \Omega_{\max}]$ and encoded as a time amplitude modulation in the coupling Rabi frequency $\Omega_c(t_n) \in [\Omega_{\min}, \Omega_{\max}]$, with modulation rate of 4kHz, see Fig. 1. For the Lorenz attractor, we show a representative input signal $\Omega_c(t)$ in Fig. 2 (a). The modulated coupling laser drives the Rydberg vapour at a fixed detuning Δ_c, while the transmission $T(t)$ of the probe laser is recorded continuously. Sampling at times t_n yields a discrete output sequence $T(t_n)$ that reflects the system's response to the input. Representative transmission traces for three characteristic detunings $\Delta_c = 10$, 12, and 14 MHz are shown in Figs. 2(b–d), respectively: outside the bistable regime [panel (b)] and within the bistable

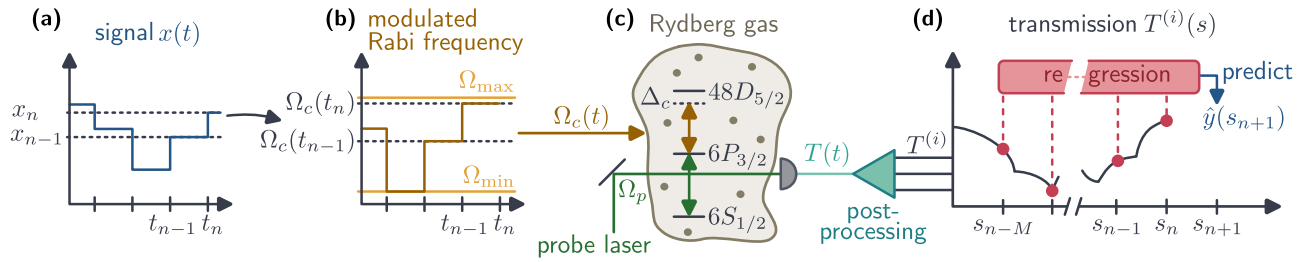

Fig. 1 | Time series prediction with a Rydberg vapour. a The time-dependent input signal $x(t)$ is sampled at discrete time steps t_n, yielding a step-wise constant function with values $x_n = x(t_n)$. **b** The signal is converted into the Rabi frequency $\Omega_c(t_n)$ of the coupling laser, which couples the intermediate state $6P_{3/2}$ to the Rydberg state $48D_{5/2}$ detuned by Δ_c. This Rabi frequency ranges within the interval $[\Omega_{\min}, \Omega_{\max}]$. **c** The caesium (Cs) atoms are first excited by a probe laser with a constant Rabi frequency Ω_p, which drives the transition from the ground state $6S_{1/2}$ to the intermediate $6P_{3/2}$. Subsequently, the atoms are excited by the modulated coupling laser. The optical response of the Cs vapour is measured by monitoring the transmission $T(t)$ of this probe laser. **d** The measured transmission $T(t)$ is post-processed after measurement using a Savitzky-Golay filter and down-sampled by a factor of 20, yielding the transmission signals $T^{(i)} = T(t_{i+20n})$. Here, $i \in [1, 20]$ labels the index of the downsampled time series, and $s_n = t_{i+20n}$ denotes the corresponding time. The transmission signal within the time interval $[s_{n-M}, s_n]$ is used to predict the signal $x(s_{n+1})$ (denoted as $\hat{y}(s_{n+1})$). This prediction is generated by a linear regression layer, which was previously trained (see text for details).

https://doi.org/10.1038/s41467-026-77083-1

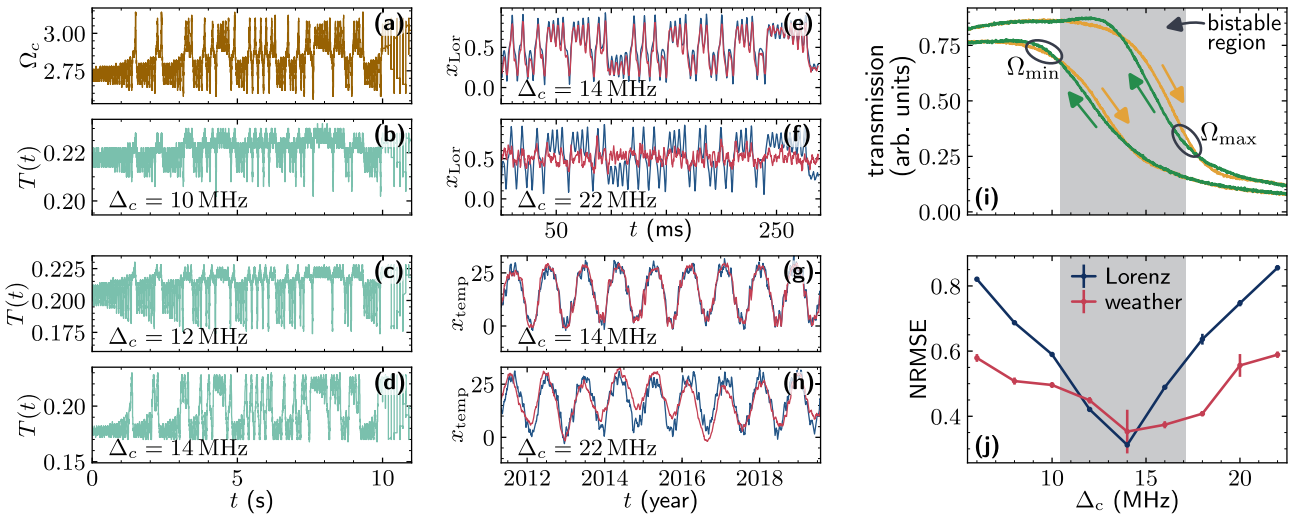

Fig. 2 | Time series prediction. a Amplitude modulated signal $\Omega_c/2\pi$ in MHz, which is input into the Rydberg system. **b**–**d** Output transmission signal $T(t)$ in arbitrary units recorded for different detunings Δ_c. The detuning is chosen such that the system is out of (panel b, its Δ_c out of the hysteresis region in panel i) and within the bistable region (panels **c**, **d**, Δ_c inside the hysteresis region in panel **i**). **e**, **f** Time series prediction for the Lorenz series x_{Lor}. A Rydberg vapour operating in the bistable region (**e**) results in a better prediction (red curve), compared to outside (**f**). The ground truth is shown in blue. **g**, **h** Prediction results on daily temperature of Beijing for detuning Δ_c, near (**g**) and out (**h**) of the bistable region. **i** The lower yellow and lower green curves correspond to the minimal Rabi frequency Ω_{min} of the coupling laser but with different scan directions of the detuning Δ_c (as indicated by arrows and colours). The upper yellow and upper green curves correspond to Ω_{max}. A closed hysteresis loop formed by the two scan directions characterizes the bistable phenomenon. The detuning interval where the bistability occurs is marked by a gray shaded box. **j** Normalised root mean square error (NRMSE) for varying detuning Δ_c on Lorenz and weather temperature time series prediction tasks. Inside the bistable region (gray shaded box), the NRMSE is lower than outside. The plotted NRMSE values correspond to the average over the 20 sampled time series, while the error bar corresponds to their standard deviation (see text for details).

region [panels (c, d)]. Specifically, the bistable region is defined by the closed hysteresis interval formed by the two scan directions of the coupling laser (shaded interval in panel (i)). When Δ_c lies within this shaded interval, the system operates within the bistable region (e.g., Δ_c = 12, 14 MHz), whereas detunings outside this interval (e.g., Δ_c = 10 MHz) correspond to the non-bistable regime. Near bistability, the peak-to-peak amplitude of the transmission is visibly enhanced, consistent with the increased collective gain inside the bistable region.

For the subsequent analysis, the raw transmission data $T(t_n)$ are first processed with a Savitzky–Golay filter (window size 10, polynomial order 3[40,41]) to suppress high-frequency noise. For a discussion of causality of this filtering process, we refer to Methods. To obtain several time series from a single run, we generate 20 downsampled transmission series by taking every 20th point with different initial offsets, see Fig. 1. Thus, each sub-series $T^{(i)}$ (with $i = 1, \ldots, 20$) contains one out of every 20 points of the original record and has one twentieth of its length. For example, for the sub series $T^{(1)}$, the downsampled series contains 1st, 21th, 41th,..., $(20t_n + i)$-th points of the original record.

The prediction task is formulated using a sliding window over each downsampled series. We fix a window length M = 200 and, for each series i, use M consecutive transmission values as input and the next value of the downsampled time series as the prediction target. Writing

$$\vec{T}_k^{(i)} = (T_k^{(i)}, T_{k+1}^{(i)}, \ldots, T_{k+M-1}^{(i)})^{\mathsf{T}} \tag{1}$$

for the k-th input window, the corresponding target is chosen as

$$y_k^{(i)} = x(t_{i+20(k+M)}). \tag{2}$$

Shifting the window generates the full set of input-target pairs $(\vec{T}_k^{(i)}, y_k^{(i)})$ which are indexed by k. Thus, the input-target pairs include transmission data of the probe laser in $\vec{T}_k^{(i)}$ as well as the consecutive point of the time series $y_k^{(i)}$ which is proportional to the Rabi frequency of the coupling laser Ω_c.

We use 70% of the input-target pairs for training and the remaining 30% for testing. For each subseries i, we train a linear regression model that maps the M-dimensional transmission window $\vec{T}_k^{(i)}$ to a scalar prediction $\hat{y}_m^{(i)}$ of the next value of the original time series. Introducing a weight vector $\vec{w}^{(i)}$ and a scalar bias $b^{(i)}$, the linear regression model is defined as $\hat{y}_m^{(i)} = \vec{T}_m^{(i)} \cdot \vec{w}^{(i)} + b^{(i)}$. The parameters $\vec{w}^{(i)}$ and $b^{(i)}$ are obtained by minimizing the mean-squared error (MSE) on the training set, $\mathrm{MSE}_{\mathrm{train}}^{(i)} = \frac{1}{N_{\mathrm{train}}^{(i)}} \sum_{k \in \mathrm{train}} (y_k^{(i)} - \hat{y}_k^{(i)})^2$, where $N_{\mathrm{train}}^{(i)}$ denotes the number of training samples in series i.

It is noted that no nonlinear activation functions are used in the readout layer. The readout operations are limited to linear regression (least squares method) and matrix multiplication, which are strictly linear calculations. Therefore, all the nonlinear processing of the input signal observed in our experiments originates from the intrinsic dynamics of the Rydberg vapor, which is characterized by the hysteresis loop in the system's response (Fig. 2i).

Figure 2(e–h) show representative prediction results. When the system is operated within the bistable regime [Fig. 2(e, g)], the predicted trajectories closely follow the Lorenz signal and the temperature record, including their short-time fluctuations. Outside the bistable region [Fig. 2(f, h)], the predictions deviate substantially from the ground truth, indicating a reduced learning performance.

The dependence on detuning is summarized in Fig. 2(i, j). Figure 2(i) displays the EIT spectrum as a function of the coupling detuning Δ_c for minimal (Ω_{min}) and maximal (Ω_{max}) Rabi frequency. For each value of Ω_c, we scan Δ_c once from low to high frequency (yellow curves) and once in the opposite direction (green), and record the probe transmission as output. The upper pair corresponds to Ω_{max}, and the lower pair to Ω_{min}. Since the modulation range of Ω_c is $\Omega_c \in [\Omega_{\mathrm{min}}, \Omega_{\mathrm{max}}]$, a transmission region exists during the modulation of the Rabi frequency Ω_c; for each detuning Δ_c, this region is bounded

https://doi.org/10.1038/s41467-026-77083-1

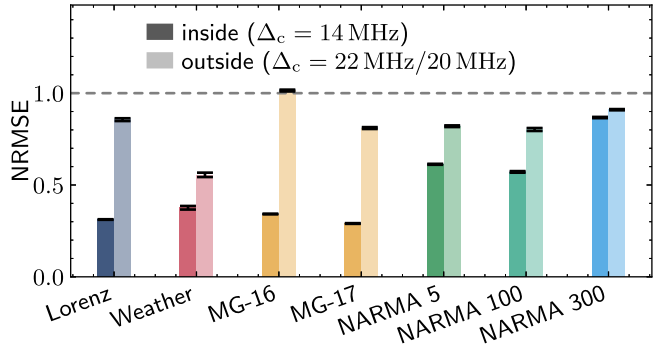

Fig. 3 | Prediction performance inside and outside the bistable region. Normalised root mean square error (NRMSE) for all benchmark tasks, comparing operation inside the bistable region ($\Delta_c = 14$ MHz) and outside ($\Delta_c = 22$ MHz, or 20 MHz for NARMA). For all tasks—Lorenz, weather temperature, Mackey--Glass ($\tau_{MG} = 16, 17$), and NARMA-n ($n = 5, 100, 300$)—the prediction error is lower inside the bistable region, where the collective susceptibility of the Rydberg vapour is enhanced. The NRMSE values correspond to the average over 20 downsampled sub-series; error bars denote their standard deviation.

by the upper pair and lower pairs. These two branches of the transmission curve form a closed hysteresis loop: in the central gray-shaded interval, the measured transmission at a given Δ_c depends on the scan history, which signals the presence of two coexisting stable states of the Rydberg vapour. Consequently, the detuning Δ_c serves as a control parameter that characterizes the proximity of the system to the bistable region and adjusts the strength of the nonlinearity.

This bistable region is located precisely in the parameter window in which the collective gain is largest and where the prediction performance of the system is found to be optimal. This is quantified by the normalised root mean squared error (NRMSE)[13], defined as

$$\mathrm{NRMSE} = avg_i\left(\sqrt{\frac{\sum_{k=1}^{N_{\mathrm{pred}}^{(i)}}\left(y_k^{(i)}-\hat{y}_k^{(i)}\right)^2}{\sum_{k=1}^{N_{\mathrm{pred}}^{(i)}}\left(y_k^{(i)}-\bar{y}^{(i)}\right)^2}}\right), \tag{3}$$

where $\bar{y}^{(i)}$ is the temporal mean of the target sequence.

Figure 2(j) presents the NRMSE as a function of detuning: the error exhibits a clear minimum inside the bistable window and increases again outside it. The error bars denote the standard deviation over the twenty downsampled sub-series.

In summary, the Rydberg vapour shows its best prediction performance on both tasks when operated near the bistable regime adjusted by detuning Δ_c, where the collective gain is largest. The correlation between the EIT hysteresis and the minimum NRMSE points to emergent collective effects, rather than single-atom physics, as the key resource for enhanced learning capacity.

Standard benchmark tasks

To quantify the nonlinear capacity of the Rydberg reservoir beyond the Lorenz and temperature tasks, we evaluate its performance on multiple standard benchmarks from the reservoir computing literature: the Mackey-Glass (MG) chaotic time series and the NARMA-n task, see Fig. 3.

The Mackey-Glass system is a delay-differential equation that generates chaotic dynamics for sufficiently large delay parameters (see Methods). We tested our system with delays $\tau_{MG} = 16$ and 17. Operating inside the bistable region, the reservoir successfully tracks the chaotic dynamics, achieving NRMSE values of 0.34 and 0.29, respectively, which are a substantial improvement over the values obtained outside the bistable region ($\Delta_c = 22$ MHz), where NRMSE values are 1.01 and 0.81, respectively.

The NARMA-n (nonlinear autoregressive moving average) benchmark is the established standard for evaluating a reservoir's ability to nonlinearly transform past inputs (see Methods). In Fig. 3 we evaluated the complexities $n = 5$, 100, and 300 at two detunings, one within and one outside the bistable region. Further data for additional n and detuning values are given in the Methods. Inside the bistable region, where the collective susceptibility is enhanced, the system maintains a low prediction error (NRMSE ≈0.61 for NARMA-5 and NRMSE ≈0.57 for NARMA-100). Outside the bistable region ($\Delta_c = 20$ MHz), the performance is degraded (NRMSE ≈0.82 for NARMA-5 and NRMSE ≈0.80 for NARMA-100). For NARMA-300, which requires memory exceeding the $M = 200$ readout window boundary, the performance collapses to NRMSE ≈ 0.87 (inside) and NRMSE ≈ 0.91 (outside), demonstrating that the system memory is window-bounded (see Methods). These results show that the system operates in a high-gain, noise-resilient regime where the enhanced collective susceptibility provides the main performance boost.

Theoretical model

The experimental results we have just presented reveal a correlation between improved learning capability and the regime in which the Rydberg vapour displays bistability. In order to gain an understanding of this relation, we are going to describe the Rydberg vapour using a mean-field model, see e.g. Refs. 27, 31, 32, and analyse the learning capability of the modelled system. This minimal theoretical model is designed to capture the essential features of the many-body phase transition and bistable regime relevant to the reservoir computing response. It employs an all-to-all mean-field approximation, a standard description for collective dynamics in Rydberg ensembles, and is derived from the Lindblad quantum master equation. The model describes collective phenomena involving atomic interactions and driven-dissipative processes, without invoking strong quantum correlations or entanglement as the origin of the observed dynamics.

The dilute vapour of laser-driven Rydberg atoms is modelled as N identical two-level systems with ground $|g\rangle$ and Rydberg $|e\rangle$ states (see Methods). The atoms are driven with Rabi frequency Ω and detuning Δ, while dissipation enters through spontaneous emission with rate γ and dephasing with rate γ_d. The interaction between the atoms in the Rydberg state is modelled as an all-to-all energy shift term in the Hamiltonian, i.e. $H_{\mathrm{int}} = \frac{V}{N-1}\sum_{j<k}|e\rangle\langle e|_j|e\rangle\langle e|_k$. In the thermodynamic limit, the dynamics is described by the mean-field equations of motion for the average population $n(t) = \frac{1}{N}\sum_{j=1}^{N}\langle|e\rangle\langle e|_j\rangle$ and optical coherence $q(t) = \frac{1}{N}\sum_{j=1}^{N}\langle|e\rangle\langle g|_j\rangle$. Since in a dilute vapour at room temperature γ_d typically exceeds γ and Ω, the coherence relaxes on a much shorter timescale ($\dot{q} \gg \dot{n}$), justifying its adiabatic elimination (see Methods). Therefore, the dynamics is well described by an equation for the average Rydberg population alone. This reads

$$\dot{n} = -\frac{\Omega^2\Gamma\left(n-\frac{1}{2}\right)}{\Gamma^2+(\Delta-nV)^2} - \gamma n =: F(n), \tag{4}$$

where we have defined the combined dissipation rate $\Gamma = \frac{1}{2}(\gamma+\gamma_d)$. This nonlinear differential equation captures the interplay of coherent driving, interactions, dephasing, and spontaneous emission. Depending on the parameter values, the model displays one or two stable solutions for the steady-state Rydberg density n_{ss}, which are shown in Fig. 4(a).

In the experiment, the input signal is encoded by modulating the Rabi frequency. The system operates in a regime characterized by the EIT spectrum curves shown in Fig. 2(i), in which a more pronounced hysteresis is observed for larger Rabi frequencies. We find that the mean-field model displays a similar response in the stationary Rydberg density n_{ss} when operating at Rabi frequencies around the lower critical point at which the bistable region emerges. This is illustrated in Fig. 4(b), in which we show the stationary Rydberg densities along the

https://doi.org/10.1038/s41467-026-77083-1

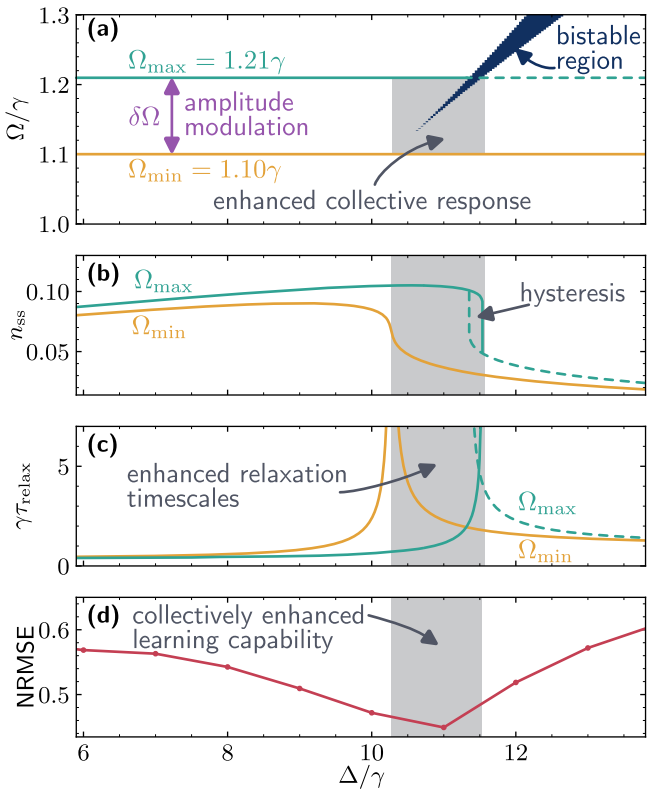

Fig. 4 | Mean-field dynamical response and learning capacity. a Phase diagram of the mean-field equation (4). The blue region marks the bistable domain where two stable stationary solutions exist. The yellow (green) horizontal lines indicate the minimum (maximum) Rabi frequency of the input signal of the learning protocol, see (**d**). The gray shadowed area indicates the region in which collective effects are most prominent for the considered Rabi frequencies. Its left (right) boundary corresponds to the detuning at which the relaxation time for the minimum (maximum) Rabi frequency displays a maximum; see (**c**). **b** Stationary Rydberg density n_{ss} for varying detuning along the horizontal cuts $\Omega/\gamma = 1.1$ and $\Omega/\gamma = 1.21$. For the case $\Omega/\gamma = 1.21$ hysteresis is observed. We denote the solution with the lower density with a dashed line. **c** Relaxation time τ_{relax} along the same cuts as in (**b**) for the stable stationary solutions. Within the bistable region, two relaxation times are possible, one for each stable solution. The solid (dashed) line corresponds to the solution with higher (lower) density. The longest relaxation times occur near the boundary of the bistable region. **d** Normalised root mean square error (NRMSE) for the prediction of the Lorenz input signal, fixing the parameters to $\Omega/\gamma = 1.1$, modulation amplitude $\delta\Omega/\Omega = 0.1$, modulation period $\gamma T = 20$, noise strength $D/\gamma = 0.0001$, and for different detunings (points). In all panels $V/\gamma = 100$ and $\gamma_d/\gamma = 10$.

maximum and minimum Rabi frequencies used in the learning protocol. In this region, collective effects result in a strong nonlinear response near the boundaries of the bistable regime, as well as hysteresis. This strong nonlinearity enhances the system's gain within the shaded region of Fig. 4(b), which, in the presence of thermal fluctuations and noise, improves the effective signal quality. In the experiment, this enhancement is reflected by the increased peak-to-peak value from Fig. 2(b)–(d) (see also Methods).

In order to theoretically analyse the correlation between these collective effects and the enhanced learning capability, we need to complement the mean-field equation (4) with a stochastic term that models the presence of noise in the experiment. We then consider the following stochastic equation for the Rydberg density: $\dot{n} = F(n) + \sqrt{nD}\xi(t)$, where $\xi(t)$ is a white noise term, and D a constant controlling its overall strength. The input signals to be predicted are then introduced analogously as in the experiment, by modulating the Rabi frequency in a piecewise fashion, with maximum modulation amplitude $\delta\Omega := \Omega_{max} - \Omega_{min} = 0.1\Omega$ and modulation period $\gamma T = 20$, see Fig. 1. The corresponding NRMSE for the Lorenz input is shown in Fig. 4(d) for different Δ/γ along a cut at $\Omega/\gamma = 1.1$. The NRMSE displays a dip around $\Delta/\gamma \sim 11$, coinciding with the region in which collective effects are most prominent; see the corresponding shadowed region in Fig. 4(b) and (d), hence supporting our previous hypothesis based on the experimental results; see Fig. 2(i) and (j). Therefore, our theoretical findings align with the experimental finding that the learning capability is improved in the bistable region, where collective effects are more prominent.

Experiment and theory also align in the observation that relaxation dynamics slows down in the regime in which the learning capability is improved. Theoretically, characteristic relaxation times, τ_{relax}, can be obtained by linearizing Eq. (4) around each of its stationary solutions, n_{ss} (see Methods). The typical behaviour of the relaxation time within the regime of operation is shown in Fig. 4 (c). We observe that near the boundaries of the bistable regime, the so-called spinodal lines[27], the relaxation times increase considerably, in agreement with experimental observations (see Methods). This prolonged relaxation time is characteristic of complex systems undergoing critical behaviour and is also referred to critical slowing down[31,42–46].

Discussion

In this work, we have experimentally demonstrated that a driven-dissipative Rydberg vapour displays improved time-series prediction performance when operated near a bistable phase transition. This improvement is consistently observed across all benchmark tasks and is reproduced by a mean-field model, establishing a direct link between emergent collective phenomena and learning capability in Rydberg atomic systems.

Our analysis identifies the underlying mechanism: near bistability, the collective susceptibility peaks, providing a large effective gain that amplifies the contrast between different input levels in the output. The signal-to-noise ratio, by contrast, remains approximately flat across detunings (Fig. 6c) and is not the driver of the improvement. The NARMA benchmarks and IPC analysis further reveal that outside the bistable region, the operating point lies on the quadratic tail of the EIT transfer curve, encoding the input through a basis that the linear readout cannot invert; inside the bistable region, the large gain maps inputs onto a nearly linear basis, to which the linear readout is naturally matched.

The enhanced relaxation times observed near the phase boundary (Fig. 5) are consistent with critical slowing down. However, these timescales (~0.14 ms) remain shorter than the effective sample interval after downsampling (5 ms), so the vapour itself resets between successive input steps and does not provide fading memory through its physical relaxation dynamics. The temporal memory available to the readout layer originates instead from the sliding window of size M. The dominant computational resource is therefore the instantaneous nonlinear transformation provided by the collective susceptibility, not the dynamical memory of the reservoir.

Although the overall prediction accuracy is not yet competitive with established reservoir computing platforms, which report significantly lower normalised root mean squared errors[13,22–24], our results show that the collectively enhanced gain near a many-body phase transition is a tunable and experimentally accessible computational resource. We stress that this gain mechanism is general rather than specific to Rydberg systems[23,24,47]; its distinctive realisation here is as a many-body phase transition that is continuously tunable through a single control parameter. Future work may implement advanced methods from the reservoir computing toolbox, such as time-multiplexing and feedback[47–49], combined with reduced downsampling, to further improve the prediction performance in this Rydberg vapour setup. Future research could also investigate the relation between prolonged relaxation time and learning capacity and the

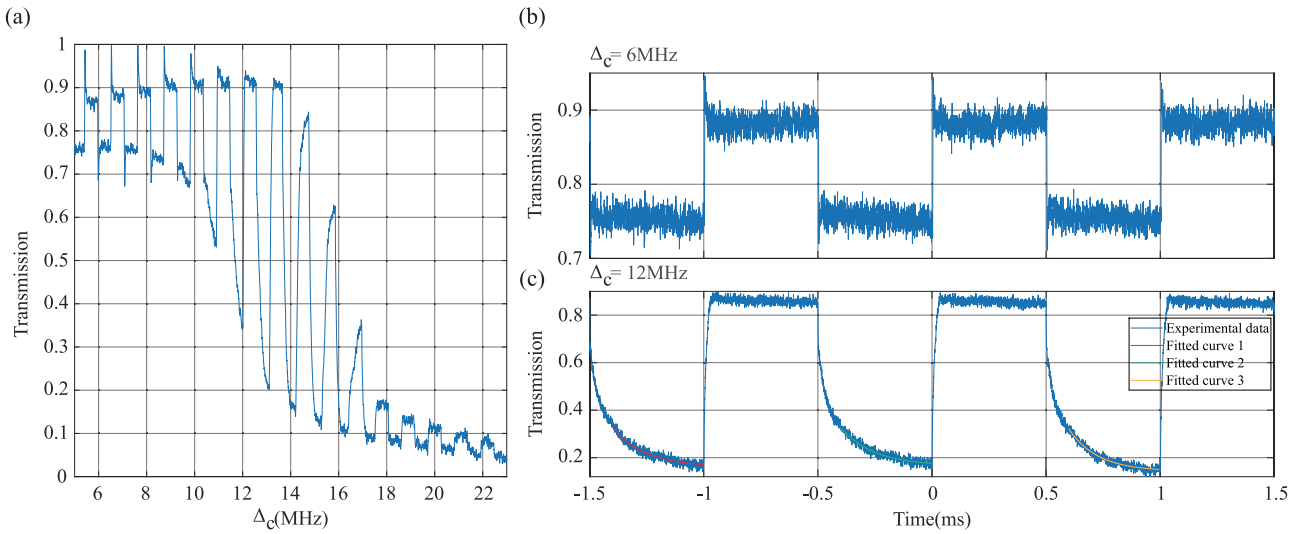

Fig. 5 | Experimental analysis of the relaxation times. Measurement of the transmission of the probe laser when the Rabi frequency Ω_c of the coupling light is amplitude modulated by a square pulse with frequency 1 kHz, duty cycle 50%, and modification depth 15%. In (**a**), the detuning of the coupling light Δ_c is swept from 6 MHz to 22 MHz linearly in time. Instead, in (**b**, **c**) the detuning is fixed to 6 MHz, and 12 MHz, respectively. **b** Corresponds to a point outside the bistable regime, while (**c**) corresponds to a point within the bistable regime. In (**c**) an exponential relaxation is fitted to the experimental data (see text) at three different periods, obtaining the relaxation times τ_1 = 0.139 ms, τ_2 = 0.148 ms and τ_3 = 0.125 ms.

specific mechanistic role of relaxation time in mediating the learning process.

Methods

Time series generation

The Lorenz oscillator $x(t)$ that we used is defined by the differential equation

$$\begin{aligned}\dot{x}(t) &= \sigma[y(t) - x(t)],\\ \dot{y}(t) &= \rho x(t) - y(t) - x(t)z(t),\\ \dot{z}(t) &= x(t)y(t) - \beta z(t),\end{aligned} \tag{5}$$

where $\sigma = 10, \rho = 28, \beta = 8/3$, time step $t_n - t_{n-1} = 0.04$s, total time 640s. Thus, the Rabi frequency of the coupling laser is modulated by $x(t)$ at a rate of 4kHz per bit. The Mackey-Glass series (MG) is defined by the delay-differential equation

$$\dot{x}(t) = \frac{a\,x(t-\tau_{\mathrm{MG}})}{1 + x(t-\tau_{\mathrm{MG}})^{10}} - b\,x(t), \tag{6}$$

with parameters a = 0.2, b = 0.1, and delay τ_{MG}. For $\tau_{\mathrm{MG}} > 17$, the dynamics become chaotic. We tested delays τ_{MG} = 16 and 17. The NARMA-n (nonlinear auto-regressive moving average) benchmark[22] is defined by the recurrence relation

$$y_{k+1} = \alpha y_k + \beta y_k \sum_{j=0}^{n-1} y_{k-j} + \gamma u_{k-n+1} u_k + \delta, \tag{7}$$

where $u_k \in [0, 0.5]$ is the input drawn uniformly at random, α = 0.2, β = 0.04, γ = 1.5, and δ = 0.001. We evaluated complexities n = 5, 10, and 15.

Experimental protocol for benchmark tasks

For each benchmark time series (MG and NARMA-n), the dataset consists of 3500 training points and 1500 testing points. To obtain statistically meaningful error bars, we perform 20 realisations, leading to a total dataset size of 10^5. Except for the modulation waveform and small shifts of the detuning, all experimental parameters are kept identical to those described in the main text.

Before applying the time-dependent modulation, the operating point is set by tuning the detuning Δ_c in the absence of modulation to maximise the signal-to-noise ratio of the transmission signal. The modulation sequence is then applied, and the corresponding optical transmission is recorded. After each measurement, the modulation sequence is switched to the next benchmark. Small drifts in the experimental detuning between runs mean that the system remains within the bistable region but samples slightly different operating points across realisations, contributing to the spread captured by the error bars in Fig. 3.

Data processing and causality

Prior to model training, the raw transmission data $T(t_n)$ are smoothed with a symmetric Savitzky–Golay filter (window size 10, polynomial order 3[40,41]) applied offline to the full recorded trace. Because this filter is symmetric (non-causal), we verified that it does not bias the prediction results by conducting a control experiment using a strictly causal finite impulse response (FIR) filter. The prediction performance was highly consistent between the two filters (with a slight reduction in NRMSE for the causal filter), confirming that the offline symmetric smoothing has a negligible impact on the results.

All time-series prediction uses the causal sliding-window strategy described in the main text: only transmission values at times s_n and earlier are used to predict the input at time s_{n+1}.

Derivation of the mean-field model

We describe the dilute vapour of Rydberg atoms as an ensemble of N two-level systems, with ground state $|g\rangle$ and Rydberg state $|e\rangle$. This two-level reduction follows from adiabatic elimination of the intermediate EIT state, valid at the comparatively low Rydberg densities of our experiment; at much higher densities, a full three-level treatment becomes necessary[34]. The dynamics is described by a Lindblad quantum master equation for the reduced state of the system ρ ($\hbar = 1$):

$$\partial_t \rho = -i[H, \rho] + \sum_{j=1}^{N} \left(\mathcal{D}_{L_{j,\mathrm{s}}}[\rho] + \mathcal{D}_{L_{j,\mathrm{d}}}[\rho] \right), \tag{8}$$

where we have defined the dissipator $\mathcal{D}_L[\rho] = L\rho L^\dagger - \{L^\dagger L, \rho\}/2$, which models the processes of spontaneous emission and dephasing

through the jump operators $L_{j,s} = \sqrt{\gamma}|g\rangle\langle e|_j$ and $L_{j,d} = \sqrt{\gamma_d}|e\rangle\langle e|_j$, respectively. The system Hamiltonian reads

$$H = -\Delta\sum_{j=1}^{N}|e\rangle\langle e|_j + \frac{\Omega}{2}\sum_{j=1}^{N}(|e\rangle\langle g|_j + |g\rangle\langle e|_j) + H_{\text{int}}, \tag{9}$$

where we model the interaction between atoms in the Rydberg state with an all-to-all energy shift: $\frac{V}{N-1}\sum_{j<k}|e\rangle\langle e|_j|e\rangle\langle e|_k$. In the thermodynamic limit, we consider the dynamics of the average Rydberg population, $n(t) = \frac{1}{N}\sum_{j=1}^{N}\langle|e\rangle\langle e|_j\rangle$, and average optical coherence $q(t) = \frac{1}{N}\sum_{j=1}^{N}\langle|e\rangle\langle g|_j\rangle$, for which we obtain the following equations of motion using the mean-field approximation:

$$\begin{aligned}\dot{n} &= \Omega\,\mathrm{Im}[q] - \gamma n,\\ \dot{q} &= -i(\Delta - nV)q - \Gamma q - i\Omega\left(n - \frac{1}{2}\right),\end{aligned} \tag{10}$$

where we have omitted the time labels, denoted the derivative with respect to time with a dot, and defined $\Gamma = (\gamma + \gamma_d)/2$. Assuming $\gamma_d \gg \gamma, \Omega$, the relaxation dynamics of the average optical coherence is much faster than that of the average Rydberg population. Then, we adiabatically eliminate the coherences by setting $\dot{q} = 0$ and replacing:

$$q = -\frac{i\Omega\left(n - \frac{1}{2}\right)}{i(\Delta - nV) + \Gamma} \tag{11}$$

in the dynamics of the average Rydberg population. This yields the mean-field equation presented in the main text, which is used for the numerical analysis presented there.

Order-of-magnitude estimates place the experiment in the collective regime that the all-to-all model is meant to capture. At 47 °C, the caesium density $n \approx 3.6 \times 10^{11}\mathrm{cm}^{-3}$[37] corresponds to a mean interatomic spacing $a \approx 0.8\,\mu$m, while the blockade radius of the $48D_{5/2}$ pair state is $R_b \approx 2\,\mu$m to $3\,\mu$m[37]. Since $R_b \gtrsim a$, of order ten to several tens of atoms lie within a single blockade volume and respond collectively rather than independently, which is precisely the regime in which a mean-field all-to-all treatment provides a faithful minimal description of the bistable transition. Consistently, the value $V/\gamma = 100$ used in the model reflects a van der Waals interaction at the mean spacing (~10^2–10^3 MHz) that far exceeds the effective linewidth (~MHz). The model fixes these dimensionless ratios so as to reproduce the macroscopic bistability rather than to resolve the distance-dependent interaction potential.

Doppler averaging and velocity-dependent interactions are omitted; the model reproduces the qualitative dependence of prediction error on detuning without them. More microscopic extensions, such as Doppler averaging and the full three-level EIT treatment, represent natural directions for future theoretical work.

Theoretical analysis of the relaxation times

Relaxation times are analysed by linearizing Eq. (4) around each of its stationary solutions, i.e., introducing $n(t) = n_{ss} + \delta n(t)$ and keeping only linear terms in $\delta n(t)$. This results in a linear equation for the fluctuation dynamics, $\delta\dot{n} = -\tau_{\text{relax}}^{-1}\delta n$, where $\tau_{\text{relax}} = (|\frac{\partial F(n)}{\partial n}|_{n_{ss}})^{-1}$ defines the characteristic relaxation time.

Experimental analysis of the relaxation times

In order to obtain the relaxation time of the Rydberg system τ_{relax}, we measure the transmission of the probe laser as the Rabi frequency of the coupling laser Ω_c is amplitude modulated. The amplitude modulation corresponds to a square wave with frequency 1kHz, duty cycle 50%, and modification depth 15%. In Fig. 5(a), the detuning is swept linearly in time from 6 MHz to 22 MHz. When the detuning crosses the bistable region, the response is enhanced, while the relaxation time increases. This is analysed in more detail in Fig. 5(b, c), where the detuning Δ_c is fixed outside or inside the bistable region, respectively,

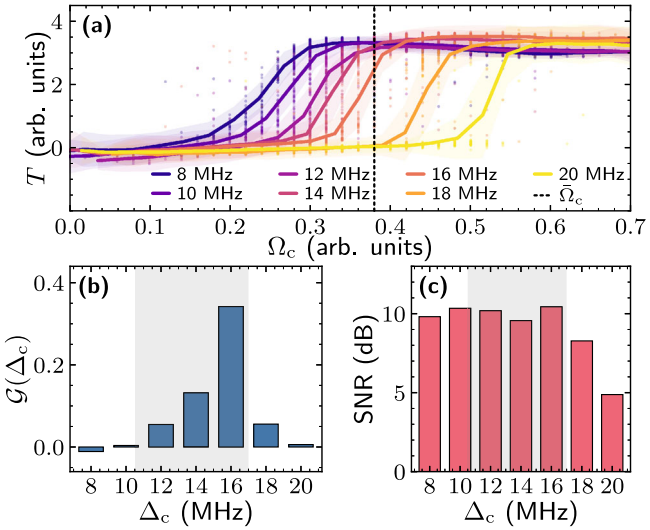

Fig. 6 | Steady-state transfer curves, effective gain, and signal-to-noise ratio. **a** Binned transmission $\langle T\rangle$ as a function of the input drive Ω_c in arbitrary units for coupling detunings Δ_c = 8–20 MHz. Scattered points show individual measurements; solid lines are the bin means $\langle T\rangle_b$ and shaded bands the $\pm1\sigma$ within-bin standard deviation. The vertical dashed line marks the median operating point $\bar{\Omega}_c$ at which the effective gain in (**b**) is evaluated. **b** Effective gain $\mathcal{G}(\Delta_c)$ from Eq. (12). The collective susceptibility is sharply enhanced inside the bistable region (gray shaded interval), with a peak of 0.34 at Δ_c = 16 MHz approximately thirty times larger than the values at Δ_c = 8 and 20 MHz. **c** Signal-to-noise ratio of the transfer curves from Eq. (13). The SNR remains high and approximately flat across Δ_c = 8–16 MHz, demonstrating that the V-shape of the prediction error is set by the gain peak in (**b**) rather than by a noise minimum.

by an ultra-stable cavity and the Pound-Drever-Hall (PDH) method[50–52]. This allows us to obtain the relaxation time by fitting the function $A\exp(-t/\tau) + B$ to every period of the transmission signal, obtaining the values τ_1 = 0.139 ms, τ_2 = 0.148 ms and τ_3 = 0.125 ms for the data shown in panel (c). Notice that in panel (b), the relaxation times are orders of magnitude shorter.

Origin of the learning performance enhancement

To identify the physical origin of the V-shaped detuning dependence of the prediction error observed in Fig. 2(j) and Fig. 3, we dissect the response of the Rydberg vapour into three properties: (i) the local sensitivity of the transmission to the input, (ii) the noise level of the response, and (iii) the structure of the temporal information encoded in the reservoir. The analysis is performed on the dataset of the NARMA task, in which the coupling Rabi frequency is amplitude modulated by a discrete-step sequence drawn from a Gaussian distribution, which allows the reconstruction of the system response and the computation of the information processing capacity (IPC).

Effective gain and signal-to-noise ratio. Based on the data of the NARMA task, Figure 6(a) shows the experimentally measured transfer curve $\langle T\rangle(\Omega_c)$, i.e., the transmission as a function of the coupling Rabi frequency, for detunings Δ_c = 8–20 MHz. To construct these curves, the range of Ω_c values is divided into equally spaced bins; within each bin b, all individual transmission measurements (scattered points) are pooled to yield a bin mean $\langle T\rangle_b$ (solid lines) and a within-bin standard deviation (shaded bands). Each curve has a sigmoidal shape, with the inflection point shifting to larger Ω_c as Δ_c increases. For detunings inside the bistable region (Δ_c = 12–18 MHz), the inflection point falls close to the median operating point $\bar{\Omega}_c$ (vertical dashed line), so the system operates near the steepest part of its transfer function. Outside the bistable region, $\bar{\Omega}_c$ falls on a flatter portion of the sigmoid, where the local slope is considerably smaller.

https://doi.org/10.1038/s41467-026-77083-1

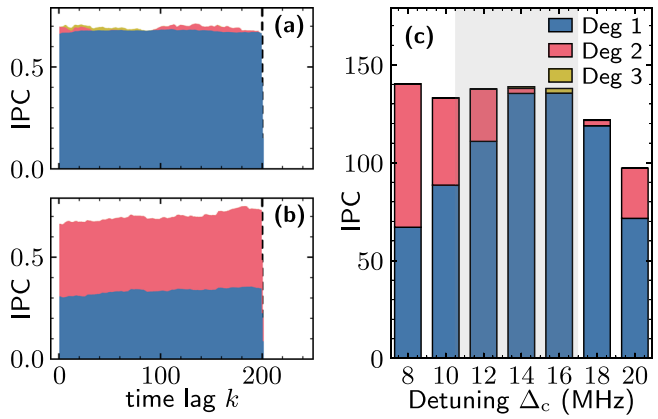

Fig. 7 | Information processing capacity (IPC) of the Rydberg reservoir. a Lag-resolved IPC inside the bistable region ($\Delta_c = 14$ MHz), stacked by polynomial degree (blue: linear $d = 1$, red: quadratic $d = 2$, yellow: cubic $d = 3$). The capacity is dominated by the linear channel and remains essentially constant for all lags $k < 200$, before dropping abruptly to zero at $k = 200$ (vertical dashed line), the size M of the sliding readout window. **b** Lag-resolved IPC outside the bistable region ($\Delta_c = 8$ MHz). About half of the capacity now resides in the quadratic channel, indicating that the input is encoded through the nonlinear tail of the EIT hysteresis loop -- a representation the linear readout cannot invert. **c** Total IPC summed over lags $k = 1$–300 as a function of detuning, resolved by polynomial degree. The quadratic contribution dominates at the smallest detuning, collapses to nearly zero inside the bistable region (gray shaded interval), and reappears at $\Delta_c = 20$ MHz, mirroring the V-shaped NRMSE profile of the linear readout.

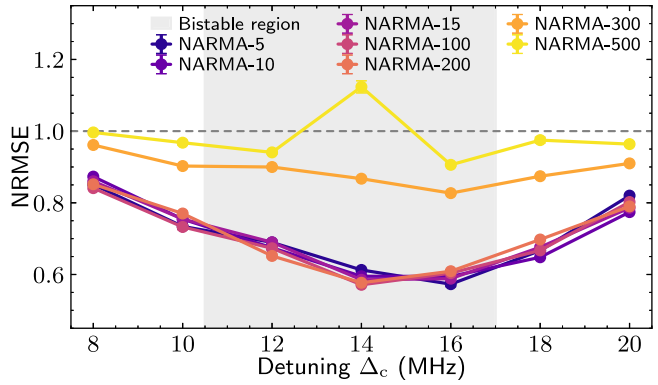

Fig. 8 | NARMA performance and the readout-defined memory horizon. Normalised root mean square error (NRMSE) on the NARMA-n benchmark for $n = 5, 10, 15, 100, 200, 300, 500$ as a function of coupling detuning Δ_c. For all tasks with memory depth $n \le 200$, the error reproduces the V-shape observed in Fig. 2(j), with the minimum located inside the bistable region (gray shaded interval). For $n \ge 300$, which exceeds the sliding readout window $M = 200$, the NRMSE collapses to the trivial baseline NRMSE ≈ 0.9 at every detuning. The transition at $n = M$ identifies the readout window, not the physical relaxation of the Rydberg vapour, as the operative memory horizon.

Based on these data, we evaluate the effective gain,

$$\mathcal{G}(\Delta_c) = \left.\frac{\partial \langle T \rangle}{\partial \Omega_c}\right|_{\Omega_c = \bar{\Omega}_c}, \tag{12}$$

defined as the local slope of the binned transfer curve evaluated at the median operating point $\bar{\Omega}_c = \mathrm{median}(\Omega_c^{(i)})$ (vertical dashed line in Fig. 6(a)). As shown in Fig. 6(b), $\mathcal{G}(\Delta_c)$ peaks sharply inside the bistable region, reaching 0.34 at $\Delta_c = 16$ MHz. This enhancement is a direct signature of the collective amplification near the bistable phase transition: small variations of the input are translated into large, well-separated reservoir states that can be decoded by a linear model.

The second observable is the signal-to-noise ratio of the transfer curve,

$$\mathrm{SNR}(\Delta_c) = 10 \log_{10}\left(\frac{\sigma^2_{\text{between}}}{\sigma^2_{\text{within}}}\right), \tag{13}$$

where

$$\sigma^2_{\text{between}} = \frac{1}{B}\sum_{b=1}^{B} (\langle T \rangle_b - \bar{T})^2, \quad \bar{T} = \frac{1}{B}\sum_{b=1}^{B} \langle T \rangle_b, \tag{14}$$

$$\sigma^2_{\text{within}} = \frac{1}{B}\sum_{b=1}^{B} \mathrm{Var}(T_b), \tag{15}$$

with B the total number of bins. Here $\sigma^2_{\text{between}}$ is the variance of the bin means around their grand mean $\bar{T}$, quantifying how well the system separates distinct input levels in its output; σ^2_{within} is the average of the within-bin variances, capturing transmission fluctuations at a fixed input level due to optical and electronic noise. As shown in Fig. 6(c), the SNR is high and approximately flat (9.5–10.5 dB) across $\Delta_c = 8$–16 MHz and drops only at the largest detunings. The noise floor is therefore essentially independent of the operating point inside the bistable window, and the V-shaped NRMSE profile cannot be ascribed to a noise minimum near the phase transition. The collective gain $\mathcal{G}$ is the dominant control parameter.

Information processing capacity. The transfer curves only describe the instantaneous response. The prediction task additionally requires the reservoir to carry temporal information about the input. We quantify this by the information processing capacity (IPC)[53], resolved by polynomial degree d and time lag k. The target basis consists of Hermite polynomials evaluated on the Gaussian-distributed input sequence, which are orthogonalised by QR decomposition to prevent double-counting of capacity across different (d, k) channels.

Figures 7 (a, b) show the lag-resolved IPC inside and outside the bistable region. At $\Delta_c = 14$ MHz [panel (a)], the capacity is almost entirely linear ($d = 1$, blue) across all lags. At $\Delta_c = 8$ MHz [panel (b)], approximately half of the capacity is carried by the quadratic channel ($d = 2$, red), with a correspondingly reduced linear contribution. The detuning dependence of the integrated capacity (summed over lags $k = 1$–300) is summarised in Fig. 7(c): the quadratic contribution is largest at small detunings, collapses to a value compatible with zero inside the bistable region, and re-emerges at $\Delta_c = 20$ MHz. Higher-order ($d \ge 3$) contributions are negligible throughout.

This basis structure explains why the linear readout layer benefits from operation inside the bistable region. Outside, the operating point $\bar{\Omega}_c$ sits on the nonlinear tail of the EIT hysteresis loop (see Fig. 8), which encodes the input through a quadratic transfer function that the linear readout cannot invert. Inside the bistable region, the same input is mapped onto an almost purely linear basis to which the linear prediction is naturally matched. We emphasise that this does not imply linear physics: the nonlinearity provided by the collective susceptibility (large $\mathcal{G}$) acts as a strong prefactor on top of the linear-dominated representation, supplying the amplification without distorting the basis.

Memory horizon. Both panels (a, b) of Fig. 7 also reveal that the total capacity stays approximately constant for lags $k < 200$ and drops abruptly to zero at $k = 200$. This boundary coincides exactly with the size $M = 200$ of the sliding readout window. The memory available to the linear regressor is therefore controlled by the readout architecture rather than by the intrinsic relaxation of the vapour. Two further observations corroborate this picture. In particular, Fig. 8 shows the NRMSE on the NARMA-n benchmark for

$n = 5, 10, 15, 100, 200, 300, 500$. For tasks with memory depth $n \leq 200$, the error reproduces the V-shape of Fig. 2(j) with a clear minimum inside the bistable region. For $n \geq 300$ the error collapses to the trivial baseline NRMSE ≈ 0.9 at every detuning. The sharp transition at $n = M = 200$ identifies the readout window, not the relaxation of the vapour, as the operative memory horizon: tasks demanding deeper history cannot be solved at any detuning, while shorter-memory tasks fully exploit the gain peak.

Data availability

Data supporting this study are openly available on[39].

Code availability

The code used to generate the results in this study is openly available on Zenodo[39]. It is licensed under the GPLv3 License.

References

1. Krotov, D. A new frontier for hopfield networks. *Nat. Rev. Phys.* **5**, 366 (2023).
2. Kennedy, J. & Eberhart, R. Particle swarm optimization. *ICNN'95* **4**, 1942 (1995).
3. Parsopoulos, K. & Vrahatis, M. Recent approaches to global optimization problems through particle swarm optimization. *Nat. Comput* **1**, 235 (2002).
4. Wang, D., Tan, D. & Liu, L. Particle swarm optimization algorithm: an overview. *Soft Comput* **22**, 387 (2018).
5. Dorigo, M., Birattari, M. & Stutzle, T. Ant colony optimization. *IEEE Comput. Intell. Mag.* **1**, 28 (2006).
6. Dorigo, M. & Blum, C. Ant colony optimization theory: a survey. *Theor. Comput Sci.* **344**, 243 (2005).
7. Ghys, É. The Lorenz Attractor, a Paradigm for Chaos. in *Chaos: Poincaré Seminar 2010*, (eds Duplantier, B. Nonnenmacher, S. &Rivasseau, V.) https://doi.org/10.1007/978-3-0348-0697-8_1 1–54 (Springer, Basel, 2013).
8. Shen, B.-W. A Review of Lorenz's Models from 1960 to 2008. *Int J. Bifurcat Chaos* **33**, 2330024 (2023).
9. Mammedov, Y. D., Olugu, E. U. & Farah, G. A. Weather forecasting based on data-driven and physics-informed reservoir computing models. *Environ. Sci. Pollut. Res Int* **29**, 24131 (2022).
10. Jaeger, H. Short term memory in echo state networks, Fraunhofer-Gesellschaft https://doi.org/10.24406/publica-fhg-291107 (2001).
11. Tanaka, G. et al. Recent advances in physical reservoir computing: a review. *Neural Netw.* **115**, 100 (2019).
12. Nakajima, K. Physical reservoir computing—an introductory perspective. *Jpn J. Appl Phys.* **59**, 060501 (2020).
13. Wringe, C., Trefzer, M. & Stepney, S. Reservoir computing benchmarks: a tutorial review and critique. *Int J. Parallel Emergent Distrib. Syst.* **40**, 313 (2025).
14. Dale, M., Miller, J. F., Stepney, S. & Trefzer, M. A. A substrate-independent framework to characterize reservoir computers. *Proc. R. Soc. A-Math. Phy.* **475**, 20180723 (2019).
15. Carroll, T. L. Optimizing memory in reservoir computers. *Chaos* **32**, 023123 (2022).
16. Gauthier, D. J., Bollt, E., Griffith, A. & Barbosa, W. A. Next generation reservoir computing. *Nat. commun.* **12**, 5564 (2021).
17. Ozturk, M. C., Xu, D. & Príncipe, J. C. Analysis and design of echo state networks. *Neural Comput* **19**, 111 (2007).
18. Sun, C. et al. A systematic review of echo state networks from design to application. *IEEE Trans. Artif. Intell.* **5**, 23 (2024).
19. Jaeger, H. & Haas, H. Harnessing nonlinearity: predicting chaotic systems and saving energy in wireless communication. *Science* **304**, 78 (2004).
20. Maass, W. *Computability in Context* https://doi.org/10.1142/9781848162778_0008 275–296 (Computer Science, 2011).
21. Soriano, M. C. et al. Delay-based reservoir computing: Noise effects in a combined analog and digital implementation. *IEEE Trans. Neural Netw.* **26**, 388 (2015).
22. Fujii, K. & Nakajima, K. Harnessing disordered-ensemble quantum dynamics for machine learning. *Phys. Rev. Appl.* **8**, 024030 (2017).
23. Mujal, P. et al. Opportunities in quantum reservoir computing and extreme learning machines. *Adv. Quantum Technol.* **4**, 2100027 (2021).
24. Sannia, A., Martínez-Peña, R., Soriano, M. C., Giorgi, G. L. & Zambrini, R. Dissipation as a resource for quantum reservoir computing. *Quantum* **8**, 1291 (2024).
25. Yan, M. et al. Emerging opportunities and challenges for the future of reservoir computing. *Nat. Commun.* **15**, 2056 (2024).
26. Ates, C., Pohl, T., Pattard, T. & Rost, J. Strong interaction effects on the atom counting statistics of ultracold Rydberg gases. *J. Phys. B-Mol. Opt.* **39**, L233 (2006).
27. Marcuzzi, M., Levi, E., Diehl, S., Garrahan, J. P. & Lesanovsky, I. Universal nonequilibrium properties of dissipative Rydberg gases. *Phys. Rev. Lett.* **113**, 210401 (2014).
28. Lesanovsky, I. & Garrahan, J. P. Out-of-equilibrium structures in strongly interacting Rydberg gases with dissipation. *Phys. Rev. A.* **90**, 011603 (2014).
29. Ding, D.-S., Busche, H., Shi, B.-S., Guo, G.-C. & Adams, C. S. Phase diagram of non-equilibrium phase transition in a strongly-interacting Rydberg atom vapour. *Phys. Rev. X.* **10**, 021023 (2020).
30. Klocke, K., Wintermantel, T., Lochead, G., Whitlock, S. & Buchhold, M. Hydrodynamic stabilization of self-organized criticality in a driven Rydberg gas. *Phys. Rev. Lett.* **126**, 123401 (2021).
31. Carr, C., Ritter, R., Wade, C., Adams, C. S. & Weatherill, K. J. Nonequilibrium phase transition in a dilute Rydberg ensemble. *Phys. Rev. Lett.* **111**, 113901 (2013).
32. Liu, Z.-K. et al. Emergence of subharmonics in a microwave driven dissipative Rydberg gas. *Phys. Rev. Res.* **6**, L032069 (2024).
33. Ding, D. et al. Ergodicity breaking from Rydberg clusters in a driven-dissipative many-body system. *Sci. Adv.* **10**, eadl5893 (2024).
34. Wadenpfuhl, K. & Adams, C. S. Emergence of synchronization in a driven-dissipative hot Rydberg vapor. *Phys. Rev. Lett.* **131**, 143002 (2023).
35. Bai, Z., Adams, C. S., Huang, G. & Li, W. Self-induced transparency in warm and strongly interacting Rydberg gases. *Phys. Rev. Lett.* **125**, 263605 (2020).
36. Wu, X. et al. Dissipative time crystal in a strongly interacting Rydberg gas. *Nat. Phys.* **20**, 1389 (2024).
37. Šibalić, N., Pritchard, J. D., Adams, C. S. & Weatherill, K. J. Arc: An open-source library for calculating properties of alkali Rydberg atoms. *Comput Phys. Commun.* **220**, 319 (2017).
38. Fleischhauer, M., Imamoglu, A. & Marangos, J. P. Electromagnetically induced transparency: optics in coherent media. *Rev. Mod. Phys.* **77**, 633 (2005).
39. Repository containing all corresponding data and source code of this manuscript https://doi.org/10.5281/zenodo.21128142 (2026).
40. Chen, J. et al. A simple method for reconstructing a high-quality NDVI time-series data set based on the Savitzky-Golay filter. *Remote Sens. Environ.* **91**, 332 (2004).
41. Cao, R. et al. A simple method to improve the quality of NDVI time-series data by integrating spatiotemporal information with the Savitzky-Golay filter. *Remote Sens. Environ.* **217**, 244 (2018).
42. Dakos, V. et al. Slowing down as an early warning signal for abrupt climate change. *Proc. Natl. Acad. Sci. USA* **105**, 14308 (2008).
43. Scheffer, M. et al. Early-warning signals for critical transitions. *Nature* **461**, 53 (2009).
44. Brookes, P. et al. Critical slowing down in circuit quantum electrodynamics. *Sci. Adv.* **7**, eabe9492 (2021).
45. Zhang, J. et al. Early warning signals of the tipping point in strongly interacting Rydberg atoms. *Phys. Rev. Lett.* **133**, 243601 (2024).

46. Wang, Y. et al. Time delay of mean-field interaction in thermal Rydberg atomic gases. *Opt. Express* **33**, 20829 (2025).
47. Sugano, C., Kanno, K. & Uchida, A. Reservoir computing using multiple lasers with feedback on a photonic integrated circuit. *IEEE J. Sel. Top. Quantum Electron.* **26**, 1 (2020).
48. Appeltant, L. et al. Information processing using a single dynamical node as complex system. *Nat. Commun.* **2**, 468 (2011).
49. Zhang, H. et al. Integrated photonic reservoir computing based on hierarchical time-multiplexing structure. *Opt. Express* **22**, 31356 (2014).
50. Black, E. D. An introduction to Pound-Drever-Hall laser frequency stabilization. *Am. J. Phys.* **69**, 79 (2001).
51. Juan, S., Mingxing, J. & Fei, J. Pound-Drever-Hall laser frequency locking technique based on orthogonal demodulation. *Optik* **168**, 348 (2018).
52. Drever, R. W. P. et al. Laser phase and frequency stabilization using an optical resonator. *Appl. Phys. B-Lasers O* **31**, 97 (1983).
53. Dambre, J., Verstraeten, D., Schrauwen, B. & Massar, S. Information processing capacity of dynamical systems. *Sci. Rep.* **2**, 514 (2012).

Acknowledgements

ZL acknowledges the technical support from Rydberg Atomic Quantum Precision Measurement Laboratebry at Shanxi University.

Author contributions

Z.L. conceived the idea for the study. Z.L. and Q.R. conducted the physical experiments. Z.L. and W.X. designed the learning model protocols. C.N and A.C. simulated the theoretical model. Z.L., Q.R., C.N., A.C., W.X., Y.T., H.W., W.Y., J.X., M.J., H.Z., L.X., S.J., L.Z. and I.L. analysed the data. The manuscript was written by Z.L., Q.R., C.N., A.C., H.W. and I.L. The research were supervised by L.Z. and I.L. All authors contributed to discussions regarding the results and analysis contained in the manuscript.

Funding

We acknowledge the National Key R&D Program of China (Grant no. 2022YFA1404003), the National Natural Science Foundation of China (Grants T2495252, 12104279, 123B2062, 12574318), Innovation Program for Quantum Science and Technology (Grant No. 2021ZD0302100), the Fund for Shanxi '1331 Project' Key Subjects Construction, 111 project (Grant No. D18001), PCSIRT (No. IRT_17R70) and Sanjin Talent Program of Shanxi Province SJYC2025280. AC acknowledges support from the Deutsche Forschungsgemeinschaft (DFG, German Research Foundation) through the Walter Benjamin programme, Grant No. 519847240, and from both the Spanish Ministerio de Ciencia, Innovación y Universidades and Universitat de les Illes Balears through the Beatriz Galindo programme (BG24/00134). IL acknowledges support from the DFG through the Research Units FOR 5413/1, Grant No. 465199066, and FOR 5522/1, Grant No. 499180199. Further support was received through the QuantERA II programme (project Co-QuaDis, DFG Grant No. 532763411) that has received funding from the EU H2020 research and innovation programme under GA No. 101017733. IL also acknowledges funding through JST-DFG 2024: Japanese-German Joint Call for Proposals on "Quantum Technologies" (Japan-JST-DFG-ASPIRE 2024) under DFG Grant No. 554561799 and support from the European Research Council through the ERC grant OPEN-2QS (Grant No. 101164443).

Competing interests

The authors declare no competing interests.

Additional information

Supplementary information The online version contains supplementary material available at https://doi.org/10.1038/s41467-026-77083-1.

Correspondence and requests for materials should be addressed to Zongkai Liu, Chris Nill or Linjie Zhang.

Peer review information *Nature Communications* thanks Lin Li, Daniel Soh, and the other anonymous, reviewer(s) for their contribution to the peer review of this work. A peer review file is available.

Reprints and permissions information is available at http://www.nature.com/reprints

Publisher's note Springer Nature remains neutral with regard to jurisdictional claims in published maps and institutional affiliations.

Open Access This article is licensed under a Creative Commons Attribution 4.0 International License, which permits use, sharing, adaptation, distribution and reproduction in any medium or format, as long as you give appropriate credit to the original author(s) and the source, provide a link to the Creative Commons licence, and indicate if changes were made. The images or other third party material in this article are included in the article's Creative Commons licence, unless indicated otherwise in a credit line to the material. If material is not included in the article's Creative Commons licence and your intended use is not permitted by statutory regulation or exceeds the permitted use, you will need to obtain permission directly from the copyright holder. To view a copy of this licence, visit http://creativecommons.org/licenses/by/4.0/.

© The Author(s) 2026

This Article in Press is shared early to give you faster access to new research. It is citable and carries a permanent DOI. The final edited version will replace it automatically.

A.2. [P2] - Spectroscopic signatures of emergent elementary excitations in a kinetically constrained long-range interacting two-dimensional spin system

Spectroscopic signatures of emergent elementary excitations in a kinetically constrained long-range interacting two-dimensional spin system

Tobias Kaltenmark,[1] Chris Nill,[1,2] Christian Groß,[3,4] and Igor Lesanovsky[1,4,5]

[1]*Institut für Theoretische Physik, Universität Tübingen, Auf der Morgenstelle 14, 72076 Tübingen, Germany*

[2]*Institute for Applied Physics, University of Bonn, Wegelerstraße 8, 53115 Bonn, Germany*

[3]*Physikalisches Institut, Universität Tübingen, Auf der Morgenstelle 14, 72076 Tübingen, Germany*

[4]*Center for Integrated Quantum Science and Technology (IQST), Universität Tübingen, Auf der Morgenstelle 14, 72076 Tübingen, Germany*

[5]*School of Physics and Astronomy and Centre for the Mathematics and Theoretical Physics of Quantum Non-Equilibrium Systems, The University of Nottingham, Nottingham NG7 2RD, United Kingdom*

(Received 25 November 2025; revised 16 January 2026; accepted 12 March 2026; published 3 April 2026)

Lattice spin models featuring kinetic constraints constitute a paradigmatic setting for the investigation of glassiness and localization phenomena. The intricate dynamical behavior of these systems is a result of the dramatically reduced connectivity between many-body configurations. This truncation of transition pathways often leads to a fragmentation of the Hilbert space, yielding highly collective and therefore often slow dynamics. Moreover, this mechanism supports the formation of characteristic elementary excitations, which we investigate here theoretically in a two-dimensional Rydberg lattice gas. We explore their properties as a function of interaction strength and range, and illustrate how they can be experimentally probed with a spectroscopic scheme. Here, we show that the transition rate to certain delocalized superposition states of elementary excitations displays collective many-body enhancement.

DOI: 10.1103/cdz9-rxn2

I. INTRODUCTION

The notion *kinetic constraint* refers to the phenomenon that strong interactions or peculiar dynamical rules severely restrict the connectivity between many-body states in Hilbert space [1,2]. Such kinetically constrained systems are ubiquitous in physics. They naturally appear in the context of quantum circuits and quantum cellular automata, whose dynamics is governed by conditional state changes implemented by quantum gates [3]. Moreover, kinetic constraints play a crucial role in the onset of glassiness [4–6], where the above-mentioned reduced connectivity between many-body states gives rise to extremely long relaxation times. Ultimately, they may even prevent thermalization by fragmenting the Hilbert space and give rise to the emergence of so-called quantum scars [7,8].

A simple platform for studying the physics of kinetically constrained systems are strongly interacting Ising models [9]. In these models, constrained dynamics are implemented by exploiting large interaction-induced energy barriers, which prevent resonant (and therefore fast) transitions between certain spin configurations. In the past, this setting has been used to study a range of interesting phenomena, including confinement dynamics [10], string breaking [11,12], frozen states [13], disorder-free (many-body) localization [14,15], and metastable phases [16]. Experimentally, such Ising models can be implemented with Rydberg atoms held in optical tweezer arrays [17]. Their strong dipolar power-law interactions provide a straightforward route for implementing kinetic constraints [18]: strong interaction-induced energy shifts prevent the resonant laser excitation of many-body states containing many Rydberg excitations, thereby implementing the Rydberg blockade constraint [19,20]. In a many-body setting this mechanism realizes the so-called PXP model, which has shown to host quantum scars [21,22]. A further constraint is the so-called antiblockade or facilitation [18,23–34]. Due to the appearance of strong mechanical forces [35]—manifesting in spin-phonon coupling [36–39]—such a scenario is challenging to implement experimentally, although recent progress has been made in one dimension [40]. In the facilitation regime, the Rydberg excitation of an atom located next to an already excited atom becomes resonantly enhanced. This manifests in an avalanchelike dynamics, nucleation dynamics [41], and, in conjunction with dissipative decay processes, enables the study of nonequilibrium universality [42,43].

In this work, we investigate elementary excitations in a two-dimensional square lattice from which Rydberg atoms are laser excited under the facilitation constraint. We show how this constraint, as well as the residual power-law tail of the interactions, determines the energetic and kinetic properties of these excitations. Moreover, we develop an effective theory for one excitation class consisting of chains of Rydberg atoms, enabling us to investigate their dynamics on large lattices. Finally, we discuss how to experimentally probe these elementary excitations via a modulated laser. Here, we also identify spectroscopic signatures of collective many-body enhancement.

II. SYSTEM

We consider a two-dimensional square lattice with dimensions N_x, N_y, and $N = N_x \times N_y$ sites. Each lattice site is

 ©2026 American Physical Society

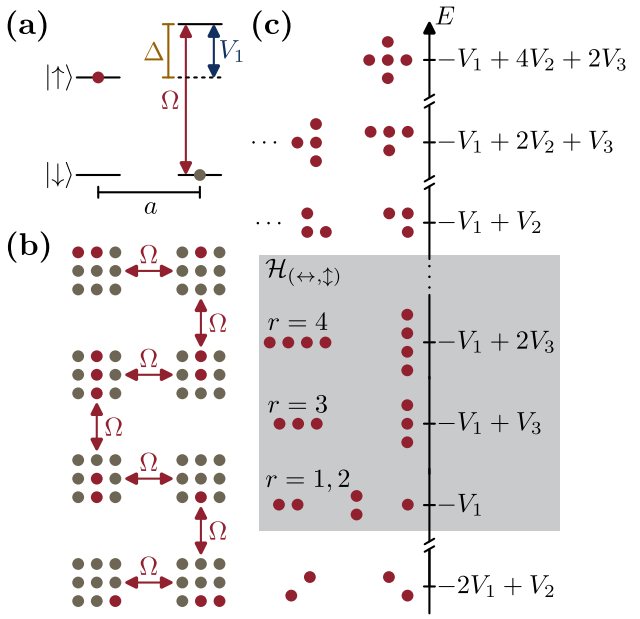

FIG. 1. Elementary excitations in a facilitated two-dimensional Rydberg square lattice. (a) Level scheme of two atoms separated by one lattice constant a. The atoms are modeled by two states: a ground state $|\downarrow\rangle$ (beige) and a Rydberg state $|\uparrow\rangle$ (red). Both states are coupled by a laser with Rabi frequency Ω and detuning Δ. The latter is chosen to compensate the nearest-neighboring Rydberg interaction, i.e., $V_1 + \Delta = 0$, which is the so-called the facilitation condition. (b) Some near-resonant processes in a 3×3 lattice, assuming that Ω is much larger than the next-next-nearest-neighbor interaction V_3. (c) Structure and energy of some elementary excitations. Here, V_2 and V_3 are the interaction energies between next-nearest and next-next-nearest neighbors, respectively. The gray box marks a subspace $\mathcal{H}_{(\leftrightarrow,\updownarrow)}$, where elementary excitations are formed by chains of Rydberg atoms. These carry energy $r\Delta$ from their r Rydberg excitations and energy $(r-1)V_1$ from the $r-1$ nearest-neighbor pairs. Under the facilitation condition, this implies a constant energy shift $-V_1$ for these elementary excitations.

occupied by a single atom, which is modeled as a two-level system, forming a fictitious spin-1/2 particle [see Fig. 1(a)]. A laser with Rabi frequency Ω and detuning Δ couples the electronic ground state $|\downarrow\rangle$ of an atom to the Rydberg state $|\uparrow\rangle$, and atoms in the Rydberg state interact via the Van der Waals interaction. The Hamiltonian that models this system is given by

$$H = \sum_{\boldsymbol{j}=(1,1)}^{(N_x,N_y)} \left(\frac{\Omega}{2}\sigma_{\boldsymbol{j}}^{(x)} + \Delta n_{\boldsymbol{j}} \right) + \frac{1}{2}\sum_{\boldsymbol{j}\neq\boldsymbol{k}} \frac{V_1}{|\boldsymbol{j}-\boldsymbol{k}|^6} n_{\boldsymbol{j}} n_{\boldsymbol{k}}. \quad (1)$$

The first term describes electronic transitions within the atoms that are induced by the laser: $\boldsymbol{j} = (j_x, j_y)$ refers to the lattice site, $\sigma_{\boldsymbol{j}}^{(x)} = |\uparrow\rangle\langle\downarrow|_{\boldsymbol{j}} + |\downarrow\rangle\langle\uparrow|_{\boldsymbol{j}} = \sigma_{\boldsymbol{j}}^{+} + \sigma_{\boldsymbol{j}}^{-}$ is the Pauli x matrix, and $n_{\boldsymbol{j}} = |\uparrow\rangle\langle\uparrow|_{\boldsymbol{j}}$ is the projector onto the Rydberg state of the $\boldsymbol{j}$th atom. The second term models the interaction between excited Rydberg atoms, where the coefficient $V_1 = C_6/a^6$ is the interaction strength between Rydberg atoms occupying nearest-neighboring lattice sites. It depends on the dispersion coefficient C_6 and the lattice spacing a. Given that the interaction rapidly decays with distance, we only consider interactions between nearest neighbors, V_1, next-nearest neighbors, $V_2 = V_1/2^3$, and next-next-nearest neighbors, $V_3 = V_1/2^6$. We assume furthermore that Rydberg atoms are excited under the facilitation condition, which means that the laser detuning is canceled by the nearest-neighbor interaction, $\Delta + V_1 = 0$. When at the same time the Rabi frequency is sufficiently small, $\Omega/2 \ll V_1$, the excitation dynamics is effectively kinetically constrained: an atom can only be resonantly excited when it is located next to exactly one Rydberg atom. Dynamically, this leads to a highly correlated formation of Rydberg excitations. An example of this is shown in Fig. 1(b) for a 3×3 lattice.

III. ELEMENTARY EXCITATIONS

To illuminate the nature of these correlated elementary excitations, we consider the spectrum of Hamiltonian (1) in the limit $\Omega = 0$. Under this condition, the eigenstates are product states in the classical spin basis $\{|\uparrow\rangle, |\downarrow\rangle\}$. In Fig. 1(c), we sketch a few of those states along with their energy. In this work, we focus on the states highlighted in the gray box, whose energy separation is multiples of the next-next-nearest neighbor interaction V_3. Assuming that $\Omega/2 \gg V_3$, these states form a near-resonant subspace $\mathcal{H}_{(\leftrightarrow,\updownarrow)}$ in which many-body configurations are strongly coupled by the laser. As can be seen, Rydberg excitations in $H_{(\leftrightarrow,\updownarrow)}$ are forced to form consecutive chains, whose overall number is conserved: they can neither vanish, nor can two or more chains merge. This effect has been studied in detail in one-dimensional lattices [27,30,36,37]. In two dimensions, the situation is more involved as these chains can grow in vertical and horizontal directions. Nevertheless, excitations can explore the entire lattice and are therefore mobile [see Fig. 1(b)]. In contrast, there are also immobile excitations that are formed by configurations in which Rydberg atoms populate next-nearest-neighboring lattice sites, where they interact with strength V_2. As an example, consider the triangular configuration with energy $-V_1 + V_2$, shown in Fig. 1(c). Assuming that $\Omega/2 \ll V_2$, the Rydberg atoms in the diagonal lattice sites cannot be resonantly removed. Nevertheless, further Rydberg atoms can be added resonantly. Consequently, the overall dynamics reduce to that of pinned one-dimensional chains that can grow and shrink, but are unable to explore the full lattice.

The dynamics of the mobile excitations are described by the Hamiltonian

$$H_{(\leftrightarrow,\updownarrow)} = \frac{\Omega}{2}\mathbf{T} + V_3 \sum_{r=3}^{N} (r-2)\mathbf{P}_r - V_1. \quad (2)$$

Here, $\mathbf{T}$ is a kinetic term, that gives rise to expansion and shrinking of Rydberg chains. It dynamically connects Rydberg chains that differ by a single Rydberg atom, as shown in Fig. 1(b). The second term assigns an energy to each chain, which is proportional to its length r and is given by the number of next-next-nearest-neighbored Rydberg atom pairs. Here, the operator $\mathbf{P}_r$ projects onto all vertical and horizontal chains with length r. The last, constant, contribution results from the energetic "cost" $r\Delta$ of exciting r Rydberg atoms, which is

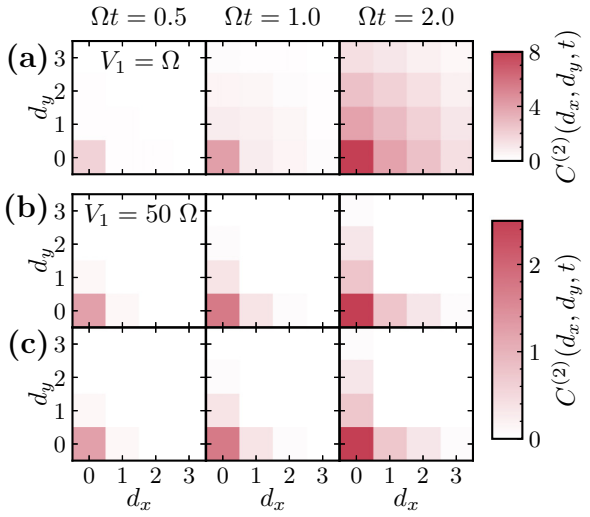

FIG. 2. Emergence of the kinetic constraint. Correlation function $C^{(x)}(d_x, d_y, t)$ in a 4×4 lattice with an initial single excitation positioned at site (2,2). (a),(b) Data obtained by evolving the system under the full Hamiltonian (1), for weak interaction $V_1 = \Omega$ and strong interaction $V_1 = 50\,\Omega$, respectively. In the latter case, a single Rydberg excitation initiates the growth of chains of Rydberg excitations along the rows and columns of the lattice [see Fig. 1(b)]. (c) Correlations calculated from the reduced model (2), for $V_1 = 50\,\Omega$. Rows (b) and (c) are in excellent agreement, which demonstrates that the reduced model description becomes appropriate when the interaction strength is sufficiently large. The snapshots are taken at times $\Omega t = 0.5, 1, 2$.

partially compensated by $(r-1)V_1$ nearest-neighbor interactions. With the facilitation condition, this results in a constant energy shift of $-V_1$ for all Rydberg chains. The derivation of Hamiltonian (2) is shown in the Appendix A, where we also provide the explicit forms of $\mathbf{T}$ and $\mathbf{P}_r$. Furthermore, we show that the dimension of the subspace $\mathcal{H}_{(\leftrightarrow,\updownarrow)}$ grows only polynomially in the system size, which dramatically simplifies numerical simulations.

In the following we benchmark the reduced model $H_{(\leftrightarrow,\updownarrow)}$ against the full Hamiltonian (1). To this end we time-evolve an initial state with a single Rydberg excitation at site (2,2) in a 4×4 lattice. For both models, we compute the integrated density-density correlations $C^{(2)}(\boldsymbol{d}, t) = \sum_j \langle n_j n_{j+\boldsymbol{d}} \rangle_t$. Here, $\langle n_j n_{j+\boldsymbol{d}} \rangle_t$ quantifies the probability of an atom at site $\boldsymbol{j}$ to be excited simultaneously with another atom at a distance $\boldsymbol{d} = (d_x, d_y)$. In Fig. 2(a), we show the density-density correlations in the case of weak interaction, i.e., $V_1 = \Omega$, computed for the full Hamiltonian (1). Here, fluctuations are strong enough to overcome diagonal energy contributions V_2. This is reflected in an isotropic build up of correlations over time. However, when $V_2 \gg \Omega/2$, transitions including V_2 are effectively forbidden and correlations are only formed between atoms that are located in the same row or column [see Fig. 2(b)]. Here only states in the subspace $\mathcal{H}_{(\leftrightarrow,\updownarrow)}$, i.e., Rydberg chains, are populated and the dynamics is faithfully described by the reduced model (2). This can be seen in Fig. 2(c), which shows data that are effectively indistinguishable from the full simulation.

IV. SPECTROSCOPY

In the following, we propose a spectroscopic scheme to experimentally probe elementary excitations and to measure their energies. To this end, we initialize the system in a state without Rydberg atoms, i.e., $|0\rangle = |\downarrow\rangle^{\otimes N_x N_y}$, which is the natural starting point of any experiment. When $V_1 \gg \Omega/2$, this state is kinetically disconnected from the remaining Hilbert space and merely acquires a second-order light shift. On the contrary, many-body configurations that host Rydberg atoms, in particular those contained in $\mathcal{H}_{(\leftrightarrow,\updownarrow)}$, are generally near-resonantly coupled by the laser. This leads to the formation of the mobile elementary excitations, i.e., many-body eigenstates that are formed from superpositions of the classical configurations shown in Fig. 1(c). To probe these, we periodically modulate the Rabi frequency around a central value $\Omega/2$ with frequency ω_s and small amplitude $\Omega_s \ll \Omega/2$. Thus, the many-body Hamiltonian is modified according to

$$H'(t) = H + \frac{\Omega_s}{2} \cos(\omega_s t) \sum_j \sigma_j^{(x)}. \tag{3}$$

When the modulation frequency ω_s matches the eigenenergy of an elementary excitation, Rydberg atoms can be coherently excited [see inset of Fig. 3(a)]. We consider in the following the time-averaged Rydberg density, $\bar{n} = \frac{1}{\tau} \int_0^\tau \mathrm{d}t \langle \sum_j n_j \rangle_t$, where τ is the length of the averaging time window. Note that the integration time τ has to be long enough in order to reach sufficient spectral resolution [see Fig. 4 in Appendix B]. In Figs. 3(a) and 3(b) we show $\bar{n}$ as a function of ω_s and V_1 for a 2×2 and 3×3 lattice. For a strong nearest-neighbor interaction, i.e., when the facilitation constraint is present, one observes sharp spectral features at specific modulation frequencies. To show that these spectral lines correspond to elementary excitations described by the reduced model Hamiltonian (2) we compute its eigenvalues E and eigenstates $|E\rangle$. From these, we calculate the expected resonance positions $\omega_s = |E|$ and show them as gray-black curves in Figs. 3(a) and 3(b). Indeed, when V_1 is sufficiently large, i.e., when the facilitation constraint is present and the reduced model is valid, there is excellent agreement with the data computed from the full Hamiltonian (3). The transition rate, i.e., the strength of the spectral lines obtained in the reduced model, can be estimated by Fermi's golden rule. It is proportional to the transition matrix element $M_E = |\langle E| \sum_j \sigma_j^{(x)} |0\rangle|^2 = |\langle E| \sum_j \sigma_j^{+} |0\rangle|^2$, which we plot in gray scale in Fig. 3. Note that for small nearest-neighbor interactions V_1, we also observe signatures of excitations, which are not captured by the reduced model (2). For example, in the 2×2 lattice we observe one spectral feature at $\omega_s \approx |-V_1 + V_2|$, which belongs to excitations in which Rydberg atoms form a triangular pattern [see also Fig. 1(c)]. As the Rydberg interaction grows, exciting those states becomes increasingly hard. This is because these states can only be accessed from the initial state $|0\rangle$, via the excitation of multiple Rydberg atoms through a sequence of off-resonant processes.

As a final study, we analyze the excitation spectrum of an 11×11 lattice using the reduced model Hamiltonian (2). We calculate the resonance positions from the eigenenergies and show the corresponding transition matrix element M_E in Fig. 3(c). We observe several transition lines. For large V_1,

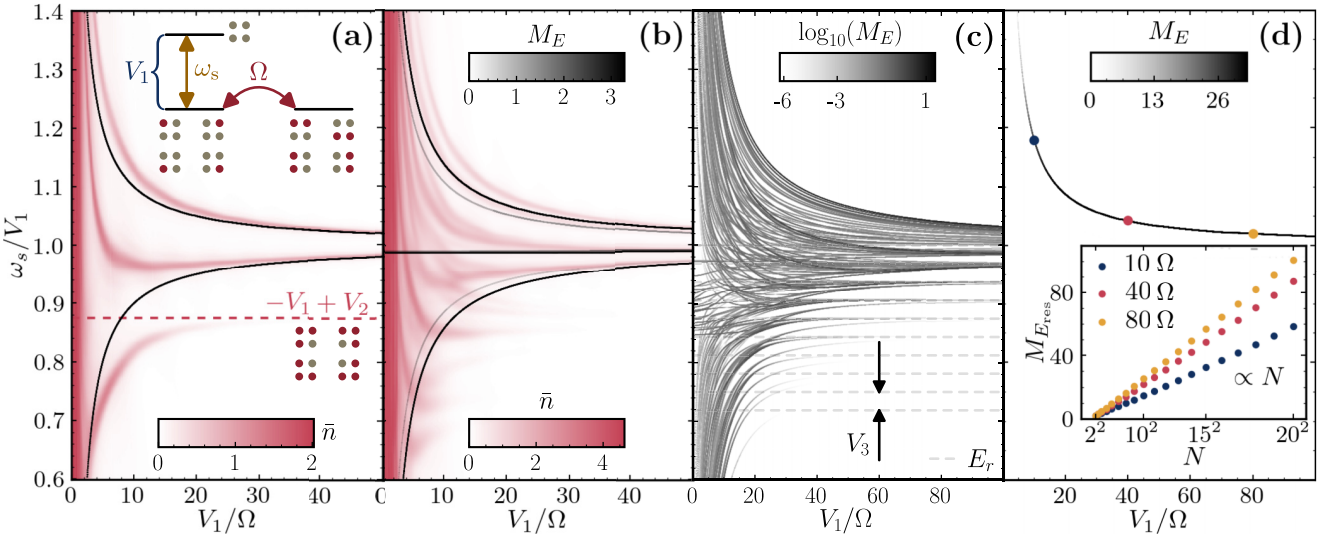

FIG. 3. Spectroscopy and collective enhancement. (a),(b) Excitation spectrum for a 2×2 and 3×3 lattice as a function of the interaction strength V_1 and modulation frequency ω_s. In red we show the time-averaged number of Rydberg atoms $\bar{n}$, which is calculated considering the full dynamics under the Hamiltonian (3), with $\Omega_s = 0.2\,\Omega$. To evaluate $\bar{n}$ we discretize the integral with sampling points $\Omega t \in \{1, 2, \ldots, 30\}$. The gray scale shows the transition matrix element M_E at the expected resonance energy, computed with the spectrum of the reduced model Hamiltonian (2). Note that the matrix elements in a 2×2 lattice are constant ($M_E = 2$), in contrast to the matrix elements in a 3×3 lattice. This is a result of the next-next-nearest-neighbor interaction V_3, which does not contribute for a 2×2 lattice. The inset of panel (a) illustrates the idea behind the spectroscopic scheme: the Rabi frequency modulation at frequency ω_s probes excitations, which are formed by (kinetically constrained) many-body states that are near-resonantly coupled by the laser (Rabi frequency Ω). For intermediate interaction strength we observe excitations of many-body configurations that are not contained in the subspace $\mathcal{H}_{(\leftrightarrow,\updownarrow)}$, e.g., triangular patterns of Rydberg atoms with energy $-V_1 + V_2$. With increasing interaction strength only excitations contained in $\mathcal{H}_{(\leftrightarrow,\updownarrow)}$ are excited. (c) Spectrum of an 11×11 lattice, calculated with the reduced model (2). Here, we used a logarithmic scale $\log_{10}(M_E)$ to increase the contrast of the spectral lines. The gray dashed lines correspond to the energies $-V_1 + (r-2)V_3$ of Rydberg chains with length $r \geqslant 2$ [see Appendix A]. (d) Collectively enhanced spectral line in the 11×11 lattice. The inset depicts the transition matrix element $M_{E_{\rm res}}$ evaluated with the corresponding eigenstate at energy $E_{\rm res}$ for different lattice sizes $N = N_x \times N_y$ with $N_x = N_y \in \{2, 3, \ldots, 20\}$.

they are located at $\omega_s = V_1 - V_3(r-2)$ with $r \in \{2, \ldots, 11\}$, which indicates that they correspond to excitations that are mainly formed by chains of Rydberg atoms of length r [see Fig. 1(c)]. Note that we use a logarithmic color scale as the strength of the lines varies considerably. Plotting the data on a linear scale, as in Fig. 3(d), reveals that there is one dominant (collectively enhanced) line whose strength grows proportional to the size N of the lattice (see inset). This is in fact the strongest possible scaling with system size, which can be seen by writing the matrix element as $M_E = N|\langle E|s\rangle|^2 \leqslant N$. Here, $|s\rangle = \frac{1}{\sqrt{N}} \sum_j \sigma_j^+ |0\rangle$ is a spin-wave state, which corresponds to a single Rydberg excitation delocalized over the entire lattice. This shows that the elementary excitation that corresponds to the collectively enhanced line is predominantly formed by many-body states that contain short Rydberg chains and single excitations.

V. CONCLUSIONS AND OUTLOOK

A two-dimensional long-range interacting Rydberg gas under facilitation conditions features a host of elementary excitations. We have developed an effective theory for a particular class of mobile excitations, which emerge when nearest-neighbor and next-nearest-neighbor interactions are sufficiently strong. Their energies can be spectroscopically determined by applying an appropriately modulated excitation laser and a subsequent measurement of the Rydberg atom number. In the future it would be interesting to investigate how the properties of the elementary excitations are affected when the condition of strong next-nearest-neighbor interaction is systematically relaxed. If solely nearest-neighbor interactions are present, the physics reduces to that of a two-dimensional transverse field Ising model, which already displays intriguing collective properties, such as metastability [44] and quasiparticle confinement [2]. Therefore, it would be interesting to explore many-body relaxation processes and their dependence on the facilitation constraint as well as the residual long-range interactions. Moreover, a quantitative characterization of transport properties, such as diffusion constants, as well as long-time relaxation dynamics represent a particularly promising avenue for future research. Computationally, these will be formidable tasks. However, quantum simulators based on trapped Rydberg atoms may ultimately offer such capability. They could thus yield novel insights into relaxation pathways and timescales, which may allow one to identify glassy dynamics. Currently though, the required long observation times still pose a technical challenge.

ACKNOWLEDGMENTS

We acknowledge funding from the Deutsche Forschungsgemeinschaft (DFG, German Research Foundation) through the Research Unit FOR 5413/1 (Grants No. 465199066 and No. 465199066), and through the Research Unit FOR

5522/1 (Grant No. 499180199). We acknowledge support from the Leverhulme Trust (Grant No. RPG-2024-112) and the European Union under the Horizon Europe program HORIZON-CL4-2022-QUANTUM-02-SGA via the Project No. 101113690 (PASQuanS2.1). We also acknowledge funding through JST-DFG 2024: Japanese-German Joint Call for Proposals on "Quantum Technologies" (Japan-JST-DFG-ASPIRE 2024) under DFG Grant No. 554561799. This work is also supported by the ERC grant OPEN-2QS (Grant No. 101164443). C.G. acknowledges support by the Alfried Krupp von Bohlen and Halbach foundation.

DATA AVAILABILITY

The data that support the findings of this article are openly available [45].

APPENDIX A: REDUCED HILBERT SPACE AND COORDINATES

A chain of Rydberg atoms, i.e., a many-body state in the reduced Hilbert space $\mathcal{H}_{(\leftrightarrow,\updownarrow)}$, can be uniquely specified by four coordinates (c_x, r_x, c_y, r_y). The relative coordinates (r_x, r_y) encode the length of the chain in the horizontal and vertical directions, respectively. For open boundary conditions, r_k is an integer in the range $1,\ldots,N_k$ for $k \in \{x, y\}$. Note that vertical chains ($r_y \geqslant 2$) have a width of one atom in the horizontal direction ($r_x = 1$), and vice versa for horizontal chains. Accordingly, we impose

$$r_k \geqslant 2 \Longrightarrow r_l = 1 \quad \text{for } k \neq l. \tag{A1}$$

The remaining coordinates $\mathbf{c} = (c_x, c_y)$ denote the center of the chain on the two-dimensional lattice. For chains of odd length, this center coincides with a lattice site, whereas for even chain lengths it lies halfway between two neighboring lattice sites. We therefore choose centers coinciding with lattice sites as odd integers c_k, and centers located between two sites as even integers. The center coordinates map to lattice sites via $\boldsymbol{j} = (\frac{c_x+1}{2}, \frac{c_y+1}{2})$, so that c_k takes integer values in the range $1,\ldots,2N_k-1$ for $k = x, y$. Since each center coordinate pair (c_k, r_k) is chosen such that either both coordinates are even or odd, the sum $c_k + r_k$ and difference $c_k - r_k$ are even integers. Therefore, they refer to positions between two lattice sites and give for horizontal and vertical Rydberg chains the right, upper $(c_k + r_k)$ and left, lower $(c_k - r_k)$ boundary, respectively. With this, we enforce the boundary conditions that Rydberg chains are not allowed to exceed the lattice, and require

$$0 \leqslant c_k - r_k, \quad 2N_k \geqslant c_k + r_k, \quad \text{for } k \in \{x, y\}. \tag{A2}$$

Here, we used 0 for the left lattice boundary and $2N_k$ for the right boundary.

Combining all constraints, the coordinates for horizontal chains (fixed $r_x \geqslant 2$) are given by $c_x \in \{r_x, r_x + 2, \ldots, 2N_x - r_x\}$, $r_y = 1$, and $c_y \in \{1, 3, \ldots, 2N_y - 1\}$. Hence, there are $(N_x - r_x + 1) \times 1 \times N_y$ distinct horizontal chains of length r_x. Similarly, there are $N_x \times 1 \times (N_y - r_y + 1)$ vertical chains of fixed length $r_y \geqslant 2$. The dimension of the reduced space $\mathcal{H}_{(\leftrightarrow,\updownarrow)}$ is therefore obtained by summing over all admissible chain lengths $r_x \in \{2,\ldots,N_x\}$ and $r_y \in \{2,\ldots,N_y\}$, and adding the $N_x \times N_y$ configurations with a single Rydberg excitation ($r_x = r_y = 1$), yielding

$$\dim(\mathcal{H}_{(\leftrightarrow,\updownarrow)}) = \frac{N_x N_y}{2}(N_x + N_y). \tag{A3}$$

Thus, the dimension of the reduced space scales polynomially with the system size.

In the following we construct the projection of the Hamiltonian (1) onto the subspace $\mathcal{H}_{(\leftrightarrow,\updownarrow)}$, which results in the Hamiltonian $H_{(\leftrightarrow,\updownarrow)}$, Eq. (2). The first term in the Hamiltonian (1) induces single spin flips (electronic state changes due to the laser). Due to the facilitation constraint these flips lead in $\mathcal{H}_{(\leftrightarrow,\updownarrow)}$ to processes that expand and shrink the size of a chain of Rydberg atoms by one atom. Therefore, horizontal chains can change their size in the x direction via four different processes: expansion or shrinking at the right boundary via the operators $|c_x+1\rangle\langle c_x| \otimes |r_x+1\rangle\langle r_x| + |c_x\rangle\langle c_x+1| \otimes |r_x\rangle\langle r_x+1|$, and the same processes at the left boundary, represented by $|c_x\rangle\langle c_x+1| \otimes |r_x+1\rangle\langle r_x| + |c_x+1\rangle\langle c_x| \otimes |r_x\rangle\langle r_x+1|$. Note that a change in the relative coordinate also implies a change of the center of mass position. All these processes, which leave the position and width in the y coordinate invariant, are represented by the kinetic energy operator

$$T_x = \sum_{c_x=1}^{2N_x-2} \sum_{c_y=1}^{2N_y-1} \sum_{r_x=1}^{N_x-1} \sum_{r_y=1}^{N_y} (|c_x+1\rangle\langle c_x| + \text{H.c.}) \otimes (|r_x+1\rangle\langle r_x| + \text{H.c.}) \otimes |c_y, 1\rangle\langle c_y, 1|. \tag{A4}$$

Note that here $1 \leqslant c_x \leqslant 2N_x - 2$ and $1 \leqslant r_x \leqslant N_x - 1$, which is due to the boundary conditions. Through similar reasoning, where c_x, r_x and c_y, r_y interchange roles, we obtain the corresponding expression for the kinetic energy vertical chains T_y. Combining both yields the total kinetic energy operator $\mathbf{T} = T_x + T_y$ [see Eq. (2)].

The remaining part of Hamiltonian (2) is diagonal and assigns an energy to each basis state. This energy only depends on the number of excited atoms, and the number of interacting Rydberg pairs. Therefore, for a chain with length $r = \max(r_x, r_y)$, the energy is given by

$$\begin{aligned} E_r &= r\Delta + \Theta(r-1)V_1(r-1) + \Theta(r-2)V_3(r-2), \\ E_r &\overset{\text{fac.}}{=} -V_1 + \Theta(r-2)(r-2)V_3. \end{aligned} \tag{A5}$$

Here, $\Theta(x)$ is the Heaviside step function, which is equal to zero for $x \leqslant 0$ and one for $x > 0$. Note that there is no contribution containing V_2, because Rydberg chains do not include pairs of excited next-nearest-neighboring atoms. Finally, we define the projection operators

$$\begin{aligned} P_{(r_x,r_y)} &= \sum_{c_x,c_y=1}^{2N_x-1,2N_y-1} |c_x, r_x, c_y, r_y\rangle\langle c_x, r_x, c_y, r_y|, \\ \mathbf{P}_r &= P_{(r,1)} + P_{(1,r)}, \end{aligned} \tag{A6}$$

which project all vertical and horizontal chains of length r onto itself. Together with the kinetic energy operator this yields Hamiltonian (2) of the main text.

Lastly, we provide an expression for the number operators $n_{\boldsymbol{j}}$ in the reduced space $\mathcal{H}_{(\leftrightarrow,\updownarrow)}$, which is necessary for

calculating the correlations in the main part. The number operator n_j projects the atom at site $\boldsymbol{j}$ to the excited state and leaves the state of the remaining atoms invariant. To conserve this structure in the reduced space, we use the coordinates of a Rydberg chain $|c_x, r_x, c_y, r_y\rangle$, to determine if it includes a Rydberg atom at site $\boldsymbol{j}$. For this, we first convert the site $\boldsymbol{j}$ to the center coordinates with the transformation above, yielding $\boldsymbol{c_j} = (2j_x - 1, 2j_y - 1)$. From the derivation of $\dim(\mathcal{H}_{(\leftrightarrow,\updownarrow)})$, we use that the boundaries of a Rydberg chain are given by $(c_k - r_k)$ and $(c_k + r_k)$, for $k = x, y$. A Rydberg chain $|c_x, r_x, c_y, r_y\rangle$, then includes an excitation at lattice site $\boldsymbol{j}$, if $\boldsymbol{c_j}$ is within the boundaries of the Rydberg chain, i.e.,

$$\begin{pmatrix} c_x - r_x \\ c_y - r_y \end{pmatrix} \leqslant \begin{pmatrix} 2j_x - 1 \\ 2j_y - 1 \end{pmatrix} \leqslant \begin{pmatrix} c_x + r_x \\ c_y + r_y \end{pmatrix}. \tag{A7}$$

The number operator n_j in the reduced space, projects onto all states satisfying this condition, i.e., all states in $\mathcal{N}_j = \{|c_x, r_x, c_y, r_y\rangle \in \mathcal{H}_{(\leftrightarrow,\updownarrow)} | \text{Eq. (A7) is satisfied}\}$, and reads

$$n_j = \sum_{|c_x,r_x,c_y,r_y\rangle \in \mathcal{N}_j} |c_x, r_x, c_y, r_y\rangle\langle c_x, r_x, c_y, r_y|. \tag{A8}$$

APPENDIX B: SPECTROSCOPY AND COHERENT EVOLUTION

In Fig. 3 we show the time-averaged density of Rydberg atoms, $\bar{n}$, as a function of the laser frequency ω_s. In this figure a number of spectral lines are clearly visible. In the following we discuss the impact of the overall coherent evolution time on the observability of these features. To make the point, we consider a system of two atoms. Under facilitation conditions ($\Delta + V_1 = 0$ and $V_1 \gg \Omega/2$), their dynamics is described by Hamiltonian (1) and the subspace $\mathcal{H}_{(\leftrightarrow,\updownarrow)}$ is spanned by the states $|\uparrow\downarrow\rangle, |\downarrow\uparrow\rangle, |\uparrow\uparrow\rangle$. The eigenvalues of Hamiltonian (1) in this subspace are

$$E_\pm = \Delta \pm \frac{\Omega}{\sqrt{2}}, \quad E_0 = \Delta. \tag{B1}$$

The eigenstate corresponding to eigenvalue E_0 is the antisymmetric superposition $(|\uparrow\downarrow\rangle - |\downarrow\uparrow\rangle)/\sqrt{2}$. Since the operator that effectuates transitions is conserving the symmetry of the initial state $|\downarrow\downarrow\rangle$ [see Eq. (3)], the transition rate to the antisymmetric state vanishes and it cannot be excited in the spectroscopy. Hence, only two spectral lines are observed. In Fig. 4(a) we present the time evolution of the Rydberg density $\langle n\rangle_t = \langle n_1\rangle_t + \langle n_2\rangle_t$ as a function of the modulation frequency ω_s/V_1. As can be seen, the two expected spectral lines become visible only when the time exceeds $\Omega t > 5$. This shows that the spectroscopy requires a minimal coherence time in order to reach the necessary resolution. In Figs. 4(b) and 4(c) we show the time-averaged Rydberg density $\bar{n} = \frac{1}{\tau}\int_0^\tau \mathrm{d}t\,\langle n\rangle_t$ with an integration time $\tau_1 = 2/\Omega$ [panel (b)] and $\tau_2 = 10/\Omega$ [panel (c)].

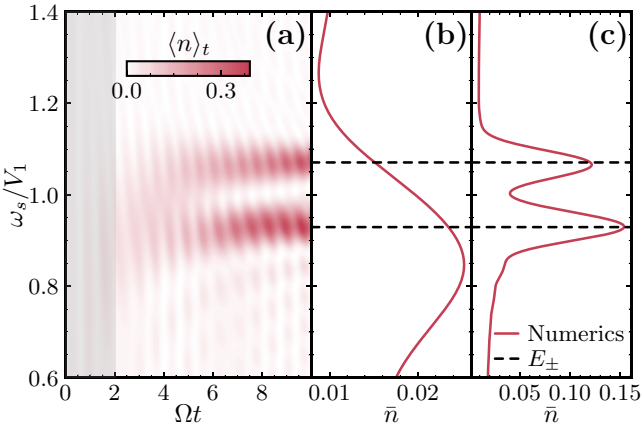

FIG. 4. Time-resolved spectroscopy signal of two facilitated atoms. (a) Time evolution of the Rydberg density $\langle n\rangle_t$ under a modulated laser of two facilitated atoms for varying modulation frequency ω_s and $\Omega_s = 0.2\,\Omega$, and $V_1 = 10\,\Omega$. (b) Time-averaged Rydberg density $\bar{n}$ in the time window, indicated by the gray shading in panel (a). The average $\bar{n}$ is evaluated for $\tau = 2/\Omega$, using 200 equidistant sampling points of the integral. The red line depicts $\bar{n}(\omega_s)$ and the dashed black lines indicate the theoretical eigenvalues at $\omega_s = |E_\pm|$, Eq. (B1). (c) Time-averaged Rydberg density $\bar{n}$ for the full time window ($\tau = 10/\Omega$). The integral is evaluated with 1000 equidistant sampling points. We observe that the spectral lines only become visible for sufficiently long coherent evolution times.

[1] N. Cancrini, F. Martinelli, C. Roberto, and C. Toninelli, Kinetically constrained models, in *New Trends in Mathematical Physics*, edited by V. Sidoravičius (Springer Netherlands, Dordrecht, 2009), pp. 741–752.

[2] L. Pavešić, D. Jaschke, and S. Montangero, Constrained dynamics and confinement in the two-dimensional quantum Ising model, Phys. Rev. B **111**, L140305 (2025).

[3] S. Gopalakrishnan and B. Zakirov, Facilitated quantum cellular automata as simple models with non-thermal eigenstates and dynamics, Quantum Sci. Technol. **3**, 044004 (2018).

[4] F. Ritort and P. Sollich, Glassy dynamics of kinetically constrained models, Adv. Phys. **52**, 219 (2003).

[5] D. Chandler and J. P. Garrahan, Dynamics on the way to forming glass: Bubbles in space-time, Annu. Rev. Phys. Chem. **61**, 191 (2010).

[6] I. Lesanovsky and J. P. Garrahan, Kinetic constraints, hierarchical relaxation, and onset of glassiness in strongly interacting and dissipative Rydberg gases, Phys. Rev. Lett. **111**, 215305 (2013).

[7] C. J. Turner, A. A. Michailidis, D. A. Abanin, M. Serbyn, and Z. Papić, Weak ergodicity breaking from quantum many-body scars, Nat. Phys. **14**, 745 (2018).

[8] M. Serbyn, D. A. Abanin, and Z. Papić, Quantum many-body scars and weak breaking of ergodicity, Nat. Phys. **17**, 675 (2021).

[9] R. Islam, C. Senko, W. C. Campbell, S. Korenblit, J. Smith, A. Lee, E. E. Edwards, C.-C. J. Wang, J. K. Freericks, and C. Monroe, Emergence and frustration of magnetism with variable-range interactions in a quantum simulator, Science **340**, 583 (2013).

[10] F. Liu, R. Lundgren, P. Titum, G. Pagano, J. Zhang, C. Monroe, and A. V. Gorshkov, Confined quasiparticle dynamics in long-range interacting quantum spin chains, Phys. Rev. Lett. **122**, 150601 (2019).

[11] R. Verdel, F. Liu, S. Whitsitt, A. V. Gorshkov, and M. Heyl, Real-time dynamics of string breaking in quantum spin chains, Phys. Rev. B **102**, 014308 (2020).
[12] A. De, A. Lerose, D. Luo, F. M. Surace, A. Schuckert, E. R. Bennewitz, B. Ware, W. Morong, K. S. Collins, Z. Davoudi, A. V. Gorshkov, O. Katz, and C. Monroe, Observation of string-breaking dynamics in a quantum simulator, arXiv:2410.13815.
[13] O. Hart and R. Nandkishore, Hilbert space shattering and dynamical freezing in the quantum Ising model, Phys. Rev. B **106**, 214426 (2022).
[14] J. Smith, A. Lee, P. Richerme, B. Neyenhuis, P. W. Hess, P. Hauke, M. Heyl, D. A. Huse, and C. Monroe, Many-body localization in a quantum simulator with programmable random disorder, Nat. Phys. **12**, 907 (2016).
[15] P. Karpov, R. Verdel, Y.-P. Huang, M. Schmitt, and M. Heyl, Disorder-free localization in an interacting 2D lattice gauge theory, Phys. Rev. Lett. **126**, 130401 (2021).
[16] S. B. Rutkevich, Decay of the metastable phase in $d = 1$ and $d = 2$ Ising models, Phys. Rev. B **60**, 14525 (1999).
[17] A. Browaeys and T. Lahaye, Many-body physics with individually controlled Rydberg atoms, Nat. Phys. **16**, 132 (2020).
[18] M. M. Valado, C. Simonelli, M. D. Hoogerland, I. Lesanovsky, J. P. Garrahan, E. Arimondo, D. Ciampini, and O. Morsch, Experimental observation of controllable kinetic constraints in a cold atomic gas, Phys. Rev. A **93**, 040701(R) (2016).
[19] E. Urban, T. A. Johnson, T. Henage, L. Isenhower, D. D. Yavuz, T. G. Walker, and M. Saffman, Observation of Rydberg blockade between two atoms, Nat. Phys. **5**, 110 (2009).
[20] A. Gaëtan, Y. Miroshnychenko, T. Wilk, A. Chotia, M. Viteau, D. Comparat, P. Pillet, A. Browaeys, and P. Grangier, Observation of collective excitation of two individual atoms in the Rydberg blockade regime, Nat. Phys. **5**, 115 (2009).
[21] A. Chandran, T. Iadecola, V. Khemani, and R. Moessner, Quantum many-body scars: A quasiparticle perspective, Annu. Rev. Condens. Matter Phys. **14**, 443 (2023).
[22] G. Giudici, F. M. Surace, and H. Pichler, Unraveling PXP many-body scars through floquet dynamics, Phys. Rev. Lett. **133**, 190404 (2024).
[23] C. Ates, T. Pohl, T. Pattard, and J. M. Rost, Antiblockade in Rydberg excitation of an ultracold lattice gas, Phys. Rev. Lett. **98**, 023002 (2007).
[24] T. Amthor, C. Giese, C. S. Hofmann, and M. Weidemüller, Evidence of antiblockade in an ultracold Rydberg gas, Phys. Rev. Lett. **104**, 013001 (2010).
[25] H. Schempp, G. Günter, M. Robert-de Saint-Vincent, C. S. Hofmann, D. Breyel, A. Komnik, D. W. Schönleber, M. Gärttner, J. Evers, S. Whitlock, and M. Weidemüller, Full counting statistics of laser excited Rydberg aggregates in a one-dimensional geometry, Phys. Rev. Lett. **112**, 013002 (2014).
[26] A. Urvoy, F. Ripka, I. Lesanovsky, D. Booth, J. P. Shaffer, T. Pfau, and R. Löw, Strongly correlated growth of Rydberg aggregates in a vapor cell, Phys. Rev. Lett. **114**, 203002 (2015).
[27] M. Marcuzzi, J. Minar, D. Barredo, S. de Léséleuc, H. Labuhn, T. Lahaye, A. Browaeys, E. Levi, and I. Lesanovsky, Facilitation dynamics and localization phenomena in Rydberg lattice gases with position disorder, Phys. Rev. Lett. **118**, 063606 (2017).
[28] F. Letscher, O. Thomas, T. Niederprüm, M. Fleischhauer, and H. Ott, Bistability versus metastability in driven dissipative Rydberg gases, Phys. Rev. X **7**, 021020 (2017).
[29] M. Ostmann, M. Marcuzzi, J. P. Garrahan, and I. Lesanovsky, Localization in spin chains with facilitation constraints and disordered interactions, Phys. Rev. A **99**, 060101(R) (2019).
[30] M. Magoni, P. P. Mazza, and I. Lesanovsky, Emergent bloch oscillations in a kinetically constrained Rydberg spin lattice, Phys. Rev. Lett. **126**, 103002 (2021).
[31] K. Klocke, T. M. Wintermantel, G. Lochead, S. Whitlock, and M. Buchhold, Hydrodynamic stabilization of self-organized criticality in a driven Rydberg gas, Phys. Rev. Lett. **126**, 123401 (2021).
[32] F. Liu, Z.-C. Yang, P. Bienias, T. Iadecola, and A. V. Gorshkov, Localization and criticality in antiblockaded two-dimensional Rydberg atom arrays, Phys. Rev. Lett. **128**, 013603 (2022).
[33] T. Zhang and Z. Cai, Quantum slush state in Rydberg atom arrays, Phys. Rev. Lett. **132**, 206503 (2024).
[34] D. Brady, J. Bender, P. Mischke, S. Ohler, T. Niederprüm, H. Ott, and M. Fleischhauer, Griffiths phase in a facilitated Rydberg gas at low temperatures, Phys. Rev. Res. **6**, 013052 (2024).
[35] R. Faoro, C. Simonelli, M. Archimi, G. Masella, M. M. Valado, E. Arimondo, R. Mannella, D. Ciampini, and O. Morsch, van der Waals explosion of cold Rydberg clusters, Phys. Rev. A **93**, 030701(R) (2016).
[36] M. Magoni, P. P. Mazza, and I. Lesanovsky, Phonon dressing of a facilitated one-dimensional Rydberg lattice gas, SciPost Phys. Core **5**, 041 (2022).
[37] M. Magoni, C. Nill, and I. Lesanovsky, Coherent spin-phonon scattering in facilitated Rydberg lattices, Phys. Rev. Lett. **132**, 133401 (2023).
[38] D. Brady and M. Fleischhauer, Non-classical spin-phonon correlations induced by Rydberg facilitation in a lattice, arXiv:2504.19679.
[39] V. Lienhard, R. Martin, Y. T. Chew, T. Tomita, K. Ohmori, and S. de Léséleuc, Generation of motional squeezed states for neutral atoms in optical tweezers Phys. Rev. Lett. **135**, 253404 (2025).
[40] L. Zhao, P. R. Datla, W. Tian, M. M. Aliyu, and H. Loh, Observation of quantum thermalization restricted to Hilbert space fragments and $\mathbb{Z}_{2k}$ scars, Phys. Rev. X **15**, 011035 (2025).
[41] P. Osterholz, F. Bensch, S. Tang, S. B. Sheela, B. Sbierski, I. Lesanovsky, and C. Groß, Collective cluster nucleation dynamics in quantum magnets, arXiv:2512.04656.
[42] R. Gutiérrez, C. Simonelli, M. Archimi, F. Castellucci, E. Arimondo, D. Ciampini, M. Marcuzzi, I. Lesanovsky, and O. Morsch, Experimental signatures of an absorbing-state phase transition in an open driven many-body quantum system, Phys. Rev. A **96**, 041602(R) (2017).
[43] S. Helmrich, A. Arias, G. Lochead, T. M. Wintermantel, M. Buchhold, S. Diehl, and S. Whitlock, Signatures of self-organized criticality in an ultracold atomic gas, Nature (London) **577**, 481 (2020).
[44] L. Pavešić, M. D. Liberto, and S. Montangero, Scattering and induced false vacuum decay in the two-dimensional quantum Ising model, arXiv:2509.02702.
[45] T. Kaltenmark, C. Nill, C. Gross, and I. Lesanovsky, Data and Code for: Spectroscopic signatures of emergent elementary excitations in a kinetically constrained long-range interacting two-dimensional spin system, Zenodo (2025), https://doi.org/10.5281/zenodo.17629915.

A.3. [P3] - Entanglement of mechanical oscillators mediated by a Rydberg tweezer chain

Entanglement of mechanical oscillators mediated by a Rydberg tweezer chain

Cedric Wind,[1,*] Chris Nill,[1,2,*] Julia Gamper,[1] Samuel Germer,[1] Valerie Mauth,[1] Wolfgang Alt,[1] Igor Lesanovsky,[2,3] and Sebastian Hofferberth[1]

[1]*Institut für Angewandte Physik, University of Bonn, Wegelerstrasse 8, 53115 Bonn, Germany*

[2]*Institut für Theoretische Physik and Center for Integrated Quantum Science and Technology, Universität Tübingen, Auf der Morgenstelle 14, 72076 Tübingen, Germany*

[3]*School of Physics and Astronomy and Centre for the Mathematics and Theoretical Physics of Quantum Non-Equilibrium Systems, The University of Nottingham, Nottingham NG7 2RD, United Kingdom*

(Received 13 October 2025; accepted 8 April 2026; published 5 May 2026)

Mechanical systems provide a unique test bed for studying quantum phenomena at macroscopic length scales. However, realizing quantum states that feature quantum correlations among macroscopic mechanical objects remains an experimental challenge. Here, we propose a quantum system in which two micro-electromechanical oscillators interact through a chain of Rydberg atoms confined in optical tweezers. We demonstrate that the coherent dynamics of the system generate entanglement between the oscillators. Furthermore, we utilize the tunability of the radiative decay of the Rydberg atoms for dissipative entanglement generation. Our results highlight the potential to exploit the flexibility and tunability of Rydberg atom chains to generate nonclassical correlations between distant mechanical oscillators.

DOI: 10.1103/qqf3-wx7m

I. INTRODUCTION

Many experimental platforms explore entanglement and its applications using microscopic objects, such as photons [1–3], atoms [4,5], and ions [6,7]. Extending entanglement to macroscopic objects, such as massive mechanical oscillators, is challenging, as decoherence usually becomes more pronounced with increasing system size [8–11]. However, entangled macroscopic systems, and in particular mechanical oscillators, offer new opportunities to probe the quantum-classical boundary [12,13] and to explore novel regimes of quantum acoustics [14–17]. Moreover, they may serve as a test bed for models of quantum gravity [18–20].

So far, mechanical oscillators have predominantly been entangled using opto- and electromechanical coupling to cavities [21–23]. A notable exception is a recent experiment, where micro-electromechanical oscillators with GHz resonance frequencies are coupled to superconducting qubits that mediate entanglement [24]. In a parallel development, micro-electromechanical oscillators have been realized that feature similar resonance frequencies, but offer dramatically enhanced coherence times of the order of one millisecond [25,26]. These devices confine GHz acoustic modes in micrometer-scale piezoelectric structures and permit efficient transduction between mechanical and electrical degrees of freedom.

In this work, we propose to entangle two GHz micro-electromechanical oscillators by coupling them to opposite ends of a chain of tweezer-trapped Rydberg atoms, as sketched in Fig. 1(a). Rydberg atoms feature strong electric dipole transitions in the GHz-frequency regime that enable resonant interaction with the electromechanical oscillators [27–29]. Moreover, trapping atoms in arrays of optical tweezer traps [30,31] allows for precise control of the interatomic distance as well as the distance between the atoms and the oscillators. Here, the spatial dependence of the underlying dipolar interactions permits control over the atom-atom and atom-oscillator coupling. We build our investigation on a model that captures the essential coherent and dissipative processes of this hybrid system. This model allows us to show that coherent excitation transport through the Rydberg chain mediates entanglement between the oscillators. Furthermore, we present a scheme for dissipative entanglement generation that exploits atomic decay processes. The entanglement among the oscillators at the end of the dissipative dynamics is probabilistic. We discuss how the likelihood for obtaining entangled states can be enhanced through particular choices of the system parameters.

II. MECHANICAL OSCILLATORS COUPLED BY A RYDBERG ATOM CHAIN

As depicted in Fig. 1(a), the system we consider is composed of two micro-electromechanical oscillators, which are linked to the two ends of a chain of N Rydberg atoms. The Hamiltonian of this system is given by

$$H = H_{\mathrm{osc}} + H_{\mathrm{chain}} + H_{\mathrm{couple}}. \tag{1}$$

Here, $H_{\mathrm{osc}} = \omega(a^\dagger a + b^\dagger b)$ is the Hamiltonian describing the relevant modes of the two oscillators with resonance frequency ω and corresponding ladder operators a, $a^\dagger$ and b, $b^\dagger$, respectively. Throughout this work, we set $\hbar = 1$. We model the decoherence of the oscillator modes as an excitation decay with rate κ. The system is considered to be in a zero-

[*]These authors contributed equally to this work.

 ©2026 American Physical Society

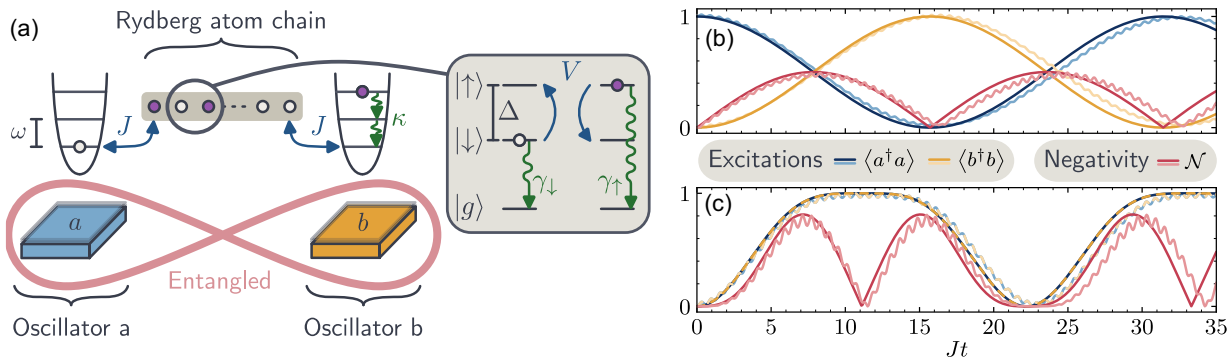

FIG. 1. Mechanical oscillators linked by a Rydberg atom chain. (a) Schematic of the oscillator-atom system illustrating the levels, coupling strengths, and decay rates introduced in the main text. Excitations in the Rydberg spin chain and the oscillators are depicted as violet filled circles, while white filled circles indicate the absence of excitations. (b),(c) Coherent evolution of the number of excitations in the oscillators $\langle a^\dagger a\rangle$, $\langle b^\dagger b\rangle$ and oscillator entanglement quantified by the negativity $\mathcal{N}$. The results correspond to the system presented in (a) with $N = 2$ atoms and $V = 10J$. The system is initialized in (b) $|\psi_1\rangle$ and (c) $|\psi_2\rangle$ [see Eqs. (7) and (8)]. Dark lines are obtained from the effective Hamiltonian (6), while lighter, semitransparent lines show the exact dynamics under the full Hamiltonian (1). In (c), $\langle b^\dagger b\rangle$ is shown as a dashed curve to improve visibility.

temperature environment, so that any heating from outside can be neglected (see Appendix B).

In the chain, each atom is modeled with two Rydberg states, denoted by the spin states $|\uparrow\rangle$ and $|\downarrow\rangle$ with energy separation Δ. We consider the two Rydberg states to spontaneously decay with rates $\gamma_\uparrow$ and $\gamma_\downarrow$ to an effective ground state $|g\rangle$, as illustrated in the inset in Fig. 1(a). This simplifies the decay dynamics of real Rydberg atoms but captures the essential aspect of the decay, namely, the depopulation of the Rydberg state. Due to the zero-temperature environment, blackbody-induced transitions to neighboring Rydberg states are not present. We treat the interaction between the Rydberg atoms in the chain as dipolar flip-flop interaction between nearest neighbors with strength V [30,32], described by the Hamiltonian

$$H_{\text{chain}} = V\sum_{i=1}^{N-1}(|\downarrow\rangle\langle\uparrow|_i \otimes |\uparrow\rangle\langle\downarrow|_{i+1} + \text{H.c.}) + \Delta\sum_{i=1}^{N}\mathcal{P}_\uparrow^{(i)}, \tag{2}$$

where $\mathcal{P}_\uparrow^{(i)} = |\uparrow\rangle\langle\uparrow|_i$ is the projector onto the higher-lying Rydberg state, and H.c. denotes the Hermitian conjugate. To simplify our analysis, couplings to next-nearest neighbors and beyond are neglected throughout this work.

The two outer atoms of the chain couple to the electric field of the corresponding electromechanical oscillator. This results in a dipolar coupling between the atoms and the oscillators [27,33]. We assume resonant coupling with $\omega = \Delta$. Under this condition, the coupling Hamiltonian is given by

$$H_{\text{couple}} = J(|\downarrow\rangle\langle\uparrow|_1 \otimes a^\dagger + |\downarrow\rangle\langle\uparrow|_N \otimes b^\dagger + \text{H.c.}). \tag{3}$$

The parameter J quantifies the interaction strength between the mechanical systems and the Rydberg atoms. For realistic experimental parameters, as discussed in Appendix A, the minimal atom-oscillator distance will limit the atom-oscillator coupling J to be smaller than the atom-atom interaction V for typical tweezer distances. At the same time, the decay rates of the Rydberg atoms $\gamma_\uparrow$, $\gamma_\downarrow$ and oscillators κ are orders of magnitude smaller than the coherent interaction strengths J and V. Consequently, the coherent dynamics of the system are experimentally accessible on timescales where $\gamma_\downarrow t$, $\gamma_\uparrow t$, $\kappa t \ll 1$. Furthermore, the decay rates of the Rydberg states can be artificially increased in experiments by laser dressing [34–36]. We will analyze the generation of entanglement between the oscillators for both purely coherent dynamics and dynamics with engineered dissipation in Secs. III and IV, respectively.

To assess the entanglement of the oscillators, we analyze their reduced density matrix ρ_{ab}, which is obtained by performing a partial trace over the atom chain. In general, the reduced density matrix will represent a mixed state. To quantify the entanglement of this state, we use the negativity [37,38], which for our system is calculated as

$$\mathcal{N}(\rho_{ab}) = \tfrac{1}{2}[\|T_a \text{tr}_{\text{chain}}(\rho)\|_1 - 1].$$

Here, ρ is the density matrix of the full system, tr_{chain} the partial trace over the Rydberg chain, T_a the partial transpose with respect to oscillator a, and $\|\cdot\|_1$ the trace norm. The oscillators are entangled if the negativity is larger than zero, with the largest negativity being reached by a maximally entangled state [37]. One choice for such a maximally entangled state is $|\phi_{\max}\rangle = \frac{1}{\sqrt{n+1}}\sum_{i=0}^{n}|i\rangle_a \otimes |i\rangle_b$, with n being an integer number [38]. Here, $|i\rangle_{a/b}$ is the Fock state of oscillators a and b, respectively. This state has negativity $\mathcal{N}(|\phi_{\max}\rangle\langle\phi_{\max}|) = n/2$ and the oscillators contain, on average, $\langle\phi_{\max}|a^\dagger a + b^\dagger b|\phi_{\max}\rangle = n$ excitations. In fact, the negativity is bounded from above by

$$\mathcal{N} \leqslant \frac{\lceil\langle a^\dagger a + b^\dagger b\rangle\rceil}{2}, \tag{4}$$

where $\lceil\cdot\rceil$ denotes the ceiling function.

This allows us to give an upper bound for the negativity that we can expect in our system. To construct the upper bound, we utilize that the operator

$$\mathcal{M} = a^\dagger a + b^\dagger b + \sum_{i=1}^{N}\mathcal{P}_\uparrow^{(i)}$$

commutes with the full Hamiltonian (1) and thus $\mu = \langle \mathcal{M} \rangle$ is conserved under coherent evolution. This operator counts the number of atoms in the state $|\uparrow\rangle$ together with the number of excitations in the oscillators. Throughout this work, we call μ the total excitation number and refer to atoms in state $|\uparrow\rangle$ as spin excitations. It follows that the number of excitations in the initial state of the system defines an upper bound on the maximum reachable negativity during the time evolution with

$$\mathcal{N}_{\max} \leqslant \frac{\lceil \mu \rceil}{2}. \tag{5}$$

This shows that a higher total number of initial excitations allows for higher negativity values.

III. DETERMINISTIC ENTANGLEMENT GENERATION THROUGH COHERENT EVOLUTION

In this section, we illuminate the mechanisms that underlie the entanglement generation between the oscillators. To that end, we focus on the purely coherent dynamics, which are experimentally accessible on timescales $\gamma_\downarrow t,\ \gamma_\uparrow t,\ \kappa t \ll 1$, where dissipation is negligible. The coherent evolution of the system is governed by the full Hamiltonian (1). This Hamiltonian only indirectly describes any effective coupling between the oscillators via the atom-atom and atom-oscillator coupling; see Eqs. (2) and (3). We now exploit that for typical experimental parameters, $J \ll V$. This allows us to perturbatively derive an effective Hamiltonian that directly couples the oscillators. To do so, it is necessary to compute the eigenstates of H_{chain}. For arbitrary chain lengths N, this is possible using the Jordan-Wigner transformation [39]. To illustrate the principle, we consider a chain of two atoms, where the eigenstates are the spin-singlet state $|S\rangle = (|\uparrow\downarrow\rangle - |\downarrow\uparrow\rangle)/\sqrt{2}$ and the spin-triplet states $|\uparrow\uparrow\rangle$, $|\downarrow\downarrow\rangle$, and $|T\rangle = (|\uparrow\downarrow\rangle + |\downarrow\uparrow\rangle)/\sqrt{2}$. Expressing the chain Hamiltonian (2) in its eigenbasis and employing a Schrieffer-Wolff transformation [40,41], we obtain the effective Hamiltonian

$$\begin{aligned} H_{\text{eff}} = &- \frac{J^2}{V}(a^\dagger b + a b^\dagger)(|\downarrow\downarrow\rangle\langle\downarrow\downarrow| + |\uparrow\uparrow\rangle\langle\uparrow\uparrow| \\ &- |S\rangle\langle S| - |T\rangle\langle T|) \\ &- \frac{J^2}{V}[(a^{\dagger 2} + b^{\dagger 2})|\downarrow\downarrow\rangle\langle\uparrow\uparrow| + (a^2 + b^2)|\uparrow\uparrow\rangle\langle\downarrow\downarrow|] \\ &+ \left(V + \frac{J^2 \mathcal{M}}{V}\right)(|T\rangle\langle T| - |S\rangle\langle S|) + \mathcal{M}\omega. \end{aligned} \tag{6}$$

Here, the third line represents the energy of the basis states of the system, while the first two lines contain qualitatively different coupling terms. The first line describes a direct oscillator-oscillator coupling that generates entanglement, where the sign of the coupling depends on the state of the chain. The second line describes an indirect coupling at higher order, which involves exchange of excitation pairs between oscillators and chain.

To illustrate the roles of these coupling terms, we consider two different initial states,

$$|\psi_1\rangle = |1\rangle_a \otimes |S\rangle \otimes |0\rangle_b, \tag{7}$$

$$|\psi_2\rangle = |0\rangle_a \otimes |\uparrow\uparrow\rangle \otimes |0\rangle_b. \tag{8}$$

In state $|\psi_1\rangle$, one excitation resides in oscillator a and the chain is in the singlet state, which contains one spin excitation. In state $|\psi_2\rangle$, both spins are initially excited and the oscillators are in the ground state $|0\rangle$. Both states have the same total number of excitations, $\mu = 2$, and, consequently, have the same upper bound of the maximum reachable negativity according to Eq. (5).

For these initial states, the time evolution of the oscillator excitation number as well as the negativity under the effective Hamiltonian (6) can be calculated analytically. They are given by

$$\begin{aligned} &\langle\psi_1|a^\dagger a|\psi_1\rangle = 1 - \langle\psi_1|b^\dagger b|\psi_1\rangle = \frac{1}{2}\left[1 + \cos\left(\frac{\tau}{2\sqrt{2}}\right)\right], \\ &\langle\psi_2|a^\dagger a|\psi_2\rangle = \langle\psi_2|b^\dagger b|\psi_2\rangle = 1 - \cos^4\left(\frac{\tau}{2}\right), \\ &\mathcal{N}(|\psi_1\rangle\langle\psi_1|) = \frac{1}{2}\left|\sin\left(\frac{\tau}{2\sqrt{2}}\right)\right|, \\ &\mathcal{N}(|\psi_2\rangle\langle\psi_2|) = \frac{1}{2}[1 - \cos(\tau)]|\sin(\tau)| + \frac{1}{8}\left[1 + \cos(\tau)\right] \\ &\qquad \times \left[\sqrt{5\cos^2(\tau) - 6\cos(\tau) + 5} - 1 - \cos(\tau)\right], \end{aligned}$$

where $\tau = \frac{2\sqrt{2}J^2}{V}t$. In Figs. 1(b) and 1(c), we present the analytic results together with the numerical solution of the full Hamiltonian (1). The effective model captures the overall dynamics, while the observed deviations can be explained by omitting higher-order corrections in the effective Hamiltonian. For both initial states, entanglement between the oscillators gets periodically created and destroyed during the evolution of the system. We find in Figs. 1(b) and 1(c) that a higher negativity is reached during the time evolution of $|\psi_2\rangle$ compared to $|\psi_1\rangle$. This can be understood by considering the allowed exchange processes for the two initial states. For $|\psi_1\rangle$, only single-excitation exchange between the oscillators via the first term in H_{eff} is possible, such that the number of excitations $\langle a^\dagger a + b^\dagger b\rangle$ in the oscillators remains fixed at one. Hence, a stricter bound on the negativity, $\mathcal{N}(|\psi_1\rangle\langle\psi_1|) \leqslant 1/2$, is imposed according to Eq. (4). On the contrary, for $|\psi_2\rangle$, the exchange of excitation pairs with the chain via the second term in H_{eff} allows the system to transfer the two excitations, initially in the atom chain, into the oscillators. Although this pair exchange still couples the oscillators only indirectly via the chain, it enables the system to reach entangled states with more excitations in the oscillators. This leads to the larger negativity reached for this initial state.

IV. PROBABILISTIC ENTANGLEMENT GENERATION THROUGH DISSIPATIVE PROCESSES

For the creation of correlated oscillator states, one would ideally stop the coherent dynamics when the maximum negativity is reached. While this is, in principle, possible, e.g., by removing the atoms with repulsive optical tweezers, this requires exact timing and precise knowledge of the system parameters. In the following, we discuss a scheme where artificially enhanced dissipation in the atomic chain is exploited to generate an entangled oscillator state and, at the same time,

to stop the coherent dynamics of entanglement creation and destruction automatically.

To illustrate this idea, we consider a separable initial state of the form

$$|\psi_{\text{init}}\rangle = |0\rangle_a \otimes |\uparrow\rangle^{\otimes N} \otimes |0\rangle_b, \tag{9}$$

where all atoms are in the Rydberg state $|\uparrow\rangle$ and the oscillators are in the vacuum state. Over the course of the dissipative time evolution—which we discuss in detail below—this state will eventually evolve into a product state, where the atomic chain is found in $|g\rangle^{\otimes N}$. We refer to this state as the final state. From this point onward, the coupling between the atom chain and the oscillators stops and the latter merely continue the evolution under their individual harmonic oscillator Hamiltonians, which can neither create nor remove correlations. The precise sequence and timing of the atomic decay events—which form a so-called quantum jump trajectory—are, however, probabilistic. This also means that the entanglement of the final oscillator state, which is reached when all atoms have decayed, is probabilistic.

A. Mechanism of dissipative entanglement generation

We simulate quantum trajectories of the full system using the quantum jump method discussed in Refs. [42,43]. In this framework, the evolution of the initial state, defined in Eq. (9), is governed by the non-Hermitian Hamiltonian $\mathcal{H} = H - \frac{i}{2}\sum_\alpha L_\alpha^\dagger L_\alpha$, with the jump operators

$$L_\alpha \in \{\sqrt{\gamma_\uparrow}|g\rangle\langle\uparrow|_1, \ldots, \sqrt{\gamma_\uparrow}|g\rangle\langle\uparrow|_N, \sqrt{\gamma_\downarrow}|g\rangle\langle\downarrow|_1, \ldots, \sqrt{\gamma_\downarrow}|g\rangle\langle\downarrow|_N, \sqrt{\kappa}a, \sqrt{\kappa}b\}.$$

Here, the first $2N$ terms capture the decay from the Rydberg states $|\uparrow\rangle$ and $|\downarrow\rangle$ to the state $|g\rangle$, while the last two describe the decay of the oscillators. These jumps occur at random times, reflecting the probabilistic nature of the quantum trajectories.

To elucidate the role of the Rydberg atom decay in the evolution of the system, we consider a system with $N = 5$ atoms, with an interaction strength $V = 3J$ and decay rates $\gamma_\uparrow = \gamma_\downarrow = 0.2J$ for the Rydberg state. For simplicity, we switch off the oscillator decay ($\kappa = 0$). In Fig. 2(a), we depict the time evolution of the number of excitations in the oscillators and the number of spin excitations within the atomic chain for a single selected trajectory. We compare the time evolution of the negativity of the reduced oscillator state for this selected trajectory to that of the fully coherent evolution without decay of the same system in Fig. 2(b). A striking observation is that the negativity during this dissipative evolution reaches a significantly higher value compared to the purely coherent evolution until $Jt = 12$. This can be explained as follows: In the selected trajectory, the first and all following decays take place via the decay channel $|\downarrow\rangle \to |g\rangle$. The corresponding collapse operators $\sqrt{\gamma_\downarrow}|g\rangle\langle\downarrow|_k$, with k the index of the atom, do not change the total number of excitations μ in the system. Hence, during the evolution, all initial spin excitations are converted to oscillator excitations, as shown in Fig. 2(a). Thus, the negativity of the final state reached by this trajectory can approach the maximum negativity bound in accordance with Eq. (4). In the absence of decay, excitations are continuously exchanged between chain and oscillators, with some excitations present in the chain at all times. Hence, the negativity of this coherent evolution remains lower.

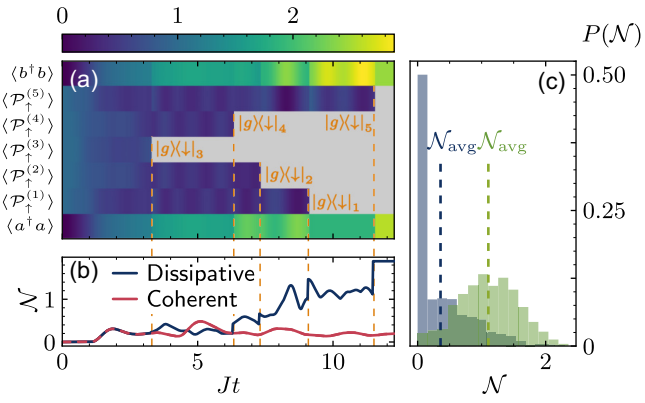

FIG. 2. Entanglement generation through atom chain dissipation. (a) Time evolution of excitations in the sites of the spin chain $\langle \mathcal{P}_\uparrow^{(i)}\rangle$ and the number of excitations in the oscillators $\langle a^\dagger a\rangle$, $\langle b^\dagger b\rangle$ for a selected single trajectory and system parameters $V = 3J$, $\gamma_\downarrow = \gamma_\uparrow = 0.2J$, and $\kappa = 0$. The system is initially prepared in the state $|\psi_{\text{init}}\rangle = |0\rangle_a \otimes |\uparrow\uparrow\uparrow\uparrow\uparrow\rangle \otimes |0\rangle_b$. Atom decay is marked with the corresponding jump operator, with $\sqrt{\gamma_\downarrow}$ omitted. Atoms that have decayed to the ground state are colored gray. (b) Time evolution of the oscillator negativity $\mathcal{N}$ for the trajectory shown in (a) (blue) in comparison to the purely coherent evolution (red) for the same parameters. (c) Probability distributions $P(\mathcal{N})$ of final-state negativities $\mathcal{N}$ for 2000 trajectories using the parameters from (a) with $\gamma_\uparrow = 0.2J$ (blue) and $\gamma_\uparrow = 0$ (green). The averages of the negativity distributions $\mathcal{N}_{\text{avg}}$ are depicted by vertical dashed lines.

In the selected example trajectory, only decay from state $|\downarrow\rangle$ occurred. In contrast, any decay from state $|\uparrow\rangle$ reduces the total number of excitations μ by one. Hence, the achievable negativity also reduces according to Eq. (5). In particular, if all atoms decay via this decay channel, the total number of excitations contained within the system is $\mu = 0$, resulting in a completely unentangled final state. These considerations suggest that to maximize the negativity reached by the system, it is beneficial to increase $\gamma_\downarrow$, while keeping $\gamma_\uparrow$ unchanged at its minimal value given by spontaneous decay of the Rydberg state.

To further investigate the impact of decay from state $|\uparrow\rangle$ on the entanglement generation, we now analyze a collection of trajectories. For each trajectory, we propagate the system until the atomic chain has fully decayed to $|g\rangle^{\otimes N}$. This *naturally* defines the end of the dissipative dynamics and occurs at a stochastic time that differs between trajectories. We then evaluate the oscillator negativity $\mathcal{N}$ for the corresponding final oscillator state. Repeating this procedure yields a distribution $P(\mathcal{N})$ of final-state negativities, whose shape can be controlled. This is shown in Fig. 2(c), where we plot the distributions for two different rates of decay from the state $|\uparrow\rangle$: $\gamma_\uparrow = 0.2J$ and $\gamma_\uparrow = 0$. The distribution for $\gamma_\uparrow = 0.2J$ features a long tail extending to high negativity values, which are close to the upper negativity bound, $\mathcal{N} \leqslant 2.5$. However, about half of the 2000 sampled trajectories yield near-zero negativity. When $\gamma_\uparrow = 0$, the distribution has fewer trajectories with near-zero negativity. In addition, higher negativity values

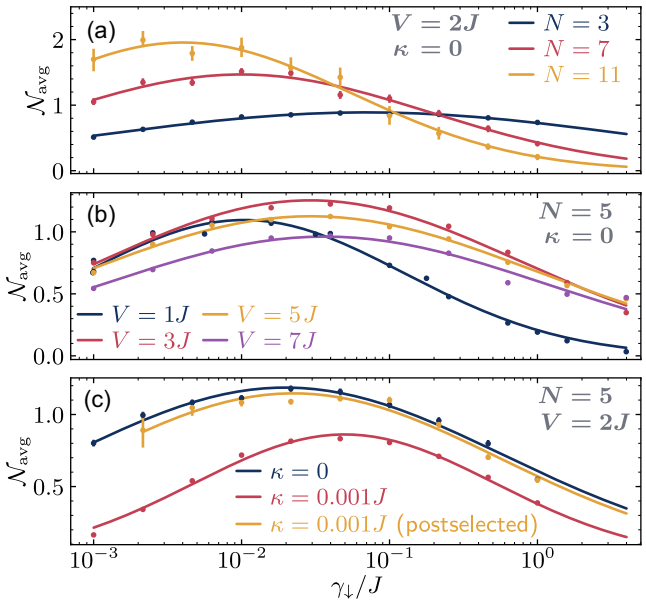

FIG. 3. Parameter dependence of average final-state negativity. (a) The average final-state negativity $\mathcal{N}_{\mathrm{avg}}$ as a function of $\gamma_\downarrow$ for different atom numbers N and fixed parameters $V = 2J$, $\kappa = 0$, and $\gamma_\uparrow = 0.001J$. Averages are taken over 1000 trajectories for $N = 3$ and $N = 7$, and over 100 trajectories for $N = 11$. (b) $\mathcal{N}_{\mathrm{avg}}$ as a function of $\gamma_\downarrow$ for different coupling strengths V with $N = 5$, $\kappa = 0$, and $\gamma_\uparrow = 0.001J$. Each data point is averaged over 1000 trajectories. (c) Comparison of two cases, with ($\kappa = 0.001J$) and without oscillator decay. Parameters are $V = 2J$, $N = 5$, and $\gamma_\uparrow = 0.001J$. For the case with oscillator decay, we also show results after postselecting trajectories that complete within a cutoff time of $0.3/\kappa$. For $\gamma_\downarrow = 0.001J$, the data point is missing because no trajectory satisfied the postselection criterion. Averages are taken over 10^4 trajectories. In all panels, log-normal curves are fitted to the data.

are reached more often. Consequently, the average final-state negativity $\mathcal{N}_{\mathrm{avg}}$ is higher when $\gamma_\uparrow = 0$, as marked in Fig. 2(c).

Note that the average negativity $\mathcal{N}_{\mathrm{avg}}$ describes the average of the single-trajectory negativities and should not be confused with the negativity of the ensemble-averaged state. In general, these two values are not the same because the negativity is a nonlinear quantity [44].

B. Parameter dependence of final-state entanglement

Having shown that $\gamma_\uparrow$ strongly influences the generated entanglement, we next explore how the parameters N, V, $\gamma_\downarrow$, and κ impact the negativity reached by the system. Here, we consider experimentally feasible parameter ranges, as discussed in Appendix A. For this investigation, we set $\gamma_\uparrow = 0.001J$, which, for typical experimental parameters, corresponds to the natural decay rate of Rydberg states. We focus in the following specifically on the average final-state negativity $\mathcal{N}_{\mathrm{avg}}$, which is calculated from histograms of the type shown in Fig. 2(c). In Fig. 3, we show the average negativity $\mathcal{N}_{\mathrm{avg}}$ as a function of $\gamma_\downarrow$. We find that for all considered parameters, the resulting scaling with $\gamma_\downarrow$ is well described by the Gaussian function on a logarithmic scale, $\mathcal{N}_{\mathrm{avg}}(\gamma_\downarrow) = \frac{A}{\gamma_\downarrow} \exp(-\frac{(\ln \gamma_\downarrow - \nu)^2}{2\sigma^2})$, where A, ν, and σ are fit parameters. This shape reflects the interplay of two competing mechanisms: On the one hand, increasing $\gamma_\downarrow$ reduces the ratio of decay from the state $|\uparrow\rangle$ compared to $|\downarrow\rangle$. Thereby, unwanted decays from state $|\uparrow\rangle$, which would remove excitations from the system, become less likely and the average negativity increases. On the other hand, a larger decay rate $\gamma_\downarrow$ results in an earlier first decay event, which splits the chain and divides the full system into two uncoupled subsystems. After such an event, each subchain is only coupled to one of the mechanical oscillators. Quantum correlations can still build up within each of these two subsystems, but no longer between them. Therefore, the oscillators cannot end up in an entangled state if the two subsystems are not already entangled with each other prior to the first decay. Consequently, a too high $\gamma_\downarrow$ suppresses the entanglement generation. In particular, the optimal decay rate $\gamma_\downarrow$—at which the maximum of $\mathcal{N}_{\mathrm{avg}}$ is reached—is smaller than J, such that the system has enough time to transfer excitations into the oscillators and build up correlations. This highlights the importance of engineering $\gamma_\downarrow$ for the dissipative entanglement generation.

In Fig. 3(a), we investigate the role of the number of atoms, N, in the Rydberg atom chain. We find that increasing N results in larger maximal $\mathcal{N}_{\mathrm{avg}}$. This is because the chosen initial state, defined in Eq. (9), contains more excitations for longer chains, which increases the reachable negativity according to Eq. (5). However, a larger N also increases the number of possible decay channels, resulting in an earlier first decay event. Additionally, the time for initial correlation buildup scales with N, as excitations must travel through a longer chain for correlations to form between the two oscillators.

Thus, the optimal decay rate $\gamma_\downarrow$ shifts towards lower values for higher N. This trend suggests that increasing the number of atoms N, while keeping the atomic decay rates $\gamma_\uparrow$ and $\gamma_\downarrow$ minimal, may be best. We stress that this is only correct for the idealized case of infinitely long-lived mechanical oscillators ($\kappa = 0$), for which the available time for correlation buildup is limited only by the Rydberg decay rates.

Next, we study the role of the interaction strength V, while keeping $N = 5$ and $\kappa = 0$ fixed. Among the investigated values of V, the highest average final-state negativity $\mathcal{N}_{\mathrm{avg}}$ is reached for $V = 3J$ and $\gamma_\downarrow \approx 0.03J$, as shown in Fig. 3(b). For $V = 1J$, the maximum $\mathcal{N}_{\mathrm{avg}}$ shifts towards lower $\gamma_\downarrow$ and is smaller overall. The reason is that a smaller V decelerates the excitation hopping in the chain. This results in a slower correlation buildup that is more likely to be interrupted by the first decay. Interestingly, we also observe a reduction of the maximum of $\mathcal{N}_{\mathrm{avg}}$ for larger $V = 5J$, $7J$. This we understand by considering the effective Hamiltonian (6), which we derived for $N = 2$ atoms and $V \gg J$. We see that the chain mediates a coherent coupling among the oscillator with effective rate J^2/V. Thus, the process of transporting spin excitations out of the chain into the oscillators takes longer the larger V becomes. As a consequence, the initially fully excited spin chain remains longer close to fully excited. This, in turn, increases the probability of the detrimental decay from state $|\uparrow\rangle$ in the spin chain, resulting in a reduced average negativity.

Up to this point, we have considered idealized oscillators without any internal decay ($\kappa = 0$). To illustrate the impact

of a finite oscillator lifetime, we compare in Fig. 3(c) the ideal system with one where $\kappa = 0.001J$, a value which is achievable with current state-of-the-art devices; see Appendix A. We find that excitation loss due to oscillator decay yields a reduction of $\mathcal{N}_{\text{avg}}$, in accordance to Eq. (5). The reduction becomes more severe for smaller $\gamma_\downarrow$, which also results in a shift of the optimal $\gamma_\downarrow$ to higher values. This is because the time it takes for all atoms to decay increases as the value of $\gamma_\downarrow$ decreases. Evidently, the longer this time is, the more likely it is for the oscillators to decay to an uncorrelated state. To remedy this, one can postselect only those trajectories where all atoms decay to state $|g\rangle$ in a time that is short compared to the oscillator lifetime. Experimentally, the occupation of state $|g\rangle$ can be measured sufficiently fast compared to the oscillator lifetime to implement such a postselection strategy [45]. In Fig. 3(c), we present a postselected dataset to which only trajectories contribute in which all atoms decay to the state $|g\rangle$ in under $0.3/\kappa$. This postselection increases $\mathcal{N}_{\text{avg}}$ to nearly the same value as in the case without oscillator decay, at the cost of the fraction of accepted trajectories reducing drastically when $\gamma_\downarrow$ is small. For example, for $\gamma_\downarrow = 0.001J$, which corresponds to the natural decay rate, no trajectory out of 10 000 satisfies the postselection requirement. In contrast, the acceptance fraction for the optimal decay rate $\gamma_\downarrow = 0.02J$ is 6.3%.

V. CONCLUSION AND OUTLOOK

In this work, we demonstrated how a chain of Rydberg atoms can mediate entanglement between two micro-electromechanical oscillators. In particular, we shed light on the influence of both coherent and dissipative effects during this process. While dissipation renders entanglement generation probabilistic, we showed that under certain circumstances, decay events may even enhance the creation of quantum correlations.

An interesting topic for future investigation concerns exploiting the knowledge of the atomic decay events. For example, if it was possible to experimentally identify the decay time and decay channel of the individual atoms, one could—in the absence of oscillator decay—construct the conditioned pure state of the oscillators [46]. Experimentally, this could become accessible with time- and spatially resolved photon collection using high-numerical-aperture objectives and/or cavity-assisted collection that directs the emitted photons to detectors [47,48]. However, as shown towards the end of the previous section, even simpler postselection protocols yield larger average negativities. Searching for more efficient postselection schemes thus seems like a worthwhile endeavor.

A further pathway for boosting oscillator entanglement is to introduce time-dependent coherent coupling protocols, as in Rydberg atom tweezer quantum simulators and computers [49,50]. In these studies, it would be interesting to lift the approximation of the nearest-neighbor interaction among the atoms and to incorporate power-law potentials. This may improve the robustness of the entanglement generation since the loss of an atom would not automatically lead to two decoupled subchains. In a similar vein, using two-dimensional Rydberg tweezer arrays to mediate interactions between the oscillators could enhance robustness to atom loss.

ACKNOWLEDGMENTS

The research leading to these results has received funding from the Deutsche Forschungsgemeinschaft (DFG, German Research Foundation) under Project No. 449905436, Research Unit FOR 5413/1, Grant No. 465199066, and Germany's Excellence Strategy—Cluster of Excellence Matter and Light for Quantum Computing (ML4Q) EXC 2004/1—390534769, from the European Union's Horizon 2020 program under the ERC grants SUPERWAVE (Grant No. 101071882) and OPEN-2QS (Grant No. 101164443). This work was also supported by the QuantERA II programme (project CoQuaDis, DFG Grant No. 532763411) that has received funding from the EU H2020 Research and Innovation Programme under Grant Agreement No. 101017733.

DATA AVAILABILITY

The data that support the findings of this article are openly available [51].

APPENDIX A: EXPERIMENTAL CONSTRAINTS ON PARAMETER CHOICES

The parameter ranges explored in the main text are informed by experimental consideration that we outline here. Among the various micro-electromechanical oscillator platforms capable of achieving high frequencies and long lifetimes [15,52–55], we take guidance from high-overtone bulk acoustic resonators (HBARs). These devices are particularly promising for quantum acoustic experiments due to their exceptionally high quality factors. State-of-the-art HBARs typically operate at resonance frequencies ω around 5 GHz, with decay rates around 1 kHz [25,26,56].

This resonance frequency can be matched to transitions between Rydberg states with principal quantum numbers around 90, which exhibit natural lifetimes of the order of 1 ms [57]. Off-resonant dressing with lower-lying states can strongly enhance the decay rate. For instance, in rubidium, dressing the Rydberg state with the first excited state allows the increase of the decay rate of up to ∼3 MHz.

The large dipole matrix elements between such high-lying Rydberg states enable strong coupling to the evanescent field of the HBAR. For realistic atom-surface separations of 20 μm to 30 μm, we estimate the coupling strength J to be in the range of 0.5 to 1.2 MHz using the calculation methods and material constants outlined in [27,58]. Similarly, the dipole-dipole interaction V between Rydberg atoms is substantial, with C_3 coefficients of the order of $\sim 80\,\text{GHz}\,\mu\text{m}^3$. This yields interatomic couplings of roughly 1 to 10 MHz for separations of 20 μm to 40 μm [30,32,57]. For simplicity, we fix the atom-oscillator coupling strength to be $J = 1$ MHz and scale the other parameters accordingly for the parameter scans presented in Sec. IV B.

Finally, we estimate the center-to-center oscillator separation. Including the atom-oscillator distance of 20 μm to 30 μm at each end, the parameters of Fig. 2 ($N = 5$ atoms with 10 μm spacing) yield a separation of the order of 80 μm to 100 μm. For larger chains, e.g., $N = 15$, this increases to several-hundred micrometers.

APPENDIX B: ZERO-TEMPERATURE ENVIRONMENT

We assume a zero-temperature environment for the treatment of dissipation in the system. As a consequence, heating of the oscillators and blackbody-induced transitions between Rydberg states vanish.

In experiments, temperatures down to $T \approx 10$ mK are typically reached within a ^{3}He/^{4}He dilution refrigerator [59]. At these temperatures, thermal heating of an oscillator mode at the considered frequencies around 5 GHz is negligible since $k_B T \ll \hbar\omega$, where k_B is the Boltzmann constant. Furthermore, blackbody-induced transitions are also strongly suppressed and are negligible compared to spontaneous decay [57].

[1] A. Aspect, J. Dalibard, and G. Roger, Experimental test of Bell's inequalities using time-varying analyzers, Phys. Rev. Lett. **49**, 1804 (1982).

[2] X.-L. Wang, L.-K. Chen, W. Li, H.-L. Huang, C. Liu, C. Chen, Y.-H. Luo, Z.-E. Su, D. Wu, Z.-D. Li, H. Lu, Y. Hu, X. Jiang, C.-Z. Peng, L. Li, N.-L. Liu, Y.-A. Chen, C.-Y. Lu, and J.-W. Pan, Experimental ten-photon entanglement, Phys. Rev. Lett. **117**, 210502 (2016).

[3] A. Kam, S. Tsesses, Y. Ilin, K. Cohen, Y. Lumer, L. Fridman, S. Lotan, A. Patsyk, L. Nemirovsky-Levy, M. Orenstein, M. Segev, and G. Bartal, Near-field photon entanglement in total angular momentum, Nature (London) **640**, 634 (2025).

[4] T. van Leent, M. Bock, F. Fertig, R. Garthoff, S. Eppelt, Y. Zhou, P. Malik, M. Seubert, T. Bauer, W. Rosenfeld, W. Zhang, C. Becher, and H. Weinfurter, Entangling single atoms over 33 km telecom fibre, Nature (London) **607**, 69 (2022).

[5] S. Saha, M. Shalaev, J. O'Reilly, I. Goetting, G. Toh, A. Kalakuntla, Y. Yu, and C. Monroe, High-fidelity remote entanglement of trapped atoms mediated by time-bin photons, Nat. Commun. **16**, 2533 (2025).

[6] J. D. Jost, J. P. Home, J. M. Amini, D. Hanneke, R. Ozeri, C. Langer, J. J. Bollinger, D. Leibfried, and D. J. Wineland, Entangled mechanical oscillators, Nature (London) **459**, 683 (2009).

[7] V. Krutyanskiy, M. Galli, V. Krcmarsky, S. Baier, D. A. Fioretto, Y. Pu, A. Mazloom, P. Sekatski, M. Canteri, M. Teller, J. Schupp, J. Bate, M. Meraner, N. Sangouard, B. P. Lanyon, and T. E. Northup, Entanglement of trapped-ion qubits separated by 230 meters, Phys. Rev. Lett. **130**, 050803 (2023).

[8] W. H. Zurek, Decoherence, einselection, and the quantum origins of the classical, Rev. Mod. Phys. **75**, 715 (2003).

[9] M. Schlosshauer, Quantum decoherence, Phys. Rep. **831**, 1 (2019).

[10] M. Aspelmeyer, T. J. Kippenberg, and F. Marquardt, Cavity optomechanics, Rev. Mod. Phys. **86**, 1391 (2014).

[11] X. Liu, J. F. Vignola, H. J. Simpson, B. R. Lemon, B. H. Houston, and D. M. Photiadis, A loss mechanism study of a very high Q silicon micromechanical oscillator, J. Appl. Phys. **97**, 023524 (2005).

[12] S. Belli, R. Bonsignori, G. D'Auria, L. Fant, M. Martini, S. Peirone, S. Donadi, and A. Bassi, Entangling macroscopic diamonds at room temperature: Bounds on the continuous-spontaneous-localization parameters, Phys. Rev. A **94**, 012108 (2016).

[13] M. Bild, M. Fadel, Y. Yang, U. von Lüpke, P. Martin, A. Bruno, and Y. Chu, Schrödinger cat states of a 16-microgram mechanical oscillator, Science **380**, 274 (2023).

[14] W. H. Renninger, P. Kharel, R. O. Behunin, and P. T. Rakich, Bulk crystalline optomechanics, Nat. Phys. **14**, 601 (2018).

[15] Y. Chu and S. Gröblacher, A perspective on hybrid quantum opto- and electromechanical systems, Appl. Phys. Lett. **117**, 150503 (2020).

[16] M. Chegnizadeh, M. Scigliuzzo, A. Youssefi, S. Kono, E. Guzovskii, and T. J. Kippenberg, Quantum collective motion of macroscopic mechanical oscillators, Science **386**, 1383 (2024).

[17] Q. R. Rahman, I. Kladarić, M.-E. Kern, L. Lachman, Y. Chu, R. Filip, and M. Fadel, Genuine quantum non-Gaussianity and metrological sensitivity of fock states prepared in a mechanical resonator, Phys. Rev. Lett. **134**, 180801 (2025).

[18] S. Bose, I. Fuentes, A. A. Geraci, S. M. Khan, S. Qvarfort, M. Rademacher, M. Rashid, M. Toroš, H. Ulbricht, and C. C. Wanjura, Massive quantum systems as interfaces of quantum mechanics and gravity, Rev. Mod. Phys. **97**, 015003 (2025).

[19] C. Anastopoulos and B.-L. Hu, Gravitational decoherence: A thematic overview, AVS Quantum Sci. **4**, 015602 (2022).

[20] S. Bose, A. Mazumdar, M. Schut, and M. Toroš, Entanglement witness for the weak equivalence principle, Entropy **25**, 448 (2023).

[21] C. F. Ockeloen-Korppi, E. Damskägg, J.-M. Pirkkalainen, M. Asjad, A. A. Clerk, F. Massel, M. J. Woolley, and M. A. Sillanpää, Stabilized entanglement of massive mechanical oscillators, Nature (London) **556**, 478 (2018).

[22] R. Riedinger, A. Wallucks, I. Marinković, C. Löschnauer, M. Aspelmeyer, S. Hong, and S. Gröblacher, Remote quantum entanglement between two micromechanical oscillators, Nature (London) **556**, 473 (2018).

[23] L. M. de Lépinay, C. F. Ockeloen-Korppi, M. J. Woolley, and M. A. Sillanpää, Quantum mechanics–free subsystem with mechanical oscillators, Science **372**, 625 (2021).

[24] M.-H. Chou, H. Qiao, H. Yan, G. Andersson, C. R. Conner, J. Grebel, Y. J. Joshi, J. M. Miller, R. G. Povey, X. Wu, and A. N. Cleland, Deterministic multi-phonon entanglement between two mechanical resonators on separate substrates, Nat. Commun. **16**, 1450 (2025).

[25] Y. Yang, I. Kladarić, M. Drimmer, U. von Lüpke, D. Lenterman, J. Bus, S. Marti, M. Fadel, and Y. Chu, A mechanical qubit, Science **386**, 783 (2024).

[26] V. J. Gokhale, B. P. Downey, D. S. Katzer, N. Nepal, A. C. Lang, R. M. Stroud, and D. J. Meyer, Epitaxial bulk acoustic wave resonators as highly coherent multi-phonon sources for quantum acoustodynamics, Nat. Commun. **11**, 2314 (2020).

[27] M. Gao, Y.-x. Liu, and X.-B. Wang, Coupling Rydberg atoms to superconducting qubits via nanomechanical resonator, Phys. Rev. A **83**, 022309 (2011).

[28] F. Bariani, J. Otterbach, H. Tan, and P. Meystre, Single-atom quantum control of macroscopic mechanical oscillators, Phys. Rev. A **89**, 011801(R) (2014).

[29] M. Khazali, Progress towards macroscopic spin and mechanical superposition via Rydberg interaction, Phys. Rev. A **98**, 043836 (2018).
[30] S. de Léséleuc, V. Lienhard, P. Scholl, D. Barredo, S. Weber, N. Lang, H. P. Büchler, T. Lahaye, and A. Browaeys, Observation of a symmetry-protected topological phase of interacting bosons with Rydberg atoms, Science **365**, 775 (2019).
[31] D. Bluvstein, S. J. Evered, A. A. Geim, S. H. Li, H. Zhou, T. Manovitz, S. Ebadi, M. Cain, M. Kalinowski, D. Hangleiter, J. P. Bonilla Ataides, N. Maskara, I. Cong, X. Gao, P. Sales Rodriguez, T. Karolyshyn, G. Semeghini, M. J. Gullans, M. Greiner, V. Vuletić, *et al.*, Logical quantum processor based on reconfigurable atom arrays, Nature (London) **626**, 58 (2024).
[32] D. Barredo, H. Labuhn, S. Ravets, T. Lahaye, A. Browaeys, and C. S. Adams, Coherent excitation transfer in a spin chain of three Rydberg atoms, Phys. Rev. Lett. **114**, 113002 (2015).
[33] R. Stevenson, J. Minář, S. Hofferberth, and I. Lesanovsky, Prospects of charged-oscillator quantum-state generation with Rydberg atoms, Phys. Rev. A **94**, 043813 (2016).
[34] B. Bégoc, G. Cichelli, S. P. Singh, F. Bensch, V. Amico, F. Perciavalle, D. Rossini, L. Amico, and O. Morsch, Controlled dissipation for Rydberg atom experiments, Phys. Rev. A **112**, 023312 (2025).
[35] H. Schempp, G. Günter, S. Wüster, M. Weidemüller, and S. Whitlock, Correlated exciton transport in Rydberg-dressed-atom spin chains, Phys. Rev. Lett. **115**, 093002 (2015).
[36] S. Whitlock, H. Wildhagen, H. Weimer, and M. Weidemüller, Diffusive to nonergodic dipolar transport in a dissipative atomic medium, Phys. Rev. Lett. **123**, 213606 (2019).
[37] G. Vidal and R. F. Werner, Computable measure of entanglement, Phys. Rev. A **65**, 032314 (2002).
[38] R. Horodecki, P. Horodecki, M. Horodecki, and K. Horodecki, Quantum entanglement, Rev. Mod. Phys. **81**, 865 (2009).
[39] P. Coleman, *Introduction to Many Body Physics* (Cambridge University Press, Cambridge, 2008).
[40] J. R. Schrieffer and P. A. Wolff, Relation between the Anderson and Kondo Hamiltonians, Phys. Rev. **149**, 491 (1966).
[41] G. T. Landi, Eigenoperator approach to Schrieffer-Wolff perturbation theory and dispersive interactions, arXiv:2409.10656.
[42] J. Dalibard, Y. Castin, and K. Mølmer, Wave-function approach to dissipative processes in quantum optics, Phys. Rev. Lett. **68**, 580 (1992).
[43] M. B. Plenio and P. L. Knight, The quantum-jump approach to dissipative dynamics in quantum optics, Rev. Mod. Phys. **70**, 101 (1998).
[44] Y. Li, X. Chen, and M. P. A. Fisher, Quantum Zeno effect and the many-body entanglement transition, Phys. Rev. B **98**, 205136 (2018).
[45] A. M. Falconi, R. Panza, S. Sbernardori, R. Forti, R. Klemt, O. A. Karim, M. Marinelli, and F. Scazza, Microsecond-scale high-survival and number-resolved detection of ytterbium atom arrays Phys. Rev. Lett. **135**, 203402 (2025).
[46] S. Gammelmark, B. Julsgaard, and K. Mølmer, Past quantum states of a monitored system, Phys. Rev. Lett. **111**, 160401 (2013).
[47] M. Hijlkema, B. Weber, H. P. Specht, S. C. Webster, A. Kuhn, and G. Rempe, A single-photon server with just one atom, Nat. Phys. **3**, 253 (2007).
[48] A. L. Shaw, A. Soper, D. Shadmany, A. Kumar, L. Palm, D.-Y. Koh, V. Kaxiras, L. Taneja, M. Jaffe, D. I. Schuster, and J. Simon, A cavity array microscope for parallel single-atom interfacing Nature (London) **650**, 320 (2026).
[49] S. J. Evered, D. Bluvstein, M. Kalinowski, S. Ebadi, T. Manovitz, H. Zhou, S. H. Li, A. A. Geim, T. T. Wang, N. Maskara, H. Levine, G. Semeghini, M. Greiner, V. Vuletić, and M. D. Lukin, High-fidelity parallel entangling gates on a neutral-atom quantum computer, Nature (London) **622**, 268 (2023).
[50] P. Scholl, H. J. Williams, G. Bornet, F. Wallner, D. Barredo, L. Henriet, A. Signoles, C. Hainaut, T. Franz, S. Geier, A. Tebben, A. Salzinger, G. Zürn, T. Lahaye, M. Weidemüller, and A. Browaeys, Microwave engineering of programmable XXZ Hamiltonians in arrays of Rydberg atoms, PRX Quantum **3**, 020303 (2022).
[51] C. Wind *et al.*, Repository containing all corresponding data and source code of this manuscript: 10.5281/zenodo.18243071 (2025).
[52] A. D. O'Connell, M. Hofheinz, M. Ansmann, R. C. Bialczak, M. Lenander, E. Lucero, M. Neeley, D. Sank, H. Wang, M. Weides, J. Wenner, J. M. Martinis, and A. N. Cleland, Quantum ground state and single-phonon control of a mechanical resonator, Nature (London) **464**, 697 (2010).
[53] Y. Chu, P. Kharel, W. H. Renninger, L. D. Burkhart, L. Frunzio, P. T. Rakich, and R. J. Schoelkopf, Quantum acoustics with superconducting qubits, Science **358**, 199 (2017).
[54] X. Han, C.-L. Zou, and H. X. Tang, Multimode strong coupling in superconducting cavity piezoelectromechanics, Phys. Rev. Lett. **117**, 123603 (2016).
[55] Y. Luo, H. H. Diamandi, H. Li, R. Bi, D. Mason, T. Yoon, X. Guo, H. Tang, R. O. Behunin, F. J. Walker, C. Ahn, and P. T. Rakich, Lifetime-limited Gigahertz-frequency mechanical oscillators with millisecond coherence times, arXiv:2504.07523.
[56] U. von Lüpke, I. C. Rodrigues, Y. Yang, M. Fadel, and Y. Chu, Engineering multimode interactions in circuit quantum acoustodynamics, Nat. Phys. **20**, 564 (2024).
[57] N. Šibalić, J. Pritchard, C. Adams, and K. Weatherill, ARC: An open-source library for calculating properties of alkali Rydberg atoms, Comput. Phys. Commun. **220**, 319 (2017).
[58] U. von Lüpke, Quantum control of a multimode bulk acoustic wave resonator, Ph.D. thesis, ETH Zurich, 2023.
[59] F. Pobell, *Matter and Methods at Low Temperatures* (Springer, Berlin, 2007).

A.4. [P4] – Magic running- and standing-wave optical traps for Rydberg atoms

Editors' Suggestion

Magic running- and standing-wave optical traps for Rydberg atoms

Lukas Ahlheit,[1,*] Chris Nill,[1,2] Daniil Svirskiy,[1] Jan de Haan,[1] Simon Schroers,[1] Wolfgang Alt,[1] Nina Stiesdal,[1] Igor Lesanovsky,[2,3] and Sebastian Hofferberth[1,†]

[1]*Institut für Angewandte Physik, University of Bonn, Wegelerstraße 8, 53115 Bonn, Germany*

[2]*Institut für Theoretische Physik and Center for Integrated Quantum Science and Technology, Universität Tübingen, Auf der Morgenstelle 14, 72076 Tübingen, Germany*

[3]*School of Physics and Astronomy and Centre for the Mathematics and Theoretical Physics of Quantum Non-Equilibrium Systems, The University of Nottingham, Nottingham, NG7 2RD, United Kingdom*

(Received 29 October 2024; accepted 6 January 2025; published 24 January 2025; corrected 11 July 2025)

Magic trapping of ground and Rydberg states, which equalizes the AC Stark shifts of these two levels, enables increased ground-to-Rydberg state coherence times. We measure via photon storage and retrieval how the ground-to-Rydberg state coherence depends on trap wavelength for two different traps and find different optimal wavelengths for a one-dimensional optical lattice trap and a running wave optical dipole trap. Comparison to theory reveals that this is caused by the Rydberg electron sampling different potential landscapes. The observed difference increases for higher principal quantum numbers, where the extent of the Rydberg electron wave function becomes larger than the optical lattice period. Our analysis shows that optimal magic trapping conditions depend on the trap geometry, in particular for optical lattices and tweezers.

DOI: 10.1103/PhysRevA.111.013115

I. INTRODUCTION

Converting photons into propagating or stationary coherent excitations in atomic ensembles is a key aspect to quantum memory schemes [1–6]. Photon storage times in atomic media are limited by various decoherence mechanisms, including thermal atomic motion, which can be reduced by using ultracold atoms, and inhomogeneous differential light shifts between atoms sharing the coherence [4,7–9]. The latter can be reduced by turning off optical traps or by using magic wavelength traps where both involved atomic states experience the same light shift [10]. This approach is common for quantum memories based on hyperfine ground-state transitions and enables photon storage on minute timescales [11].

Slow light and photon storage schemes involving one or more Rydberg states enable mapping of strong atomic interactions onto propagating or stored photons [12–20]. Compared to transitions between hyperfine ground states, one challenge of using Rydberg states is that the two-photon excitation scheme usually results in large k-vector mismatch between probe and control light, leading to a faster loss of coherence with faster atomic motion [4]. This motional dephasing can be prevented by trapping the atoms in a standing-wave optical lattice. The extent of the Rydberg electron wave function, comparable to the lattice period in typical optical traps, requires careful calculation of the magic condition. The quivering motion of the almost-free Rydberg electron in the electric trapping field leads to a repulsive ponderomotive potential [21–23], which gives rise to a repulsive optical potential for the entire Rydberg atom [24]. One solution is an effectively blue-detuned trap for both the ground state and Rydberg state [25–28]. Another approach is to use a red-detuned trap for the ground state, which at the same time near-resonantly couples the Rydberg state to a lower-lying atomic state [24,29,30] to overcome the repulsive ponderomotive potential. Such near-resonant traps with minimized differential AC Stark shift were employed in an optical lattice to increase ground-to-Rydberg state coherence to approximately 20 μs, approaching the Rydberg state lifetime [30]. In such an optical lattice, the Rydberg electron samples the potential landscape surrounding the atomic core. Therefore, the trapping geometry will influence the exact magic wavelength when the size of the Rydberg electron wave function gets comparable to the trap dimensions [21].

In this paper, we explore this geometry dependence in detail by comparing magic trapping wavelengths for atoms in a one-dimensional optical lattice and a single-beam running-wave trap. For experimentally determining the magic trapping conditions, we measure the coherence time of a collective ground-state-Rydberg-state excitation as a function of trapping wavelengths. We review ground- and Rydberg-state potentials and derive magic trapping conditions as function of trap laser wavelength and Rydberg-state principal quantum number n. Our experiments show that both the longitudinal standing wave as well as the radial trap shape influence the magic condition. We find that the experimentally best magic condition is obtained by minimizing the variance of the differential light shift across the atomic ensemble. We verify the modification of optimal wavelengths for lattice trapped atoms for the increasing Rydberg electron wave function with n.

II. EXPERIMENTAL SETUP

Figure 1(a) shows the relevant level scheme of ^{87}Rb and the involved lasers for magic trapping and Rydberg excitation.

*Contact author: ahlheit@iap.uni-bonn.de
†Contact author: hofferberth@iap.uni-bonn.de

 ©2025 American Physical Society

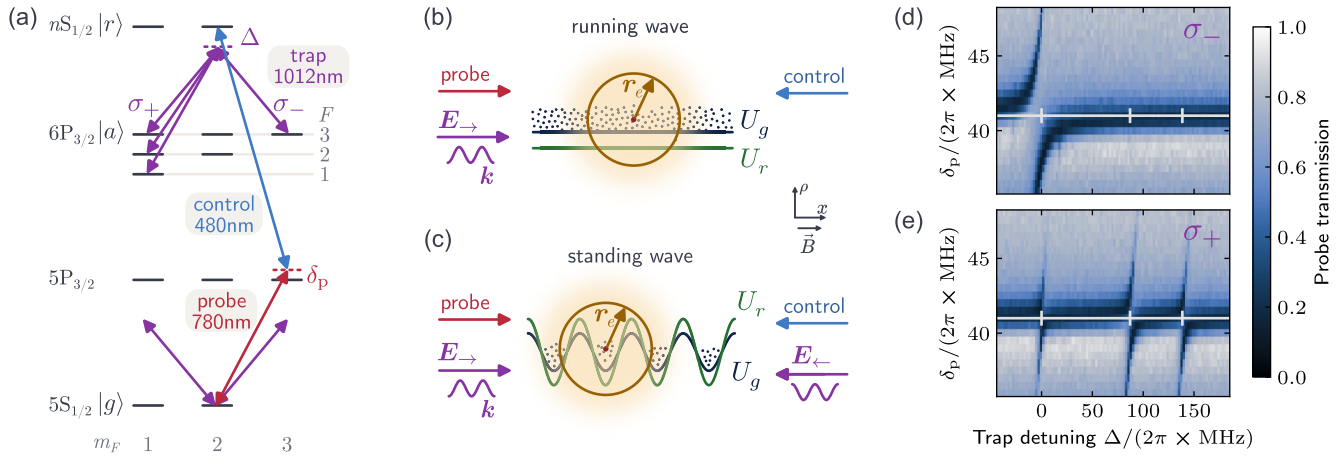

FIG. 1. Setup for the magic wavelength trap. (a) Energy level diagram of relevant ^{87}Rb hyperfine states. The red and blue arrows indicate the two-photon excitation (probe, control) from the ground state $|g\rangle$ to the Rydberg state $|r\rangle$. The purple arrows show possible couplings between the Rydberg state $|r\rangle$ and different $6P_{3/2}$ hyperfine states by the circularly polarized trapping laser light. The detuning Δ is the one of the trapping laser from the transition between the $6P_{3/2}$ hyperfine state $|a\rangle$ and the Rydberg state $|r\rangle$. (b), (c) The used colinear optical beams in the two trapping configurations. We compare a (b) running wave trap made of an incident beam with electric field $\boldsymbol{E}_\rightarrow$, with (c) a standing wave trap, formed by adding a counterpropagating beam with electric field $\boldsymbol{E}_\leftarrow$. The two-photon excitation beams counterpropagate along the trap axis. The magnetic field points along the probe beam to define the quantization axis. The blue and green lines illustrate the trapping potential experienced by ground-state and Rydberg atoms, respectively. The case sketched here is for a nonmagic trap detuning where the two different states experience different trapping potentials. r_e indicates the extent of the Rydberg electron wave function for $76S$. (d), (e) Experimentally measured probe laser transmission spectroscopy of the two-photon transition to $108S$ for varying the probe detuning δ_p and the trap laser detuning Δ. The control field is detuned by $2\pi \times 41$ MHz (white horizontal line) relative to the bare $|5P_{3/2}, F = 3, m_F = 3\rangle - |r\rangle$ transition. When the trapping beam drives (d) σ^- or (e) σ^+ transitions, we observe one or three hyperfine transitions, respectively.

To create attractive potentials for both the ground and the Rydberg states, we employ a $\lambda_T \approx 1012$ nm trap laser. This laser creates a far-of-resonant dipole trap for atoms in the ground state $|g\rangle = |5S_{1/2}, F = 2, m_F = 2\rangle$. To also trap atoms in the Rydberg state $|r\rangle = |nS_{1/2}, m_J = 1/2\rangle$, it near-resonantly couples the Rydberg state to the lower-lying $|6P_{3/2}\rangle$ state. As indicated in the level scheme, the trap can couple $|r\rangle$ to different $6P_{3/2}$ hyperfine states depending on its polarization. We use σ^- polarized trapping light to couple only to a single, well-defined hyperfine state $|a\rangle = |6P_{3/2}, F = 3, m_F = 3\rangle$. We define the trap detuning as $\Delta = \omega - \omega_{ra}$, where ω is the laser frequency and ω_{ra} is the transition frequency between $|r\rangle$ and $|a\rangle$. To create the collective ground-state-Rydberg-state excitation, we use the two-photon excitation scheme shown in Fig. 1(a). Few-photon probe pulses of 780 nm together with a strong 480 nm control field couple $|g\rangle$ via the intermediate state $|5P_{3/2}, F = 3, m_F = 3\rangle$ to $|r\rangle$. Both beams are focused onto the trapped atoms. The probe beam has a $1/e^2$ intensity waist radius of 5.1 μm and the counterpropagating control beam has a waist radius of 45.1 μm.

Figures 1(b) and 1(c) show the two different trap geometries where we investigate the magic trapping of Rydberg atoms. The probe and control beams are colinear with the trapping beams. Figure 1(b) shows the running-wave trap that is created by a single trapping beam with electric field $\boldsymbol{E}_\rightarrow$ focused at the atom cloud center with a $1/e^2$ radius of 24.8 μm. In Fig. 1(c) this single beam is retroreflected into electric field $\boldsymbol{E}_\leftarrow$ to form a standing-wave lattice. Throughout this paper, we set the incoming power in the standing wave to be one-fourth of the power used for the running wave to have the same maximum intensity in both geometries. The resulting ground-state central trap depth is 12 μK k_B. We apply a magnetic field parallel to the probe beam, along which we also define the quantization axis of the system. We load ultracold ^{87}Rb atoms at a temperature of $T \sim 2$ μK into either of the two geometries. We adjust the number of atoms in the final trap between 500 and 5000 atoms depending on the target Rydberg state [31]. The axial dimension of the atomic distribution is determined by the initial atom preparation and has a $1/e^2$ half-width of 40.8 μm. In the radial direction, the atom distribution is defined by the investigated trap geometry and has a $1/e^2$ half-width of 13.4 μm.

In Figs. 1(d) and 1(e) we show the probe transmission spectroscopy to $|r\rangle = 108S_{1/2}$ in the presence of the trap laser as a function of probe detuning δ_p and trap detuning Δ. In Fig. 1(d) the trapping field drives σ^- transitions. At $\Delta = 0$ MHz, the coupling between $|r\rangle$ and $|6P_{3/2}, F = 3, m_F = 3\rangle$ results in an avoided crossing. The white horizontal line marks the ground-to-Rydberg transition measured in free space. In Fig. 1(e) the trap drives σ^+ transitions, and avoided crossings appear for $|6P_{3/2}, F = 1, 2, 3, m_F = 1\rangle$. The observed level spacing is in agreement with known $6P_{3/2}$ hyperfine splitting [32], which is indicated by white ticks. Our combination of polarizations allows us to realize an isolated four-level system with three beams propagating parallel to the quantization axis. We avoid any rotation of optically pumped spin-orientation in the experiment sequence, open transitions [33], or perpendicular beams [34].

III. THEORY: TRAPPING POTENTIAL

In the following, we review the theory of Rydberg atom optical trapping, which in particular has to take into account that the Rydberg wave function is large compared to the optical wavelength [21]. Our derivation follows the one given by Lampen *et al.* [30]. For each geometry we derive the trapping potentials U_g and U_r experienced by an atom in the ground and the Rydberg states, respectively. The trapping laser, at position $\boldsymbol{r}$ and time t, is generally characterized by the vector potential $\boldsymbol{A}(\boldsymbol{r},t)$. In the Coulomb gauge, the resulting electric field is given by $\boldsymbol{E}(\boldsymbol{r},t) = -\partial\boldsymbol{A}(\boldsymbol{r},t)/\partial t$. We consider the atom core to be located at position $\boldsymbol{r}$ and the single valence electron at $\boldsymbol{r}+\boldsymbol{r}_e$ in the core potential $V_c(\boldsymbol{r}_e)$. For both the ground and Rydberg states, the Hamiltonian is given by the minimal-coupling Hamiltonian of an electron in an electromagnetic field

$$\begin{aligned} H &= \frac{1}{2m_e}(\boldsymbol{p}_e - e\boldsymbol{A}(\boldsymbol{r}+\boldsymbol{r}_e,t))^2 + eV_c(\boldsymbol{r}_e) \\ &= \underbrace{\frac{\boldsymbol{p}_e^2}{2m_e} + eV_c(\boldsymbol{r}_e)}_{H_0} \underbrace{-\frac{e\boldsymbol{A}(\boldsymbol{r}+\boldsymbol{r}_e,t)\cdot\boldsymbol{p}_e}{m_e}}_{H_1} + \underbrace{\frac{e^2\boldsymbol{A}^2(\boldsymbol{r}+\boldsymbol{r}_e,t)}{2m_e}}_{H_2}. \end{aligned} \tag{1}$$

Here, e and m_e are the electron charge and mass and $\boldsymbol{p}_e$ the momentum operator of the electron. The Hamiltonian [second row of Eq. (1)] is now in the form of a hydrogen-like Hamiltonian H_0 perturbed by $H_{1,2}$. For an eigenstate $|q\rangle$ of H_0, the energy is given as $\hbar\omega_q|q\rangle = H_0|q\rangle$. We calculate the energy shift of both the ground and Rydberg states by treating $H_{1,2}$ in perturbation theory. Therefore, the time dependence of $H_{1,2}$ has to be decomposed in Floquet-modes using the Floquet-quasi-energy approach [35,36]. Hence, a concrete form of the vector potential is needed.

For two counterpropagating Gaussian beams, as we use to form our trap configuration, the vector potential is given by

$$\begin{aligned} \boldsymbol{A}(\boldsymbol{r}+\boldsymbol{r}_e,t) = \frac{\boldsymbol{\epsilon}}{\omega}(&E_{\rightarrow}(\boldsymbol{r})\sin[(\boldsymbol{r}+\boldsymbol{r}_e)\cdot\boldsymbol{k} - \omega t] \\ &- E_{\leftarrow}(\boldsymbol{r})\sin[(\boldsymbol{r}+\boldsymbol{r}_e)\cdot\boldsymbol{k} + \omega t]), \end{aligned} \tag{2}$$

with the polarization $\boldsymbol{\epsilon}$ and the wave vector $\boldsymbol{k} = k\hat{\boldsymbol{e}}_x$ of the trap laser propagating along the x axis. For a running-wave configuration, the electric field amplitude in the backwards direction is $E_{\leftarrow}(\boldsymbol{r}) = 0$. Note that we assume that the Gaussian-shaped field amplitude is homogeneous over the diameter of the Rydberg (ground-state) atom. Therefore, we set $E_{\rightarrow(\leftarrow)}(\boldsymbol{r}+\boldsymbol{r}_e) \approx E_{\rightarrow(\leftarrow)}(\boldsymbol{r})$.

First, we calculate the energy shift caused by H_1 acting on an eigenstate $|q\rangle$ of the unperturbed Hamiltonian. A detailed derivation is outlined in Appendix A. We first decompose H_1 in Floquet modes as

$$H_1 = \frac{e\boldsymbol{A}(\boldsymbol{r}+\boldsymbol{r}_e)\cdot\boldsymbol{p}_e}{m_e}e^{i\omega t} + \frac{e\boldsymbol{A}^*(\boldsymbol{r}+\boldsymbol{r}_e)\cdot\boldsymbol{p}_e}{m_e}e^{-i\omega t}, \tag{3}$$

see Appendix B for the expanded form of the vector potential in Eq. (B2). For the energy correction in second order, we then obtain

$$U_q^{(1)}(\boldsymbol{r}) \approx |\boldsymbol{A}(\boldsymbol{r})|^2 \sum_{j\neq q}\frac{\omega_{qj}^2}{\hbar}\left(\frac{|\langle q|\boldsymbol{\epsilon}\cdot\boldsymbol{r}_e|j\rangle|^2}{\omega_{qj}-\omega} + \frac{|\langle q|\boldsymbol{\epsilon}^*\cdot\boldsymbol{r}_e|j\rangle|^2}{\omega_{qj}+\omega}\right), \tag{4}$$

where $\omega_{qj} = \omega_q - \omega_j$.

Thus, we obtain the dynamic polarizability $\alpha_g^{(b)}$ arising from the bound-state transitions in

$$U_g^{(1)}(\boldsymbol{r}) \approx -\alpha_g^{(b)}\omega^2|\boldsymbol{A}(\boldsymbol{r})|^2. \tag{5}$$

For the energy shift of the Rydberg state $U_r^{(1)}$, the resonance approximation can be made. This is possible since the electromagnetic field with frequency ω is only in near resonance to the transition from $|a\rangle$ to $|r\rangle$. Therefore, other transitions are negligible, and the summation in Eq. (4) becomes drastically simplified. With $\Delta = \omega - \omega_{ra}$ and our polarization, we obtain

$$U_r^{(1)} \approx -\frac{D_{ar}^2}{8\hbar\Delta}\omega^2|\boldsymbol{A}(\boldsymbol{r})|^2, \tag{6}$$

with the reduced dipole matrix element $D_{ar} = \langle a||e\boldsymbol{r}_e||r\rangle$.

The energy shift arising from H_2 is nonvanishing in first-order perturbation theory. Therefore, we decompose H_2 in Floquet modes, see Eq. (B3). The first-order energy shift of state $|q\rangle$ only depends on Floquet mode 0, thus

$$U_q^{(2)} \approx \frac{e^2}{2m_e}\langle q|2\boldsymbol{A}(\boldsymbol{r}+\boldsymbol{r}_e)\boldsymbol{A}^*(\boldsymbol{r}+\boldsymbol{r}_e)|q\rangle. \tag{7}$$

We explicitly evaluate $U_q^{(2)}$ by using the expanded form of the vector potential [see Eq. (B4)] and obtain

$$\begin{aligned} U_q^{(2)} \approx -\frac{\alpha_f}{4}[&4E_{\rightarrow}(\boldsymbol{r})E_{\leftarrow}(\boldsymbol{r})\cos^2(kx)\theta_q \\ &- 2E_{\rightarrow}(\boldsymbol{r})E_{\leftarrow}(\boldsymbol{r})\sin(2kx)\langle q|\sin(2kx_e)|q\rangle \\ &+ 2E_{\rightarrow}(\boldsymbol{r})E_{\leftarrow}(\boldsymbol{r})[1-\theta_q] \\ &+ (E_{\rightarrow}(\boldsymbol{r}) - E_{\leftarrow}(\boldsymbol{r}))^2], \end{aligned} \tag{8}$$

where $\alpha_f = -e^2/m_e\omega^2$ is the free-electron polarizability. Since $\sin(2kx_e)$ is an odd function $\langle q|\sin(2kx_e)|q\rangle = 0$ due to parity arguments. We introduce the landscape factor $\theta_q = \langle q|\cos(2kx_e)|q\rangle$ to describe the electron wave-function sampling the variation of the optical lattice potential [30,37]. This term becomes significant when the extension of the radial wave function becomes comparable to the optical trap period. In this case, the optical dipole approximation breaks down. However, for the ground state the dipole approximation with $kx_e \ll 1$ can be applied and thus $\theta_g = \langle g|\cos(2kx_e)|g\rangle \approx 1$.

In contrast, for the Rydberg state, the landscape factor θ_r has to be calculated explicitly. In our case, $|r\rangle = |nS_{1/2}, m_J = 1/2\rangle$ is an S state. To calculate the landscape factor as a function of n, we use spherical Bessel functions as

$$\theta_n = \langle nS|\cos(2kx_e)|nS\rangle = \int_0^\infty dr_e P_{n,0}(r_e)j_0(2kr_e), \tag{9}$$

where $P_{n,0}(r_e)$ is the radial probability density of an atom in state $|nS\rangle$, and $j_0(2kr_e)$ is the spherical Bessel function of the first kind for zero angular momentum [30].

Summarizing the derived terms, we obtain the energy shift for ground-state atoms as

$$U_g(\boldsymbol{r}) \approx U_g^{(1)}(\boldsymbol{r}) + U_g^{(2)}(\boldsymbol{r}) \tag{10}$$

$$= -\underbrace{\left(\alpha_g^{(\mathrm{b})} + \alpha_f\right)}_{\alpha_g}\omega^2|\boldsymbol{A}(\boldsymbol{r})|^2. \tag{11}$$

Here, α_g is the well-known dynamic polarizability of the ground-state atom [37–39]. For the Rydberg state, we obtain

$$U_r(\boldsymbol{r}) \approx U_r^{(1)}(\boldsymbol{r}) + U_r^{(2)}(\boldsymbol{r}) \tag{12}$$

$$= -\frac{D_{ar}^2}{8\hbar\Delta}\omega^2|\boldsymbol{A}(\boldsymbol{r})|^2 + U_r^{(2)}(\boldsymbol{r}). \tag{13}$$

We split the potentials into the axially periodic potential $U_g^{\sim}(\boldsymbol{r})$, denoted with $\sim$, and the axially nonperiodic potential $U_g^{-}(\boldsymbol{r})$, denoted as $-$, thus

$$U_g(\boldsymbol{r}) = U_g^{\sim}(\boldsymbol{r}) + U_g^{-}(\boldsymbol{r}), \tag{14}$$

$$U_g^{\sim}(\boldsymbol{r}) = -\alpha_g E_{\rightarrow}(\boldsymbol{r})E_{\leftarrow}(\boldsymbol{r})\cos^2(kx), \tag{15}$$

$$U_g^{-}(\boldsymbol{r}) = -\frac{\alpha_g}{4}(E_{\rightarrow}(\boldsymbol{r}) - E_{\leftarrow}(\boldsymbol{r}))^2. \tag{16}$$

For numerical calculations, we use matrix elements provided by the ARC package [40]. For the Rydberg state, we obtain

$$U_r(\boldsymbol{r}) = U_r^{\sim}(\boldsymbol{r}) + U_r^{-}(\boldsymbol{r}), \tag{17}$$

$$U_r^{\sim}(\boldsymbol{r}) = -E_{\rightarrow}(\boldsymbol{r})E_{\leftarrow}(\boldsymbol{r})\cos^2(kx)\left(\frac{D_{ar}^2}{4\hbar\Delta} + \alpha_f\theta_n\right), \tag{18}$$

$$U_r^{-}(\boldsymbol{r}) = -\frac{D_{ar}^2}{16\hbar\Delta}[E_{\rightarrow}(\boldsymbol{r}) - E_{\leftarrow}(\boldsymbol{r})]^2 - \frac{\alpha_f}{4}[2E_{\rightarrow}(\boldsymbol{r})E_{\leftarrow}(\boldsymbol{r})(1-\theta_n) + [E_{\rightarrow}(\boldsymbol{r}) - E_{\leftarrow}(\boldsymbol{r})]^2]. \tag{19}$$

The light shifts of the ground and Rydberg states correspond to our measured avoided crossing in Figs. 1(d) and 1(e). In the rest of the paper, we decompose positions $\boldsymbol{r}$ into the radial position ρ and the axial position x.

Determining the magic detuning

We can now calculate the differential light shift $U_r(\rho, x, \Delta) - U_g(\rho, x)$ using Eqs. (14) to (19). In Fig. 2 we show the differential light shift for the 76S Rydberg state for our two different trap geometries. The first row shows the potential for the running wave ($E_{\leftarrow} = 0$), and the second, third, and fourth rows illustrate the standing-wave potential ($E_{\leftarrow} = 0.87E_{\rightarrow}$, limited by the power loss over the retroreflection optical path). To illustrate the extent of the atomic cloud in the trap, the dashed contour lines show the position where the ground-state trapping potential $U_g(\rho, x)$ equals two times the atom thermal energy k_BT. The first row shows the differential light shift for a running-wave trap. The trap detuning Δ_n^{rw} that satisfies $U_r(\rho, x, \Delta_n^{\mathrm{rw}}) - U_g(\rho, x) = 0$ is found analytically:

$$\frac{D_{ar}^2}{4\hbar\Delta_n^{\mathrm{rw}}} = \alpha_g - \alpha_f. \tag{20}$$

The change in differential light shift as a function of trap laser detuning Δ comes solely from the Rydberg-state potential because of the near-resonant coupling to the $|a\rangle \rightarrow |r\rangle$ transition.

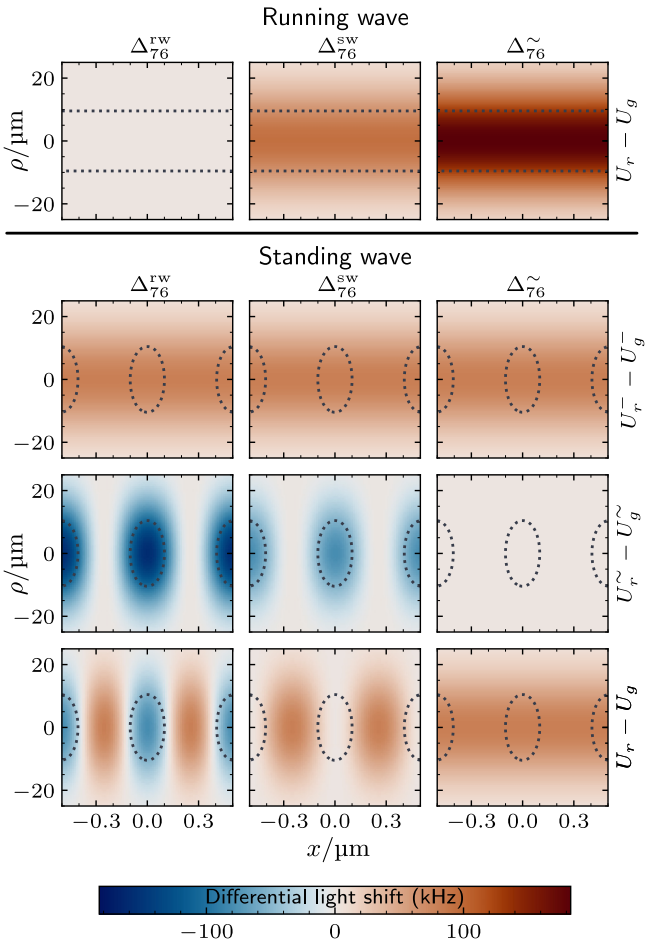

FIG. 2. Calculated differential light shift between ground state and Rydberg state 76S for running and standing-wave configuration with varying trap detunings Δ (columns). The light shifts from Eqs. (14) to (19) are evaluated for radial position ρ and axial position x relative to the trap center. The dotted lines indicate the atomic distribution, see main text. For a running wave (first row), the differential light shift vanishes everywhere at the detuning $\Delta_{76}^{\mathrm{rw}}/2\pi = 336$ MHz (left column). The potential of the standing wave trap can be decomposed into a nonperiodic ($-$) (second row) and a periodic ($\sim$) (third row) component. For detuning $\Delta_{76}^{\sim}/2\pi = 548$ MHz (right column), the periodic light shift vanishes, while a nonperiodic component remains. For our experimental parameters, the full standing-wave trap (fourth row) shows an optimal detuning around $\Delta_{76}^{\mathrm{sw}}/2\pi = 413$ MHz (center column), where the standard deviation of the light shift over the whole atom cloud is minimal (see Fig. 3).

The second and third rows in Fig. 2 separately show the two contributions to the differential shift in the standing wave, as introduced in Eqs. (14) to (19). The second row shows the differential light shift from the nonperiodic components $U_{(g,r)}^{-}$. For our imbalanced standing wave, this differential light shift component only weakly depends on the trap detuning Δ. In the third row, the differential light shift from the periodic components $U_{(g,r)}^{\sim}$ is shown. We find the detuning $\Delta_n^{\sim}$ that

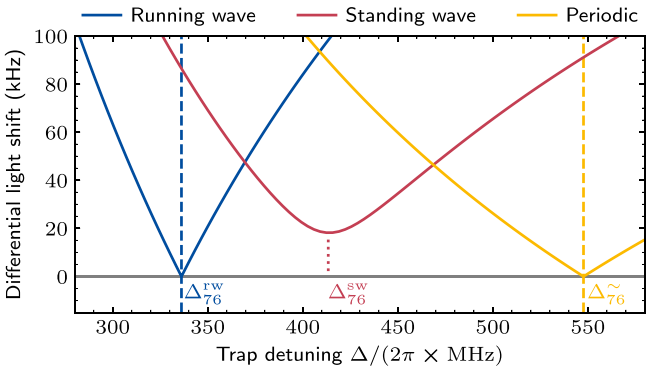

FIG. 3. Standard deviation of the differential light shift between ground state and Rydberg state 76S evaluated inside the dotted volumes highlighted in Fig. 2 for our experimental parameters. The vertical dashed lines show $\Delta_{76}^{\mathrm{rw}}$ and $\Delta_{76}^{\sim}$ from Eqs. (20) and (21). The standard deviation of the differential light shift in a full standing wave shows an optimal trap detuning $\Delta_{76}^{\mathrm{sw}}$ between $\Delta_{76}^{\mathrm{rw}}$ and $\Delta_{76}^{\sim}$.

satisfies $U_r^{\sim}(\rho, x, \Delta_n^{\sim}) - U_g^{\sim}(\rho, x) = 0$ analytically by

$$\frac{D_{ar}^2}{4\hbar\Delta_n^{\sim}} = \alpha_g - \alpha_f\theta_n. \tag{21}$$

The third column shows the potential for $\Delta = \Delta_{76}^{\sim}$, where the differential light shift from the periodic components is canceled. The differential potential in a standing wave is given by the sum of the periodic and the nonperiodic components, and is shown in the fourth row of Fig. 2. The periodic and nonperiodic components of the full standing wave do not have the same radial and axial dependence, and therefore, it is not possible to find a single, position-independent magic detuning. Instead, we consider the detuning that minimizes the inhomogeneity of the differential light shift across the atomic cloud.

We quantify this by calculating the standard deviation of the light shift over the active volume of the atomic cloud. This volume is determined by both the atomic cloud shape and the excitation beams. We consider the cloud volume inside $U_g(\rho, x) \leqslant U_g(0, 0) + 2k_BT$ and two times the $1/e^2$ radius of our probe beam. The middle column of Fig. 2 shows the differential light shift for the detuning $\Delta_{76}^{\mathrm{sw}}$ where the standard deviation is minimal.

Figure 3 shows the standard deviation of the differential light shift as function of trap detuning for the running wave, the standing wave, as well as for the purely periodic potential component. The minimum of the standard deviations in the running wave and the purely periodic potentials coincide with the calculated optimal detunings described by Eqs. (20) and (21). The optimum detuning for the full standing-wave trap lies between the magic detunings for the running wave and the periodic potential. Neither of the limiting cases describe our implemented standing-wave trap well.

IV. EXPERIMENTAL RESULTS

We measure the trap-induced decoherence for single photons stored as collective excitations in the medium [2,3,12,41,42]. We read out the stored probe photons after a variable storage time t_s. The retrieved photons are detected

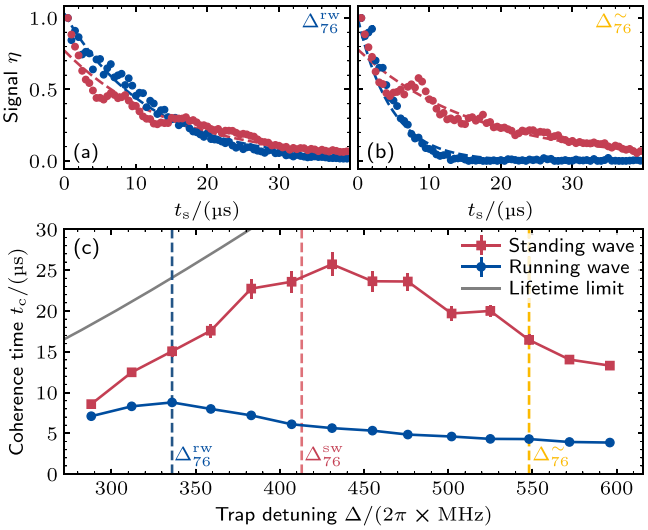

FIG. 4. Photon storage measurements with Rydberg state 76S for different trap laser detunings. (a), (b) Normalized retrieved signal η as a function of storage time t_s for atoms trapped in a standing wave (red) and running wave (blue). Panel (a) is measured for $\Delta_{76}^{\mathrm{rw}}$ and (b) at $\Delta_{76}^{\sim}$. Exponential fits of Eq. (22) to the data, shown here as dashed lines, are used to extract a coherence time t_c. (c) The coherence time t_c as function of trap laser detuning. The dashed vertical lines mark the analytic magic conditions for running wave Eq. (20), and periodic potential Eq. (21), as well as the optimal standing wave detuning $\Delta_{76}^{\mathrm{sw}}$.

by fiber-coupled single-photon counting modules. We normalize the time-dependent retrieval signal $\eta(t_s)$ to the value for the shortest storage time of 0.5 µs. The control laser is on-resonance with the $|5P_{3/2}, F = 3, m_F = 3\rangle - |r\rangle$ transition during both the photon storage and retrieval.

In Figs. 4(a) and 4(b) we show $\eta(t_s)$ for 76S for the running-wave and the standing-wave trap introduced in Fig. 1. The standing-wave measurements in Figs. 4(a) and 4(b) show two additional oscillations on top of the exponential decay. The oscillation with a period of 8 µs results from the excitation of Rydberg molecule states in the storage process. These Rydberg dimers, made of a Rydberg atom and a ground-state atom, form due to scattering between the Rydberg electron and the ground-state atom [43,44]. Photons are stored in a superposition of collective Rydberg atom and dimer excitations, causing the beat signal on top of the retrieval curve. The amplitude of the beat signal scales with the atomic density. The Rydberg dimer excitation energy is shifted compared to the Rydberg atom transition by the dimer binding energy. For $n = 76$ the binding energy is 114 kHz [42]. For atoms in the lattice, there is also a less prominent second oscillation with a 24 µs period, which stems from the motion of the atoms in the lattice wells [30]. The observed frequency is close to the axial trap frequency, but deviates slightly due to the anharmonicity of the trapping potential. With both of these oscillations present, we use a simple exponential fit with the function

$$f(t_s) = Ae^{-t_s/t_c}. \tag{22}$$

to average through the oscillations and extract a model-independent coherence time t_c. We expect to measure the longest coherence time at the optimal detuning calculated in Fig. 3.

In Fig. 4(c) we show the fitted coherence time as a function of trap laser detuning Δ. The coherence time for the running wave peaks at the magic detuning $\Delta_{76}^{\mathrm{rw}}$, see Figs. 4(a) and 4(b). For the standing wave, we find a clear discrepancy from the pure periodic potential of Eq. (21). Instead, the experimental result agrees well with the magic detuning $\Delta_{76}^{\mathrm{sw}}$ obtained by the standard deviation calculation shown in Fig. 3. The optimal detuning will only approach the simple lattice calculation in the limiting case where atoms do not experience the radial variation of the trap potential. The waist of the probe laser beam should be at least 20 times smaller than the trap waist to reach this limit.

We calculate the coherence time limit due to admixture of the fast-decaying $6P_{3/2}$ state, which scales with Δ^2 [30], and show it as a gray line in Fig. 4. We find the same optimal detunings when we subtract this contribution to the coherence time from our measured data. The decoherence caused by the differential light shift is the only significant detuning dependent mechanism for our experimental parameters. Other effects like atomic motion and Rydberg-Rydberg-interaction generally limit the coherence time, but are independent of the trap detuning [9].

We show in Fig. 5(a) the optimal detunings Δ_n^{trap} for different principal quantum numbers n and the two trap configurations. The magic detunings move closer to resonance for higher n because of the smaller dipole matrix elements $D_{ar} \propto (n - 3.13)^{-3/2}$. From the experimental detunings and the known matrix elements we extract an n-dependent effective polarizability for our experimental configurations defined as

$$\alpha_n^{\mathrm{trap}} := \frac{D_{ar}^2}{4\hbar\Delta_n^{\mathrm{trap}}}. \tag{23}$$

In Fig. 5(b) we show the increasing difference of this polarizability for the two trap geometries as function of principal quantum number. The running-wave polarizability α_n^{rw} and the periodic trap polarizability $\alpha_n^{\sim}$ satisfy the magic conditions

$$\alpha_n^{\mathrm{rw}} = \alpha_g - \alpha_f, \tag{24}$$

$$\alpha_n^{\sim} = \alpha_g - \alpha_f\theta_n, \tag{25}$$

and show in their difference the n scaling of the landscape factor θ_n, see Eq. (9). The difference between the running and standing waves indicates that the trapping geometry plays an important role for the optical confinement of high n Rydberg states. The top axis in Fig. 5 shows the Rydberg electron orbital diameter $2 \cdot \langle r \rangle$ as a function of Rydberg state. For low n ($n \lesssim 30$), the size of the Rydberg electron wave function is small in comparison to the lattice periodicity, as shown in Fig. 5(a) for $n = 25$. The case for Rydberg state $n = 76$ is shown as well, where the electron orbital already spans more than one lattice site. Here, the magic conditions between the running and standing waves are modified significantly. For very large n ($n \gtrsim 100$) the landscape factor goes to zero as the free electron samples more and more lattice sites. The resulting difference between α^{rw} and $\alpha^{\sim}$ becomes constant, shown by the arrow with length $|\alpha_f|/\alpha_g$.

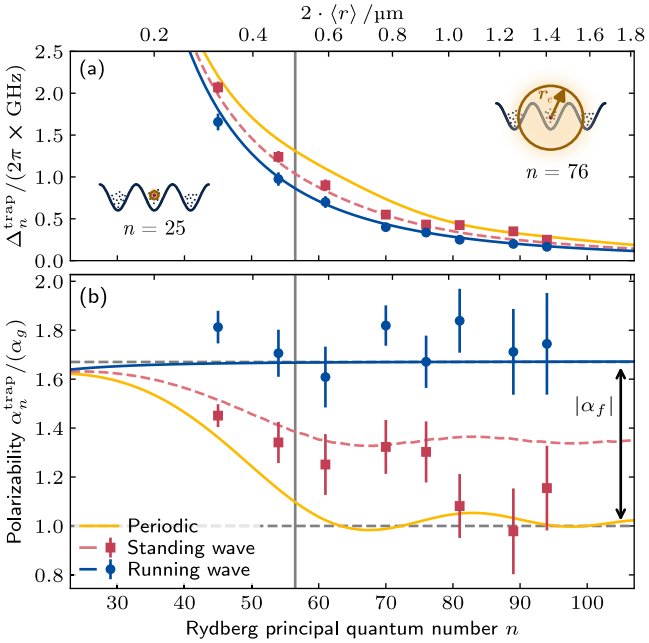

FIG. 5. Magic detunings for our running-wave and standing-wave trap as function of Rydberg state. (a) Optimal detunings Δ_n^{trap} determined by measurements as in Fig. 4(c) for a range of Rydberg principal quantum numbers n and for the different trap configurations. The solid lines show the analytic solution for the running wave (blue) and the periodic potential (yellow), from Eqs. (20) and (21), respectively. The optimal detuning Δ_n^{sw} for the full standing wave is extracted from the standard deviation of the differential light shift across the atomic cloud (red, dashed line). The vertical gray line marks the standing-wave trap periodicity (506 nm) in comparison to the Rydberg electron orbital diameter $2 \cdot \langle r \rangle$ on the top x axis. Experimental data for the running wave and the standing wave are shown as blue circles and red squares, respectively. The two schematic drawings highlight the size of the Rydberg electron wave function in relation to the standing-wave trap periodicity. (b) Polarizability calculated from the data shown in (a) as described by Eq. (23).

V. CONCLUSION

In this paper we studied how coherence between ground and Rydberg states depends on the trap geometry. This dependence is caused by the Rydberg electron that due to the nonnegligible size of its wave function, explores the potential landscape around the Rydberg atom. To obtain an intuitive picture of this effect, we present simple calculations and graphical visualizations of the differential light shift in running-wave and standing-wave traps. We experimentally determine the detunings of least dephasing for a range of Rydberg states for both traps. The result shows that the trapping beam geometry plays an important role when creating magic optical traps for Rydberg atoms. The measured detunings are in good agreement with the values expected from our calculations. Our work shows that it is necessary to take the size of both Rydberg atom and trapping beams into account when trapping Rydberg atoms. The results obtained in this work are of importance for magic trapping of Rydberg polaritons, collectively excited ensembles, and for experiments with individual Rydberg atoms.

ACKNOWLEDGMENTS

We are grateful to Wilson S. Martins for valuable discussions. The experimental data and analysis code underlying the results presented in this paper is freely accessible in the open-access Zenodo database at Ref. [49]. The research leading to these results received funding from the Deutsche Forschungsgemeinschaft (DFG, German Research Foundation) under Project No. 449905436, Research Unit FOR 5413/1, Grant No. 465199066, and Germany's Excellence Strategy, Cluster of Excellence Matter and Light for Quantum Computing (ML4Q) EXC 2004/1 390534769, from the European Union's Horizon 2020 program under the ERC grant SUPERWAVE (Grant No. 101071882). IL is grateful for financing from the Baden-Württemberg Stiftung through Project No. BWST_ISF2019-23.

APPENDIX A: ENERGY CORRECTION CAUSED BY H_1

We derive the energy correction of an eigenstate $|q\rangle$ of the unperturbed Hamiltonian H_0 due to $H^{(1)}$ from Eq. (1). We utilize time-dependent perturbation theory, specifically, the Floquet quasienergy formalism [35,45]. The first-order correction in H_1 vanishes due to parity arguments of the dipole operator. Thus, we derive the second-order energy shift of an atom in state $|q\rangle$. To do so, we expand H_1 in Floquet modes m, and therefore, express the vector potential $\boldsymbol{A}(\boldsymbol{r},t)$ in factors $e^{im\omega\tau}$, see Eq. (B2). From this we see that the only contribution is for $m=1$, thus

$$U_q^{(1)} \approx \frac{e^2}{m_e^2}\sum_{j\neq q}\frac{1}{\hbar}\left(\frac{|\langle q|\boldsymbol{A}(\boldsymbol{r}+\boldsymbol{r}_e)\cdot\boldsymbol{p}_e|j\rangle|^2}{\omega_{qj}-\omega}+\frac{|\langle q|\boldsymbol{A}^*(\boldsymbol{r}+\boldsymbol{r}_e)\cdot\boldsymbol{p}_e|j\rangle|^2}{\omega_{qj}+\omega}\right), \tag{A1}$$

where we use $\boldsymbol{p}_e\cdot\boldsymbol{A}(\boldsymbol{r}+\boldsymbol{r}_e)=\boldsymbol{A}(\boldsymbol{r}+\boldsymbol{r}_e)\cdot\boldsymbol{p}_e$ in the Coulomb gauge. We now expand the vector potential $\boldsymbol{A}(\boldsymbol{r}+\boldsymbol{r}_e)=\boldsymbol{A}(\boldsymbol{r})+\boldsymbol{\nabla}_r\boldsymbol{A}(\boldsymbol{r})\cdot\boldsymbol{r}_e+\ldots$ for a small electron radius $\boldsymbol{r}_e$. We use $\boldsymbol{A}(\boldsymbol{r})=\boldsymbol{\epsilon}A(\boldsymbol{r})$ and the commutation identity of the hydrogen atom $\langle q|\boldsymbol{\epsilon}\cdot\boldsymbol{p}_e|j\rangle = im_e\omega_{qj}\langle q|e\,\boldsymbol{\epsilon}\cdot\boldsymbol{r}_e|j\rangle$ [46] to simplify the expectation value with

$$U_q^{(1)} = \frac{e^2}{m_e^2}\sum_{j\neq q}\frac{1}{\hbar}\left(\frac{|\langle q|[\boldsymbol{A}(\boldsymbol{r})+\boldsymbol{\nabla}_r\boldsymbol{A}(\boldsymbol{r})\cdot\boldsymbol{r}_e+\ldots]\cdot\boldsymbol{p}_e|j\rangle|^2}{\omega_{qj}-\omega}+\frac{|\langle q|[\boldsymbol{A}^*(\boldsymbol{r})+\boldsymbol{\nabla}_r\boldsymbol{A}^*(\boldsymbol{r})\cdot\boldsymbol{r}_e+\ldots]\cdot\boldsymbol{p}_e|j\rangle|^2}{\omega_{qj}+\omega}\right) \tag{A2}$$

$$= \frac{e^2}{m_e^2}\sum_{j\neq q}\frac{1}{\hbar}\left(\frac{|A(\boldsymbol{r})\langle q|\boldsymbol{\epsilon}\cdot\boldsymbol{p}_e|j\rangle+\langle q|[\boldsymbol{\nabla}_r\boldsymbol{A}(\boldsymbol{r})\cdot\boldsymbol{r}_e]\cdot\boldsymbol{p}_e|j\rangle+\ldots|^2}{\omega_{qj}-\omega}+\frac{|A^*(\boldsymbol{r})\langle q|\boldsymbol{\epsilon}\cdot\boldsymbol{p}_e|j\rangle+\langle q|[\boldsymbol{\nabla}_r\boldsymbol{A}^*(\boldsymbol{r})\cdot\boldsymbol{r}_e]\cdot\boldsymbol{p}_e|j\rangle+\ldots|^2}{\omega_{qj}+\omega}\right) \tag{A3}$$

$$= \frac{e^2}{\hbar m_e^2}\sum_{j\neq q}\left[|A(\boldsymbol{r})|^2\left(\frac{|\langle q|\boldsymbol{\epsilon}\cdot\boldsymbol{p}_e|j\rangle|^2}{\omega_{qj}-\omega}+\frac{|\langle q|\boldsymbol{\epsilon}^*\cdot\boldsymbol{p}_e|j\rangle|^2}{\omega_{qj}+\omega}\right)+\left(\frac{|\langle q|[\boldsymbol{\nabla}_r\boldsymbol{A}(\boldsymbol{r})\cdot\boldsymbol{r}_e]\cdot\boldsymbol{p}_e|j\rangle|^2}{\omega_{qj}-\omega}+\frac{|\langle q|[\boldsymbol{\nabla}_r\boldsymbol{A}^*(\boldsymbol{r})\cdot\boldsymbol{r}_e]\cdot\boldsymbol{p}_e|j\rangle|^2}{\omega_{qj}+\omega}\right)\right]+\ldots \tag{A4}$$

$$= -|\boldsymbol{A}(\boldsymbol{r})|^2\omega^2\underbrace{\left[-\sum_{j\neq q}\frac{\omega_{qj}^2}{\omega^2}\left(\frac{|\langle q|e\boldsymbol{\epsilon}\cdot\boldsymbol{r}_e|j\rangle|^2}{\hbar(\omega_{qj}-\omega)}+\frac{|\langle q|e\boldsymbol{\epsilon}^*\cdot\boldsymbol{r}_e|j\rangle|^2}{\hbar(\omega_{qj}+\omega)}\right)\right]}_{\text{bound-state polarizability }\alpha_q^{(b)}}$$

$$+\frac{e^2}{\hbar m_e^2}\sum_{j\neq q}\left(\frac{|\langle q|[\boldsymbol{\nabla}_r\boldsymbol{A}(\boldsymbol{r})\cdot\boldsymbol{r}_e]\cdot\boldsymbol{p}_e|j\rangle|^2}{\omega_{qj}-\omega}+\frac{|\langle q|[\boldsymbol{\nabla}_r\boldsymbol{A}^*(\boldsymbol{r})\cdot\boldsymbol{r}_e]\cdot\boldsymbol{p}_e|j\rangle|^2}{\omega_{qj}+\omega}\right)+\ldots \tag{A5}$$

Here, the first summand is the dynamic dipole polarizability $\alpha_q^{(b)}(\omega)$ of the bound states in the atom. Note that $\alpha_q^{(b)}(\omega)$ is not the dynamic polarizability of the atom in state $|q\rangle$ since there is an additional contribution from the coupling to the continuum of unbound states [40]. When setting $|q\rangle=|g\rangle$, we obtain the bound-state contribution of the dynamic polarizability of the ground-state atom $\alpha_g^{(b)}$, see Eq. (5) of the main text.

The second summand in Eq. (A5) represents the quadrupole polarizability arising from the gradient of the vector potential [35]. For a ground-state atom this contribution is negligible since the gradient is negligible over the size r_e of the atom. The contributions from higher-order expansions of the potential $\boldsymbol{A}(\boldsymbol{r}+\boldsymbol{r}_e)$ lead to higher-order polarizabilities (i.e., hyperpolarizabilities). The first higher-order term contains a quadrupole transition between $|g\rangle$ and $|j\rangle$, the second an octupole transition, and so on. These contributions are negligible compared to the dipole transition, and consequently, the energy correction for a ground-state atom due to $H^{(1)}$ reduces to Eq. (5) with

$$U_g^{(1)}(\boldsymbol{r}) \approx -\alpha_g^{(b)}\omega^2|\boldsymbol{A}(\boldsymbol{r})|^2. \tag{A6}$$

If the atom is in the Rydberg state ($|q\rangle=|r\rangle$), the calculation of the polarizability includes the summation over many matrix elements. However, the frequency ω is chosen to be near resonant to the hyperfine state $|a\rangle=|6P_{3/2},F=3,m_F=3\rangle$. In the experiment, the trap laser has σ^- polarization. For this polarization, all other hyperfine transitions to $6P_{3/2}$ are dipole forbidden.

Therefore, we can perform the resonance approximation since terms including other transitions than $|a\rangle$ to $|r\rangle$ are smaller by orders of magnitude.

The contribution from the quadrupole transitions in Eq. (A5) is strongly suppressed since the trapping laser is off-resonant to these transitions. Additionally, our trap laser couples the Rydberg state to a low-lying state. Thus, the expectation value is primarily influenced by the spatial extent of the low-lying state's wave function, which defines the region over which the electric field gradient is evaluated, and the gradient is small in this region. Therefore, we only consider the contribution from the resonant dipole transition.

With these approximations, $U_r^{(1)}$ simplifies to

$$U_r^{(1)} \approx |\boldsymbol{A}(\boldsymbol{r})|^2 \frac{\omega_{ra}^2}{\hbar}\left(\frac{|\langle r|e\,\boldsymbol{\epsilon}\cdot\boldsymbol{r}_\mathrm{e}|a\rangle|^2}{\omega_{ra}-\omega}+\frac{|\langle r|e\,\boldsymbol{\epsilon}^*\cdot\boldsymbol{r}_\mathrm{e}|a\rangle|^2}{\omega_{ra}+\omega}\right). \tag{A7}$$

We now perform the rotating wave approximation with $\omega_{ra}+\omega \gg \omega_{ra}-\omega$ and introduce the detuning $\Delta=\omega-\omega_{ra}$. We use $\omega_{ra}^2 \approx \omega^2$ and obtain

$$U_r^{(1)} \approx \omega^2 |\boldsymbol{A}(\boldsymbol{r})|^2 \frac{|\langle r|e\,\boldsymbol{\epsilon}\cdot\boldsymbol{r}_\mathrm{e}|a\rangle|^2}{\hbar\Delta}. \tag{A8}$$

We express the dipole matrix elements in terms of the reduced dipole matrix element D_{ar} for our polarization $\boldsymbol{\epsilon}$ as

$$|\langle r|e\,\boldsymbol{\epsilon}\cdot\boldsymbol{r}_\mathrm{e}|a\rangle|^2 = \left|\langle r|\frac{e}{\sqrt{2}}(\hat{\boldsymbol{e}}_x+i\hat{\boldsymbol{e}}_y)\cdot\boldsymbol{r}_\mathrm{e}|a\rangle\right|^2 = \frac{1}{2}|\langle r|e(\boldsymbol{x}_\mathrm{e}+i\boldsymbol{y}_\mathrm{e})|a\rangle|^2 \tag{A9}$$

$$=: \frac{1}{2}\left|\frac{1}{2}\langle nS_{1/2}, J=1/2||d||6P_{3/2}, J=3/2\rangle\right|^2 \tag{A10}$$

$$=: \frac{1}{8}D_{ar}^2. \tag{A11}$$

We calculate the reduced dipole element of this transition using the ARC package [40]. By combining these results with the definition of the vector potential $\boldsymbol{A}(\boldsymbol{r})$, we arrive at Eq. (6) in the main text, which we write out as

$$U_r^{(1)} \approx -\frac{D_{ar}^2}{8\hbar\Delta}\omega^2|\boldsymbol{A}(\boldsymbol{r})|^2 = -\frac{D_{ar}^2}{16\hbar\Delta}[(E_\rightarrow(\boldsymbol{r})-E_\leftarrow(\boldsymbol{r}))^2+4E_\rightarrow(\boldsymbol{r})E_\leftarrow(\boldsymbol{r})\cos(\boldsymbol{kr})]. \tag{A12}$$

APPENDIX B: VECTOR POTENTIAL

The vector potential of Eq. (2) can be reformulated using trigonometric relations. Note that we assume that the field amplitude is homogeneous over the diameter of the Rydberg (ground-state) atom. Thus, we set $E_{\rightarrow(\leftarrow)}(\boldsymbol{r}+\boldsymbol{r}_\mathrm{e}) \approx E_{\rightarrow(\leftarrow)}(\boldsymbol{r})$. We then write

$$\begin{aligned}\omega\boldsymbol{A}(\boldsymbol{r}+\boldsymbol{r}_\mathrm{e},t) = {}& \sin(\boldsymbol{kr}_\mathrm{e})\boldsymbol{\epsilon}[E_\leftarrow(\boldsymbol{r})[\sin(\boldsymbol{kr})\sin(\omega t)-\cos(\boldsymbol{kr})\cos(\omega t)]+E_\rightarrow(\boldsymbol{r})[\sin(\boldsymbol{kr})\sin(\omega t)+\cos(\boldsymbol{kr})\cos(\omega t)]]\\ &+\cos(\boldsymbol{kr}_\mathrm{e})\boldsymbol{\epsilon}[E_\leftarrow(\boldsymbol{r})[-\sin(\boldsymbol{kr})\cos(\omega t)-\cos(\boldsymbol{kr})\sin(\omega t)]+E_\rightarrow(\boldsymbol{r})[\sin(\boldsymbol{kr})\cos(\omega t)-\cos(\boldsymbol{kr})\sin(\omega t)]].\end{aligned} \tag{B1}$$

The dependence of the electron radius $\boldsymbol{r}_\mathrm{e}$ is factored out now. Alternatively, the vector potential can be expressed as

$$\boldsymbol{A}(\boldsymbol{r}+\boldsymbol{r}_\mathrm{e},t) = \underbrace{\boldsymbol{\epsilon}\left(\frac{[E_\rightarrow(\boldsymbol{r})-E_\leftarrow(\boldsymbol{r})]}{2w}\sin[\boldsymbol{k}(\boldsymbol{r}+\boldsymbol{r}_\mathrm{e})]-\frac{i[E_\rightarrow(\boldsymbol{r})+E_\leftarrow(\boldsymbol{r})]}{2w}\cos[\boldsymbol{k}(\boldsymbol{r}+\boldsymbol{r}_\mathrm{e})]\right)}_{\boldsymbol{A}(\boldsymbol{r}+\boldsymbol{r}_\mathrm{e})} e^{-i\omega t}+\boldsymbol{A}^*(\boldsymbol{r}+\boldsymbol{r}_\mathrm{e})e^{i\omega t}, \tag{B2}$$

where $\boldsymbol{A}(\boldsymbol{r}+\boldsymbol{r}_\mathrm{e})$ is the time-independent vector potential. This representation is needed for the time-dependent perturbation theory using Floquet quasienergies. It follows,

$$\boldsymbol{A}^2(\boldsymbol{r}+\boldsymbol{r}_\mathrm{e},t) = \boldsymbol{A}^2(\boldsymbol{r}+\boldsymbol{r}_\mathrm{e})e^{-2i\omega t}+2\boldsymbol{A}(\boldsymbol{r}+\boldsymbol{r}_\mathrm{e})\boldsymbol{A}^*(\boldsymbol{r}+\boldsymbol{r}_\mathrm{e})+(\boldsymbol{A}^*)^2(\boldsymbol{r}+\boldsymbol{r}_\mathrm{e})e^{2i\omega t}. \tag{B3}$$

For the time-independent squared vector potential we obtain

$$\begin{aligned}4\omega^2|\boldsymbol{A}(\boldsymbol{r}+\boldsymbol{r}_\mathrm{e})|^2 = {}& E_\rightarrow(\boldsymbol{r})^2+E_\leftarrow(\boldsymbol{r})^2+2E_\rightarrow(\boldsymbol{r})E_\leftarrow(\boldsymbol{r})\cos(2\boldsymbol{kr}_\mathrm{e})(2\cos^2(\boldsymbol{kr})-1)\\ &-4E_\rightarrow(\boldsymbol{r})E_\leftarrow(\boldsymbol{r})\sin(2\boldsymbol{kr}_\mathrm{e})\sin(\boldsymbol{kr})\cos(\boldsymbol{kr}).\end{aligned} \tag{B4}$$

In the limit of $\boldsymbol{kr}_\mathrm{e} \rightarrow 0$, this expression reduces to

$$4\omega^2|\boldsymbol{A}(\boldsymbol{r})|^2 = 4E_\rightarrow(\boldsymbol{r})E_\leftarrow(\boldsymbol{r})\cos^2(\boldsymbol{kr})+[E_\rightarrow(\boldsymbol{r})-E_\leftarrow(\boldsymbol{r})]^2. \tag{B5}$$

[1] K.-J. Boller, A. Imamoğlu, and S. E. Harris, Observation of electromagnetically induced transparency, Phys. Rev. Lett. **66**, 2593 (1991).

[2] D. F. Phillips, A. Fleischhauer, A. Mair, R. L. Walsworth, and M. D. Lukin, Storage of light in atomic vapor, Phys. Rev. Lett. **86**, 783 (2001).

[3] C. Liu, Z. Dutton, C. H. Behroozi, and L. V. Hau, Observation of coherent optical information storage in an atomic medium using halted light pulses, Nature (London) **409**, 490 (2001).

[4] B. Zhao, Y.-A. Chen, X.-H. Bao, T. Strassel, C.-S. Chuu, X.-M. Jin, J. Schmiedmayer, Z.-S. Yuan, S. Chen, and J.-W. Pan, A millisecond quantum memory for scalable quantum networks, Nat. Phys. **5**, 95 (2009).

[5] A. I. Lvovsky, B. C. Sanders, and W. Tittel, Optical quantum memory, Nat. Photon. **3**, 706 (2009).

[6] S. Zhang, J. Shi, Z. Cui, Y. Wang, Y. Wu, L. Duan, and Y. Pu, Realization of a programmable multipurpose photonic quantum memory with over-thousand qubit manipulations, Phys. Rev. X **14**, 021018 (2024).

[7] C. P. Sun, S. Yi, and L. You, Decoherence of collective atomic spin states due to inhomogeneous coupling, Phys. Rev. A **67**, 063815 (2003).

[8] J. Simon, H. Tanji, J. K. Thompson, and V. Vuletić, Interfacing collective atomic excitations and single photons, Phys. Rev. Lett. **98**, 183601 (2007).

[9] S. Schmidt-Eberle, T. Stolz, G. Rempe, and S. Dürr, Dark-time decay of the retrieval efficiency of light stored as a Rydberg excitation in a noninteracting ultracold gas, Phys. Rev. A **101**, 013421 (2020).

[10] A. G. Radnaev, Y. O. Dudin, R. Zhao, H. H. Jen, S. D. Jenkins, A. Kuzmich, and T. A. B. Kennedy, A quantum memory with telecom-wavelength conversion, Nat. Phys. **6**, 894 (2010).

[11] Y. O. Dudin, L. Li, and A. Kuzmich, Light storage on the time scale of a minute, Phys. Rev. A **87**, 031801(R) (2013).

[12] M. Fleischhauer and M. D. Lukin, Dark-state polaritons in electromagnetically induced transparency, Phys. Rev. Lett. **84**, 5094 (2000).

[13] M. D. Lukin, M. Fleischhauer, R. Cote, L. M. Duan, D. Jaksch, J. I. Cirac, and P. Zoller, Dipole blockade and quantum information processing in mesoscopic atomic ensembles, Phys. Rev. Lett. **87**, 037901 (2001).

[14] T. Peyronel, O. Firstenberg, Q.-Y. Liang, S. Hofferberth, A. V. Gorshkov, T. Pohl, M. D. Lukin, and V. Vuletić, Quantum nonlinear optics with single photons enabled by strongly interacting atoms, Nature (London) **488**, 57 (2012).

[15] Y. O. Dudin and A. Kuzmich, Strongly interacting Rydberg excitations of a cold atomic gas, Science **336**, 887 (2012).

[16] O. Firstenberg, T. Peyronel, Q.-Y. Liang, A. V. Gorshkov, M. D. Lukin, and V. Vuletić, Attractive photons in a quantum nonlinear medium, Nature (London) **502**, 71 (2013).

[17] D. Maxwell, D. J. Szwer, D. Paredes-Barato, H. Busche, J. D. Pritchard, A. Gauguet, K. J. Weatherill, M. P. A. Jones, and C. S. Adams, Storage and control of optical photons using Rydberg polaritons, Phys. Rev. Lett. **110**, 103001 (2013).

[18] C. Tresp, C. Zimmer, I. Mirgorodskiy, H. Gorniaczyk, A. Paris-Mandoki, and S. Hofferberth, Single-photon absorber based on strongly interacting Rydberg atoms, Phys. Rev. Lett. **117**, 223001 (2016).

[19] H. Busche, P. Huillery, S. W. Ball, T. Ilieva, M. P. A. Jones, and C. S. Adams, Contactless nonlinear optics mediated by long-range Rydberg interactions, Nat. Phys. **13**, 655 (2017).

[20] L. Drori, B. C. Das, T. D. Zohar, G. Winer, E. Poem, A. Poddubny, and O. Firstenberg, Quantum vortices of strongly interacting photons, Science **381**, 193 (2023).

[21] S. K. Dutta, J. R. Guest, D. Feldbaum, A. Walz-Flannigan, and G. Raithel, Ponderomotive optical lattice for Rydberg atoms, Phys. Rev. Lett. **85**, 5551 (2000).

[22] H. A. H. Boot and R. B. R.-S.-Harvie, Charged particles in a non-uniform radio-frequency field, Nature (London) **180**, 1187 (1957).

[23] D. L. Freimund, K. Aflatooni, and H. Batelaan, Observation of the Kapitza-Dirac effect, Nature (London) **413**, 142 (2001).

[24] M. Saffman and T. G. Walker, Analysis of a quantum logic device based on dipole-dipole interactions of optically trapped Rydberg atoms, Phys. Rev. A **72**, 022347 (2005).

[25] D. Barredo, V. Lienhard, P. Scholl, S. de Léséleuc, T. Boulier, A. Browaeys, and T. Lahaye, Three-dimensional trapping of individual Rydberg atoms in ponderomotive bottle beam traps, Phys. Rev. Lett. **124**, 023201 (2020).

[26] B. Ravon, P. Méhaignerie, Y. Machu, A. D. Hernández, M. Favier, J. M. Raimond, M. Brune, and C. Sayrin, Array of individual circular Rydberg atoms trapped in optical tweezers, Phys. Rev. Lett. **131**, 093401 (2023).

[27] T. Topcu and A. Derevianko, Intensity landscape and the possibility of magic trapping of alkali-metal Rydberg atoms in infrared optical lattices, Phys. Rev. A **88**, 043407 (2013).

[28] C. Hölzl, A. Götzelmann, E. Pultinevicius, M. Wirth, and F. Meinert, Long-lived circular Rydberg qubits of alkaline-earth atoms in optical tweezers, Phys. Rev. X **14**, 021024 (2024).

[29] E. A. Goldschmidt, D. G. Norris, S. B. Koller, R. Wyllie, R. C. Brown, J. V. Porto, U. I. Safronova, and M. S. Safronova, Magic wavelengths for the $5s$–$18s$ transition in rubidium, Phys. Rev. A **91**, 032518 (2015).

[30] J. Lampen, H. Nguyen, L. Li, P. R. Berman, and A. Kuzmich, Long-lived coherence between ground and Rydberg levels in a magic-wavelength lattice, Phys. Rev. A **98**, 033411 (2018).

[31] We adjust the final atom number by varying the initial magneto-optical trap loading parameters. For $n > 70$ we use lower atomic densities to reduce the formation of Rydberg molecules as discussed later in the main text. As we vary n we thereby also reduce density-dependent dephasing [47,48].

[32] C. Glaser, F. Karlewski, J. Kluge, J. Grimmel, M. Kaiser, A. Günther, H. Hattermann, M. Krutzik, and J. Fortágh, Absolute frequency measurement of rubidium $5S-6P$ transitions, Phys. Rev. A **102**, 012804 (2020).

[33] H. Nguyen, J. Lampen, P. R. Berman, and A. Kuzmich, Differential nuclear-spin-dependent light shifts and state mixing of Rydberg atoms, Phys. Rev. A **100**, 033412 (2019).

[34] L. Li, Y. O. Dudin, and A. Kuzmich, Entanglement between light and an optical atomic excitation, Nature (London) **498**, 466 (2013).

[35] N. B. Delone and V. P. Krainov, *Atoms in Strong Light Fields*, 1st ed., Springer Series in Chemical Physics (Springer, Berlin, 1985).

[36] V. Novičenko, E. Anisimovas, and G. Juzeliūnas, Floquet analysis of a quantum system with modulated periodic driving, Phys. Rev. A **95**, 023615 (2017).

[37] T. Topcu and A. Derevianko, Dynamic polarizability of Rydberg atoms: Applicability of the near-free-electron approximation, gauge invariance, and the Dirac sea, Phys. Rev. A **88**, 042510 (2013).

[38] R. Grimm, M. Weidemüller, and Y. B. Ovchinnikov, Optical Dipole Traps for Neutral Atoms, in *Advances In Atomic, Molecular, and Optical Physics*, Vol. 42, edited by B. Bederson and H. Walther (Academic Presss, New York, 2000), pp. 95–170.

[39] *Springer Handbook of Atomic, Molecular, and Optical Physics*, Springer Handbooks, edited by G. W. F. Drake (Springer, Cham, Switzerland, 2023).

[40] E. J. Robertson, N. Šibalić, R. M. Potvliege, and M. P. A. Jones, ARC 3.0: An expanded Python toolbox for atomic physics calculations, Comput. Phys. Commun. **261**, 107814 (2021).

[41] M. Fleischhauer and M. D. Lukin, Quantum memory for photons: Dark-state polaritons, Phys. Rev. A **65**, 022314 (2002).

[42] I. Mirgorodskiy, F. Christaller, C. Braun, A. Paris-Mandoki, C. Tresp, and S. Hofferberth, Electromagnetically induced transparency of ultra-long-range Rydberg molecules, Phys. Rev. A **96**, 011402(R) (2017).

[43] C. H. Greene, A. S. Dickinson, and H. R. Sadeghpour, Creation of polar and nonpolar ultra-long-range Rydberg molecules, Phys. Rev. Lett. **85**, 2458 (2000).

[44] V. Bendkowsky, B. Butscher, J. Nipper, J. P. Shaffer, R. Löw, and T. Pfau, Observation of ultralong-range Rydberg molecules, Nature (London) **458**, 1005 (2009).

[45] N. B. Delone and V. P. Krainov, AC Stark shift of atomic energy levels, Phys. Usp. **42**, 669 (1999).

[46] M. Traini, Electric polarizability of the hydrogen atom: A sum rule approach, Eur. J. Phys. **17**, 30 (1996).

[47] S. Baur, D. Tiarks, G. Rempe, and S. Dürr, Single-photon switch based on Rydberg blockade, Phys. Rev. Lett. **112**, 073901 (2014).

[48] A. Gaj, A. T. Krupp, J. B. Balewski, R. Löw, S. Hofferberth, and T. Pfau, From molecular spectra to a density shift in dense Rydberg gases, Nat. Commun. **5**, 4546 (2014).

[49] https://doi.org/10.5281/zenodo.14003106.

Correction: A sign error in Eq. (2) has been fixed.

A.5. [P5] - Resonant stroboscopic Rydberg dressing: Electron-motion coupling and multibody interactions

Letter

Resonant stroboscopic Rydberg dressing: Electron-motion coupling and multibody interactions

Chris Nill [1,2] Sylvain de Léséleuc [3,4] Christian Groß [5] and Igor Lesanovsky [1,6]

[1]*Institut für Theoretische Physik and Center for Integrated Quantum Science and Technology, Universität Tübingen, Auf der Morgenstelle 14, 72076 Tübingen, Germany*

[2]*Institute for Applied Physics, University of Bonn, Wegelerstraße 8, 53115 Bonn, Germany*

[3]*Institute for Molecular Science, National Institutes of Natural Sciences, 444-8585 Okazaki, Japan*

[4]*RIKEN Center for Quantum Computing (RQC), 351-0198 Wako, Japan*

[5]*Physikalisches Institut and Center for Integrated Quantum Science and Technology, Universität Tübingen, Auf der Morgenstelle 14, 72076 Tübingen, Germany*

[6]*School of Physics and Astronomy and Centre for the Mathematics and Theoretical Physics of Quantum Non-Equilibrium Systems, The University of Nottingham, Nottingham NG7 2RD, United Kingdom*

(Received 4 December 2024; accepted 14 April 2025; published 29 April 2025)

Rydberg dressing traditionally refers to a technique where interactions between cold atoms are imprinted through the far off-resonant continuous-wave excitation of high-lying Rydberg states. Dipolar interactions between these electronic states are then translated into effective interactions among ground-state atoms. Motivated by recent experiments, we investigate two dressing protocols, in which Rydberg atoms are resonantly excited in a stroboscopic fashion. The first one is nonadiabatic, meaning Rydberg states are excited by short pulses. In this case, mechanical forces among Rydberg atoms result in electron-motion coupling, which generates effective multibody interactions. In the second, adiabatic protocol, Rydberg states are excited by smoothly varying laser pulses. We show that also, in this protocol, substantial multibody interactions emerge.

DOI: 10.1103/PhysRevA.111.L041104

Introduction. Many current quantum simulation and computation platforms based on trapped ultracold atoms harness the properties of electronic Rydberg states [1–9]. These are highly excited states in which atoms are strongly polarizable and thus can interact over long distances. These interactions are typically orders of magnitude stronger than those between ground-state atoms. Additionally, the short lifetime of Rydberg states is incompatible with the timescales of ultracold quantum dynamics. Rydberg dressing is a way to overcome this problem [10,11]. In this process, the ground state of ultracold atoms is coupled to a Rydberg state via a far-detuned continuous-wave laser. This weak admixture of the Rydberg state enables sufficiently strong interactions and longer lifetimes, allowing for quantum simulations of novel phases, phase transitions, and dynamics [12–18].

Recent developments have shown that stroboscopic dressing schemes may offer advantages over the conventional Rydberg dressing approach. The underlying idea is related to earlier works which employ external periodic driving to shape dynamical processes in cold atomic gases [19–26]. In stroboscopic dressing, Rydberg states are excited periodically using laser pulses, rather than through continuous off-resonant excitation. This ensures that Rydberg states are populated only during discrete intervals, reducing overall interaction time and aligning the dynamics with the slower timescales of ultracold atoms. Pulsed excitation protocols have also been studied in Refs. [27,28] for realizing Floquet systems based on PXP models [29–31], where the Rydberg blockade prevents the simultaneous excitation of nearby Rydberg atoms.

In this work, we study theoretically resonant stroboscopic Rydberg dressing in a cold-atom tweezer array [5]. Specifically, we focus on two protocols, with the aim of creating effective spin Hamiltonians: the first involves short pulses, which break the Rydberg blockade [32–37]. In this case, the coupling between electronic excitation and the mechanical motion of atoms within their traps generates controllable spin-motion entanglement and multibody interactions that cannot be reduced to a sum of two-body terms [38,39]. The second protocol relies on slow adiabatic pulses. Here, the strength of the effectively generated multibody interactions is controlled by the detuning of the Rydberg excitation laser and the spatial separation between the atoms.

General model. We consider ultracold atoms of mass m confined in optical tweezers, as shown in Fig. 1(a), in which they perform quantized oscillatory motion, characterized by the trap frequency ω and the displacement coordinate x_j. The equilibrium distance between two neighboring atoms is a_0. The electronic degrees of freedom of each atom are modeled by two long-lived ground states ($|\downarrow\rangle$, $|\uparrow\rangle$), which form a fictitious spin, along with the Rydberg state $|r\rangle$. Rydberg atoms separated by the distance x interact with the potential $V(x)$. Considering only interactions between nearest neighbors, the Hamiltonian of this system is given by ($\hbar = 1$)

$$H_0 = \omega \sum_j a_j^\dagger a_j + V \sum_j n_j n_{j+1} + G \sum_j n_j n_{j+1}(x_j - x_{j+1}). \tag{1}$$

Here $n_j = |r\rangle\langle r|_j$ is the projector on the Rydberg state of atom j, $V = V(a_0)$ is the interaction energy between nearest-neighbor Rydberg atoms, and $G = \partial V(x)/\partial x|_{x=a_0}$ is the corresponding potential gradient [40]. The latter gives

 ©2025 American Physical Society

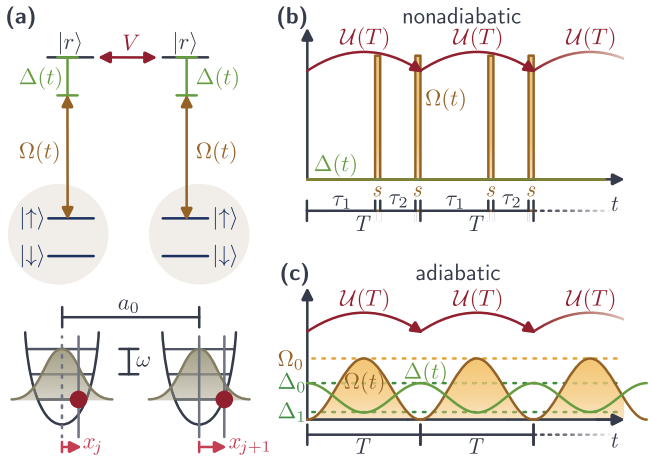

FIG. 1. Atomic levels and dressing protocols. (a) Two atoms trapped in tweezers which are modeled as one-dimensional harmonic oscillators with trapping frequency ω. Their equilibrium separation is a_0, and the displacement from their individual equilibrium positions is given by x_j and x_{j+1}, respectively. Each atom is modeled by two long-lived ground states ($|\uparrow\rangle, |\downarrow\rangle$) and a Rydberg state $|r\rangle$. Neighboring atoms in the state $|r\rangle$ interact with the strength V. A globally applied laser couples $|\uparrow\rangle$ and $|r\rangle$ with the time-dependent Rabi frequency $\Omega(t)$ and the detuning $\Delta(t)$. (b) The dressing protocols consist of periodic sequences of pulses of length T. In the nonadiabatic dressing protocol, two short π pulses of duration s are applied, which break the Rydberg blockade [see Eq. (3)]. In between the two pulses, interacting Rydberg states are excited, which generates effective interactions among atoms in the state $|\uparrow\rangle$. (c) In the adiabatic dressing protocol, the Rabi frequency $\Omega(t)$ and the detuning $\Delta(t)$ are varied smoothly [see Eqs. (9) and (10)]. Rydberg states are excited during the pulses, but deexcited at the end. Dynamical phases accumulated during this process translate into effective interactions among atoms in the state $|\uparrow\rangle$.

rise to a coupling between electronic and motional degrees of freedom, which are represented through raising and lowering operators: $x_j = x_0(a_j + a_j^\dagger)$, with the harmonic oscillator length $x_0 = \sqrt{1/(2m\omega)}$.

The idea of Rydberg dressing is to generate effective interactions among atoms in the state $|\uparrow\rangle$ (see Fig. 1) by virtually or temporarily coupling this state to the Rydberg level $|r\rangle$. This coupling is achieved by a laser with the time-dependent detuning (with respect to the $|\uparrow\rangle$-$|r\rangle$ transition) $\Delta(t)$ and the Rabi frequency $\Omega(t)$. This laser coupling is described by the Hamiltonian [41]

$$H_{\rm L}(t) = \Omega(t)\sum_j (|\uparrow\rangle\langle\uparrow|r_j e^{-i\kappa x_j} + \text{H.c.}) + \Delta(t)\sum_j n_j, \quad (2)$$

where κ is the projection of the laser wave vector onto the axis connecting neighboring atoms (we assume here that the atoms are positioned on a one-dimensional (1D) chain in the x direction). In this work, we consider stroboscopic dressing pulses, i.e., the laser parameters $\Delta(t)$ and $\Omega(t)$, are periodic functions with period T, as shown in Fig. 1. Our goal is to derive expressions for the time-evolution operator $\mathcal{U}(T)$ that propagates the system from the stroboscopic time nT to $(n+1)T$. Rydberg states will only be excited during the dressing pulses, but (ideally) Rydberg excitations are present neither in the initial state nor in the states which the system assumes at the end of each pulse. Therefore, the time-evolution operator $U(T)$ only operates in the $|\uparrow\rangle$-$|\downarrow\rangle$ manifold and is generated by an effective spin Hamiltonian, which we construct in the following for two different dressing protocols.

Nonadiabatic dressing protocol. This protocol, which is shown in Fig. 1(b), consists of two short resonant π pulses applied during a dressing cycle. Each pulse has duration s; one is applied at time τ_1 and the other at time $T - s$. Mathematically, this sequence is modeled by choosing the parameters of the laser Hamiltonian (2) as $\Delta(t) = 0$ and

$$\Omega(t) = \frac{\pi}{2s}\left[\Pi_{\tau_1,\tau_1+s}(t) + \Pi_{T-s,T}(t)\right], \quad (3)$$

where $\Pi_{a,b}(t) = \Theta(t-a) - \Theta(t-b)$ and Θ is the Heaviside step function. One dressing cycle can be decomposed as follows. The system starts at $t = 0$ in a spin state, $|\psi_0\rangle$, where no Rydberg excitations are present. During the time interval $0 \leqslant t \leqslant \tau_1$, the system evolves under the Hamiltonian H_0, Eq. (1), since the laser Hamiltonian H_L is 0. No Rydberg excitations are created, since H_0 conserves the total excitation number. The first π pulse excites all $|\uparrow\rangle$ states to the Rydberg state $|r\rangle$. This assumes that the pulse is sufficiently strong in order to overcome the interaction among Rydberg atoms; i.e., it needs to break the Rydberg blockade, which is possible when $V \ll \pi/(2s)$. Note that this process may also lead to oscillatory excitations due to momentum transfer from the laser to the atoms. In the following time interval of length τ_2, nearest-neighbor atoms in the Rydberg state interact, and further coupling between the electronic and motional degrees of freedom occurs. The dressing cycle concludes with a second π pulse, applied during the time interval $T - s \leqslant t \leqslant T$, that deexcites the Rydberg states.

The time-evolution operator which propagates the system over a dressing cycle of duration T can be expressed as a product of unitary operators. For a general pulse duration s, this is

$$\mathcal{U}(T,s) = e^{-is(H_{\rm L}+H_0)}e^{-iH_0\tau_2}e^{-is(H_{\rm L}+H_0)}e^{-iH_0\tau_1}. \quad (4)$$

In the limit of short π pulses, i.e., for pulses in which $s \ll t_0$ is smaller than any timescale t_0 in the free evolution due to H_0, the time-evolution operator can be calculated analytically [42], yielding

$$\mathcal{U}(T) = \prod_j e^{-iTH_{j,\rm eff}}\mathcal{D}(\mathcal{J}_j)e^{-iT\omega a_j^\dagger a_j}. \quad (5)$$

We note that recent experiments [39,43] have demonstrated that this condition can indeed be met. In the following, we analyze the terms of $\mathcal{U}(T)$ step by step. We begin with the last term, $e^{-iT\omega a_j^\dagger a_j}$, which is the simplest one and describes the free oscillatory motion of the atoms in their traps over the length T of a dressing cycle. The first term of $\mathcal{U}(T)$ is the evolution under the effective spin Hamiltonian $H_{j,\rm eff}$, which describes the time evolution of the spin at site j during a dressing cycle as

$$H_{j,\rm eff} = \frac{\tau_2 V}{T}\mathcal{P}_j\mathcal{P}_{j+1} + \frac{\tau_2}{T}\frac{\mathcal{G}_j^2}{\omega}[\text{sinc}(\omega\tau_2) - 1] + \frac{\eta^2\sin(\omega\tau_2)}{T}\mathcal{P}_j + \frac{\pi}{T}\mathcal{P}_j. \quad (6)$$

Here, the first term is the "conventional" dressing potential, i.e., the interaction V among Rydberg atoms in Hamiltonian (6), is mapped onto atoms in the $|\uparrow\rangle$ state but with the weaker effective strength $V_{\text{eff}} = \tau_2 V/T$ and the projector $\mathcal{P}_j = |\uparrow\rangle\langle\uparrow|_j$. The factor of τ_2/T is the proportion of the time during which the system is in the Rydberg state during a dressing cycle. Further terms emerge in the effective spin Hamiltonian, with the next one being an interaction that is mediated by the oscillation of the atoms in their tweezer traps. It depends on the gradient G and the oscillator length x_0 through the operator

$$\mathcal{G}_j = \begin{cases} Gx_0\mathcal{P}_j\mathcal{P}_{j+1}, & \text{for } N = 2, \\ Gx_0\mathcal{P}_j(\mathcal{P}_{j+1} - \mathcal{P}_{j-1}), & \text{for } N > 2. \end{cases} \tag{7}$$

For two atoms, this contribution, which is generated by the coupling between electronic and motional degrees of freedom, merely modifies the interaction strength between atoms in the $|\uparrow\rangle$ state. For more than two atoms, however, it results in a multibody interaction [44,45]. This can be understood as follows: when an atom j is surrounded by two or no atoms in the $|\uparrow\rangle$ state, the net mechanical force acting on it when excited to the $|\uparrow\rangle$ state is 0. Hence, $\mathcal{G}_j = 0$. For other configurations, $\mathcal{G}_j$ assumes a nonzero value. Distinguishing these cases necessitates an operator which acts on site j as well as on the two neighboring sites, hence generating a three-body interaction. The term $\eta^2 \sin(\omega\tau_2)\mathcal{P}_j/T$ in the effective Hamiltonian accounts for the momentum transfer during laser excitation. It is quantified by the Lamb-Dicke parameter $\eta = \kappa x_0$ [46–48]. The last term, $\frac{\pi}{T}\mathcal{P}_j$, arises due to the application of two π pulses during the dressing cycle, which leads to a phase shift of π for all atoms in the state $|\uparrow\rangle$.

Let us now return to the middle term of the unitary evolution operator (5). It depends on the displacement operator $\mathcal{D}(\mathcal{J}_j) = \exp \mathcal{J}_j a_j^\dagger - \mathcal{J}_j^\dagger a_j$, with argument $\mathcal{J}_j = (\frac{\mathcal{G}_j}{\omega} + i\eta\mathcal{P}_j)(e^{-i\omega\tau_2} - 1)$. It displaces atom j in position (momentum) space by the real (imaginary) part of $\mathcal{J}_j$, which is an operator that acts on the spin degrees of freedom [49]. This term therefore results in spin-motion coupling. The amount of the displacement further depends on the oscillation phase $\omega\tau_2$, which can be utilized to control the spin-motion coupling. If the oscillation phase is 0 or a multiple of 2π, $\mathcal{J}_j$ vanishes and spin and motional degrees of freedom decouple.

For a dressing cycle with such decoupled spin and motion, the time-evolution operator separates into an operator acting on the spins,

$$\mathcal{U}_{\text{spin}}(T) = \prod_j e^{-iTH_{j,\text{eff}}}, \tag{8}$$

and one acting on the harmonic oscillatory motion of the atoms, $\mathcal{U}_{\text{osc}} = \prod_j e^{-iT\omega a_j^\dagger a_j}$. However, multibody interactions still remain in the effective spin Hamiltonian due to its dependence on $\mathcal{G}_j^2$.

To illustrate the effect of the spin-motion coupling, we consider in Fig. 2 a system of two atoms which are initialized in the motional ground state $|0\rangle_j$. As the initial state, we choose $|\psi_0\rangle = \bigotimes_{j=1}^{N=2}[\frac{1}{\sqrt{2}}(|\uparrow\rangle_j + |\downarrow\rangle_j) \otimes |0\rangle_j]$, which is not an eigenstate of the effective spin Hamiltonian and thus leads to nontrivial dynamics. In the figure, we study the dynamics

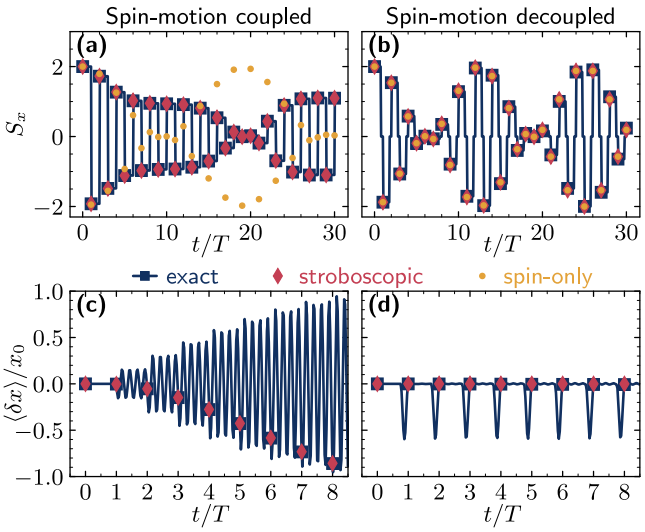

FIG. 2. Nonadiabatic dressing protocol. (a) Evolution of the expectation value of the total spin component S_x for two atoms (see text). Choosing $\omega\tau_2 = 0.01\pi$, the oscillatory motion is coupled to the spin dynamics. This leads to entanglement between the two degrees of freedom, causing spin decoherence (see Supplemental Material [42]). Numerically exact results calculated by $\mathcal{U}(T, s)$, Eq. (4), are shown as blue squares, and the stroboscopic evolution under the unitary $\mathcal{U}(T)$, Eq. (5), is shown as red diamonds. For comparison, we show the evolution of S_x in the absence of this spin-motion coupling calculated by Eq. (8) with yellow dots. The initial state $|\psi_0\rangle$ is defined in the main text. (b) When choosing $\omega\tau_2 = 2\pi$, spin and motion decouple. (c) Dynamics of the average interatomic distance $\langle\delta x\rangle$ (see text). For $\omega\tau_2 = 0.01\pi$, spin-motion coupling results in oscillations of the interatomic distance after a dressing cycle. (d) When choosing $\omega\tau_2 = 2\pi$, the motional degrees of freedom return to their initial state after each cycle. In all simulations the harmonic oscillator basis is truncated to contain a maximum of five excitations, and the parameters values are $T = 8.1\pi/\omega$, $V = 10.1\omega$, $\eta = 0.6$, and $s = \pi/(2 \times 10^4\omega)$. For panels (a) and (c), we use $Gx_0 = 5\omega$, and for panels (b) and (d), we set $Gx_0 = 0.3\omega$. Note that, in experiment, the values for V and G can, in fact, be tuned independently using microwave dressing of Rydberg states [50–53].

of two observables of the system: the expectation value of the x component of the total spin, $S_x = \sum_{j=1}^{N=2}\langle|\uparrow\rangle\langle\uparrow|\downarrow\rangle_j + |\downarrow\rangle\langle\downarrow|\uparrow\rangle_j\rangle$, and the expectation value of the distance $\langle\delta x\rangle/x_0 = \langle x_2 - x_1\rangle/x_0$ between the atoms. The time evolution of the observables is calculated numerically exactly through $\mathcal{U}(T, s)$ for finite π pulse length s, Eq. (4), and compared to the time evolution operator $\mathcal{U}(T)$ in the short-pulse limit $s \ll t_0$, Eq. (5). For $\omega\tau_2 = 2\pi$, both degrees of freedom perform a separable evolution, where the spins perform oscillations in the observable S_x. Conversely, spins and motion couple when $\omega\tau_2 = 0.1\pi$, which results in a nontrivial spin-dynamic of S_x compared to the spin-only dynamics. This is shown in Figs. 2(a) and 2(b), where we display the behavior of the spin observable S_x as a function of time for both cases. Spin-motion coupling also affects the evolution of the distance $\langle\delta x\rangle$ between the atoms: With spin-motion coupling, the distance varies strongly at each stroboscopic time step nT, while it remains constant in the decoupled case [see Figs. 2(c) and 2(d)]. To approximately decouple spin and motion, one can

scale the time interval τ_2 between the pulses to yield $\omega\tau_2 \ll 1$ (while adjusting V such that $V_{\text{eff}} = V\tau_2/T$ remains on the order of unity). Dressing with such ultrastrong laser pulses has been experimentally demonstrated in Refs. [39,43]. We discuss this special case in the Supplemental Material [42]. There, we also illustrate how a spin-motion echo sequence can decouple spin and motional dynamics.

Adiabatic dressing protocol. This dressing protocol employs slowly changing laser parameters rather than short pulses. It is sketched in Fig. 1(c). The time evolution during a dressing cycle of length T is assumed to be adiabatic, in the sense that the spin state at its beginning and its end is the same. Moreover, the state shall be smoothly connected to the instantaneous eigenstates during the adiabatic pulse, which contain components of Rydberg states. This necessity to be slow, i.e., to avoid nonadiabatic transitions, is in conflict with the finite lifetimes of Rydberg states. Hence, an appropriate parameter regime needs to be identified that ensures pulses which are much shorter than the Rydberg atom's lifetime. This is indeed possible, as shown in the Supplemental Material [42]. There, we additionally show that, for strongly trapped atoms, one can neglect the coupling between the electronic degrees of freedom and the oscillatory motion [54–62]. For simplicity, and to make the calculations tractable, we disregard spin-motion coupling in the following, setting the potential gradient G and the Lamb-Dicke parameter η to 0.

In the adiabatic dressing protocol, the Rabi frequency and the detuning are smoothly varied according to Fig. 3(a) as

$$\Omega(t) = \Omega_0 \sin^2(\pi t/T), \tag{9}$$

$$\Delta(t) = \Delta_0 - (\Delta_0 - \Delta_1)\sin^2(\pi t/T). \tag{10}$$

The dynamical phase that is accumulated during this pulse differs for each spin configuration and yields an effective Hamiltonian in the spin space which in general contains multibody interactions. As an example, we consider a system with $N = 3$ atoms positioned in an equilateral triangle whose sides have the length a_0. The effective spin Hamiltonian can generally be written in terms of the projectors $\mathcal{P}_j = |{\uparrow}\rangle\langle{\uparrow}|_j$:

$$H_{\text{eff}} = \mathcal{V}_3\mathcal{P}_1\mathcal{P}_2\mathcal{P}_3 + \mathcal{V}_2\sum_{i\neq j}\mathcal{P}_i\mathcal{P}_j + \mathcal{V}_1\sum_i \mathcal{P}_i + \mathcal{V}_0, \tag{11}$$

where $\mathcal{V}_k$ describes the effective k-body interaction strength. The evolution under this effective spin Hamiltonian over a time T then generates the dynamical phase $\varphi_{\mathcal{C}}$ of the spin configuration $\mathcal{C} \in \{{\downarrow\downarrow\downarrow}, {\downarrow\downarrow\uparrow}, \ldots, {\uparrow\uparrow\uparrow}\}$:

$$e^{-iH_{\text{eff}}T} = \sum_{\mathcal{C}} e^{-i\varphi_{\mathcal{C}}}|\mathcal{C}\rangle\langle\mathcal{C}|. \tag{12}$$

Comparing coefficients, we can now link the k-body interaction strength to the dynamical phases. Due to the symmetry of the system, the phases $\varphi_{\mathcal{C}}$ depend only on $|{\uparrow}\rangle$ spins that are contained in configuration $\mathcal{C}$. We thus use a shorthand notation, φ_α, where the subscript α refers to the number of atoms in the $|{\uparrow}\rangle$ state; i.e., we have $\varphi_{\downarrow\downarrow\downarrow} = \varphi_0$, $\varphi_{\uparrow\downarrow\downarrow} = \varphi_{\downarrow\uparrow\downarrow} = \varphi_{\downarrow\downarrow\uparrow} = \varphi_\uparrow$, etc. With this, we obtain

$$\begin{aligned} \mathcal{V}_0 T &= \varphi_0, & \mathcal{V}_1 T &= \varphi_\uparrow - \varphi_0, \\ \mathcal{V}_2 T &= \varphi_{\uparrow\uparrow} - 2\varphi_\uparrow + \varphi_0, & \mathcal{V}_3 T &= \varphi_{\uparrow\uparrow\uparrow} - 3\varphi_{\uparrow\uparrow} + 3\varphi_\uparrow - \varphi_0. \end{aligned} \tag{13}$$

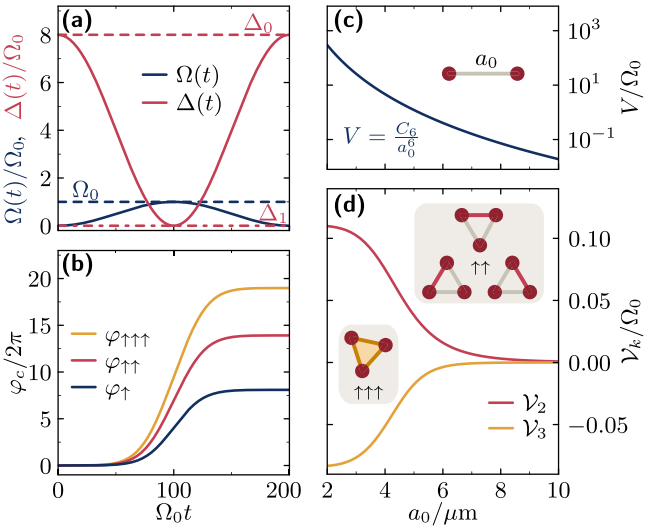

FIG. 3. Adiabatic dressing protocol. (a) Time-dependent Rabi frequency $\Omega(t)$ and detuning $\Delta(t)$ for a dressing cycle with duration $T = 200/\Omega_0$, where $\Delta_0 = 8\Omega_0$ and $\Delta_1 = 0$. (b) Accumulated dynamical phase $\varphi_{\mathcal{C}}$ in a system of three atoms placed on an equilateral triangle. Here, the initial configurations $\mathcal{C}$ need to be distinguished only by their number of atoms in the $|{\uparrow}\rangle$ state. The interaction strength is $V = 4\Omega_0$. (c) Bare van der Waals interaction between Rydberg atoms as a function of the interatomic distance a_0. We use the dispersion coefficient $C_6 = 119$ GHZ μm^6 of state $61S_{1/2}$ of potassium with the Rabi frequency $\Omega_0 = 2\pi \times 1$ MHz. (d) Effective two- and three-body interaction strength, $\mathcal{V}_2$ and $\mathcal{V}_3$, for varying interatomic distance a_0. The calculation is based on the bare van der Waals interaction shown in panel (c). The closer the interatomic distance, the higher is the relative contribution of the three-body interaction $\mathcal{V}_3$.

In the following, we construct the effective spin Hamiltonian (11) for an exemplary case and show that indeed rather generically three-body interactions emerge.

Using numerical integration [63], we solve for each initial state from $\mathcal{C}$ the time-dependent Schrödinger equation with the Hamiltonian $H(t) = H_0 + H_{\text{L}}(t)$ [Eqs. (1) and (2)] and the adiabatic pulse [Eqs. (9) and (10)]. We then extract the adiabatically accumulated dynamical phase $\varphi_{\mathcal{C}}$ as a function of the laser parameters and the interaction strength V. An example is shown in Fig. 3(b). From these phases, we can then calculate the interaction coefficients $\mathcal{V}_k$ using the above-described procedure. We assume here that the bare interaction between atoms in Rydberg states is given by a van der Waals interaction of the form $V = C_6/a_0^6$ [see Fig. 3(c)], where C_6 is the dispersion coefficient [64]. Based on this, we calculate the effective k-body interaction strength as a function of the interatomic distance a_0, which is shown in Fig. 3(d). This results in two- and three-body potentials, which have a characteristic flat-top form [65]. The larger the interparticle separation, i.e., the smaller the bare interaction V, the more dominant becomes the two-body interaction. A detailed analysis of the ratio $\mathcal{V}_3/\mathcal{V}_2$ is outlined in the Supplemental Material [42].

Conclusions and outlook. We discussed the theory underlying two stroboscopic Rydberg dressing protocols for generating effective spin Hamiltonians. The nonadiabatic protocol relies on the application of fast resonant laser pulses

which break the Rydberg blockade. This results in state-dependent mechanical forces causing a coupling between motional and electronic degrees of freedom. As a consequence, effective multibody spin interactions are generated, but also spin decoherence emerges which can be mitigated by an appropriate timing of the laser pulses. The adiabatic protocol, on the other hand, is implemented by smoothly varying laser pulses. During the adiabatic evolution, the system probes interacting configurations of Rydberg atoms, which generate spin-dependent dynamical phases resulting in effective k-body spin interactions. For a system of three atoms, we analyzed two-body and three-body interactions and their dependence on the interparticle distance.

There are a number of avenues for interesting future work. The considerations of this Letter are based on simple 1D and 2D systems, and the effect of different lattice geometries and multidimensional oscillatory excitations certainly merits further exploration. Additionally, quantum optimal control techniques may allow engineering stroboscopic dressing protocols that reduce spin-motion coupling or enhance adiabaticity while minimizing spin decoherence. In particular, it would be interesting to explore whether two-body interactions could be completely removed, leading to many-body Hamiltonians that feature solely multibody interactions.

Acknowledgments. We thank W. Martins, A. Cabot, and J. Wilkinson for fruitful discussions. We acknowledge funding from the Deutsche Forschungsgemeinschaft within Project No. GR4741/4 and the research units FOR5413 (Grant No. 465199066) and FOR5522 (Grant No. 499180199). This work builds on ideas which were developed when applying to the JST-DFG 2024: Japanese-German Joint Call for Proposals on "Quantum Technologies" (Japan-JST-DFG-ASPIRE 2024) and for which funding will be received under DFG Grant No. 554561799. We also acknowledge funding from the Horizon Europe programme HORIZON-CL4-2022-QUANTUM-02-SGA via Project No. 101113690 (PASQuanS2.1) and via the Horizon-MSCA-Doctoral Network QLUSTER (HORIZON-MSCA-2021-DN-01-GA101072964), the Alfried Krupp von Bohlen and Halbach Foundation, and the state of Baden-Württemberg through bwHPC Grant No. INST 40/575-1 FUGG (JUSTUS 2 cluster). S.d.L. acknowledges funding from the MEXT Quantum Leap Flagship Program (MEXT Q-LEAP) under Grant No. JPMXS0118069021 and JST Moonshot R&D Program Grant No. JPMJMS2269. C.G. and S.d.L. acknowledge funding from the NINS-DAAD exchange program (Quantum Simulation/Computation: From Rydberg Dressing to Ultrafast Interaction).

[1] T. F. Gallagher, *Rydberg Atoms*, Cambridge Monographs on Atomic, Molecular and Chemical Physics (Cambridge University, Cambridge, England, 1994).

[2] M. Saffman, T. G. Walker, and K. Mølmer, Quantum information with Rydberg atoms, Rev. Mod. Phys. **82**, 2313 (2010).

[3] H. Bernien, S. Schwartz, A. Keesling, H. Levine, A. Omran, H. Pichler, S. Choi, A. S. Zibrov, M. Endres, M. Greiner, V. Vuletić, and M. D. Lukin, Probing many-body dynamics on a 51-atom quantum simulator, Nature (London) **551**, 579 (2017).

[4] M. Morgado and S. Whitlock, Quantum simulation and computing with Rydberg-interacting qubits, AVS Quantum Sci. **3**, 023501 (2021).

[5] A. Browaeys and T. Lahaye, Many-body physics with individually controlled Rydberg atoms, Nat. Phys. **16**, 132 (2020).

[6] W. Lee, M. Kim, H. Jo, Y. Song, and J. Ahn, Coherent and dissipative dynamics of entangled few-body systems of Rydberg atoms, Phys. Rev. A **99**, 043404 (2019).

[7] H. Levine, A. Keesling, G. Semeghini, A. Omran, T. T. Wang, S. Ebadi, H. Bernien, M. Greiner, V. Vuletić, H. Pichler, and M. D. Lukin, Parallel implementation of high-fidelity multiqubit gates with neutral atoms, Phys. Rev. Lett. **123**, 170503 (2019).

[8] M. Magoni, R. Joshi, and I. Lesanovsky, Molecular dynamics in Rydberg tweezer arrays: Spin-phonon entanglement and Jahn-Teller effect, Phys. Rev. Lett. **131**, 093002 (2023).

[9] J. T. Wilson, S. Saskin, Y. Meng, S. Ma, R. Dilip, A. P. Burgers, and J. D. Thompson, Trapping alkaline earth Rydberg atoms optical tweezer arrays, Phys. Rev. Lett. **128**, 033201 (2022).

[10] Y.-Y. Jau, A. M. Hankin, T. Keating, I. H. Deutsch, and G. W. Biedermann, Entangling atomic spins with a Rydberg-dressed spin-flip blockade, Nat. Phys. **12**, 71 (2016).

[11] J. Zeiher, R. van Bijnen, P. Schauß, S. Hild, J.-y. Choi, T. Pohl, I. Bloch, and C. Gross, Many-body interferometry of a Rydberg-dressed spin lattice, Nat. Phys. **12**, 1095 (2016).

[12] P. Fromholz, M. Tsitsishvili, M. Votto, M. Dalmonte, A. Nersesyan, and T. Chanda, Phase diagram of Rydberg-dressed atoms on two-leg triangular ladders, Phys. Rev. B **106**, 155411 (2022).

[13] R. M. W. van Bijnen and T. Pohl, Quantum magnetism and topological ordering via Rydberg dressing near Förster resonances, Phys. Rev. Lett. **114**, 243002 (2015).

[14] J. Zeiher, J.-y. Choi, A. Rubio-Abadal, T. Pohl, R. van Bijnen, I. Bloch, and C. Gross, Coherent many-body spin dynamics in a long-range interacting Ising chain, Phys. Rev. X **7**, 041063 (2017).

[15] A. Geißler, I. Vasić, and W. Hofstetter, Condensation versus long-range interaction: Competing quantum phases in bosonic optical lattice systems at near-resonant Rydberg dressing, Phys. Rev. A **95**, 063608 (2017).

[16] R. Khasseh, S. H. Abedinpour, and B. Tanatar, Phase diagram and dynamics of Rydberg-dressed fermions in two dimensions, Phys. Rev. A **96**, 053611 (2017).

[17] E. Guardado-Sanchez, P. T. Brown, D. Mitra, T. Devakul, D. A. Huse, P. Schauß, and W. S. Bakr, Probing the quench dynamics of antiferromagnetic correlations in a 2D quantum Ising spin system, Phys. Rev. X **8**, 021069 (2018).

[18] P. Weckesser, K. Srakaew, T. Blatz, D. Wei, D. Adler, S. Agrawal, A. Bohrdt, I. Bloch, and J. Zeiher, Realization of a Rydberg-dressed extended Bose Hubbard model, arXiv:2405.20128.

[19] P. J. Bardroff, I. Bialynicki-Birula, D. S. Krähmer, G. Kurizki, E. Mayr, P. Stifter, and W. P. Schleich, Dynamical localization: Classical vs quantum oscillations in momentum spread of cold atoms, Phys. Rev. Lett. **74**, 3959 (1995).

[20] R. Blümel, *Chaos in Atomic Physics*, Cambridge Monographs on Atomic, Molecular, and Chemical Physics, Vol. 10 (Cambridge University, Cambridge, England, 1997).

[21] M. Frasca, Strong laser–atom interaction as a quantum kicked dynamics, Phys. Lett. A **290**, 277 (2001).
[22] F. Haake, *Quantum Signatures of Chaos*, Springer Series in Synergetics, Vol. 54 (Springer, Berlin, 2010).
[23] F. L. Moore, J. C. Robinson, C. Bharucha, P. E. Williams, and M. G. Raizen, Observation of dynamical localization in atomic momentum transfer: A new testing ground for quantum chaos, Phys. Rev. Lett. **73**, 2974 (1994).
[24] F. L. Moore, J. C. Robinson, C. F. Bharucha, B. Sundaram, and M. G. Raizen, Atom optics realization of the quantum δ-kicked rotor, Phys. Rev. Lett. **75**, 4598 (1995).
[25] J. C. Robinson, C. F. Bharucha, K. W. Madison, F. L. Moore, B. Sundaram, S. R. Wilkinson, and M. G. Raizen, Can a single-pulse standing wave induce chaos in atomic motion? Phys. Rev. Lett. **76**, 3304 (1996).
[26] J. A. Yeazell, M. Mallalieu, and C. R. Stroud, Observation of the collapse and revival of a Rydberg electronic wave packet, Phys. Rev. Lett. **64**, 2007 (1990).
[27] N. U. Köylüoğlu, N. Maskara, J. Feldmeier, and M. D. Lukin, Floquet engineering of interactions and entanglement in periodically driven Rydberg chains, arXiv:2408.02741.
[28] J. Feldmeier, N. Maskara, N. U. Köylüoğlu, and M. D. Lukin, Quantum simulation of dynamical gauge theories in periodically driven Rydberg atom arrays, arXiv:2408.02733.
[29] P. Fendley, K. Sengupta, and S. Sachdev, Competing density-wave orders in a one-dimensional hard-boson model, Phys. Rev. B **69**, 075106 (2004).
[30] I. Lesanovsky and H. Katsura, Interacting Fibonacci anyons in a Rydberg gas, Phys. Rev. A **86**, 041601(R) (2012).
[31] A. Hudomal, J.-Y. Desaules, B. Mukherjee, G.-X. Su, J. C. Halimeh, and Z. Papić, Driving quantum many-body scars in the PXP model, Phys. Rev. B **106**, 104302 (2022).
[32] M. D. Lukin, M. Fleischhauer, R. Cote, L. M. Duan, D. Jaksch, J. I. Cirac, and P. Zoller, Dipole blockade and quantum information processing in mesoscopic atomic ensembles, Phys. Rev. Lett. **87**, 037901 (2001).
[33] J.-H. Choi, B. Knuffman, T. C. Liebisch, A. Reinhard, and G. Raithel, Cold Rydberg atoms, Adv. At. Mol. Opt. Phys. **54**, 131 (2007).
[34] M. Weidemüller, There can be only one, Nat. Phys. **5**, 91 (2009).
[35] J. D. Pritchard, D. Maxwell, A. Gauguet, K. J. Weatherill, M. P. A. Jones, and C. S. Adams, Cooperative atom-light interaction in a blockaded Rydberg ensemble, Phys. Rev. Lett. **105**, 193603 (2010).
[36] A. Gaëtan, Y. Miroshnychenko, T. Wilk, A. Chotia, M. Viteau, D. Comparat, P. Pillet, A. Browaeys, and P. Grangier, Observation of collective excitation of two individual atoms in the Rydberg blockade regime, Nat. Phys. **5**, 115 (2009).
[37] D. Barredo, S. Ravets, H. Labuhn, L. Béguin, A. Vernier, F. Nogrette, T. Lahaye, and A. Browaeys, Demonstration of a strong Rydberg blockade in three-atom systems with anisotropic interactions, Phys. Rev. Lett. **112**, 183002 (2014).
[38] F. M. Gambetta, W. Li, F. Schmidt-Kaler, and I. Lesanovsky, Engineering nonbinary Rydberg interactions via phonons in an optical lattice, Phys. Rev. Lett. **124**, 043402 (2020).
[39] V. Bharti, S. Sugawa, M. Kunimi, V. S. Chauhan, T. P. Mahesh, M. Mizoguchi, T. Matsubara, T. Tomita, S. de Léséleuc, and K. Ohmori, Strong spin-motion coupling in the ultrafast dynamics of Rydberg atoms, Phys. Rev. Lett. **133**, 093405 (2024).
[40] M. Magoni, P. Mazza, and I. Lesanovsky, Phonon dressing of a facilitated one-dimensional Rydberg lattice gas, SciPost Phys. Core **5**, 041 (2022).
[41] J. I. Cirac, R. Blatt, P. Zoller, and W. D. Phillips, Laser cooling of trapped ions in a standing wave, Phys. Rev. A **46**, 2668 (1992).
[42] See Supplemental Material at http://link.aps.org/supplemental/10.1103/PhysRevA.111.L041104 for the derivation of $\mathcal{U}(T)$, a discussion about dressing under ultrastrong laser pulses, and the spin-motion echo. Additionally, it discusses decoherence in the adiabatic dressing protocol, the ratio $\mathcal{V}_3/\mathcal{V}_2$, and spin-motion coupling.
[43] T. P. Mahesh, T. Matsubara, Y. T. Chew, T. Tomita, S. de Léséleuc, and K. Ohmori, Generation of 480 nm picosecond pulses for ultrafast excitation of Rydberg atoms, arXiv:2408.02324.
[44] F. M. Gambetta, C. Zhang, M. Hennrich, I. Lesanovsky, and W. Li, Long-range multibody interactions and three-body antiblockade in a trapped Rydberg ion chain, Phys. Rev. Lett. **125**, 133602 (2020).
[45] C. Nill, K. Brandner, B. Olmos, F. Carollo, and I. Lesanovsky, Many-body radiative decay in strongly interacting Rydberg ensembles, Phys. Rev. Lett. **129**, 243202 (2022).
[46] I. I. Ryabtsev, I. I. Beterov, D. B. Tretyakov, V. M. Entin, and E. A. Yakshina, Doppler- and recoil-free laser excitation of Rydberg states via three-photon transitions, Phys. Rev. A **84**, 053409 (2011).
[47] J. Eschner, G. Morigi, F. Schmidt-Kaler, and R. Blatt, Laser cooling of trapped ions, J. Opt. Soc. Am. B **20**, 1003 (2003).
[48] S. Stenholm, The semiclassical theory of laser cooling, Rev. Mod. Phys. **58**, 699 (1986).
[49] K. E. Cahill and R. J. Glauber, Ordered expansions in boson amplitude operators, Phys. Rev. **177**, 1857 (1969).
[50] D. Petrosyan and K. Mølmer, Binding potentials and interaction gates between microwave-dressed Rydberg atoms, Phys. Rev. Lett. **113**, 123003 (2014).
[51] S. Sevinçli and T. Pohl, Microwave control of Rydberg atom interactions, New J. Phys. **16**, 123036 (2014).
[52] P. Scholl, H. J. Williams, G. Bornet, F. Wallner, D. Barredo, L. Henriet, A. Signoles, C. Hainaut, T. Franz, S. Geier, A. Tebben, A. Salzinger, G. Zürn, T. Lahaye, M. Weidemüller, and A. Browaeys, Microwave engineering of programmable XXZ Hamiltonians in arrays of Rydberg atoms, PRX Quantum **3**, 020303 (2022).
[53] M. Kastner, P. Osterholz, and C. Gross, Ancilla-free measurement of out-of-time-ordered correlation functions: General measurement protocol and Rydberg atom implementation, arXiv:2403.08670.
[54] M. H. Goerz, T. Calarco, and C. P. Koch, The quantum speed limit of optimal controlled phasegates for trapped neutral atoms, J. Phys. B: At. Mol. Opt. Phys. **44**, 154011 (2011).
[55] T. Keating, R. L. Cook, A. M. Hankin, Y.-Y. Jau, G. W. Biedermann, and I. H. Deutsch, Robust quantum logic in neutral atoms via adiabatic Rydberg dressing, Phys. Rev. A **91**, 012337 (2015).
[56] A. Mitra, M. J. Martin, G. W. Biedermann, A. M. Marino, P. M. Poggi, and I. H. Deutsch, Robust Mølmer-Sørensen gate for neutral atoms using rapid adiabatic Rydberg dressing, Phys. Rev. A **101**, 030301(R) (2020).

[57] A. Mitra, S. Omanakuttan, M. J. Martin, G. W. Biedermann, and I. H. Deutsch, Neutral-atom entanglement using adiabatic Rydberg dressing, Phys. Rev. A **107**, 062609 (2023).

[58] M. M. Müller, M. Murphy, S. Montangero, T. Calarco, P. Grangier, and A. Browaeys, Implementation of an experimentally feasible controlled-phase gate on two blockaded Rydberg atoms, Phys. Rev. A **89**, 032334 (2014).

[59] F. Robicheaux, T. M. Graham, and M. Saffman, Photon-recoil and laser-focusing limits to Rydberg gate fidelity, Phys. Rev. A **103**, 022424 (2021).

[60] N. Schine, A. W. Young, W. J. Eckner, M. J. Martin, and A. M. Kaufman, Long-lived Bell states in an array of optical clock qubits, Nat. Phys. **18**, 1067 (2022).

[61] S. Trotzky, P. Cheinet, S. Fölling, M. Feld, U. Schnorrberger, A. M. Rey, A. Polkovnikov, E. A. Demler, M. D. Lukin, and I. Bloch, Time-resolved observation and control of superexchange interactions with ultracold atoms in optical lattices, Science **319**, 295 (2008).

[62] Z. Zhang, M. Yuan, B. Sundar, and K. R. A. Hazzard, Motional decoherence in ultracold-Rydberg-atom quantum simulators of spin models, Phys. Rev. A **110**, 053321 (2024).

[63] J. R. Johansson, P. D. Nation, and F. Nori, QuTiP 2: A Python framework for the dynamics of open quantum systems, Comput. Phys. Commun. **184**, 1234 (2013).

[64] L. Béguin, A. Vernier, R. Chicireanu, T. Lahaye, and A. Browaeys, Direct measurement of the van der Waals interaction between two Rydberg atoms, Phys. Rev. Lett. **110**, 263201 (2013).

[65] J. B. Balewski, A. T. Krupp, A. Gaj, S. Hofferberth, R. Löw, and T. Pfau, Rydberg dressing: Understanding of collective many-body effects and implications for experiments, New J. Phys. **16**, 063012 (2014).

SUPPLEMENTAL MATERIAL

Resonant stroboscopic Rydberg dressing: electron-motion coupling and multi-body interactions

Chris Nill[1,2], Sylvain de Léséleuc[3,4], Christian Groß[5], and Igor Lesanovsky[1,6]

[1]*Institut für Theoretische Physik and Center for Integrated Quantum Science and Technology, Universität Tübingen, Auf der Morgenstelle 14, 72076 Tübingen, Germany*
[2]*Institute for Applied Physics, University of Bonn, Wegelerstraße 8, 53115 Bonn, Germany*
[3]*Institute for Molecular Science, National Institutes of Natural Sciences, 444-8585 Okazaki, Japan*
[4]*RIKEN Center for Quantum Computing (RQC), 351-0198 Wako, Japan*
[5]*Physikalisches Institut and Center for Integrated Quantum Science and Technology, Universität Tübingen, Auf der Morgenstelle 14, 72076 Tübingen, Germany*
[6]*School of Physics and Astronomy and Centre for the Mathematics and Theoretical Physics of Quantum Non-Equilibrium Systems, The University of Nottingham, Nottingham, NG7 2RD, United Kingdom*

CONTENTS

I. Analysis of the non-adiabatic dressing protocol 1
A. Derivation of the time evolution operator $\mathcal{U}(T)$ at stroboscopic times 1
B. Spin decoherence due to spin-motion coupling under ultra-strong laser pulses 5
C. Decoupling spin-motion with a spin-motion echo 6

II. Analysis of the adiabatic dressing protocol 7
A. Adiabaticity and finite Rydberg lifetime: A case study 7
B. Relative strength of multi-body interactions 8
C. Spin-motion coupling 8

References 9

I. ANALYSIS OF THE NON-ADIABATIC DRESSING PROTOCOL

A. Derivation of the time evolution operator $\mathcal{U}(T)$ at stroboscopic times

The non-adiabatic dressing sequence, see Fig. 1(b) in the main text, is decomposed into four phases. During the first one of duration τ_1, the system is described by the free evolution under the Rydberg Hamiltonian ($\hbar = 1$)

$$H_0 = \omega \sum_j a_j^\dagger a_j + V \sum_j n_j n_{j+1} + G \sum_j n_j n_{j+1}(x_j - x_{j+1}), \tag{S1}$$

where ω is the trapping frequency of the atoms with harmonic oscillator operators a_j and $a_j^\dagger$. The Rydberg interaction strength is parametrized by V, and the gradient of the potential by G. The projector onto an atom in Rydberg state $|r\rangle$ is given by $n_j = |r\rangle\langle r|_j$.

During the second phase of duration s, the laser Hamiltonian with Rabi frequency Ω and projected wave vector κ (the axis connecting the two atoms is the chosen as x-axis) is acing. This leads to the additional Hamiltonian

$$H_L = \sum_j \Omega \left(|\uparrow\rangle\langle r|_j \, e^{-i\kappa x_j} + |r\rangle\langle\uparrow|_j \, e^{i\kappa x_j} \right), \tag{S2}$$

where the position operator of atom j with atomic mass is

$$x_j = x_0(a_j + a_j^\dagger) = \sqrt{\frac{1}{2m\omega}}(a_j + a_j^\dagger). \tag{S3}$$

The Lamb-Dicke parameter is then given as $\eta = \kappa x_0$. During the third phase of the dressing sequence, with duration τ_2, only H_0 is acting (the laser is switched off), while during he fourth phase is the same as the second. Consequently, the time-evolution operator of a sequence of length $T = \tau_1 + \tau_2 + 2s$ is given by

$$\mathcal{U}_{\tau_1+\tau_2+2s} = \underbrace{e^{-is(H_L+H_0)}}_{\mathcal{U}_\pi} e^{-iH_0\tau_2} e^{-is(H_L+H_0)} e^{-iH_0\tau_1}. \tag{S4}$$

First, we evaluate now

$$\mathcal{U}_\pi = e^{-is(H_L+H_0)} \tag{S5}$$

$$= \exp\left\{-is\Omega \sum_j \left(|\uparrow\rangle\langle r|_j \, e^{-i\kappa x_j} + |r\rangle\langle\uparrow|_j \, e^{i\kappa x_j} + \frac{\omega}{\Omega} a_j^\dagger a_j + \frac{V}{\Omega} n_j n_{j+1} + \frac{G_j}{\Omega} n_j n_{j+1}(x_j - x_{j+1}) \right)\right\}. \tag{S6}$$

We consider a strong laser driving which breaks the Rydberg blockade and is by magnitudes the largest energy scale with $V/\Omega \ll 1$, $\omega/\Omega \ll 1$, $G_j/\Omega \ll 1$, thus

$$\mathcal{U}_\pi = e^{-isH_L} = \exp\left\{-is\Omega \sum_j \left(|\uparrow\rangle\langle r|_j \, e^{-i\kappa x_j} + |r\rangle\langle\uparrow|_j \, e^{i\kappa x_j} \right)\right\}. \tag{S7}$$

In addition, $\Omega s = \pi/2$ is chosen such that the laser performs π pulses, which reduce effectively to instantaneous pulses

$$\mathcal{U}_\pi = \prod_j \exp\left\{-i\Omega s \left(|\uparrow\rangle\langle r|_j \, e^{-i\kappa x_j} + |r\rangle\langle\uparrow|_j \, e^{i\kappa x_j} \right) + 0 \cdot |\downarrow\rangle\langle\downarrow|_j \right\} \tag{S8}$$

$$= \prod_j \left[|\downarrow\rangle\langle\downarrow|_j - i \left(|\uparrow\rangle\langle r|_j \, e^{-i\kappa x_j} + |r\rangle\langle\uparrow|_j \, e^{i\kappa x_j} \right) \right]. \tag{S9}$$

The time-evolution operator from Eq. (S4) for a sequence reads then

$$\mathcal{U}_{\tau_1+\tau_2+2s} = \underbrace{\mathcal{U}_\pi e^{-iH_0\tau_2} \mathcal{U}_\pi}_{\mathcal{U}_\mathcal{R}} e^{-iH_0\tau_1}. \tag{S10}$$

The expression $\mathcal{U}_\mathcal{R}$ can be evaluated as

$$\mathcal{U}_\mathcal{R} = \mathcal{U}_\pi e^{-iH_0\tau_2} \mathcal{U}_\pi = \underbrace{\mathcal{U}_\pi \mathcal{U}_\pi}_{\prod_j (|\downarrow\rangle\langle\downarrow|_j - \mathcal{P}_j - n_j)} \mathcal{U}_\pi^\dagger e^{-iH_0\tau_2} \mathcal{U}_\pi \tag{S11}$$

$$= \prod_j \left(|\downarrow\rangle\langle\downarrow|_j - \mathcal{P}_j - n_j \right) \exp\left\{-i\tau_2 \left(\omega \sum_j \underbrace{\mathcal{U}_\pi^\dagger a_j^\dagger a_j \mathcal{U}_\pi}_{A} + V \sum_j \underbrace{\mathcal{U}_\pi^\dagger n_j n_{j+1} \mathcal{U}_\pi}_{\mathcal{P}_j \mathcal{P}_{j+1}} + \sum_j G_j \underbrace{\mathcal{U}_\pi^\dagger n_j n_{j+1}(x_j - x_{j+1}) \mathcal{U}_\pi}_{\mathcal{P}_j \mathcal{P}_{j+1}(x_j - x_{j+1})} \right)\right\}, \tag{S12}$$

where we define the projector onto atom j in state $|\uparrow\rangle$ as $\mathcal{P}_j = |\uparrow\rangle\langle\uparrow|_j$. In addition,

$$A = \omega \left(a_j^\dagger a_j + i\eta(n_j - \mathcal{P}_j)(a_j - a_j^\dagger) + \eta^2(n_j + \mathcal{P}_j) \right). \tag{S13}$$

The time-evolution operator for a dressing sequence then is

$$\begin{aligned}
\mathcal{U}_{\tau_1+\tau_2+2s} = & \left[\prod_j \left(|\downarrow\rangle\langle\downarrow|_j - \mathcal{P}_j - n_j \right) \right] \\
& \cdot \exp\left\{ -i\tau_2 \left(\omega \sum_j \left(a_j^\dagger a_j + i\eta(n_j - \mathcal{P}_j)(a_j - a_j^\dagger) + \eta^2(n_j + \mathcal{P}_j) \right) + \sum_j G_j \mathcal{P}_j \mathcal{P}_{j+1}(x_j - x_{j+1}) \right) \right\} \\
& \cdot \exp\left\{ -i\tau_1 \left(\omega \sum_j a_j^\dagger a_j + \sum_j G_j n_j n_{j+1}(x_j - x_{j+1}) \right) \right\} \\
& \cdot \exp\left\{ -i\tau_2 V \sum_j \mathcal{P}_j \mathcal{P}_{j+1} \right\} \cdot \exp\left\{ -i\tau_1 V \sum_j n_j n_{j+1} \right\}.
\end{aligned} \tag{S14}$$

We consider an initial state $|\psi_0\rangle$ in which no Rydberg excitations are present. Thus, multiplying $\prod_j(\mathbb{1}-n_j)$ onto the time evolution does not affect the initial state. Since $\mathcal{U}_{\tau_1+\tau_2+2s}$ commutes with n_j, we can write

$$\mathcal{U}_{\tau_1+\tau_2+2s} = \mathcal{U}_{\tau_1+\tau_2+2s}\cdot\prod_j(\mathbb{1}-n_j) \tag{S15}$$

$$\begin{aligned}
&= \prod_j\left(|\downarrow\rangle\langle\downarrow|_j - \mathcal{P}_j\right)\exp\left\{-i\tau_2\left(\omega\sum_j\left(a_j^\dagger a_j - i\eta\mathcal{P}_j(a_j-a_j^\dagger)+\eta^2\mathcal{P}_j\right)+\sum_j G_j\mathcal{P}_j\mathcal{P}_{j+1}(x_j-x_{j+1})\right)\right\}\\
&\quad\cdot\exp\left\{-i\tau_1\omega\sum_j a_j^\dagger a_j\right\}\cdot\exp\left\{-i\tau_2 V\sum_j\mathcal{P}_j\mathcal{P}_{j+1}\right\}
\end{aligned} \tag{S16}$$

$$\begin{aligned}
&= \prod_j\left(|\downarrow\rangle\langle\downarrow|_j - \mathcal{P}_j\right)\\
&\quad\underbrace{\cdot\exp\left\{-i\tau_2\left(\omega\sum_j\left(a_j^\dagger a_j - i\eta\mathcal{P}_j(a_j-a_j^\dagger)+\eta^2\mathcal{P}_j\right)+\sum_j G_j\mathcal{P}_j\mathcal{P}_{j+1}(x_j-x_{j+1})\right)\right\}\cdot\exp\left\{i\tau_2\omega\sum_j a_j^\dagger a_j\right\}}_{\text{spin-motion coupling dynamics}}\\
&\quad\underbrace{\cdot\exp\left\{-i(\tau_1+\tau_2)\omega\sum_j a_j^\dagger a_j\right\}}_{\text{free-oscillator dynamics}}\underbrace{\cdot\exp\left\{-i(\tau_1+\tau_2)\frac{\tau_2 V}{\tau_1+\tau_2}\sum_j\mathcal{P}_j\mathcal{P}_{j+1}\right\}}_{\text{spin-spin dynamics}}.
\end{aligned} \tag{S17}$$

Gradient operator $\mathcal{G}_j$
Introducing the gradient operator enables us to commute the summands with

$$\begin{aligned}
\sum_j G_j\mathcal{P}_j\mathcal{P}_{j+1}(x_j-x_{j+1}) &= \sum_j G_j\mathcal{P}_j\mathcal{P}_{j+1}x_j - \sum_j G_j\mathcal{P}_j\mathcal{P}_{j+1}x_{j+1}\\
&= \sum_j G_j\mathcal{P}_j\mathcal{P}_{j+1}x_j - \sum_j G_{j-1}\mathcal{P}_{j-1}\mathcal{P}_j x_j\\
&= \sum_j\left(G_j\mathcal{P}_{j+1} - G_{j-1}\mathcal{P}_{j-1}\right)\mathcal{P}_j x_j\\
&= \sum_j\left(G_j\mathcal{P}_{j+1} - G_{j-1}\mathcal{P}_{j-1}\right)\mathcal{P}_j x_0(a_j+a_j^\dagger)\\
&=: \sum_j\mathcal{G}_j(a_j+a_j^\dagger).
\end{aligned} \tag{S18}$$

Note, that $[\mathcal{G}_j,\mathcal{G}_l]=0\,\forall j,l$ and $\mathcal{G}_j^2\neq\mathcal{G}_j$.

The spin-motion term (blue) can be further simplified using the gradient operator $\mathcal{G}_j$, see Eq. (S18), as

$$\exp\left\{-i\tau_2\left(\omega\sum_j\left(a_j^\dagger a_j - i\eta\mathcal{P}_j(a_j-a_j^\dagger)+\eta^2\mathcal{P}_j\right)+\sum_j G_j\mathcal{P}_j\mathcal{P}_{j+1}(x_j-x_{j+1})\right)\right\}\cdot\exp\left\{i\tau_2\omega\sum_j a_j^\dagger a_j\right\} \tag{S19}$$

and since all terms commute now in j

$$= \prod_j\exp\left\{-i\tau_2\left(\omega a_j^\dagger a_j - i\eta\omega\mathcal{P}_j(a_j-a_j^\dagger)+\eta^2\omega\mathcal{P}_j+\mathcal{G}_j(a_j+a_j^\dagger)\right)\right\}\cdot\exp\left\{i\tau_2\omega a_j^\dagger a_j\right\}. \tag{S20}$$

We complete the square with

$$= \prod_j \exp\left\{ -i\tau_2\omega \left[\left(a_j^\dagger \underbrace{-i\eta\mathcal{P}_j + \frac{\mathcal{G}_j}{\omega}}_{\mathcal{J}_j^\dagger} \right) \left(a_j + \underbrace{i\eta\mathcal{P}_j + \frac{\mathcal{G}_j}{\omega}}_{\mathcal{J}_j} \right) + \eta^2\mathcal{P}_j - \mathcal{J}_j^\dagger\mathcal{J}_j \right] \right\} \cdot \exp\left\{ i\tau_2\omega a_j^\dagger a_j \right\} \tag{S21}$$

$$= \prod_j \exp\Big\{ -i\tau_2\omega \left[(a_j + \mathcal{J}_j)^\dagger (a_j + \mathcal{J}_j) + \eta^2\mathcal{P}_j - \mathcal{J}_j^\dagger\mathcal{J}_j \right] \Big\} \cdot \exp\left\{ i\tau_2\omega a_j^\dagger a_j \right\} \tag{S22}$$

and introduce the displacement operator with $a + \alpha = \mathcal{D}^\dagger(\alpha) a \mathcal{D}(\alpha)$, thus

$$= \prod_j \exp\Big\{ -i\tau_2\omega \left[\left(\mathcal{D}^\dagger(\mathcal{J}_j) a_j \mathcal{D}(\mathcal{J}_j) \right)^\dagger \mathcal{D}^\dagger(\mathcal{J}_j) a_j \mathcal{D}(\mathcal{J}_j) + \eta^2\mathcal{P}_j - \mathcal{J}_j^\dagger\mathcal{J}_j \right] \Big\} \cdot \exp\left\{ i\tau_2\omega a_j^\dagger a_j \right\} \tag{S23}$$

$$= \prod_j \exp\left\{ -i\tau_2\omega \left[\mathcal{D}^\dagger(\mathcal{J}_j) a^\dagger \underbrace{\mathcal{D}(\mathcal{J}_j)\mathcal{D}^\dagger(\mathcal{J}_j)}_{\mathbb{1}} a \mathcal{D}(\mathcal{J}_j) + \eta^2\mathcal{P}_j - \mathcal{J}_j^\dagger\mathcal{J}_j \right] \right\} \cdot \exp\left\{ i\tau_2\omega a_j^\dagger a_j \right\}. \tag{S24}$$

Note that all terms in exp commute now, thus

$$= \prod_j \exp\Big\{ -i\tau_2\omega \left[\mathcal{D}^\dagger(\mathcal{J}_j) a_j^\dagger a_j \mathcal{D}(\mathcal{J}_j) \right] \Big\} \cdot \exp\left\{ i\tau_2\omega a_j^\dagger a_j \right\} \cdot \exp\left\{ -i\tau_2\omega \left(\eta^2\mathcal{P}_j - \mathcal{J}_j^\dagger\mathcal{J}_j \right) \right\}. \tag{S25}$$

Since $\mathcal{D}(\mathcal{J}_j)$ is a unitary operator and thus invertible it follows

$$= \prod_j \mathcal{D}^\dagger(\mathcal{J}_j) \underbrace{\mathrm{e}^{-i\tau_2\omega a_j^\dagger a_j} \mathcal{D}(\mathcal{J}_j) \mathrm{e}^{i\tau_2\omega a_j^\dagger a_j}}_{\text{Baker-Campbell-Hausdorff}} \cdot \exp\left\{ -i\tau_2\omega \left(\eta^2\mathcal{P}_j - \mathcal{J}_j^\dagger\mathcal{J}_j \right) \right\} \tag{S26}$$

$$= \prod_j \mathcal{D}^\dagger(\mathcal{J}_j) \exp\Big\{ \mathcal{J}_j e^{-i\tau_2\omega} a_j^\dagger - \mathcal{J}_j^\dagger e^{i\tau_2\omega} a_j) \Big\} \cdot \exp\left\{ -i\tau_2\omega \left(\eta^2\mathcal{P}_j - \mathcal{J}_j^\dagger\mathcal{J}_j \right) \right\} \tag{S27}$$

$$= \prod_j \mathcal{D}(-\mathcal{J}_j) \mathcal{D}\left(\mathcal{J}_j e^{-i\tau_2\omega} \right) \cdot \exp\left\{ -i\tau_2\omega \left(\eta^2\mathcal{P}_j - \mathcal{J}_j^\dagger\mathcal{J}_j \right) \right\} \tag{S28}$$

$$= \prod_j \exp\Big\{ -i\mathcal{J}_j^\dagger\mathcal{J}_j \sin(\omega\tau_2) - i\tau_2\omega \left(\eta^2\mathcal{P}_j - \mathcal{J}_j^\dagger\mathcal{J}_j \right) \Big\} \cdot \mathcal{D}\left(\mathcal{J}_j (e^{-i\omega\tau_2} - 1) \right) \tag{S29}$$

$$= \prod_j \exp\Big\{ -i\tau_2\omega \left[\mathcal{J}_j^\dagger\mathcal{J}_j \left(\mathrm{sinc}(\omega\tau_2) - 1 \right) + \eta^2\mathcal{P}_j \right] \Big\} \cdot \mathcal{D}\left(\mathcal{J}_j (e^{-i\omega\tau_2} - 1) \right) \tag{S30}$$

$$= \prod_j \exp\left\{ -i\tau_2\omega \left[\left(\frac{\mathcal{G}_j^2}{\omega^2} + \eta^2\mathcal{P}_j \right) \left(\mathrm{sinc}(\omega\tau_2) - 1 \right) + \eta^2\mathcal{P}_j \right] \right\} \cdot \mathcal{D}\left[\left(\frac{\mathcal{G}_j}{\omega} + i\eta\mathcal{P}_j \right) (e^{-i\omega\tau_2} - 1) \right]. \tag{S31}$$

If we insert this result now in Eq. (S17), we obtain

$$\mathcal{U}_{\tau_1+\tau_2+2s} = \prod_j (|\downarrow\rangle\langle\downarrow|_k - \mathcal{P}_j) \exp\left\{-i\tau_2\omega \left[\left(\frac{\mathcal{G}_j^2}{\omega^2} + \eta^2\mathcal{P}_j\right)(\mathrm{sinc}(\omega\tau_2) - 1) + \eta^2\mathcal{P}_j\right]\right\}$$
$$\cdot \exp\left\{-i(\tau_1+\tau_2)\frac{\tau_2 V}{\tau_1+\tau_2}\mathcal{P}_j\mathcal{P}_{j+1}\right\} \cdot \mathcal{D}\left[\left(\frac{\mathcal{G}_j}{\omega} + i\eta\mathcal{P}_j\right)(e^{-i\omega\tau_2} - 1)\right] \cdot \exp\left\{-i(\tau_1+\tau_2)\omega a_j^\dagger a_j\right\} \quad \text{(S32)}$$

$$= \prod_j (|\downarrow\rangle\langle\downarrow|_k - \mathcal{P}_j) \exp\left\{-i(\tau_1+\tau_2)\left[\frac{\tau_2 V}{\tau_1+\tau_2}\mathcal{P}_j\mathcal{P}_{j+1} + \frac{\mathcal{G}_j\tau_2}{\tau_1+\tau_2}\frac{\mathcal{G}_j}{\omega}(\mathrm{sinc}(\omega\tau_2) - 1) + \frac{\sin(\omega\tau_2)}{\tau_1+\tau_2}\eta^2\mathcal{P}_j\right]\right\}$$
$$\cdot \mathcal{D}\left[\left(\frac{\mathcal{G}_j}{\omega} + i\eta\mathcal{P}_j\right)(e^{-i\omega\tau_2} - 1)\right] \cdot \exp\left\{-i(\tau_1+\tau_2)\omega a_j^\dagger a_j\right\} \quad \text{(S33)}$$

$$= \prod_j e^{-i\pi\mathcal{P}_j} \exp\left\{-i(\tau_1+\tau_2)\left[\frac{\tau_2 V}{\tau_1+\tau_2}\mathcal{P}_j\mathcal{P}_{j+1} + \frac{\mathcal{G}_j\tau_2}{\tau_1+\tau_2}\frac{\mathcal{G}_j}{\omega}(\mathrm{sinc}(\omega\tau_2) - 1) + \frac{\sin(\omega\tau_2)}{\tau_1+\tau_2}\eta^2\mathcal{P}_j\right]\right\}$$
$$\cdot \mathcal{D}\left[\left(\frac{\mathcal{G}_j}{\omega} + i\eta\mathcal{P}_j\right)(e^{-i\omega\tau_2} - 1)\right] \cdot \exp\left\{-i(\tau_1+\tau_2)\omega a_j^\dagger a_j\right\} \quad \text{(S34)}$$

$$= \prod_j \exp\left\{-i(\tau_1+\tau_2)\left[\frac{\tau_2 V}{\tau_1+\tau_2}\mathcal{P}_j\mathcal{P}_{j+1} + \frac{\mathcal{G}_j\tau_2}{\tau_1+\tau_2}\frac{\mathcal{G}_j}{\omega}(\mathrm{sinc}(\omega\tau_2) - 1) + \frac{\sin(\omega\tau_2)}{\tau_1+\tau_2}\eta^2\mathcal{P}_j + \frac{\pi}{\tau_1+\tau_2}\mathcal{P}_j\right]\right\}$$
$$\cdot \mathcal{D}\left[\left(\frac{\mathcal{G}_j}{\omega} + i\eta\mathcal{P}_j\right)(e^{-i\omega\tau_2} - 1)\right] \cdot \exp\left\{-i(\tau_1+\tau_2)\omega a_j^\dagger a_j\right\}. \quad \text{(S35)}$$

We now again utilize the short laser pulses introduced earlier, see Eq. (S7). This allows us to write $T = \tau_1 + \tau_2 + 2s \approx \tau_1 + \tau_2$ to obtain the time evolution operator Eq. (5) of the main text,

$$\mathcal{U}(T) = \prod_j \underbrace{\exp\left\{-iT\left[\frac{\tau_2 V}{T}\mathcal{P}_j\mathcal{P}_{j+1} + \frac{\mathcal{G}_j\tau_2}{T}\frac{\mathcal{G}_j}{\omega}(\mathrm{sinc}(\omega\tau_2) - 1) + \frac{\sin(\omega\tau_2)\eta^2 + \pi}{T}\mathcal{P}_j\right]\right\}}_{\text{effective spin dynamics}}$$
$$\cdot \underbrace{\mathcal{D}\left[\left(\frac{\mathcal{G}_j}{\omega} + i\eta\mathcal{P}_j\right)(e^{-i\omega\tau_2} - 1)\right]}_{\text{spin-motion coupling}} \cdot \underbrace{\exp\left\{-iT\omega a_j^\dagger a_j\right\}}_{\text{free oscillator evolution}}. \quad \text{(S36)}$$

B. Spin decoherence due to spin-motion coupling under ultra-strong laser pulses

In this section, we investigate spin-motion coupling effects under ultra-strong laser pulses which are experimentally investigated in Ref. [1]. Here, the laser pulses are characterized by a large Rabi frequency $\Omega_0 \gg V$ that effectively overcomes the Rydberg interaction V. This interaction is much stronger than the trap frequency with $V \gg \omega$. As well as in the main text, each laser pulse is designed as a π pulse with $\Omega_0 s = \pi/2$, resulting in a tiny pulse duration s. Thus, for these ultra-strong pulses, the product $\omega\tau_2$ of the atomic oscillations becomes tiny, $\omega\tau_2 \ll 1$.

As shown in the main text, the system's time evolution operator $\mathcal{U}(T)$ simplifies (see Eq. (5) in the main text) when strictly $\omega\tau_2 = 0$, indicating that spin and oscillatory motion decouple. However, here we do not match this condition perfectly.

In order to understand the impact of residual spin-motion coupling in the limit $\omega\tau_2 \ll 1$, we perform the same study as in Fig. 2 of the main text. Specifically, we show the time evolution of S_x for small values of $\omega\tau_2$ in Fig. S1(a). We compare the exact evolution of S_x which includes spin-motion coupling (see Eq. (4) of main text) with the effective spin dynamics calculated by Eq. (6) of the main text. We observe that deviations during time evolution occur. In particular, the effective spin dynamics lead to periodic oscillations, while the exact dynamics show damped oscillations. This mismatch of exact- and effective spin dynamics, which here results in damped oscillations, can be interpreted as spin decoherence, which arises due to the entanglement between oscillatory degrees of freedom and spins. In Fig. S1(b), we reduce $\omega\tau_2$ by a factor of 200 compared to panel (a), while proportionally increasing V and G to maintain the effective interaction strength $V_{\text{eff}} = \tau_2 V/T$ and the effective gradient operator $\mathcal{G}_{j,\text{eff}} = \tau_2\mathcal{G}_j/T$. These effective quantities occur in the effective Hamiltonian, see Eq. (6) of the main text, and define the oscillation

envelopes of S_x. Compared to panel (a), we observe that the spin decoherence in S_x does not decrease and deviations between exact- and effective spin dynamics are still present in panel (b). This can be explained by expanding the collective displacement operator $\mathcal{J}_j$ (see main text). It couples spins and oscillatory motion and is the origin of the observed spin decoherence. For $\omega\tau_2 \ll 1$,

$$\mathcal{J}_j \approx -i\tau_2\mathcal{G}_j + \omega\tau_2\eta\mathcal{P}_j = -i\mathcal{G}_{j,\text{eff}} + \omega\tau_2\eta\mathcal{P}_j. \tag{S37}$$

As we show, $\mathcal{J}_j$ is dependent on the effective gradient operator $\mathcal{G}_{j,\text{eff}}$. Therefore, $\mathcal{J}_j$ remains unchanged for same $\mathcal{G}_{j,\text{eff}} = \tau_2\mathcal{G}_j$. This is why reducing $\omega\tau_2$ while increasing G does not reduce spin decoherence. On the other hand, reducing $\mathcal{G}_{j,\text{eff}}$ without changing $\omega\tau_2$ reduces spin decoherence. This means that by reducing the effective gradient, spin-motion coupling decreases, which ultimately removes spin decoherence as shown in Fig. S1(c).

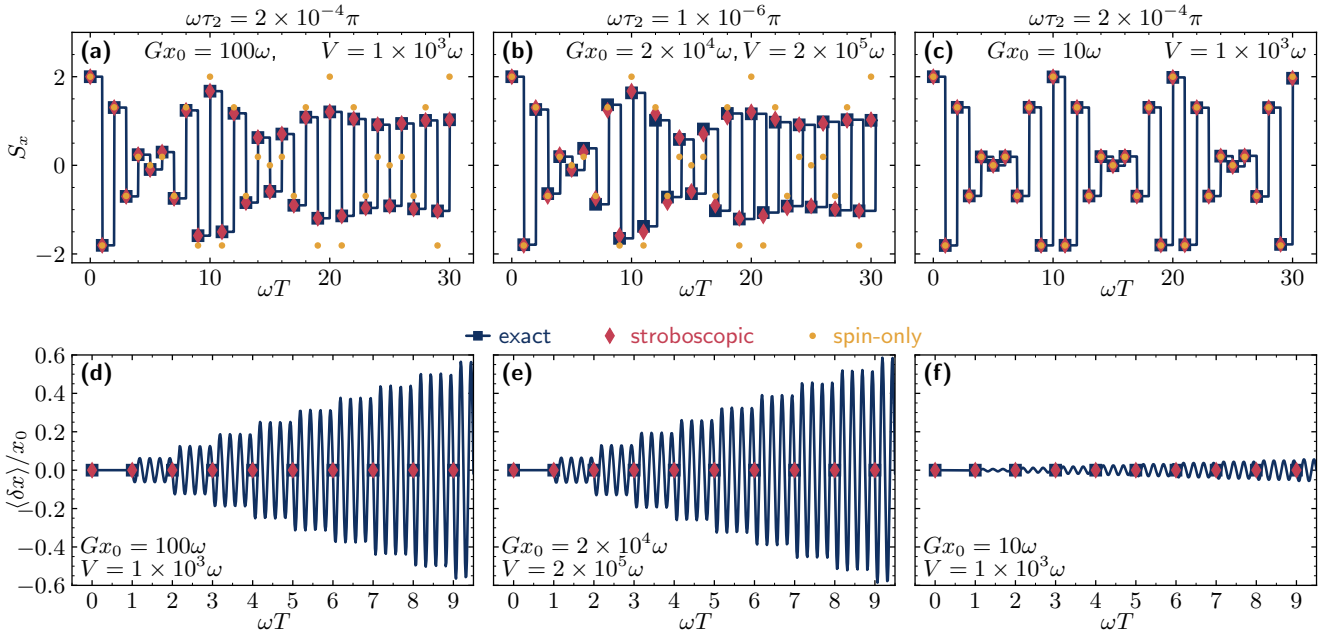

FIG. S1. **Spin-motion coupling for ultra-strong laser pulses. (a)** Exact- (blue) and effective spin dynamics (yellow) of S_x deviate significantly. Under the effective spin dynamics (Eq. (6) of the main text), periodic oscillations occur. However, due to spin-motion coupling, the exact dynamics (Eq. (4) of the main text) show damped oscillations which we associate with spin decoherence. Here, we set $\omega\tau_2 = 2\times10^{-4}$ and the Rydberg interaction $V = 1000\omega$. **(b)** Scaling down τ_2 and proportionally adjusting V and G cannot reduce spin decoherence in S_x compared to panel (a). **(c)** Reducing the effective gradient weakens spin decoherence, compared to (a) and (b). Thus, effective spin dynamics coincide with the exact dynamics. **(d)-(f)** The amplitude of the interatomic distance $\langle\delta x\rangle$ is mainly affected by the effective gradient $Gx_0\tau_2$ and impacts the observed spin decoherence. In all simulations the harmonic oscillator basis is truncated to contain a maximum of 5 excitations, the parameters values are $T = 8\pi/\omega$, $\eta = 0.6$ and $s = \pi/(2\times10^7\omega)$.

C. Decoupling spin-motion with a spin-motion echo

In the main text, we examined how adjusting the oscillation phase, $\omega\tau_2$, allows to decouple spin-motion dynamics. Here, we explore a complementary approach using a spin-motion echo. This method is based on setting the total sequence duration to satisfy $T = n\pi/\omega$ with n as an odd integer. The spin-motion echo relies on the application of two successive dressing sequences that enable the decoupling. Each sequence is describes by the time evolution operator $\mathcal{U}(T)$. To illustrate, we evaluate the time evolution operator, see Eq. (5) of the main text, for both successive

sequences

$$\begin{aligned}\mathcal{U}^2(T=\frac{n\pi}{\omega}) &= \prod_j e^{-iTH_{j,\text{eff}}}\mathcal{D}(\mathcal{J}_j)e^{-iT\omega a_j^\dagger a_j}\cdot e^{-iTH_{j,\text{eff}}}\mathcal{D}(\mathcal{J}_j)e^{-iT\omega a_j^\dagger a_j}\\ &= \prod_j e^{-2iTH_{j,\text{eff}}}\mathcal{D}(\mathcal{J}_j)\underbrace{e^{-iT\omega a_j^\dagger a_j}\mathcal{D}(\mathcal{J}_j)e^{iT\omega a_j^\dagger a_j}}_{\text{Baker-Campbell-Hausdorff}}e^{-2iT\omega a_j^\dagger a_j}\\ &= \prod_j e^{-2iTH_{j,\text{eff}}}\mathcal{D}(\mathcal{J}_j)\mathcal{D}(\mathcal{J}_j e^{-i\pi n})e^{-2iT\omega a_j^\dagger a_j}\\ &= \prod_j e^{-2iTH_{j,\text{eff}}}\mathcal{D}(\underbrace{[1+e^{-i\pi n}]}_{=0,\text{ if } n \text{ is odd}}\mathcal{J}_j)e^{-2iT\omega a_j^\dagger a_j}\\ &= \prod_j e^{-2iTH_{j,\text{eff}}}e^{-2iT\omega a_j^\dagger a_j}.\end{aligned} \tag{S38}$$

We see directly that spin-motion dynamics decouple under the chosen sequence duration for two successive applications of $\mathcal{U}(T)$. This justifies the spin-motion decoupling for the spin-motion echo.

II. ANALYSIS OF THE ADIABATIC DRESSING PROTOCOL

A. Adiabaticity and finite Rydberg lifetime: A case study

During the adiabatic dressing sequence, we require the state to be smoothly connected to the instantaneous eigenstates. This preserves the population of all basis states $\mathcal{C}$ after an adiabatic sequence. To quantify the adiabaticity of a sequence, we define the in-adiabaticity

$$\mathcal{E}(T) = 1 - \max_{\mathcal{C}} |\langle \mathcal{C}|\,\mathcal{U}(T)\,|\mathcal{C}\rangle|, \tag{S39}$$

where $\mathcal{C}$ is a basis state (configuration) of the Pauli z-basis. We evaluate $\mathcal{E}$ for all basis states and take the maximum. Importantly, $\mathcal{E}$ measures how adiabatic the dressing sequence is. For a completely adiabatic sequence, $\mathcal{E}=0$. As we show later, increasing the sequence duration T improves the in-adiabaticity.

On the other hand, we excite Rydberg states coherently during the dressing sequence. With increasing sequence duration T, the spontaneous decay probability p increases as well, leading to higher decoherence. The decay probability p is approximately given by the time-integrated Rydberg excitation $\int_0^T \mathrm{d}t \sum_j \langle n_j\rangle(t)$ during the sequence with decay rate Γ of Rydberg state $|r\rangle$ as

$$p(\Omega_0 T) = 1 - \exp\left(-\Gamma\int_0^T \mathrm{d}t \sum_j \langle n_j\rangle(t)\right) \approx \Gamma\int_0^T \mathrm{d}t \sum_j \langle n_j\rangle(t). \tag{S40}$$

In order for the system to stay coherent during a dressing sequence, $p \ll 1$ is required. To demonstrate the trade-off between adiabaticity and decoherence due to sponatenoues decay, we study the system discussed in Fig. 3 of the main text in different parameter regimes, see Tab. I.

	Ω_0/Γ	Δ_0/Γ	Δ_1/Γ	V/Γ	ΓT	$\varphi_\uparrow/(2\pi)$	$\varphi_{\uparrow\uparrow}/(2\pi)$	$\varphi_{\uparrow\uparrow\uparrow}/(2\pi)$	p	$\mathcal{E}$
(**1**)	100	800	0	400	2.00	8.09	13.91	18.98	4.0×10^{-1}	7.9×10^{-08}
(**2**)	100	800	200	400	2.00	3.93	7.58	11.04	1.8×10^{-1}	1.6×10^{-07}
(**3**)	1000	8000	0	4000	0.20	8.09	13.91	18.98	4.0×10^{-2}	7.9×10^{-08}
(**4**)	1000	8000	0	8000	0.20	8.09	13.41	17.94	3.5×10^{-2}	2.3×10^{-07}
(**5**)	1000	8000	0	4000	0.05	4.05	6.96	9.49	9.9×10^{-3}	1.6×10^{-07}
(**6**)	1000	8000	0	4000	0.01	0.45	0.73	0.98	2.2×10^{-3}	4.3×10^{-02}

TABLE I. **Adiabaticity vs. decoherence from spontaneous decay of Rydberg states.** The rows (**1** − **6**) compare dressing sequences with different parameter sets with Rabi frequency Ω_0/Γ, detunings $\Delta_{0,1}$, interaction strength V and sequence duration ΓT scaled by the decay rate Γ. For all sets, we calculate the dynamical phases φ_α, see Eqs. (13) of the main text, the in-adiabaticity $\mathcal{E}$ and the decay probability p. (**1**) Resonant dressing sequence (Δ_1=0) for same parameters as in Fig. 3(b) of main text. Here, Rydberg states can be excited resonantly. (**2**) Compared to (1), for a dressing sequence which does not approach resonance ($\Delta_1 = 200\Gamma$), dynamical phases reduce. (**3**) In comparison to case (1), all parameters are scaled by increasing Ω_0. This decreases the decay probability p. (**4**) In comparison to case (3), increasing the interaction strength V, leads to decreased dynamical phases but improved $\mathcal{E}$. This can be explained by the changed energy spectrum of the system. (**5**) Compared to (3), a decreased sequence duration ΓT leads to lower p but worse $\mathcal{E}$, where the dynamic phases decrease. (**6**) A significantly longer sequence duration compared to (5), lowers p but increases the in-adiabaticity drastically.

B. Relative strength of multi-body interactions

The effective Hamiltonian of the adiabatic dressing sequence can be decomposed into contributions of k-body interactions. Their relative strengths are affected by the distance dependent Rydberg interaction $V(a_0)$. The three-body interaction strength $\mathcal{V}_3$ increases for shorter interatomic distance a_0. Increasing a_0, the two-body interaction strength starts dominating. This is seen in Fig. S2, where we show the ratio $\mathcal{V}_3/\mathcal{V}_2$.

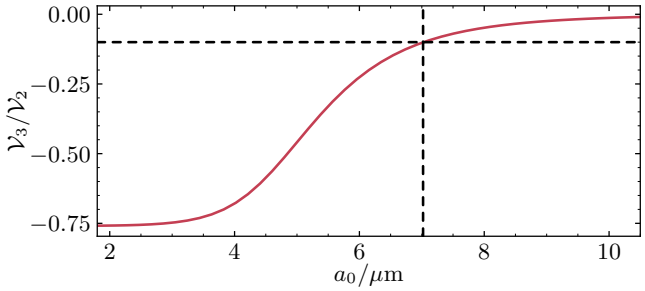

FIG. S2. **Ratio of three-body and two-body interaction strength.** Ratio of the three-body and two-body interaction strength $\mathcal{V}_3/\mathcal{V}_2$ for the parameters shown in Fig. 3(d) of the main text. With decreasing distance a_0, the three-body interaction dominates the two-body one. Specifically, for distances $a_0 \geq 7\,\mu$m, it is $\mathcal{V}_3 \leq 10/\mathcal{V}_2$.

C. Spin-motion coupling

In the main text, we consider an adiabatic dressing sequence of three spins without spin-motion coupling ($G = \eta = 0$). Now, we quantify the impact of finite spin-motion coupling and discuss under which conditions it becomes relevant. Therefore, we study a system of $N = 2$ spins coupled to a harmonic oscillator each. We analyze the spectrum of instantaneous eigenstates which illustrates the impact of the oscillatory energy levels. Additionally, we calculate the time evolution of the purity $P = \mathrm{tr}[(\mathrm{tr}_{\mathrm{osc}}[\rho(t)])^2]$ of the spin system, where $\mathrm{tr}_{\mathrm{osc}}$ is the partial trace over the oscillatory degrees of freedom and $\rho(t)$ the density matrix of the full quantum system. A purity of $P < 1$ signals entanglement between spin- and oscillatory degrees of freedom.

Figures S3(a-c) show the instantaneous eigenstates λ_α during a dressing sequence. Panel (a) shows the spectrum without spin-phonon coupling with the same parameters as in the main text. The introduction of harmonic oscillators subdivides the energy eigenstates into multiple with energy separation ω, see Figs. S3(b,c). A smaller separation of nearby eigenstates, leads to a higher transition probability between them during the sequence. This transitions ultimately lead to spin-motion entanglement. Thus, a longer sequence duration or an increased trapping frequency ω

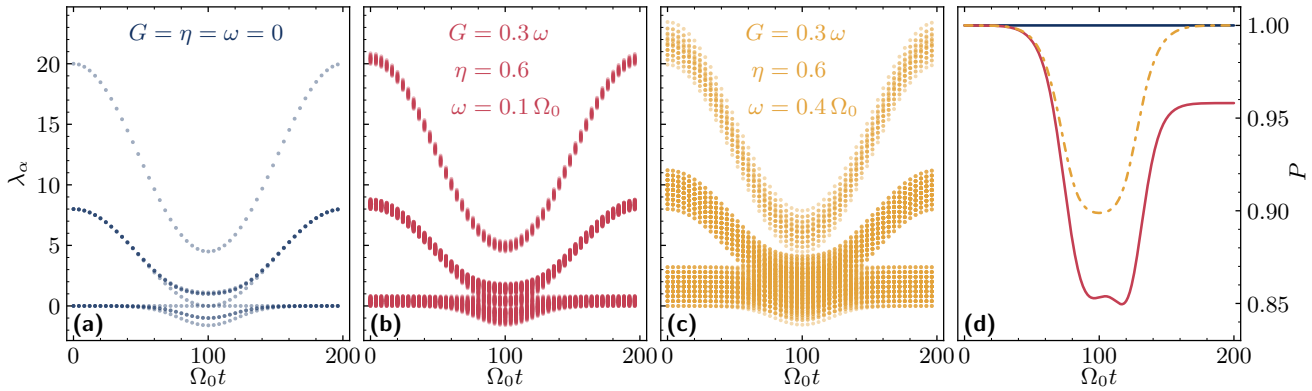

FIG. S3. **Impact of spin-motion coupling during a dressing sequence. (a)** Instantaneous eigenstates λ_α in the absence of spin-motion coupling for same parameters as in Fig. 3 of the main text. **(b)** The introduction of spin-motion coupling splits the eigenstates of different oscillator modes. The energy differences between neighboring levels is given by ω. **(c)** Increasing the trapping frequency ω increases the energy splitting and thus suppresses spin-motion entanglement. **(d)** Evolution of the spin purity P under these conditions: without spin-motion coupling (blue), P remains at one, indicating no spin-motion entanglement. Introducing spin-motion coupling with $\omega = 0.1\Omega_0$ leads to a purity of $P(T) = 0.958$ (red), meaning entanglement between spins and oscillators arises during the sequence. Increasing the trapping frequency ω, significantly reduces spin-motion coupling as confirmed by increased spin purity $P(T) \approx 1 - 3 \times 10^{-6}$. All simulations use $N = 2$ spins and a truncation of the harmonic oscillators up to 5 excitations each.

leads to less spin-motion entanglement.

In Fig. S3(d), we analyze the purity P of the three parameter sets. For no spin-motion coupling, the purity remains one during the whole sequence. Thus, the spins do not entangle with the motional degrees of freedom. For $\omega = 0.1\,\Omega_0$, we observe a decrease of the purity during the sequence until it finally reaches $P(T) = 0.958$ at the end of the sequence. Thus, spins and oscillators entangle during a dressing sequence. When increasing the trapping frequency to $\omega = 0.4\,\Omega_0$, the purity increases to $P(T) = 1 - 3 \times 10^{-6}$. Consequently, spin-motion entanglement can be reduced by increasing the trapping frequency.

[1] V. Bharti, S. Sugawa, M. Kunimi, V. S. Chauhan, T. P. Mahesh, M. Mizoguchi, T. Matsubara, T. Tomita, S. de Léséleuc, and K. Ohmori, Strong Spin-Motion Coupling in the Ultrafast Dynamics of Rydberg Atoms, Physical Review Letters **133**, 093405 (2024).

A.6. [P6] - Creating squeezed and non-classical collective motional many-body states through stroboscopic Rydberg dressing

Creating squeezed and non-classical collective motional many-body states through stroboscopic Rydberg dressing

Roman Wußler,[1] Chris Nill,[1,2] Sylvain de Léséleuc,[3] Christian Groß,[4] and Igor Lesanovsky[1,5]

[1] *Institut für Theoretische Physik and Center for Integrated Quantum Science and Technology, Universität Tübingen, Auf der Morgenstelle 14, 72076 Tübingen, Germany*
[2] *Institute for Applied Physics, University of Bonn, Wegelerstraße 8, 53115 Bonn, Germany*
[3] *RIKEN Center for Quantum Computing (RQC), 351-0198 Wako, Japan*
[4] *Physikalisches Institut and Center for Integrated Quantum Science and Technology, Universität Tübingen, Auf der Morgenstelle 14, 72076 Tübingen, Germany*
[5] *School of Physics and Astronomy and Centre for the Mathematics and Theoretical Physics of Quantum Non-Equilibrium Systems, The University of Nottingham, Nottingham, NG7 2RD, United Kingdom*

Realizing conditional quantum operations, e.g., quantum gates, for quantum computing and simulation requires controlled interactions between particles. Often, these interactions depend on the interparticle distance, and accordingly, an uncertainty of the relative particle position may translate into gate infidelities. We consider here a quantum computing platform based on an array of neutral atoms and present a method that allows to reduce the uncertainty of all interatomic distances. Our approach exploits the coupling between atomic motion and stroboscopically excited atomic Rydberg states. It allows to collectively squeeze the modes corresponding to interatomic displacements, thereby reducing distance fluctuations down to a fraction of the motional vacuum state. Furthermore, the method permits the creation of non-classical states with substantial Wigner negativity. These correlated states may allow reducing motional decoherence, increasing gate fidelity, and potentially yield a resource for quantum-enhanced metrology.

Introduction — Programmable arrays of laser-cooled atoms [1–6], polar molecules [7–9], and trapped ions [10–12] have emerged as leading platforms for quantum simulation, computation, and precision sensing. In all these systems, quantum operations are mediated by interactions that depend on interparticle distances [13–15]. Thus, the coupling of electronic (spin) degrees of freedom to atomic motion is an inherent feature of any interatomic interaction-based quantum operation [16–18].

Controlling the motional state is therefore essential. This is typically achieved by optical trapping [19–21] and laser cooling techniques [22, 23] that suppress free atomic motion and thermal fluctuations to prepare atoms near their motional ground state. However, a fundamental residual quantum uncertainty persists even at zero temperature [24–26]. Through the distance dependence of interactions, these quantum fluctuations translate directly into gate infidelities and decoherence [27–31].

A natural strategy to push below this ground-state limit is to prepare motionally squeezed states [32–35]. Single-atom motional squeezing has recently been demonstrated experimentally [36], which directly lowers the uncertainty of interatomic distances. However, in a many-atom array, an even stronger reduction can be achieved by synchronizing the motion of neighboring atoms. This requires squeezing the collective vibrational modes of the array, which is an inherent many-body operation.

Here, we demonstrate how many-body squeezed motional states can be realized in a one-dimensional chain of trapped atoms via stroboscopic Rydberg dressing [37–40]. A Bloch-Messiah decomposition [41] of the stroboscopic time-evolution operator yields closed-form expressions for the motional state of arbitrarily long chains. For experimentally feasible parameters, we demonstrate that the variance, averaged over all nearest-neighbor distances, can be reduced down to 19% of the ground-state value. Moreover, we show that by exploiting the non-quadratic nature of the Rydberg interaction potential, the generation of non-classical motional states [35, 40, 42–44] with a Wigner negativity of 0.109 is possible.

Model — We consider a chain of N two-level atoms with mass m_0 and mean spacing a_0. The internal states are an electronic ground state $|\downarrow\rangle$ and a Rydberg state $|\uparrow\rangle$ [Fig. 1(a)]. We consider that both electronic states are trapped with the same trapping frequency ω [19, 45, 46]. When two neighboring atoms are simultaneously excited to the state $|\uparrow\rangle$, they interact via the van der Waals potential $V(r) = C_6/r^6$. This is a mechanism that couples electronic and motional degrees of freedom. In the following, we restrict ourselves to the consideration of nearest-neighbor interactions [1, 2]. This is justified by the rapid $1/r^6$ decay of the van der Waals potential, which suppresses next-nearest-neighbor contributions by a factor of $(a_0/2a_0)^6 = 1/64$. The Hamiltonian reads ($\hbar = 1$)

$$H_0 = \omega \sum_{j=1}^{N} a_j^\dagger a_j + \sum_{j=1}^{N-1} V(a_0 + x_{j+1} - x_j) n_j n_{j+1}. \quad (1)$$

Here $n_j = |\uparrow\rangle\langle\uparrow|_j$ is the projector onto the Rydberg state of the j-th atom, and each trapping potential is modeled as a one-dimensional harmonic oscillator with ladder operators a_j and $a_j^\dagger$, describing the atomic motion along the

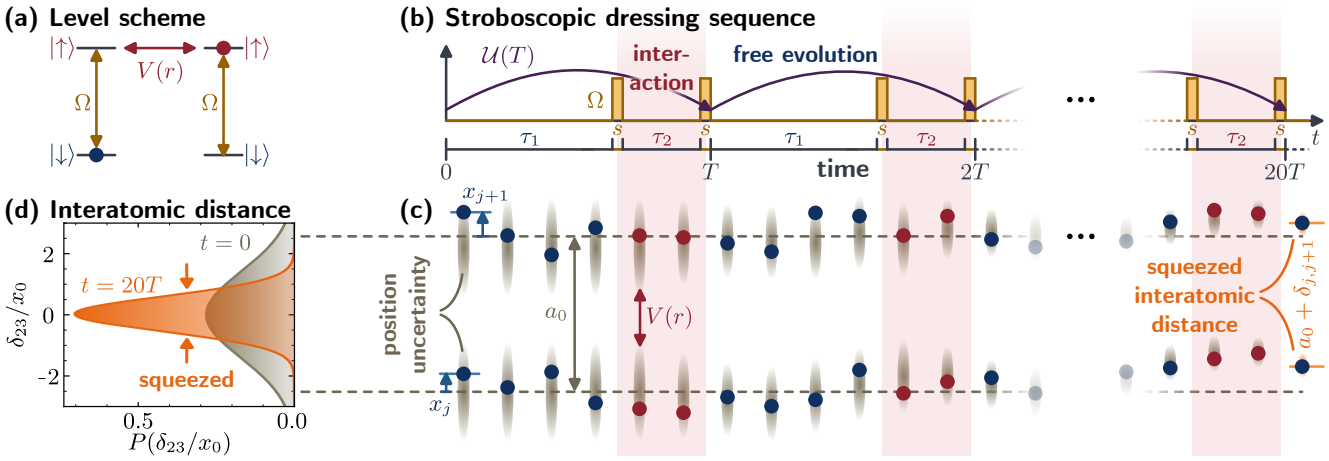

FIG. 1. **Stroboscopic Rydberg dressing for generating squeezed motional states.** (a) Level scheme of the atom's electronic states: ground state $|\downarrow\rangle$ (blue) and Rydberg state $|\uparrow\rangle$ (red), coupled by a laser with Rabi frequency Ω. Neighboring atoms simultaneously in $|\uparrow\rangle$ interact via the van der Waals potential $V(r)$. (b) The stroboscopic dressing protocol proceeds in periodic cycles of duration T, repeated up to $20T$ as shown. Each cycle consists of free evolution of duration τ_1, a resonant π-pulse of duration s and Rabi frequency Ω that transfers all atoms to $|\uparrow\rangle$, an interaction interval of duration τ_2 during which atoms in $|\uparrow\rangle$ interact via $V(r)$ and develop motional correlations, and a second π-pulse returning all atoms to $|\downarrow\rangle$. (c) Schematic time evolution of two neighboring atoms confined in optical traps with equilibrium spacing a_0 and displacements x_j from their respective equilibrium positions. Grey shading indicates the single-atom position variance of each atom. After multiple dressing cycles, the atoms' motions become correlated, reducing the fluctuations of the interatomic distance $\delta_{j,j+1} = x_{j+1} - x_j$ below the ground-state level (squeezed interatomic distance, right). (d) Probability distribution of the interatomic distance δ_{23} at $t = 0$ (motional ground state, broad) and after $m = 20$ dressing cycles (narrow), demonstrating the reduction of distance fluctuations. Results are calculated from Eqs. (EM5) and (EM6) for $N = 5$ atoms using the parameters of Eq. (EM1).

chain axis. The displacement of atom j from its equilibrium position is $x_j = x_0(a_j + a_j^\dagger)$, with the harmonic oscillator length $x_0 = 1/\sqrt{2m_0\omega}$.

We laser-excite the atoms with a stroboscopic pulse sequence, shown in Fig. 1(b). It starts from the product ground state $|\Psi(0)\rangle = |\downarrow, 0\rangle^{\otimes N}$ and proceeds in repeated cycles of duration T. The time evolution operator for m cycles is given by

$$\mathcal{U}(mT) = \Big(\underbrace{e^{-is(H_\mathrm{L}+H_0)}}_{\mathcal{U}_\pi}\, e^{-i\tau_2 H_0}\, \mathcal{U}_\pi\, e^{-i\tau_1 H_0}\Big)^m, \qquad (2)$$

and to be read from right to left: each cycle starts with free evolution under the Hamiltonian H_0 [Eq. (1)] for time τ_1, followed by a resonant π-pulse $\mathcal{U}_\pi$ of duration s that—assuming it is sufficiently strong—simultaneously excites all atoms to $|\uparrow\rangle$. This short pulse is followed by an interval of length τ_2 in which the atoms are in the Rydberg state and the evolution is governed by H_0. Finally, a second π-pulse returns all atoms to $|\downarrow\rangle$. The laser Hamiltonian

$$H_\mathrm{L} = \frac{\pi}{2s}\sum_{j=1}^{N}\Big(|\downarrow\rangle\langle\uparrow|_j\, e^{-i\kappa x_j} + |\uparrow\rangle\langle\downarrow|_j\, e^{i\kappa x_j}\Big) \qquad (3)$$

generates the π-pulses. Here, κ is the laser wave vector projected along the chain axis, and the Lamb-Dicke parameter $\eta = \kappa x_0$ quantifies the photon-recoil-induced motional excitation [27, 47, 48]. We consider the Rydberg interaction interval τ_2 to be orders of magnitude shorter than the typical Rydberg state lifetime of $\sim$50 µs, such that spontaneous emission during each dressing cycle is negligible [24, 49, 50].

Analytical treatment — To enable an analytical treatment, we work in the limit of fast and strong π-pulses, $\Omega = \pi/s \gg \omega, V(r)$, in which H_0 can be neglected during the pulses. This simplifies the operator describing the π-pulses to $\mathcal{U}_\pi = e^{-isH_\mathrm{L}}$. Within this limit, the application of $\mathcal{U}_\pi$ immediately switches all atoms between the electronic ground state and the Rydberg state. This approximation guarantees that all atoms remain in the electronic ground state at integer multiples of T. Its validity—quantified by the residual Rydberg population at stroboscopic times—improves with decreasing s, as we validate in the End Matter. The time-evolution operator $\mathcal{U}(mT)$ therefore acts solely on the motional degrees of freedom.

During the Rydberg interaction phase τ_2, all atoms simultaneously occupy the Rydberg state and experience mutual repulsion, which couples the motion of neighboring atoms, [Fig. 1(c)]. This coupling transforms the motional eigenmodes of the chain from local single-atom vibrations into collective normal modes, which can be written as $b_k = \sum_j Q_{kj} a_j$, i.e., linear combinations of the single-atom modes a_j with transformation matrix elements $Q_{1j} = 1/\sqrt{N}$ and $Q_{kj} =$

$\sqrt{2/N}\cos\{(j-1)(k-\frac{1}{2})\pi/N\}$ for $2 \le j \le N$. While b_1 describes the center-of-mass motion of the entire chain, all higher modes b_k with $k \ge 2$ capture relative motion between atoms and thus directly govern the interatomic distances. To obtain closed-form expressions for the dynamics of these modes, we expand the van der Waals potential to second order around the equilibrium distance a_0, yielding $V(r) \approx V_0 + V_1(r-a_0) + \frac{1}{2}V_2(r-a_0)^2$, where $V_0 = V(a_0)$, $V_1 = \partial V/\partial r|_{a_0}$, and $V_2 = \partial^2 V/\partial r^2|_{a_0}$ are the value, gradient, and curvature of the potential at equilibrium. This approximation is controlled by x_0/a_0; higher-order corrections are suppressed by successive powers of x_0/a_0 and are explored later on. Within this quadratic approximation, a Bloch-Messiah decomposition of $\mathcal{U}(mT)$ in the basis of the normal modes b_k yields a physically transparent structure: the protocol independently squeezes, displaces, and rotates each normal mode and, up to a global phase, the time evolution operator can be written as

$$\mathcal{U}(mT) = \prod_{k=1}^{N} \mathcal{S}_k(Z_k)\mathcal{D}_k(J_k)\mathcal{R}_k(\beta_k). \tag{4}$$

Here, $\mathcal{S}_k(Z_k) = \exp\{\frac{Z_k^*}{2}b_k^2 - \frac{Z_k}{2}(b_k^\dagger)^2\}$, $\mathcal{D}_k(J_k) = \exp\{J_k b_k^\dagger - J_k^* b_k\}$, and $\mathcal{R}_k(\beta_k) = \exp\{i\beta_k b_k^\dagger b_k\}$ are the single-mode squeezing, displacement, and rotation operators. The vibrational modes hence undergo Gaussian dynamics and all parameters Z_k, J_k, β_k are known in closed form, see End Matter. This result holds for chains of arbitrary length N.

The displacement $\mathcal{D}_k(J_k)$ of relative modes $k \ge 2$ depends on the potential gradient V_1, which imprints a force between atoms. The center-of-mass displacement J_1 is independent of V_1. It arises solely due to momentum transfer of the photon recoil during the π-pulses, quantified by the Lamb-Dicke parameter η.

Squeezing $\mathcal{S}_k(Z_k)$ of relative modes [Fig. 1(d)] originates from the interaction potential curvature V_2, which modifies the relative motional mode trap frequencies. During stroboscopic dressing, the system alternates between free evolution (duration τ_1) at the bare frequency ω and an interaction phase (duration τ_2). This interaction shifts each relative mode to an effective frequency $\tilde{\omega}_k = \sqrt{\omega^2 + 2\lambda_k x_0^2 V_2 \omega}$, where the geometric factor $\lambda_k = 4\sin^2\{(k-1)\pi/2N\}$ encodes the mode index and chain length. This periodic alternation between frequencies acts as a parametric modulation that squeezes every relative mode ($Z_k \neq 0$); if $V_2 = 0$, squeezing vanishes. Analogous to single-atom squeezing via trap frequency modulation [36], this mechanism drives collective normal modes and creates correlations between atoms.

Many-body motional squeezing — Having a closed-form expression for the time evolution of the motional state, our goal is now to engineer the stroboscopic dressing such that quantum fluctuations of the interatomic distances $\delta_{j,j+1} = x_{j+1} - x_j$ are reduced below their ground-state value [Fig. 1(d)]. To quantify these fluctuations we use the variance

$$\mathrm{Var}(\delta_{j,j+1}) = \mathrm{Var}(x_{j+1}) + \mathrm{Var}(x_j) - 2\,\mathcal{C}_{j,j+1}. \tag{5}$$

Here, $\mathcal{C}_{j,k} = \langle x_j x_k\rangle - \langle x_j\rangle\langle x_k\rangle$ is the covariance matrix which describes correlations between atoms, where the diagonal elements $\mathrm{Var}(x_j) = \mathcal{C}_{j,j}$ represent the individual variances. Equation (5) shows two complementary mechanisms to reduce interatomic distance uncertainty: (i) squeezing the individual atomic positions to minimize $\mathrm{Var}(x_j)$, and (ii) correlating the motion of neighboring atoms to achieve $\mathcal{C}_{j,j+1} > 0$, meaning that the atoms' motion synchronizes. Single-atom squeezing, which was recently demonstrated in [36], exploits solely the first mechanism. We show now that the pulsed excitation of Rydberg states additionally synchronizes the atomic positions, exploiting both mechanisms simultaneously. The build-up of positive motional correlations constitutes a many-body effect, enabling a further suppression of distance uncertainty beyond what single-atom squeezing could achieve.

Figure 2 illustrates the build-up of positional correlations and the dynamics of interatomic distances for a chain

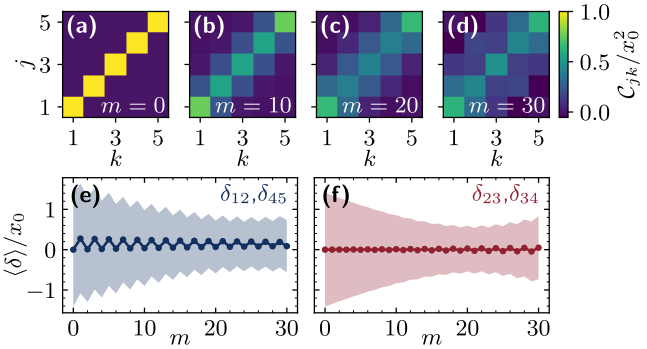

FIG. 2. **Build-up of positional correlations and dynamics of interatomic distances.** (a) - (d) Positional covariance matrix $\mathcal{C}_{jk}/x_0^2$ after $m = 0, 10, 20$ and 30 dressing cycles. Starting from the motional ground state, which exhibits no interatomic correlations (a), the protocol generates positional correlations between neighboring atoms (b), (c). At $m = 20$ (c), reduced diagonal elements (single-atom variances) and increased off-diagonal elements (inter-atom correlations) combine to yield significant squeezing of the interatomic distances. As the sequence continues (d), variances grow again while correlations persist. (e), (f) Mean interatomic distance $\langle\delta\rangle/x_0$ (solid lines) of a chain of $N = 5$ atoms, with shading indicating one standard deviation about the mean versus dressing cycle m for (e) outer atom pairs (δ_{12}, δ_{45}) and (f) inner atom pairs (δ_{23}, δ_{34}). Outer atoms oscillate with a larger amplitude due to asymmetric boundary forces, while inner atoms remain closer to their equilibrium position. The choice $\omega T \gtrsim \pi$ keeps the mean displacement bounded, see Supplemental Material [51]. In all panels, we use Eqs. (EM5), (EM6), and the parameters from Eq. (EM1), which were optimized to minimize the variance of the interatomic distances after $m = 20$ dressing cycles.

with $N = 5$ atoms. Starting from the motional ground state, which exhibits no interatomic correlations (a), stroboscopic dressing progressively generates positive off-diagonal entries in the covariance matrix $\mathcal{C}_{jk}$ (b),(c) while simultaneously reducing the diagonal entries (single-atom variances). For the chosen parameters from Eq. (EM1), after $m = 20$ cycles (c), strongly reduced diagonal elements and large off-diagonal elements combine to yield significant squeezing of the interatomic distances. Here, the variance, averaged over all nearest-neighbor distances, is approximately 19% of the initial ground-state value [see Eq. (5)]. Notably, the build-up of interatomic correlations accounts for a substantial portion of this effect: the covariance term $-2\mathcal{C}_{j,j+1}$ alone lowers the averaged variance by an additional 28% of the ground-state value, highlighting the significant advantage of establishing interatomic correlations over single-atom squeezing [36]. As the sequence continues, the single-atom variances grow again while the positional correlations persist (d). In panels (e) and (f), outer atom pairs (δ_{12}, δ_{45}) exhibit larger mean displacement amplitudes than inner atom pairs (δ_{23}, δ_{34}), since inner atoms experience counteracting nearest-neighbor restoring forces from both sides.

Non-classical states — The analytical results derived via the Bloch-Messiah decomposition in the previous discussion rely on the expansion of the interaction potential $V(r)$ around the equilibrium interatomic distances. In the following, we demonstrate that higher-order terms break the Gaussianity of the evolution and how this can be leveraged to generate non-classical states. As previously noted, the quadratic approximation is valid when $x_0/a_0 \ll 1$. To explore the boundaries of our analytical model, we compare the system's dynamics under the approximated quadratic potential with those under the exact van der Waals potential. As an indicator, we use the Wigner function $W(\delta_{12}, v_{12})$ of the relative coordinate δ_{12} and relative velocity $v_{12} = v_2 - v_1$ for $N = 2$ atoms after $m = 2$ dressing cycles. Here, the single-atom velocities are represented by $v_j = iv_0(a_j^\dagger - a_j)$, where $v_0 = \omega x_0$ denotes the characteristic ground-state velocity.

For $x_0/a_0 \approx 0.009$ [Eq. (EM1)], the atomic wave function is well localized compared to a_0, and the quadratic approximation is excellent. As seen in Fig. 3, the incorporation of higher order terms does not alter the result, making the Wigner functions in (a) and (b) indistinguishable, both showing the squeezed state predicted by the Bloch-Messiah decomposition. This confirms that the analytical framework of the previous section faithfully captures the full dynamics in this regime. The situation changes qualitatively for $x_0/a_0 \approx 0.057$ [Eq. (EM2)], where the wave function is so wide that it is also sensitive to changes in the potential's curvature. While the quadratic model still predicts a Gaussian

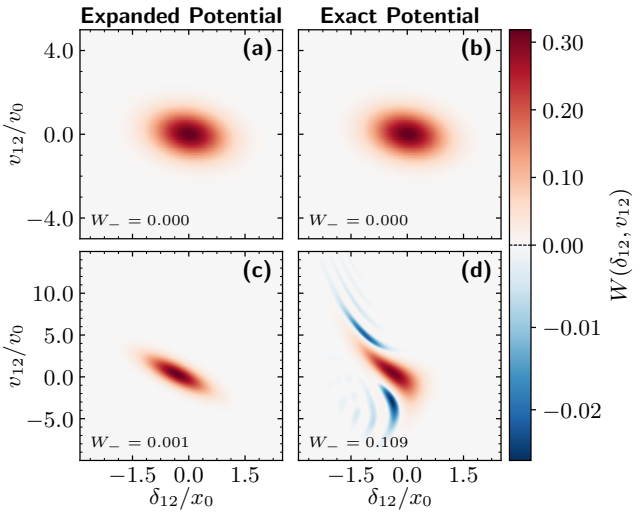

FIG. 3. **Non-classical motional states.** Wigner functions $W(\delta_{12}, v_{12})$ of the relative coordinate δ_{12} and relative velocity v_{12} for $N = 2$ atoms after $m = 2$ dressing cycles, computed using the second-order Taylor expansion of the interaction potential (left column) and the exact van der Waals potential (right column). (a), (b) For parameters from Eq. (EM1) with $x_0/a_0 \approx 0.009$, the harmonic approximation faithfully reproduces the exact result: both Wigner functions are Gaussian and squeezed. (c), (d) For parameters from Eq. (EM2) with $x_0/a_0 \approx 0.057$, the harmonic approximation yields a Gaussian squeezed state (c), but the exact dynamics produces a strongly non-Gaussian distribution with pronounced negative regions, indicated with blue in (d), signaling genuine quantum non-classicality induced by higher-order terms of the van der Waals potential.

squeezed state (c), the exact dynamics generates a Wigner function with pronounced negative regions (d), reaching a Wigner negativity of $W_- = 0.109$. This is an unambiguous signature of quantum non-classicality [52], which reveals that the higher-order contributions of the van der Waals interaction, often treated as a mere correction, act as a resource for generating non-classical motional states.

Discussion and outlook — The protocol is well within reach of current experiments. Both parameter sets [Eqs. (EM1) and (EM2)] employ ^{87}Rb atoms in optical tweezer arrays. Established sideband-cooling techniques prepare the required initial state $|\downarrow, 0\rangle^{\otimes N}$, with near-unity ground-state fidelity recently demonstrated [25].
A fundamental requirement of our analytical framework is that the laser drive constitutes by far the largest energy scale in the system ($\Omega \gg \omega, V(r)$). With Rabi frequencies of several hundreds of megahertz, this is satisfied for both configurations. Furthermore, these driving frequencies remain smaller than the energy separation to adjacent Rydberg levels, see End Matter. This large detuning effectively suppresses unwanted transitions and justifies

our approximation of a strict two-level system.
Parameter set Eq. (EM1) assumes a spacing of $a_0 = 2.7\,\mu\text{m}$ and a trap frequency $\omega = 2\pi \times 100\,\text{kHz}$ — values achievable in optical tweezer arrays [36]. The non-classical regime [Eq. (EM2)] requires a smaller interatomic spacing $a_0 = 1\,\mu\text{m}$, corresponding to tighter traps already accessible with state-of-the-art setups [40]. For these configurations, ten dressing cycles complete in $\sim 50\,\mu\text{s}$ ($T = 4.98\,\mu\text{s}$) and $\sim 300\,\mu\text{s}$ ($T = 30\,\mu\text{s}$), respectively — well within atomic coherence times of several milliseconds. Furthermore, the impact of anharmonic tweezer potentials is analyzed in the Supplemental Material [51]: for current standard optical tweezers, the Wigner function experiences shearing and non-Gaussian deformations. While realizing purely Gaussian, strongly squeezed states will require improved trap harmonicity, this inherent anharmonicity is not strictly a limitation. Instead, it can be actively leveraged as a resource for generating genuine non-classical many-body motional states [53].

Looking ahead, our findings suggest several immediate technological applications:

(i) Motional decoherence currently limits the fidelity of distance-sensitive operations, such as Rydberg interaction gates [2, 27, 54]. Integrating the squeezing protocol could improve gate performance by mitigating positional uncertainty during the gate operation.

(ii) Our protocol could directly enhance the performance of cooperative atom-light interfaces that exhibit sub- and superradiance [55–57]. In these systems, positional uncertainty worsens the delicate interference mechanisms necessary for collective emission, leading to a broadened linewidth. Utilizing the proposed squeezing approach to suppress interatomic distance fluctuations would mitigate this decoherence.

(iii) The engineered reduction of distance fluctuations directly translates to a narrowed linewidth of distance-dependent spectral features. Squeezed motional states could thus act as a resource for high-precision measurements [58, 59] of Rydberg interaction coefficients and fundamental atomic properties.

(iv) The facilitated excitation of Rydberg atoms (anti-blockade) is rather sensitive to the interatomic distances of neighboring atoms [60, 61]. Therefore, the proposed motional squeezing could stabilize these dynamics.

Data Availability — Data and code corresponding to this manuscript are publicly available [62].

Acknowledgments — This work received funding from the Horizon Europe program HORIZON-CL4-2022-QUANTUM-02-SGA via the project 101113690 (PASQuanS2.1), the Deutsche Forschungsgemeinschaft within the research units FOR 5413 (Grant No. 465199066) and FOR 5522 (Grant No. 499180199) as well as from the European Union through the ERC grant OPEN-2QS (Grant No. 101164443). We also acknowledge funding through JST-DFG 2024: Japanese-German Joint Call for Proposals on "Quantum Technologies" (Japan-JST-DFG-ASPIRE 2024) under JST Grand No. JPMJAP24C2 and DFG Grant No. 554561799, and from the Alfried Krupp von Bohlen and Halbach Foundation. RW acknowledges support from the German Academic Scholarship Foundation (Studienstiftung des deutschen Volkes). SdL thanks V. Magro for discussion and critical reading of the manuscript.

[1] A. Browaeys and T. Lahaye, Many-body physics with individually controlled Rydberg atoms, Nature Physics **16**, 132 (2020).
[2] M. Saffman, T. G. Walker, and K. Mølmer, Quantum information with Rydberg atoms, Reviews of Modern Physics **82**, 2313 (2010).
[3] C. S. Adams, J. D. Pritchard, and J. P. Shaffer, Rydberg atom quantum technologies, Journal of Physics B: Atomic, Molecular and Optical Physics **53**, 012002 (2019).
[4] D. Bluvstein, S. J. Evered, A. A. Geim, S. H. Li, H. Zhou, T. Manovitz, S. Ebadi, M. Cain, M. Kalinowski, D. Hangleiter, J. P. Bonilla Ataides, N. Maskara, I. Cong, X. Gao, P. Sales Rodriguez, T. Karolyshyn, G. Semeghini, M. J. Gullans, M. Greiner, V. Vuletić, and M. D. Lukin, Logical quantum processor based on reconfigurable atom arrays, Nature **626**, 58 (2023).
[5] M. Endres, H. Bernien, A. Keesling, H. Levine, E. R. Anschuetz, A. Krajenbrink, C. Senko, V. Vuletic, M. Greiner, and M. D. Lukin, Atom-by-atom assembly of defect-free one-dimensional cold atom arrays, Science **354**, 1024 (2016).
[6] M. Grotti, S. Marzella, G. Bettonte, D. Ottaviani, and E. Ercolessi, Practical Use Cases of Neutral Atoms Quantum Computers (2025), arXiv:2510.18732 [quant-ph].
[7] L. D. Carr, D. DeMille, R. V. Krems, and J. Ye, Cold and ultracold molecules: science, technology and applications, New Journal of Physics **11**, 055049 (2009).
[8] D. K. Ruttley, T. R. Hepworth, A. Guttridge, and S. L. Cornish, Long-lived entanglement of molecules in magic-wavelength optical tweezers, Nature **637**, 827 (2025).
[9] B. Xiang and W. Xiong, Molecular Polaritons for Chemistry, Photonics and Quantum Technologies, Chemical Reviews **124**, 2512 (2024).
[10] J. Eschner, G. Morigi, F. Schmidt-Kaler, and R. Blatt, Laser cooling of trapped ions, Journal of the Optical Society of America B **20**, 1003 (2003).
[11] C. D. Bruzewicz, J. Chiaverini, R. McConnell, and J. M. Sage, Trapped-ion quantum computing: Progress and challenges, Applied Physics Reviews **6**, 021314 (2019).
[12] I. A. Chernyshev, R. C. Farrell, M. Illa, M. J. Savage, A. Maksymov, F. Tripier, M. A. Lopez-Ruiz, A. Arrasmith, Y. de Sereville, A. Brodutch, C. Girotto, A. Kaushik, and M. Roetteler, Pathfinding quantum simulations of neutrinoless double-β decay, Nature Communications **17**, 1826 (2026).
[13] C. Monroe, W. Campbell, L.-M. Duan, Z.-X. Gong, A. Gorshkov, P. Hess, R. Islam, K. Kim, N. Linke, G. Pagano, P. Richerme, C. Senko, and N. Yao, Programmable quantum simulations of spin systems with

trapped ions, Reviews of Modern Physics **93**, 025001 (2021).
[14] X.-Q. Shao, S.-L. Su, L. Li, R. Nath, J.-H. Wu, and W. Li, Rydberg superatoms: An artificial quantum system for quantum information processing and quantum optics, Applied Physics Reviews **11**, 031320 (2024).
[15] S. Weber, C. Tresp, H. Menke, A. Urvoy, O. Firstenberg, H. P. Büchler, and S. Hofferberth, Calculation of Rydberg interaction potentials, Journal of Physics B: Atomic, Molecular and Optical Physics **50**, 133001 (2017).
[16] M. Anderlini, P. J. Lee, B. L. Brown, J. Sebby-Strabley, W. D. Phillips, and J. V. Porto, Controlled exchange interaction between pairs of neutral atoms in an optical lattice, Nature **448**, 452 (2007).
[17] M. M. Müller, M. Murphy, S. Montangero, T. Calarco, P. Grangier, and A. Browaeys, Implementation of an experimentally feasible controlled-phase gate on two blockaded Rydberg atoms, Physical Review A **89**, 032334 (2014).
[18] M. H. Goerz, T. Calarco, and C. P. Koch, The quantum speed limit of optimal controlled phasegates for trapped neutral atoms, Journal of Physics B: Atomic, Molecular and Optical Physics **44**, 154011 (2011).
[19] L. Ahlheit, C. Nill, D. Svirskiy, J. de Haan, S. Schroers, W. Alt, N. Stiesdal, I. Lesanovsky, and S. Hofferberth, Magic running- and standing-wave optical traps for Rydberg atoms, Physical Review A **111**, 013115 (2025).
[20] R. Grimm, M. Weidemüller, and Y. B. Ovchinnikov, Optical dipole traps for neutral atoms (Academic Press, 2000) pp. 95–170.
[21] T. Topcu and A. Derevianko, Possibility of triple magic trapping of clock and Rydberg states of divalent atoms in optical lattices, Journal of Physics B: Atomic, Molecular and Optical Physics **49**, 144004 (2016).
[22] A. M. Kaufman, B. J. Lester, and C. A. Regal, Cooling a Single Atom in an Optical Tweezer to Its Quantum Ground State, Physical Review X **2**, 041014 (2012).
[23] E. Clements, F. W. Knollmann, S. Corsetti, Z. Li, A. Hattori, M. Notaros, R. Swint, T. Sneh, M. E. Kim, A. D. Leu, P. Callahan, T. Mahony, G. N. West, C. Sorace-Agaskar, D. Kharas, R. McConnell, C. D. Bruzewicz, I. L. Chuang, J. Notaros, and J. Chiaverini, Sub-Doppler Cooling of a Trapped Ion in a Phase-Stable Polarization Gradient, Physical Review Letters **136**, 023201 (2026).
[24] N. Schine, A. W. Young, W. J. Eckner, M. J. Martin, and A. M. Kaufman, Long-lived Bell states in an array of optical clock qubits, Nature Physics **18**, 1067 (2022).
[25] A. L. Shaw, P. Scholl, R. Finkelstein, R. B.-S. Tsai, J. Choi, and M. Endres, Erasure cooling, control, and hyperentanglement of motion in optical tweezers, Science **388**, 845 (2025).
[26] M. A. Taylor, J. Knittel, and W. P. Bowen, Fundamental constraints on particle tracking with optical tweezers, New Journal of Physics **15**, 023018 (2013).
[27] F. Robicheaux, T. M. Graham, and M. Saffman, Photon-recoil and laser-focusing limits to Rydberg gate fidelity, Physical Review A **103**, 022424 (2021).
[28] X.-F. Shi, Suppressing Motional Dephasing of Ground-Rydberg Transition for High-Fidelity Quantum Control with Neutral Atoms, Physical Review Applied **13**, 10.1103/PhysRevApplied.13.024008 (2020).
[29] S. D. Jenkins, T. Zhang, and T. A. B. Kennedy, Motional dephasing of atomic clock spin waves in an optical lattice, Journal of Physics B: Atomic, Molecular and Optical Physics **45**, 124005 (2012).
[30] Y. Liu, Y. Sun, Z. Fu, P. Xu, X. Wang, X. He, J. Wang, and M. Zhan, Infidelity Induced by Ground-Rydberg Decoherence of the Control Qubit in a Two-Qubit Rydberg-Blockade Gate, Physical Review Applied **15**, 054020 (2021).
[31] J. Soto-Garcia and N. Chepiga, Infinite Randomness Criticality and Localization of the Floating Phase in Arrays of Rydberg Atoms Trapped with Nonperfect Tweezers, Phys. Rev. Lett. **136**, 056502 (2026).
[32] S. C. Burd, H. M. Knaack, R. Srinivas, C. Arenz, A. L. Collopy, L. J. Stephenson, A. C. Wilson, D. J. Wineland, D. Leibfried, J. J. Bollinger, D. T. C. Allcock, and D. H. Slichter, Experimental Speedup of Quantum Dynamics through Squeezing, PRX Quantum **5**, 020314 (2024).
[33] H.-Y. Lo, D. Kienzler, L. de Clercq, M. Marinelli, V. Negnevitsky, B. C. Keitch, and J. P. Home, Spin–motion entanglement and state diagnosis with squeezed oscillator wavepackets, Nature **521**, 336 (2015).
[34] L. Salvi, N. Poli, V. Vuletić, and G. M. Tino, Squeezing on Momentum States for Atom Interferometry, Physical Review Letters **120**, 033601 (2018).
[35] C. A. Rosiek, M. Rossi, A. Schliesser, and A. S. Sørensen, Quadrature Squeezing Enhances Wigner Negativity in a Mechanical Duffing Oscillator, PRX Quantum **5**, 030312 (2024).
[36] V. Lienhard, R. Martin, Y. T. Chew, T. Tomita, K. Ohmori, and S. de Léséleuc, Generation of Motional Squeezed States for Neutral Atoms in Optical Tweezers (2025), arXiv:2505.10092 [physics.atom-ph].
[37] N. U. Köylüoğlu, N. Maskara, J. Feldmeier, and M. D. Lukin, Floquet engineering of interactions and entanglement in periodically driven Rydberg chains (2024), arXiv:2408.02741 [quant-ph].
[38] J. Feldmeier, N. Maskara, N. U. Köylüoğlu, and M. D. Lukin, Quantum simulation of dynamical gauge theories in periodically driven Rydberg atom arrays (2024), arXiv:2408.02733 [quant-ph].
[39] C. Nill, S. de Léséleuc, C. Groß, and I. Lesanovsky, Resonant stroboscopic Rydberg dressing: Electron-motion coupling and multibody interactions, Physical Review A **111**, L041104 (2025).
[40] V. Bharti, S. Sugawa, M. Kunimi, V. S. Chauhan, T. P. Mahesh, M. Mizoguchi, T. Matsubara, T. Tomita, S. de Léséleuc, and K. Ohmori, Strong Spin-Motion Coupling in the Ultrafast Dynamics of Rydberg Atoms, Physical Review Letters **133**, 093405 (2024).
[41] G. Cariolaro and G. Pierobon, Reexamination of Bloch-Messiah reduction, Physical Review A **93**, 062115 (2016).
[42] M. O. Brown, S. R. Muleady, W. J. Dworschack, R. J. Lewis-Swan, A. M. Rey, O. Romero-Isart, and C. A. Regal, Time-of-flight quantum tomography of an atom in an optical tweezer, Nature Physics **19**, 569 (2023).
[43] O. Romero-Isart, A. C. Pflanzer, M. L. Juan, R. Quidant, N. Kiesel, M. Aspelmeyer, and J. I. Cirac, Optically levitating dielectrics in the quantum regime: Theory and protocols, Physical Review A **83**, 013803 (2011).
[44] D. Leibfried, D. M. Meekhof, B. E. King, C. Monroe, W. M. Itano, and D. J. Wineland, Experimental Determination of the Motional Quantum State of a Trapped Atom, Physical Review Letters **77**, 4281 (1996).
[45] C. Jansohn, A. Londoño, Y. Li, H. Nguyen, P. R. Berman, and A. Kuzmich, Magic-wavelength trapping of

alkali-metal Rydberg atoms: The role of landscape polarization modulation, Physical Review A **112**, L041101 (2025).
[46] D. Barredo, V. Lienhard, P. Scholl, S. de Léséleuc, T. Boulier, A. Browaeys, and T. Lahaye, Three-Dimensional Trapping of Individual Rydberg Atoms in Ponderomotive Bottle Beam Traps, Physical Review Letters **124**, 023201 (2020).
[47] A. Parvej and L. Mathey, Lamb-Dicke Dynamics of Interacting Rydberg Atoms Coupled to the Motion of an Optical Tweezer Array (2025), arXiv:2506.22669 [quant-ph].
[48] J. Apolín and D. P. Nadlinger, Recoil-Induced Errors and Their Correction in Photon-Mediated Entanglement between Atomic Qubits, PRX Quantum **7**, 010326 (2026).
[49] S. R. Cohen and J. D. Thompson, Quantum Computing with Circular Rydberg Atoms, PRX Quantum **2**, 030322 (2021).
[50] C. J. Picken, R. Legaie, K. McDonnell, and J. D. Pritchard, Entanglement of neutral-atom qubits with long ground-Rydberg coherence times, Quantum Science and Technology **4**, 015011 (2018).
[51] Supplemental Material, which further contains a detailed derivation of the stroboscopic time-evolution operator $\mathcal{U}(mT)$, closed form expressions of the variances, covariances, and expectation values of the interatomic separations, as well as an analysis of the protocol's stability, and the impact of anharmonic tweezer potentials.
[52] A. Kenfack and K. Zyczkowski, Negativity of the Wigner function as an indicator of non-classicality, Journal of Optics B: Quantum and Semiclassical Optics **6**, 396 (2004).
[53] P. T. Grochowski, H. Pichler, C. A. Regal, and O. Romero-Isart, Quantum control of continuous systems via nonharmonic potential modulation, Quantum **9**, 1824 (2025).
[54] R. B.-S. Tsai, X. Sun, A. L. Shaw, R. Finkelstein, and M. Endres, Benchmarking and Fidelity Response Theory of High-Fidelity Rydberg Entangling Gates, PRX Quantum **6**, 010331 (2025).
[55] J. Rui, D. Wei, A. Rubio-Abadal, S. Hollerith, J. Zeiher, D. M. Stamper-Kurn, C. Gross, and I. Bloch, A subradiant optical mirror formed by a single structured atomic layer, Nature **583**, 369 (2020).
[56] B. Olmos and I. Lesanovsky, Hybrid Sub- and Superradiant States in Emitter Arrays with Quantized Motion, Physical Review Letters **134**, 243602 (2025).
[57] K. Srakaew, P. Weckesser, S. Hollerith, D. Wei, D. Adler, I. Bloch, and J. Zeiher, A subwavelength atomic array switched by a single Rydberg atom, Nature Physics **19**, 714 (2023).
[58] T. Chalopin, C. Bouazza, A. Evrard, V. Makhalov, D. Dreon, J. Dalibard, L. A. Sidorenkov, and S. Nascimbene, Quantum-enhanced sensing using non-classical spin states of a highly magnetic atom, Nature Communications **9**, 4955 (2018).
[59] Y. Li, X. Cheng, L. Wang, X. Zhao, W. Hou, Y. Li, K. Rehan, M. Zhu, L. Yan, X. Qin, X. Peng, H. Yuan, Y. Lin, and J. Du, Multi-parameter quantum metrology with stabilized multi-mode squeezed state (2023), arXiv:2312.10379 [quant-ph].
[60] M. Magoni, C. Nill, and I. Lesanovsky, Coherent Spin-Phonon Scattering in Facilitated Rydberg Lattices, Physical Review Letters **132**, 133401 (2024).
[61] D. Brady and M. Fleischhauer, Non-Classical Spin-Phonon Correlations Induced by Rydberg Facilitation in a Lattice (2025), arXiv:2504.19679 [cond-mat].
[62] Repository containing all corresponding data and source code of this manuscript, 10.5281/zenodo.20528768 (2026).
[63] J. Mögerle, F. Hummel, A. Keil, T. Legrand, E. J. Braun, H. Menke, J. King, B. Olmos, S. Hofferberth, H. P. Büchler, and S. Weber, Accurate Modeling of Rydberg Atoms and Their Interactions: Theory and Implementation in PairInteraction (2026), arXiv:2605.14993 [physics.atom-ph].

End Matter

Experimental parameter sets

For the investigation in the main text, we use the experimental parameters

$$\begin{aligned} &a_0 = 2.7\,\mu\text{m},\ \omega = 2\pi \times 100\,\text{kHz}\,(x_0 \approx 24.1\,\text{nm}),\\ &C_6 = 4.11\,\text{GHz}\mu\text{m}^6,\ \eta = 0.121,\ \tau_2 = 890\,\text{ns},\\ &T = 4.98\,\mu\text{s},\ s = 5\,\text{ns}\,(\Omega = \pi \times 200\,\text{MHz}). \end{aligned} \tag{EM1}$$

Here, the van der Waals coefficient C_6 corresponds to ^{87}Rb atoms excited to the state $|45S\rangle$. The pairstate $|45S, 45S\rangle$ exhibits an energy separation of $3.5\,\text{GHz} \approx 5.6\Omega$ to the nearest relevant pairstate $|44P, 45P\rangle$. For this configuration, the localization parameter is $x_0/a_0 \approx 0.009$.
Additionally, we use a second parameter set

$$\begin{aligned} &a_0 = 1\,\mu\text{m},\ \omega = 2\pi \times 18\,\text{kHz}\,(x_0 \approx 56.8\,\text{nm}),\\ &C_6 = 87\,\text{MHz}\mu\text{m}^6,\ \eta = 0.286,\ \tau_2 = 20\,\text{ns},\\ &T = 30\,\mu\text{s},\ s = 1\,\text{ns}\,(\Omega = \pi \times 1\,\text{GHz}). \end{aligned} \tag{EM2}$$

In this case, C_6 corresponds to the state $|35S\rangle$ of ^{87}Rb. The energy separation of the pairstate $|35S, 35S\rangle$ to the next relevant pairstate $|34P, 35P\rangle$ is $9.15\,\text{GHz} \approx 2.9\Omega$. The localization parameter is $x_0/a_0 = 0.057$.
For both parameter sets, the Lamb-Dicke parameter η is calculated assuming a two-photon excitation scheme with typical wavelengths of $\lambda_1 = 780\,\text{nm}$ and $\lambda_2 = 480\,\text{nm}$, resulting in an effective laser wave vector $\kappa = 2\pi(1/\lambda_2 - 1/\lambda_1)$. The C_6 coefficients and all respective level spacings were computed using the pairinteraction software [63].

Validity of the fast pulse approximation

The analytical treatment in the main text relies on the fast-pulse approximation, in which the free Hamiltonian H_0 is neglected during the π-pulses, simplifying $\mathcal{U}_\pi = e^{-is(H_\text{L}+H_0)} \approx e^{-isH_\text{L}}$. A quantitative measure of the approximation quality is the residual Rydberg excitation $\langle n_\text{Ryd}\rangle = \sum_j \langle n_j\rangle$ at stroboscopic times $t = mT$, which

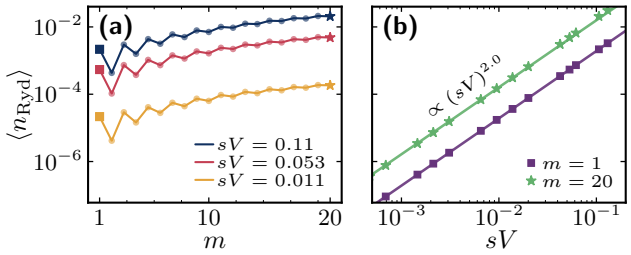

FIG. EM1. **Residual Rydberg excitation $\langle n_{\mathrm{Ryd}}\rangle$ at stroboscopic times for $N = 2$ atoms.** (a) $\langle n_{\mathrm{Ryd}}\rangle$ versus cycle number m for different control parameters sV. (b) $\langle n_{\mathrm{Ryd}}\rangle$ as a function of sV for $m = 1$ and $m = 20$ [see markers in (a)]. The clean $\propto (sV)^2$ scaling confirms that the fast-pulse approximation is controlled by the control parameter sV, and breaks down when the Rydberg interaction energy V becomes comparable to the Rabi frequency $\Omega = \pi/s$. All panels use the parameters from Eq. (EM1).

vanishes identically for perfect π-pulses but acquires a finite value when H_0 is retained during the pulse.

To assess this quantitatively for finite but small s, where the laser drive $\Omega = \pi/s \gg \omega, V(r)$ remains the dominant energy scale, we employ time-dependent perturbation theory to obtain

$$\mathcal{U}_\pi = e^{-isH_{\mathrm{L}}}\left(1 - is\int_0^1 d\tau e^{i\tau sH_{\mathrm{L}}} H_0 e^{-i\tau sH_{\mathrm{L}}} + \mathcal{O}(s^2)\right).$$

The leading correction to U_π is proportional to sH_0. Since the Rydberg interaction V is by far the largest energy scale in the free Hamiltonian ($V \gg \omega$) for both parameter sets from Eqs. (EM1) and (EM2), we can extract it to define a dimensionless control parameter sV. Consequently, at any stroboscopic time $t = mT$, the state of the system acquires a correction that is linear in this parameter: $|\Psi(mT)\rangle = |\Psi_{\mathrm{ideal}}(mT)\rangle + sV\,|\delta\Psi\rangle + \mathcal{O}((sV)^2)$. Because the ideal stroboscopic pulse sequence returns all atoms perfectly to the electronic ground state, it follows that $n_j\,|\Psi_{\mathrm{ideal}}(mT)\rangle = 0$. Therefore, the residual Rydberg population becomes $\langle n_{\mathrm{Ryd}}\rangle = (sV)^2\,\langle\delta\Psi|\sum_j n_j\,|\delta\Psi\rangle + \mathcal{O}((sV)^3)$.

Figure EM1 validates this $(sV)^2$ scaling numerically. Panel (a) shows $\langle n_{\mathrm{Ryd}}\rangle$ as a function of the cycle number m for different values of the control parameter sV. While the accumulated error expectedly grows with the number of dressing cycles, it remains highly suppressed for small values of sV. Panel (b) makes the underlying scaling explicit, plotting $\langle n_{\mathrm{Ryd}}\rangle$ directly against sV. The clean $(sV)^2$ collapse of the residual excitation for $m = 1$ and $m = 20$ confirms that the fast-pulse approximation is well-controlled as long as $sV \ll 1$, which is equivalent to $\Omega \gg V$.

Closed form expression of the time evolution operator

Within the limits discussed in the main text, the time evolution operator $\mathcal{U}(mT)$ can be expressed in closed form [Eq. (4)]. An exhaustive derivation can be found in the Supplemental Material [51]. The parameters are

$$\begin{aligned}
Z_1 &= 0,\\
J_1 &= \sqrt{N} i\eta\left(e^{-i\tau_2\omega} - 1\right)\frac{e^{-im\omega T} - 1}{e^{-i\omega T} - 1},\\
\beta_1 &= -m\omega T,
\end{aligned}$$

for the center-of-mass mode b_1 and

$$\begin{aligned}
Z_k &= \operatorname{arcsinh}\left(U_{m-1}(s_k)|B_k|\right)\frac{B_k u_k}{|B_k u_k|}e^{i\phi_k},\\
J_k &= \Bigg[\sqrt{1 + U_{m-1}^2(s_k)|B_k|^2}\,e^{i\phi_k}\left(\tilde{s}_k W_m^{(k)} - W_{m-1}^{(k)}\right)\\
&\quad - |B_k|^2 U_{m-1}(s_k) W_m^{(k)}\frac{u_k}{|u_k|}e^{i\phi_k}\Bigg] G_k\\
&\quad + B_k\Bigg[U_{m-1}(s_k)\frac{u_k}{|u_k|}\left(\tilde{s}_k W_m^{(k)} - W_{m-1}^{(k)}\right)\\
&\quad - \sqrt{1 + U_{m-1}^2(s_k)|B_k|^2}\,W_m^{(k)}\Bigg] G_k^*,\\
\beta_k &= \arg(u_k),\\
u_k &= U_{m-1}(s_k)\tilde{s}_k - U_{m-2}(s_k),\\
W_m^{(k)} &= \sum_{l=0}^{m-1} U_l(s_k),\\
s_k &= \mathrm{Re}(\tilde{s}_k),\\
\tilde{s}_k &= A_k e^{-i\phi_k},\\
\phi_k &= \omega T + (\tilde{\omega}_k - \omega)\tau_2,\\
G_k &= \frac{x_0 V_1}{2\tilde{\omega}_k}(Q_{Nk} - Q_{1k})\\
&\quad \times\left(e^{-2i\tau_2\tilde{\omega}_k} - 1 - \frac{\omega}{\tilde{\omega}_k}\left(e^{-i\tau_2\tilde{\omega}_k} - 1\right)^2\right),\\
A_k &= 1 + \frac{1}{2}\left(1 - e^{2i\tau_2\tilde{\omega}_k}\right)\frac{(\tilde{\omega}_k - \omega)^2}{2\omega\tilde{\omega}_k},\\
B_k &= \left(1 - e^{-2i\tau_2\tilde{\omega}_k}\right)\frac{\tilde{\omega}_k^2 - \omega^2}{4\omega\tilde{\omega}_k},\\
\tilde{\omega}_k &= \sqrt{\omega^2 + 2\lambda_k x_0^2 V_2\omega},
\end{aligned}$$

for all relative modes b_k with $k \geq 2$. We use the Chebyshev polynomials of the second kind U_l, which are defined by the recurrence relation

$$\begin{aligned}
U_{-2}(x) &= -1,\\
U_{-1}(x) &= 0,\\
U_l(x) &= 2xU_{l-1}(x) - U_{l-2}(x) \quad \forall l \in \mathbb{N}_0.
\end{aligned}$$

With these expressions, the positional covariances between the j-th and k-th atoms are given by

$$\mathcal{C}_{j,k} = x_0^2 \sum_{l=1}^{N} Q_{jl} Q_{kl} |\Omega_l|^2, \tag{EM3}$$

where we defined

$$\Omega_l = \sqrt{1 + U_{m-1}^2(s_l)|B_l|^2} - \frac{u_l}{|u_l|} U_{m-1}(s_l) B_l e^{i\phi_l}.$$

The expectation values of the atomic positions take the form

$$\langle x_j \rangle = 2x_0 \sum_{l=1}^{N} Q_{jl} \mathrm{Re}(\Omega_l^* J_l). \tag{EM4}$$

Using Eqs. (EM3) and (EM4), we can determine the variances

$$\mathrm{Var}(\delta_{jk}) = x_0^2 \sum_{l=2}^{N} (Q_{jl} - Q_{kl})^2 |\Omega_l|^2 \tag{EM5}$$

and expectation values

$$\langle \delta_{jk} \rangle = 2x_0 \sum_{l=2}^{N} (Q_{kl} - Q_{jl}) \mathrm{Re}(\Omega_l^* J_l) \tag{EM6}$$

of the interatomic distances δ_{jk}, thereby fully characterizing their Gaussian probability distributions.

SUPPLEMENTAL MATERIAL

Creating squeezed and non-classical collective motional many-body states through stroboscopic Rydberg dressing

Roman Wußler[1], Chris Nill[1,2], Sylvain de Léséleuc[3,4], Christian Groß[5], Igor Lesanovsky[1,6]

[1] *Institut für Theoretische Physik, Universität Tübingen, Auf der Morgenstelle 14, 72076 Tübingen, Germany*
[2] *Institute for Applied Physics, University of Bonn, Wegelerstraße 8, 53115 Bonn, Germany*
[3] *Institute for Molecular Science, National Institutes of Natural Sciences, 444-8585 Okazaki, Japan*
[4] *RIKEN Center for Quantum Computing (RQC), 351-0198 Wako, Japan*
[5] *Physikalisches Institut and Center for Integrated Quantum Science and Technology, Universität Tübingen, Auf der Morgenstelle 14, 72076 Tübingen, Germany*
[6] *School of Physics and Astronomy and Centre for the Mathematics and Theoretical Physics of Quantum Non-Equilibrium Systems, The University of Nottingham, Nottingham, NG7 2RD, United Kingdom*

Derivation of the time evolution operator $\mathcal{U}(mT)$ at stroboscopic times

The following derivation yields an intuitive, closed-form expression for the time evolution operator $\mathcal{U}(mT)$. It describes the evolution of the system during m dressing cycles of the stroboscopic dressing protocol, which is illustrated in Figs. 1(b) and (c) in the main text. Each dressing cycle is decomposed into four phases. During the first one of duration τ_1, the system evolves freely under the Rydberg Hamiltonian ($\hbar = 1$)

$$H_0 = \omega \sum_{j=1}^{N} a_j^\dagger a_j + \sum_{j=1}^{N-1} n_j n_{j+1} \left(V_0 + V_1(x_{j+1} - x_j) + \frac{V_2}{2}(x_{j+1} - x_j)^2 \right), \tag{S1}$$

where ω is the trapping frequency of the optical tweezers with the ladder operators a_j and $a_j^\dagger$, describing the quantized motion of the atoms along the chain axis. The Rydberg interaction potential is assumed to be a van der Waals potential $V(r) = C_6/r^6$, where r is the interatomic distance of two atoms. Employing a second-order Taylor expansion leads to the Rydberg interaction term in Eq. S1. The potential is parameterized by its interaction strength $V_0 = C_6/a_0^6$, gradient $V_1 = -6C_6 a_0^7$, and curvature $V_2 = 42C_6/a_0^8$, evaluated at the equilibrium distance a_0 between neighboring atoms. Since $n_j = |{\uparrow}\rangle\langle{\uparrow}|_j$ is the projector onto the Rydberg state of the j-th atom, this term only contributes if two neighboring atoms are excited to the Rydberg state. The operator

$$x_j = x_0 \left(a_j + a_j^\dagger \right) = \frac{1}{\sqrt{2 m_0 \omega}} \left(a_j + a_j^\dagger \right) \tag{S2}$$

describes the displacement of the j-th atom out of its equilibrium position, where m_0 denotes the atomic mass.
During the second phase of duration s, the system is driven by a laser with Rabi frequency $\Omega = \pi/s$, corresponding to a resonant π-pulse, which couples the ground state $|{\downarrow}\rangle$ to the Rydberg state $|{\uparrow}\rangle$. This leads to the additional laser Hamiltonian

$$H_{\mathrm{L}} = \frac{\pi}{2s} \sum_{j=1}^{N} \left(|{\downarrow}\rangle\langle{\uparrow}|_j \, e^{-i\kappa x_j} + |{\uparrow}\rangle\langle{\downarrow}|_j \, e^{i\kappa x_j} \right), \tag{S3}$$

where κ is the projection of the wave vector onto the chain axis. We consider the limit of strong laser pulses, such that $\pi/s = \Omega \gg \omega, V_0, x_0 V_1, x_0^2 V_2$ is by orders of magnitude the largest energy scale in the system, and pulses can break the Rydberg blockade. Thus, during the laser pulses, we can neglect the Rydberg Hamiltonian H_0 and only consider the evolution of the system under the laser Hamiltonian H_{L}, see End Matter. After the first π-pulse was applied, the laser is switched off again. The system then evolves freely under the Rydberg Hamiltonian H_0 for a time τ_2, before a second π-pulse of duration s is applied, completing the dressing cycle. Consequently, the time evolution operator for one dressing cycle reads

$$\mathcal{U}(T) = \underbrace{e^{-isH_{\mathrm{L}}}}_{\mathcal{U}_\pi} e^{-i\tau_2 H_0} e^{-isH_{\mathrm{L}}} e^{-i\tau_1 H_0}. \tag{S4}$$

The time evolution operator of a single π-pulse can be simplified to

$$\mathcal{U}_\pi = \exp\left\{-i\frac{\pi}{2}\sum_{j=1}^{N}\Big(|\downarrow\rangle\langle\uparrow|_j\, e^{-i\kappa x_j} + |\uparrow\rangle\langle\downarrow|_j\, e^{i\kappa x_j}\Big)\right\} = (-i)^N \prod_{j=1}^{N}\Big(|\downarrow\rangle\langle\uparrow|_j\, e^{-i\kappa x_j} + |\uparrow\rangle\langle\downarrow|_j\, e^{i\kappa x_j}\Big). \tag{S5}$$

By utilizing that $\mathcal{U}_\pi$ is unitary, the time evolution operator $\mathcal{U}(T)$ can be written as

$$\mathcal{U}(T) = \mathcal{U}_\pi \underbrace{\mathcal{U}_\pi \mathcal{U}_\pi^\dagger}_{=1} e^{-i\tau_2 H_0} \mathcal{U}_\pi e^{-i\tau_1 H_0} = \underbrace{\mathcal{U}_\pi^2}_{=(-1)^N}\, e^{-i\tau_2 \mathcal{U}_\pi^\dagger H_0 U_\pi} e^{-i\tau_1 H_0}. \tag{S6}$$

We define the Lamb-Dicke parameter $\eta = \kappa x_0$ and the projector $\mathcal{P}_j = |\downarrow\rangle\langle\downarrow|_j$ onto the ground state $|\downarrow\rangle_j$ of the j-th atom. The relation $\mathcal{U}_\pi^\dagger n_j \mathcal{U}_\pi = \mathcal{P}_j$ shows that the stroboscopic dressing protocol maps the interactions between atoms in the Rydberg states to effective interactions between ground-state atoms. Using this identity together with $\mathcal{U}_\pi^\dagger a_j \mathcal{U}_\pi = a_j - i\eta(n_j - \mathcal{P}_j)$, we obtain

$$\begin{aligned}\mathcal{U}(T) = (-1)^N \exp\Bigg\{-i\tau_2 \Bigg[&\omega\sum_{j=1}^{N}\Big(a_j^\dagger a_j + i\eta(n_j - \mathcal{P}_j)\Big(a_j - a_j^\dagger\Big) + \eta^2\Big) \\ &+ \sum_{j=1}^{N-1}\mathcal{P}_j\mathcal{P}_{j+1}\Big(V_0 + V_1(x_{j+1}-x_j) + \frac{V_2}{2}(x_{j+1}-x_j)^2\Big)\Bigg]\Bigg\} \\ \cdot \exp\Bigg\{-i\tau_1 \Bigg[&\omega\sum_{j=1}^{N} a_j^\dagger a_j + \sum_{j=1}^{N-1} n_j n_{j+1}\Big(V_0 + V_1(x_{j+1}-x_j) + \frac{V_2}{2}(x_{j+1}-x_j)^2\Big)\Bigg]\Bigg\}.\end{aligned} \tag{S7}$$

All atoms are initialized in the electronic ground state, i.e. $|\Psi(0)\rangle = |\downarrow\rangle^{\otimes N} \otimes |\Psi_{\text{motion}}(0)\rangle$. Since the operators in the exponents of $\mathcal{U}(T)$ are diagonal in the electronic basis, the system never leaves the electronic ground state at stroboscopic times. Therefore, we can project the dynamics onto this subspace by replacing the projectors with their respective eigenvalues, i.e. $n_j \to 0$ and $\mathcal{P}_j \to 1$. This leads to

$$\begin{aligned}\mathcal{U}(T) = (-1)^N e^{-i\tau_2(N\omega\eta^2 + (N-1)V_0)} \exp\Bigg\{-i\tau_2 \Bigg[&\omega\sum_{j=1}^{N}\Big(a_j^\dagger a_j - i\eta\Big(a_j - a_j^\dagger\Big)\Big) \\ &+ \sum_{j=1}^{N-1}\Big(V_1(x_{j+1}-x_j) + \frac{V_2}{2}(x_{j+1}-x_j)^2\Big)\Bigg]\Bigg\} \exp\Bigg\{-i\tau_1\omega\sum_{j=1}^{N} a_j^\dagger a_j\Bigg\}.\end{aligned} \tag{S8}$$

Due to the finite curvature of the Rydberg interaction potential, the time evolution operator contains mixed-mode terms $x_{j+1}x_j$ that couple adjacent sites. To diagonalize the quadratic term of the exponential and further simplify $\mathcal{U}(T)$, we introduce the normal modes of the system, given by

$$b_j = \sum_{k=1}^{N} Q_{kj} a_k, \tag{S9}$$

with the transformation matrix elements

$$Q_{kj} = \begin{cases} \frac{1}{\sqrt{N}} & \text{for } j = 1, \\ \sqrt{\frac{2}{N}}\cos\Big(\frac{(j-1)\left(k-\frac{1}{2}\right)\pi}{N}\Big) & \text{for } 2 \le j \le N. \end{cases} \tag{S10}$$

Since the transformation matrix Q is orthogonal, the new operators satisfy the bosonic commutation relations $[b_j, b_k^\dagger] = \delta_{jk}$ and $[b_j, b_k] = [b_j^\dagger, b_k^\dagger] = 0$. The mode $b_1 = \sum_{k=1}^{N} a_k/\sqrt{N}$ is the center-of-mass mode of the system, while all other modes b_j with $j > 1$ describe the relative motion of the atoms. Inserting the normal modes into the time evolution

operator $\mathcal{U}(T)$ for a single dressing cycle, and raising it to the power of m, we obtain the time evolution operator for m dressing cycles, given by

$$\begin{aligned}\mathcal{U}(mT) &= (-1)^{mN} e^{-im\tau_2\left(N\omega\eta^2+(N-1)\left(V_0+x_0^2V_2\right)\right)}\left(\exp\left\{-i\tau_2\omega\left[b_1^\dagger b_1 - i\sqrt{N}\eta\left(b_1-b_1^\dagger\right)\right]\right\}\exp\left\{-i\tau_1\omega b_1^\dagger b_1\right\}\right)^m \\ &\quad\cdot\prod_{k=2}^{N}\left(\exp\left\{-i\tau_2\left[\left(\omega+\lambda_k x_0^2V_2\right)b_k^\dagger b_k + x_0V_1(Q_{Nk}-Q_{1k})\left(b_k^\dagger+b_k\right)+\frac{\lambda_k x_0^2V_2}{2}\left(b_k^{\dagger 2}+b_k^2\right)\right]\right\}\right. \\ &\quad\left.\cdot\exp\left\{-i\tau_1 b_k^\dagger b_k\right\}\right)^m \\ &= \prod_{k=1}^{N}\mathcal{U}_k(mT),\end{aligned} \tag{S11}$$

where we defined

$$\lambda_k = 4\sin^2\left(\frac{(k-1)\pi}{2N}\right). \tag{S12}$$

The time evolution operator factorizes into a product over all N normal modes of the system, indicating that they decouple and evolve independently. Since the operators $\mathcal{U}_k(mT)$ are Gaussian, meaning that they contain at most quadratic bosonic operators in their exponents, we can proceed by applying a Bloch-Messiah decomposition [41] to each mode separately. Specifically, this allows us to express the time evolution operator as an ordered sequence of fundamental Gaussian unitaries

$$\mathcal{U}_k(mT) = \mathcal{S}_k(Z_k)\mathcal{D}_k(J_k)\mathcal{R}_k(\beta_k)e^{i\gamma_k}, \tag{S13}$$

where $\mathcal{S}_k(Z_k) = e^{\frac{Z_k^*}{2}b_k^2 - \frac{Z_k}{2}b_k^{\dagger 2}}$, $\mathcal{D}_k(J_k) = e^{J_k b_k^\dagger - J_k^* b_k}$ and $\mathcal{R}_k(\beta_k) = e^{i\beta_k b_k^\dagger b_k}$ denote the squeezing, displacement and rotation operators respectively. To calculate the parameters Z_k, J_k, β_k, and γ_k for each mode, we exploit the algebraic structure determined by the operators $\{1, b_k, b_k^\dagger, b_k^2, b_k^{\dagger 2}, b_k^\dagger b_k\}$. Therefore, we define the six matrices

$$\begin{aligned}M_1 &= \begin{pmatrix}0&0&0&1\\0&0&0&0\\0&0&0&0\\0&0&0&0\end{pmatrix}, \quad M_b = \frac{1}{\sqrt{2}}\begin{pmatrix}0&0&-1&0\\0&0&0&1\\0&0&0&0\\0&0&0&0\end{pmatrix}, \quad M_{b^\dagger} = \frac{1}{\sqrt{2}}\begin{pmatrix}0&-1&0&0\\0&0&0&0\\0&0&0&-1\\0&0&0&0\end{pmatrix}, \\ M_{b^2} &= \begin{pmatrix}0&0&0&0\\0&0&-2&0\\0&0&0&0\\0&0&0&0\end{pmatrix}, \quad M_{b^{\dagger 2}} = \begin{pmatrix}0&0&0&0\\0&0&0&0\\0&2&0&0\\0&0&0&0\end{pmatrix}, \quad M_{b^\dagger b} = \begin{pmatrix}0&0&0&-\frac{1}{2}\\0&-1&0&0\\0&0&1&0\\0&0&0&0\end{pmatrix},\end{aligned} \tag{S14}$$

which satisfy the same commutation relations as the corresponding bosonic operators, forming a faithful finite-dimensional matrix representation of the algebra. The Bloch-Messiah decomposition can be performed using the Baker-Campbell-Hausdorff (BCH) formula, which relies exclusively on the commutation relations among the involved operators. Therefore, the decomposition is entirely governed by the structure of the underlying Lie algebra. Since the matrices and the corresponding bosonic operators are two representations of the same Lie algebra, the time evolution matrix can be decomposed in the same way as the original bosonic operator. Consequently, we can replace the operators with their corresponding matrices, compute the matrix exponentials, and equate the result to the target matrix representing the operator $\mathcal{S}_k(Z_k)\mathcal{D}_k(J_k)\mathcal{R}_k(\beta_k)e^{i\gamma_k}$. By solving the resulting system of equations, we can calculate all parameters of interest. Up to a global phase that does not affect any expectation values, the time evolution operator is given by

$$\mathcal{U}(mT) = \prod_{k=1}^{N}\mathcal{S}_k(Z_k)\mathcal{D}_k(J_k)\mathcal{R}_k(\beta_k), \tag{S15}$$

with the parameters

$$\begin{aligned}Z_1 &= 0, \\ J_1 &= \sqrt{N}i\eta\left(e^{-i\tau_2\omega}-1\right)\frac{e^{-im\omega T}-1}{e^{-i\omega T}-1}, \\ \beta_1 &= -m\omega T,\end{aligned} \tag{S16}$$

for the center-of-mass mode b_1 and

$$\begin{aligned}
Z_k &= \operatorname{arcsinh}\big(U_{m-1}(s_k)|B_k|\big)\frac{B_k u_k}{|B_k u_k|}e^{i\phi_k},\\
J_k &= \left[\sqrt{1+U_{m-1}^2(s_k)|B_k|^2}e^{i\phi_k}\Big(\tilde{s}_k W_m^{(k)} - W_{m-1}^{(k)}\Big) - |B_k|^2 U_{m-1}(s_k)W_m^{(k)}\frac{u_k}{|u_k|}e^{i\phi_k}\right]G_k\\
&\quad + B_k\left[U_{m-1}(s_k)\frac{u_k}{|u_k|}\Big(\tilde{s}_k W_m^{(k)} - W_{m-1}^{(k)}\Big) - \sqrt{1+U_{m-1}^2(s_k)|B_k|^2}W_m^{(k)}\right]G_k^*,\\
\beta_k &= \arg(u_k),\\
u_k &= U_{m-1}(s_k)\tilde{s}_k - U_{m-2}(s_k),\\
W_m^{(k)} &= \sum_{l=0}^{m-1} U_l(s_k),\\
s_k &= \operatorname{Re}(\tilde{s}_k),\\
\tilde{s}_k &= A_k e^{-i\phi_k},\\
\phi_k &= \omega T + (\tilde{\omega}_k - \omega)\tau_2,\\
G_k &= \frac{x_0 V_1}{2\tilde{\omega}_k}(Q_{Nk} - Q_{1k})\left(e^{-2i\tau_2\tilde{\omega}_k} - 1 - \frac{\omega}{\tilde{\omega}_k}\Big(e^{-i\tau_2\tilde{\omega}_k} - 1\Big)^2\right),\\
A_k &= 1 + \frac{1}{2}\Big(1 - e^{2i\tau_2\tilde{\omega}_k}\Big)\frac{(\tilde{\omega}_k - \omega)^2}{2\omega\tilde{\omega}_k},\\
B_k &= \Big(1 - e^{-2i\tau_2\tilde{\omega}_k}\Big)\frac{\tilde{\omega}_k^2 - \omega^2}{4\omega\tilde{\omega}_k},\\
\tilde{\omega}_k &= \sqrt{\omega^2 + 2\lambda_k x_0^2 V_2 \omega},
\end{aligned} \tag{S17}$$

for all relative modes b_k where k is a natural number between 2 and N. We used the Chebyshev polynomials of the second kind U_l, which are defined by the recurrence relation

$$\begin{aligned}
U_{-2}(x) &= -1,\\
U_{-1}(x) &= 0,\\
U_l(x) &= 2xU_{l-1}(x) - U_{l-2}(x) \quad \forall l \in \mathbb{N}_0.
\end{aligned} \tag{S18}$$

Variances, covariances and expectation values of the interatomic distances

To quantify the motional squeezing discussed in the main text, we derive in this section the explicit analytical expressions for the variances, covariances, and expectation values of the interatomic distances. We assume the system to be initialized in the electronic and motional ground state $|\Psi(0)\rangle = |\downarrow, 0\rangle^{\otimes N}$. Consequently, after m dressing cycles, the system (up to a global phase that does not affect any expectation values) evolves to

$$|\Psi(mT)\rangle = \mathcal{U}(mT)\,|\Psi(0)\rangle = |\downarrow\rangle^{\otimes N}\prod_{k=1}^{N}\mathcal{S}_k(Z_k)\mathcal{D}_k(J_k)\,|0\rangle\,. \tag{S19}$$

By utilizing the transformations $\mathcal{S}_k^\dagger(r_k e^{i\theta_k})b_k\mathcal{S}_k(r_k e^{i\theta_k}) = \cosh(r_k)b_k - \sinh(r_k)e^{i\theta_k}b_k^\dagger$ and $\mathcal{D}_k^\dagger(J_k)b_k\mathcal{D}_k(J_k) = b_k + J_k$ of the annihilation operator b_k under the squeezing and displacement operators, we can calculate the expectation values of arbitrary bosonic operators. The positional covariances between two atoms are given by

$$\mathcal{C}_{j,k} = \langle x_j x_k\rangle - \langle x_j\rangle\langle x_k\rangle = x_0^2\sum_{l=1}^{N} Q_{jl}Q_{kl}|\Omega_l|^2, \tag{S20}$$

where we defined

$$\Omega_l = \sqrt{1+U_{m-1}^2(s_l)|B_l|^2} - \frac{u_l}{|u_l|}U_{m-1}(s_l)B_l e^{i\phi_l}. \tag{S21}$$

The expectation values of the atomic positions are given by

$$\langle x_j \rangle = 2x_0 \sum_{l=1}^{N} Q_{jl} \mathrm{Re}(\Omega_l^* J_l). \tag{S22}$$

Using Eqs. S20 and S22, we can determine the variances

$$\mathrm{Var}(\delta_{jk}) = \underbrace{\mathrm{Var}(x_j)}_{=\mathcal{C}_{j,j}} + \mathrm{Var}(x_k) - 2\mathcal{C}_{j,k} = x_0^2 \sum_{l=2}^{N} (Q_{jl} - Q_{kl})^2 |\Omega_l|^2 \tag{S23}$$

and expectation values

$$\langle \delta_{jk} \rangle = \langle x_k \rangle - \langle x_j \rangle = 2x_0 \sum_{l=2}^{N} (Q_{kl} - Q_{jl}) \mathrm{Re}(\Omega_l^* J_l) \tag{S24}$$

of the interatomic distances $\delta_{jk} = x_k - x_j$, thereby fully characterizing their Gaussian probability distributions. These analytical expressions form the basis of the motional dynamics of the system, presented in Fig. 2 of the main text.

Periodicities and protocol stability

For the stroboscopic dressing protocol to remain stable over many dressing cycles, the atoms must stay within their trapping potentials, requiring their individual mean displacements $\langle x_j \rangle$ to be tightly bound. To understand the conditions for this stability, shown in Fig. 2 (e) and (f), we need to analyze the periodic behavior of the variances of the interatomic distances and the expectation values of the individual atomic displacements with respect to the phase ωT. We will show in the following that while the variances are π-periodic in ωT, the mean displacements are strictly 2π-periodic.

To demonstrate this, we focus on the phase factor $e^{-i\phi_l} = e^{-i(\omega T + (\tilde{\omega}_l - \omega)\tau_2)}$, as it contains the sole dependence on the phase ωT in our analytical expressions. Under a shift of $\omega T \to \omega T + \pi$, it acquires a minus sign, $e^{-i\phi_l} \to -e^{-i\phi_l}$, which implies $\tilde{s}_l \to -\tilde{s}_l$ and, for its real part, $s_l \to -s_l$. Using the parity relation $U_m(-x) = (-1)^m U_m(x)$ of the Chebyshev polynomials, it follows that $u_l = U_{m-1}(s_l)\tilde{s}_l - U_{m-2}(s_l)$ transforms as $u_l \to (-1)^m u_l$. Therefore, $\Omega_l \to \Omega_l$ remains invariant, implying that $\mathcal{C}_{j,k}$ and $\mathrm{Var}(\delta_{jk})$ also remain invariant. Thus, they are π-periodic in ωT.

On the other hand, the expectation values $\langle x_j \rangle$ depend linearly on the displacement J_l, which includes the sum $W_m^{(k)} = \sum_{l=0}^{m-1} U_l(s_k)$. Since this sum mixes Chebyshev polynomials of both, even and odd degrees, it does not possess a simple global parity under $\omega T \to \omega T + \pi$. As a result, J_l does not return to its initial value under a π shift. A full shift of 2π is required to restore $J_l \to J_l$, demonstrating that the expectation values $\langle x_j \rangle$ are strictly 2π-periodic in ωT.

Knowing these periodicities allows us to optimize the cycle duration T, such that the variances $\mathrm{Var}(\delta_{jk})$ of the interatomic distances become minimal while the individual atoms stay tightly bound in their traps. Since $\mathrm{Var}(\delta_{jk})$ is π-periodic in ωT, we first determine T_{opt} by minimizing these variances within the half-period $\omega T \in [0, \pi)$. Because the mean displacements $\langle x_j \rangle$ are strictly 2π-periodic, the choices ωT_{opt} and $\omega T_{\mathrm{opt}} + \pi$ yield the same minimized variances but result in different atomic displacements. To prevent atom loss, we evaluate both regimes and select the cycle duration that minimizes the mean displacements $\langle x_j \rangle$, as seen in Fig. 2 (e) and (f).

Anharmonic tweezer potential

To quantify the impact of trap anharmonicities, we extend the harmonic potential by a quartic perturbation, following [36]. The corresponding correction to the Hamiltonian H_0 reads

$$H_{\mathrm{anharm}} = -\frac{\omega\epsilon}{4} \sum_{j=1}^{N} (a_j + a_j^\dagger)^4, \tag{S25}$$

where the parameter ϵ quantifies the anharmonicity of the trapping potential.

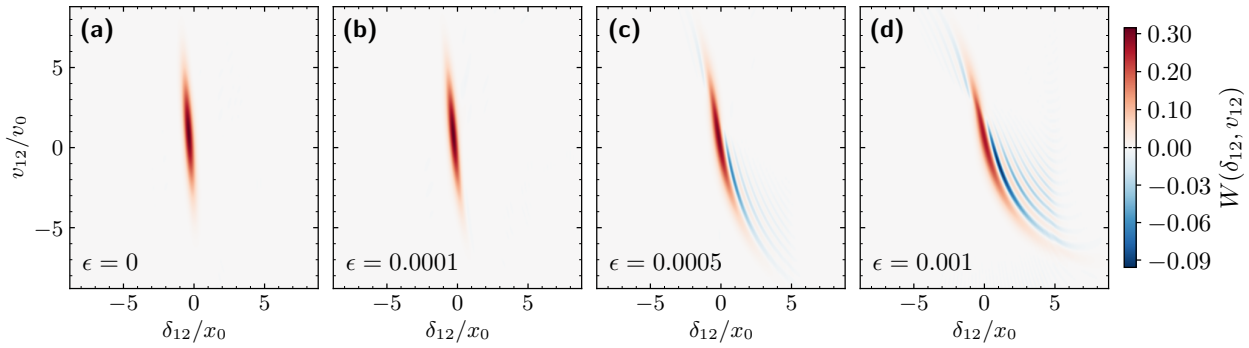

FIG. S1. **Impact of anharmonic tweezer potentials on motional squeezing.** Wigner functions $W(\delta_{12}, v_{12})$ of the relative coordinate δ_{12} and relative velocity v_{12} for $N = 2$ atoms after $m = 20$ dressing cycles, computed including the anharmonic trap Hamiltonian from Eq. (S25). **(a)** For a perfectly harmonic trap ($\epsilon = 0$), the motional state is Gaussian and well-described by the analytical prediction from Eq. (S20). **(b)–(d)** With increasing anharmonicity ϵ, the Wigner function experiences progressive shearing and non-Gaussian deformations, leading to the emergence of negative regions (indicated in blue). All panels use the parameters from Eq. (EM1).

In Fig. S1, we vary ϵ to evaluate the impact of anharmonic tweezer potentials on the motional state. For sufficiently harmonic traps with $\epsilon \leq 10^{-4}$, the motional state remains Gaussian (a), (b) and can be described by our analytical model from Eq. (S20). However, for increased values of ϵ (c), (d), the Wigner function experiences significant shearing, and pronounced negative regions emerge [35]. Current standard optical tweezers typically exhibit anharmonicities on the order of $\epsilon \approx 10^{-3}$ [36]. While realizing purely Gaussian, strongly squeezed states will require improved trap harmonicity, this inherent anharmonicity is not strictly a limitation. Instead, it can be actively leveraged as a resource for generating genuine non-classical many-body motional states [53].